Cross Section Measurement of Vector Meson Quasi-Photoproduction at High Four-Momentum Transfer using the ZEUS Detector at the HERA Collider.

PhD Thesis

Katarzyna Helena Klimek

Institute of Nuclear Physics,
Kawiory 26a, 30-055 Kraków, Poland

Kraków, 2001

Abstract

Photoproduction of vector mesons, $\gamma p \to VY$, where Y is the system into which the proton dissociates, has been measured in e^+p interactions with the ZEUS detector at HERA using an integrated luminosity of 24 pb^{-1}. The data were taken at a photon-proton center-of-mass energy $W \simeq 100$ GeV and extend up to $-t = 10$ GeV^2, where t is the square of the four-momentum transferred to the vector meson. The differential cross section $\mathrm{d}\sigma/\mathrm{d}t$ for ρ^0, ϕ and J/ψ production are compared to the expectations of phenomenological models.

Contents

1 Introduction **1**

2 Diffractive Vector Meson Production in Positron-Proton Interaction **2**
2.1 Positron-Proton Scattering . . . 2
2.2 Vector Meson Dominance Model . . . 3
2.3 Diffraction . . . 5
2.4 Diffraction in Terms of Regge Formalism . . . 5
2.5 Diffractive Photoproduction . . . 6
2.6 Vector Meson Production . . . 8
2.6.1 Expectations of the Regge Phenomenology . . . 10
2.6.2 Expectations of the pQCD Models . . . 12

3 ZEUS - a Detector at the HERA Accelerator **14**
3.1 HERA . . . 14
3.2 The ZEUS Detector . . . 16

4 Reconstruction and Event Selection **22**
4.1 Reconstruction of the Kinematic Variables . . . 22
4.2 Trigger Configuration . . . 24
4.2.1 Trigger for High t Vector Mesons . . . 24
4.2.2 Accidental Coincidences . . . 25
4.3 Event Selection . . . 25
4.4 Cross Section Evaluation . . . 27

5 Monte Carlo Simulation **30**
5.1 EPSOFT MC Generator . . . 30
5.2 DIFFVM MC generator . . . 31
5.3 Radiative Corrections . . . 32
5.4 ZEUS Monte Carlo Simulation . . . 32
5.5 REMC Trigger Efficiency . . . 33
5.5.1 Data - Monte Carlo Comparison . . . 33
5.5.2 REMC Trigger Efficiency Parameterization . . . 34
5.6 44m Tagger Acceptance . . . 37
5.6.1 Bremsstrahlung Process . . . 37
5.6.2 Photoproduction Acceptance . . . 40
5.7 Reweighting of the Monte Carlo . . . 42
5.7.1 M_Y evolution with $-t$ . . . 42
5.7.2 Forward Energy Flow . . . 48
5.7.3 Separation of Elastic and Proton-dissociative Events . . . 50
5.7.4 Reweighting of the MC for the ρ^0 meson . . . 52
5.7.5 Reweighting of the MC for the ϕ meson . . . 56
5.7.6 Reweighting of the MC for the J/ψ meson . . . 59
5.8 Resolution . . . 62
5.9 Acceptance . . . 64

6 Systematic Checks **66**

7 Experimental Results **71**
7.1 ρ^0 Photoproduction 71
7.1.1 Differential Cross Section $d\sigma/\mathrm{d}t$ 71
7.1.2 W-dependence of the Cross Section 74
7.2 ϕ Photoproduction 81
7.2.1 Differential Cross Section $d\sigma/\mathrm{d}t$ 81
7.2.2 W-dependence of the Cross Section 83
7.3 J/ψ Photoproduction 89
7.3.1 Differential Cross Section $d\sigma/dt$ 89
7.3.2 W-dependence of the Cross Section 91
7.4 Cross Sections Ratios 94

8 Comparison of the Results with Theoretical Predictions **98**
8.1 Light Vector Mesons 98
8.2 Heavy Vector Mesons 101
8.3 Discussion 103

9 Summary and Conclusions **105**

A Tables of Data **107**

List of Figures

1 The schematic diagram of positron-proton scattering via one-photon exchange. The four-vectors of the particles are given in braces. 2

2 The vector meson production in the Vector Dominance Model, where the photon fluctuates into a vector meson, which then scatters off the proton. 4

3 Three types of diffractive processes in hadron-hadron collisions: a) elastic scattering, b) single dissociation, c) double dissociation. 5

4 Total photoproduction cross section as a function of the center-of-mass energy W of the γp system. The lines correspond to Regge fits with $\alpha_{I\!P}(0) = 1.0808$ (solid) and $\alpha_{I\!P}(0) = 1.045$ (dotted). 7

5 Sketch showing the kinematic variables describing vector meson elastic photoproduction (left) and proton-dissociative photoproduction (right). 8

6 Definition of the planes and angles describing the decay of the vector meson V into two charged particles q^+ and q^-. 9

7 The diagram of the hard diffractive production of vector mesons described as two gluon exchange. 12

8 Hera collider with the four experimental halls and the preaccelerator system. . . 14

9 Integrated luminosity delivered by HERA during the data taking periods from 1993 to 1997. 16

10 Schematic view of the ZEUS detector. 18

11 Cross sectional view of the ZEUS calorimeter along the beam direction. 19

12 General layout of the ZEUS luminosity monitor and the 44m tagger. 21

13 The diffractive vector meson production signatures in the ZEUS detector with two tracks in the CTD, energy deposit in the FCAL from the proton dissociated system Y and the scattered positron detected in the 44m tagger. 22

14 Comparison between the data (dots) and the EPSOFT MC (histograms) of the measured pseudorapidity η^+ and transverse momentum p_t^+ of the positive track and the center-of-mass energy W for ρ^0,ϕ and J/ψ. The dotted lines correspond to the selection cuts. 28

15 Comparison between the data (dots) and the EPSOFT MC (histograms) of the helicity angles ϑ_h and φ_h, the vector meson pseudorapidity η_{VM} and the rapidity gap RG (the difference between the vector meson pseudorapidity and the rapidity of the most backward track in the FCAL) for ρ^0,ϕ and J/ψ. 28

16 Comparison of the REMC trigger efficiency between the data (dots) and the MC (histogram) as a function of electromagnetic energy in one section of the RCAL. 34

17 Comparison of the REMC trigger efficiency as a function of $-t$, W and M_{KK} between the data (dots) and the MC (histogram) for the ϕ meson using the standard REMC trigger simulation. 34

18 REMC efficiency for the ρ^0 meson a function of: a) sum of tracks momenta, b) positive track momentum, c) negative track momentum, together with fitted parameterization according to Eq. 53. 35

19 Comparison of the efficiency for ϕ between data (dots) and EPSOFT MC (histograms) with the REMC trigger efficiency parameterization according to Eq.53, as a function of different kinematic variables of $-t$, W and M_{KK}. 36

20 Overview of the tagging system for the photon and the electron/positron scattered under small angle. 37
21 Run 26462, the bremsstrahlung γ energy distribution in the LUMI photon calorimeter as a function of ADC counts for all events (solid histogram, up) and for events tagged in the 44m tagger (dashed histogram, up), together with the tagging efficiency A_B (dots, down). 38
22 The v_x measured in the CTD, v_x^{CTD} versus E_{max} for the bremsstrahlung data in the run range 25204-26086. Each dot corresponds to one run. The errors are not drawn. 39
23 Comparison of the 44m tagger acceptance A_B between the bremsstrahlung data from the run 22151 and the MC with the tuned parameters as a function of ADC channels in the LUMI photon calorimeter. 40
24 The acceptance of the 44m tagger as a function of the collision energy W for the photoproduction events. The shaded band corresponds to the systematic uncertainty of the tagger acceptance. The vertical lines indicate the W range used in the analysis. 40
25 The generated proton dissociative mass M_Y^{GEN} versus the reconstructed mass M_Y^{REC} for the ρ^0 EPSOFT MC. The solid line indicates a result of the linear fit in the M_Y^{GEN} range $5 < M_Y^{GEN} < 30$. 42
26 Comparison between the data (dots), EPSOFT MC (solid histograms) and DIFFVM (dotted histogram, only ρ^0) for the E_{FCAL} distributions in different t bins. The histograms are normalized to the total number of events in the histogram. Quoted mean values correspond to the data. 43
27 Comparison of β' values for different vector mesons. 46
28 Comparison between the data (dots) and the reweighted EPSOFT MC (histograms) for the E_{FCAL} distributions in few t bins. Quoted mean values correspond to the Monte Carlo. 46
29 Comparison in three t bins of the E_{FCAL} distributions between the ρ^0 data (dots), DIFFVM-g (solid histogram) and DIFFVM-q (dotted histogram), both MC samples with the M_Y distribution reweighted according to the PDFs. 47
30 Comparison in three t bins between the ρ^0 data (dots) and three reweighted MC samples for the E_{FCAL} distributions. The solid histograms correspond to EPSOFT and the dashed and dotted once to DIFFVM, reweighted according to PDFs (dashed) and to describe the measured E_{FCAL} (dotted). 48
31 The normalized energy flow distribution as a function of the pseudorapidity η for the EPSOFT MC sample (squares), DIFFVM-g (stars), DIFFVM-q (open circles) and the data (histogram) for the FCAL energy > 3 GeV in the entire t range $1.2 < -t < 10$ GeV^2 (up) and in three t bins (down). 49
32 The normalized energy flow distribution as a function of the pseudorapidity η for the EPSOFT MC sample (squares), DIFFVM-g (stars) and the data (histogram) in the FCAL energy range $3 < E_{FCAL} < 60$ GeV in the entire t range $1.2 < -t < 10$ GeV^2 (up) and in three t bins (down). 50
33 Comparison of the ratio of the number of events tagged in the PRT to all events between the data (dots) and the EPSOFT MC (histograms). The shaded band reflects the uncertainty of the M_Y distribution reweighting in the EPSOFT MC. 51

34 The differential cross section $d\sigma/dM_{\pi\pi}$ in different t bins. The solid line is the result of the fit using the Söding parameterization of Eq. 66. Only the statistical errors are shown. 55

35 The ration B/A and the diffractive photon dissociation background A_f as a function of $-t$. Dots represent this analysis and open circles the ZEUS 95 measurement. The inner error bars indicate the statistical uncertainties, the outer ones statistical and systematic errors added in quadrature. Lines are the parameterization of B/A (solid) and A_f (dashed), given by Eq. 68 and 69, respectively. 55

36 Comparison between the ρ^0 data (dots) and reweighted EPSOFT MC (histogram) for $-t$ (top), W, $M_{\pi\pi}$ and for p_t and η of the positive track in different t bins. Dashed lines indicate the selection cuts applied to the displayed variable. On all other variables the final selection cuts are imposed (Sec. 4.3). 57

37 Two kaon invariant mass distribution for ϕ in eight t bins. The solid line is a result of fit to the sum of the Breit-Wigner function convoluted with the Gaussian and the background of the form of Eq.71. The dashed line indicates fitted background. 58

38 Comparison of the ϕ data (dots) and reweighted EPSOFT MC (histogram) for $-t$ (up) and W, p_t^+ and η^+ in four t bins. Dashed lines indicate the selection cuts applied to the displayed variable. On all other variables the final selection cuts are imposed (Sec. 4.3). 59

39 The M_{ee} mass distribution for J/ψ in three t bins (dots). The solid line is the result of the fit to the sum of Gaussian (muon decay channel) and the bremsstrahlung function convoluted with th Gaussian (electron decay channel) with equal weight and a linear background. The dotted line corresponds to the fitted background described by Eq. 72. 60

40 The two electron invariant mass distribution for J/ψ meson (dots). The solid line is the result of the fit to the sum of the Gaussian (muon decay channel) and the bremsstrahlung function convoluted with the Gaussian (electron channel) with equal weights over the linear background. The dashed like indicates fitted non-resonant background, given by Eq. 72. 61

41 Comparison between the J/ψ data (dots) and reweighted EPSOFT (histogram) for $-t$ (up), W, p_t^+ and η^+ in two bins of $-t$ (down). The vertical lines show selection cuts applied to the variable shown. 62

42 The distribution $r_v = v^{gen} - v^{rec}$ for $v = -t, W, \cos\vartheta_h$ and φ_h with the RMS reflecting the resolution of the variable v, as a function on the reconstructed momentum transfer t_{rec} for the ρ^0,ϕ and J/ψ meson. 63

43 The overall acceptance as a function of $cos\vartheta_h$, φ_h and $-t$ for the ρ^0 (left column), ϕ (middle column) and J/ψ (right column) vector mesons. 64

44 The differential cross section $d\sigma/dt$ in the kinematic range $80 < W < 120$ GeV and $\frac{M_V^2}{-t} < 100$. The results of this measurement (dots) are compared to the ZEUS results using 1995 data (open circles). The solid line is the result of the fit to the power-like function of Eq. 74. The inner error bars indicate the statistical error, the outer ones the statistical and systematic uncertainties added in quadrature. 71

45 Changes of the power n resulting from different t ranges of the fit, as a function of the fit starting point $-t_0$. The inner error bars indicate the statistical uncertainty, the outer ones the statistical and systematic errors summed in quadrature. 72

46 Power-like fit of Eq. 74 to the results of this analysis (dots) alone (solid line) and to the combined data set including ZEUS 1995 data (open circles, fit as broken line). For 1995, only points included in the fit are shown. 73

47 Results of the study of the β parameter in the generated M_Y distribution (Eq. 55) as a function of $-t$ for three W bins. Circles, squares and triangles correspond to the W ranges $80 < W < 90$ GeV, $90 < W < 100$ GeV and $100 < W < 120$ GeV, respectively. For displaying reasons, the points for W_2 and W_3 they were shifted by 0.05 and 0.1 GeV^2, respectively. 74

48 The ratio B/A (left) and the diffractive photon dissociation background A_f (right) as a function of $-t$ in three W ranges together with the parameterization of Eq. 68 and 69, respectively. In the bottom row, the parameterizations for B/A and A_f are directly compared for W_1 (solid line), W_2 (broken line) and W_3 (dotted line). 76

49 The ratio of events tagged in the PRT to all events for the data (dots) and the proton-dissociative EPSOFT MC (histogram) in three W bins of $80 < W < 90$ GeV, $90 < W < 100$ GeV and $100 < W < 120$ GeV. 77

50 The differential cross sections $d\sigma/dt$ of the ρ^0 meson in the three W bins of $80 < W < 90$ GeV, $90 < W < 100$ GeV and $100 < W < 120$ GeV for $\frac{M_Y^2}{-t} < 100$ (dots), together with the result of the fit to the power-like function (Eq. 74) (dotted line) compared with the cross section measured in the full W range (open circles). The inner error bars indicate the statistical error, the outer ones the statistical and systematic uncertainties added in quadrature. 78

51 The measured normalized cross sections $(d\sigma/dt)_N$ as a function of W in five t bins together with the results of the fit to Eq. 79. The $-t$ values quoted on the plots are the average values in the t bin considered. The inner error bars show the statistical error, the outer ones the statistical and systematic uncertainties added in quadrature. 79

52 The parameter δ fitted to Eq. 79 as a function of the momentum transfer. The inner error bars indicate the statistical error, the outer ones the statistical and systematic uncertainties added in quadrature. 80

53 The differential cross section $d\sigma/\mathrm{d}t$ for the ϕ meson in the kinematic range $80 < W < 120$ GeV and $\frac{M_Y^2}{-t} < 100$ (dots). The solid line is the result of the fit to the power-like function. The inner error bars indicate the statistical error, the outer once the statistical and systematic uncertainties added in quadrature. Also shown are ZEUS results obtained for 1995. 81

54 Changes of the power n resulting from different t ranges of the fit, as a function of the fit starting point $-t_0$, for the ϕ meson. The inner error bars show the statistical uncertainty, the outer ones the statistical and systematic errors summed in quadrature. 82

55 Power-like fit of Eq. 74 (solid line) to the combined ϕ data set including this analysis (dots) and ZEUS 1995 data (open circles). For 1995, only points included in the fit are shown. 83

56 Results of the study of the β parameter in the generated M_Y distribution (Eq. 55) as a function of $-t$ for three W bins. Full circles, squares and triangles on the upper plot correspond to the ϕ meson and W ranges $80 < W < 90$ GeV, $90 < W < 100$ GeV and $100 < W < 120$ GeV, respectively. For displaying reasons, the points for W_2 and W_3 they were shifted by 0.05 and 0.1 GeV^2, respectively. The lower plot shows the comparison between the β values as a function of $-t$ for ϕ (full symbols) and ρ^0 (empty symbols) in three W ranges W_1, W_2 and W_3. 84

57 The ratio of events tagged in the PRT to all events for the ϕ data (dots) and the proton-dissociative EPSOFT MC (histogram) in three W bins of $80 < W < 90$ GeV, $90 < W < 100$ GeV and $100 < W < 120$ GeV. 86

58 The differential cross sections $d\sigma/dt$ for the ϕ meson in the three W bins of $80 < W < 90$ GeV, $90 < W < 100$ GeV and $100 < W < 120$ GeV for $\frac{M_Y^2}{-t} < 100$ (dots), together with the result of the fit to the power-like function (Eq. 74) (dotted line) compared with the cross section measured in the full W range (open circles). The inner error bars show the statistical error, the outer ones the statistical and systematic uncertainties added in quadrature. 86

59 The measured normalized cross sections $(d\sigma/dt)_N$ for ϕ as a function of W in four t bins together with the results of the fit to Eq. 79. The $-t$ values quoted on the plots are the average values in the t bin considered. The inner error bars indicate the statistical error, the outer ones the statistical and systematic uncertainties added in quadrature. 87

60 The parameter δ for the ϕ meson fitted to Eq. 79 as a function of the momentum transfer. The inner error bars indicate the statistical error, the outer ones the statistical and systematic uncertainties added in quadrature. 88

61 The differential cross section $d\sigma/dt$ for the process $\gamma p \to J/\psi Y$ in the kinematic range $80 < W < 120$ GeV and $\frac{M_Y^2}{-t} < 100$. The full points represent results from this analysis, open dots show the result of the ZEUS 95 high $-t$ measurement. The solid line corresponds to the power-like fit according to Eq. 74. The inner error bars show the statistical error, the outer once the statistical and systematic uncertainties added in quadrature. 89

62 The power n from the fit of $d\sigma/dt$ to power-like function (Eq. 74) (dots) as a function of the vector meson mass. The fits were performed in the similar t range for all three vector mesons, $1.2 < -t < 6.85$ GeV^2, $1.2 < -t < 6.5$ GeV^2 and $1.2 < -t < 6.5$ GeV^2, for ρ^0,ϕ and J/ψ, respectively. The inner error bars indicate the statistical error, the outer once the statistical and systematic uncertainties added in quadrature. 90

63 The two electron invariant mass distributions for the J/ψ meson in two W regions: $80 < W < 100$ GeV and $100 < W < 120$ GeV. The solid line is the result of the fit to the sum of the Gaussian (muon decay channel) and the bremsstrahlung function convoluted with the Gaussian (electron channel) with equal weights over the linear background. The dashed line shows fitted non-resonant background. 91

64 The comparison of the differential cross section $d\sigma/dt$ for the process $\gamma p \to J/\psi Y$ in the three kinematic ranges $80 < W < 100$ GeV (dots), $100 < W < 120$ GeV (open circles) and the entire W region of $80 < W < 120$ GeV (stars). The solid line corresponds to the power-like fit according to Eq. 74 for the full W range, the dashed and dotted lines indicate the same fit in the W range $80 < W < 100$ GeV and $100 < W < 120$ GeV, respectively. The inner error bars indicate the statistical error, the outer ones the statistical and systematic uncertainties added in quadrature. 92

65 The ratios of the cross sections $d\sigma/dt$ for ϕ to ρ^0 (top) and J/ψ to ρ^0 (bottom) for this measurement (dots) and the low $-t$ data (open circles) together with the 'fitted ratios' (solid line) obtained by dividing the results of the fit to the power-like function (Eq. 74). The shaded bands show the uncertainties of the fits to the cross sections. The dashed lines correspond to the SU(4) predictions. The inner error bars indicate the statistical error, the outer bars the statistical and systematic uncertainties added in quadrature. 94

66 The ratios of the cross sections $d\sigma/dt$ for ϕ to ρ^0 (top) and J/ψ to ρ^0 (bottom) for this measurement (dots) and low $-t$ data (triangles) as a function of $-t$ together with the results of measurements as a function of Q^2 (open symbols). The inner error bars show the statistical error, the outer bars the statistical and systematic uncertainties added in quadrature. 95

67 The results of the fit of Eq. 84 (solid line) to the cross section ratios ϕ/ρ (top) and ψ/ρ (bottom) as a function of Q^2. Only the statistical errors are shown. . . 96

68 The ratios of the cross sections $d\sigma/dt$ for ϕ to ρ^0 (top) and J/ψ to ρ^0 (bottom) for this measurement (dots) as a function of $t_S = t \cdot \mathcal{S}$ together with the results of measurements as a function of Q^2 (open symbols). The inner error bars show the statistical error, the outer bars the statistical and systematic uncertainties added in quadrature. 97

69 The proton-dissociative photoproduction of vector meson. 98

70 The comparison between the differential cross section $\mathrm{d}\sigma/\mathrm{d}t$ for the process $\gamma p \to \rho Y$ (top) and $\gamma p \to \phi Y$ (bottom), in the kinematic range $80 < W < 120$ GeV and $\frac{M_Y^2}{-t} < 100$ measured in this analysis (dots), and the theoretical calculation of these processes (solid line). The theoretical error (shaded band) comes from the uncertainties of the model parameters. The inner error bars show the statistical error, the outer ones the statistical and systematic uncertainties added in quadrature. 100

71 The comparison between the measured differential cross section $d\sigma/dt$ for the process $\gamma p \to J/\psi Y$ (dots) and the theoretical calculation of this process (solid line) in the kinematic range $80 < W < 120$ GeV and $\frac{M_Y^2}{-t} < 100$. The full points represent results from this analysis, open dots show the result of the ZEUS 95 measurement. The inner error bars give the statistical error, the outer once the statistical and systematic uncertainties added in quadrature. 102

72 The comparison between the measured and predicted differential cross section $d\sigma/dt$ for two W as a function of W in different t bins. The $-t$ values quoted on the plots are the average values in the t bin considered. Dashed lines represent the theoretical calculations. The inner error bars show the statistical error, the outer ones the statistical and systematic uncertainties added in quadrature. . . . 102

73 The comparison between the heavy mesons theoretical predictions evaluated for ρ^0 and ϕ with the measured cross sections $d\sigma/dt$. The shaded band corresponds to the uncertainty of the theoretical calculations, coming form the uncertainty of α_S and of the center-of-mass energy. 103

List of Tables

1 HERA design parameters and actual performance in 1996 and 1997. The luminosity values are typical values (specific) and typical peak values (instantaneous) towards the end of running periods. 15

2 Integrated luminosity collected with the high $-t$ VM trigger in 96-97. 33

3 Fit results for β' for the ρ^0 meson. 45

4 Fit results for β' for the ϕ meson. 45

5 Fit results for β' for the J/ψ meson. 45

6 PDG summary for the ρ^0, ϕ and J/ψ mesons. 52

7 Results for the fits to the Söding parameterization (Eq. 66) for ρ^0 in different t bins. The fit was performed in the mass range $0.55 < M_{\pi\pi} < 1.3$ GeV. 54

8 Results for the fits to the Söding parameterization (Eq. 66) for the ρ^0 meson in 9 t bins. The fit was performed in the mass range $0.55 < M_{\pi\pi} < 1.3$ GeV. The values of M_ρ and Γ_ρ were fixed to the DPG values (Tab. 6). Only the statistical errors are shown. 54

9 The final parameters of the ρ^0 MC reweighting procedure. 56

10 The fit results for the M_{KK} spectra. The fit was performed in the range $0.99 < M_{KK} < 1.14$ GeV. The background was evaluated in the region $0.99 < M_{KK} < 1.06$ GeV. 58

11 Result of the fit to the M_{ee} mass spectra of the J/ψ data. The fit was performed in the M_{ee} range of $2.6 < M_{ee} < 3.4$ GeV. The background contribution was derived in the mass window $2.98 < M_{ee} < 3.13$ GeV. 60

12 The results for the fit to M_{ee} shown in Fig. 40. The fit range is $2.6 < \mathrm{M}_{ee} < 3.4$ GeV. The fraction of background was estimated in the mass window $2.98 < \mathrm{M}_{ee} < 3.13$ GeV. 61

13 The typical resolution of the kinematic variables t, W, M_V and helicity angles $cos\vartheta_h$ and φ_h for the ρ^0,ϕ and J/ψ meson. 63

14 Results of the fits of the differential cross section $d\sigma/dt$ with the power-like function $A \cdot (-t)^{-n}$ in different t ranges. 72

15 Results for the fits to the Söding parameterization (Eq. 66) for the ρ^0 meson in three W bins and six $-t$ bins. The fit was performed in the mass range $0.55 < M_{\pi\pi} < 1.3$ GeV. The values of M_ρ and Γ_ρ were fixed to the DPG values (Tab. 6). Only statistical errors are shown. 75

16 Results of the fits of the differential cross section $d\sigma/dt$ with the power-like function $A \cdot (-t)^{-n}$ in different W bins. 76

17 Results of the power-like fit of Eq. 74 to the differential cross section $d\sigma/dt$ in the three W bins. 78

18 Results of the fit of Eq. 79 to the normalized cross section $(d\sigma/dt)_N$ for different t bins. 80

19 Results of the fits of the differential cross section $d\sigma/dt$ with the power-like function $A \cdot (-t)^{-n}$ in different t ranges. 82

20 Results of the fits to the two-kaon invariant mass spectra for the ϕ meson in three W bins and three $-t$ bins, together with the background parameterization as a function of t for each W range. The fits were performed in the mass range $0.99 < M_{KK} < 1.14$ GeV and the background was evaluated in the mass window $0.99 < M_{KK} < 1.06$ GeV. The values of M_ϕ and Γ_ϕ were fixed to the DPG values (Tab. 6). Only statistical errors are shown. 85
21 Results of the power-like fit of Eq. 74 to the differential cross section $d\sigma/dt$ in the three W bins. 87
22 Results of the fit of Eq. 79 to the normalized cross section $(d\sigma/dt)_N$ of the ϕ meson for different t bins. 88
23 The results of the fit to the measured cross section $d\sigma/dt$ with the power-like function of Eq. 74 for three vector mesons in the same t ranges, $1.2 < -t < 6.85$ GeV^2, $1.2 < -t < 6.5$ GeV^2 and $1.2 < -t < 6.5$ GeV^2, for ρ^0,ϕ and J/ψ, respectively. 90
24 The results of the fit to the two electron invariant mass spectra for the J/ψ meson for two W bins. In each case the fit range was $2.6 < M_{ee} < 3.4$ GeV. The background fraction was calculated in the region $2.98 < M_{ee} < 3.13$ GeV. Quoted errors are the statistical uncertainties only. 92
25 The results of the power-like fit of Eq. 74 to the differential cross sections $d\sigma/dt$ in the whole W range $80 < W < 120$ GeV (Sec. 7.3.1) and in the two W bins of $80 < W < 100$ GeV and $100 < W < 120$ GeV (Sec. 7.3.2). 93
26 The results of the fit of Eq. 84 to the cross section ratios ϕ/ρ and ψ/ρ as a function of Q^2. Only the statistical errors are quoted. 96
27 Tabulated values of $\frac{d\sigma}{dt}(\gamma p \to \rho Y)$ with statistical error (stat.), systematic uncertainty (syst.) and total error for the kinematic range $80 < W < 120$ GeV and $\frac{M_Y^2}{-t} < 100$. 107
28 Tabulated values of the systematic uncertainties of $\frac{d\sigma}{dt}(\gamma p \to \rho Y)$ for systematic checks listed in Sec. 6 under the same indexes. 108
29 Tabulated values of $\frac{d\sigma}{dt}(\gamma p \to \rho Y)$ with statistical error (stat.), systematic uncertainty (syst.) and total error for the kinematic range $\frac{M_Y^2}{-t} < 100$ and three W bins $80 < W < 90$ GeV, $90 < W < 100$ and $100 < W < 120$ GeV. 109
30 Tabulated values of the systematic uncertainties of $\frac{d\sigma}{dt}(\gamma p \to \rho Y)$ for $80 < W < 90$ GeV, for systematic checks listed in Sec. 6 under the same indexes. 110
31 Tabulated values of the systematic uncertainties of $\frac{d\sigma}{dt}(\gamma p \to \rho Y)$ for $90 < W < 100$ GeV, for systematic checks listed in Sec. 6 under the same indexes. 111
32 Tabulated values of the systematic uncertainties of $\frac{d\sigma}{dt}(\gamma p \to \rho Y)$ for $100 < W < 120$ GeV, for systematic checks listed in Sec. 6 under the same indexes. 112
33 Tabulated values of $\frac{d\sigma}{dt}(\gamma p \to \phi Y)$ with statistical error (stat.), systematic uncertainty (syst.) and total error for the kinematic range $80 < W < 120$ GeV and $\frac{M_Y^2}{-t} < 100$. 113
34 Tabulated values of the systematic uncertainties of $\frac{d\sigma}{dt}(\gamma p \to \phi Y)$ for systematic checks listed in Sec. 6 under the same indexes. 114
35 Tabulated values of $\frac{d\sigma}{dt}(\gamma p \to \phi Y)$ with statistical error (stat.), systematic uncertainty (syst.) and total error for the kinematic range $\frac{M_Y^2}{-t} < 100$ and three W bins $80 < W < 90$ GeV, $90 < W < 100$ and $100 < W < 120$ GeV. 115

36 Tabulated values of the systematic uncertainties of $\frac{d\sigma}{dt}(\gamma p \to \phi Y)$ for $80 < W <$ 90 GeV, for systematic checks listed in Sec. 6 under the same indexes. 116
37 Tabulated values of the systematic uncertainties of $\frac{d\sigma}{dt}(\gamma p \to \phi Y)$ for $90 < W <$ 100 GeV, for systematic checks listed in Sec. 6 under the same indexes. 117
38 Tabulated values of the systematic uncertainties of $\frac{d\sigma}{dt}(\gamma p \to \phi Y)$ for $100 < W <$ 120 GeV, for systematic checks listed in Sec. 6 under the same indexes. 118
39 Tabulated values of $\frac{d\sigma}{dt}(\gamma p \to J/\psi Y)$ with statistical error (stat.), systematic uncertainty (syst.) and total error for the kinematic range $80 < W < 120$ GeV and $\frac{M_Y^2}{-t} < 100$. 119
40 Tabulated values of the systematic uncertainties of $\frac{d\sigma}{dt}(\gamma p \to J/\psi Y)$ for systematic checks listed in Sec. 6 under the same indexes. 120
41 Tabulated values of $\frac{d\sigma}{dt}(\gamma p \to J/\psi Y)$ with statistical error (stat.), systematic uncertainty (syst.) and total error for the kinematic range $\frac{M_Y^2}{-t} < 100$ and two W bins $80 < W < 100$ GeV and $100 < W < 120$ GeV. 121
42 Tabulated values of the systematic uncertainties of $\frac{d\sigma}{dt}(\gamma p \to J/\psi Y)$ for $80 < W < 100$ GeV, for systematic checks listed in Sec. 6 under the same indexes. . . 122
43 Tabulated values of the systematic uncertainties of $\frac{d\sigma}{dt}(\gamma p \to J/\psi Y)$ for $100 < W < 120$ GeV, for systematic checks listed in Sec. 6 under the same indexes. . . 123
44 Tabulated values of the cross section ratio ϕ/ρ, with statistical error (stat.), systematic uncertainty (syst.) and total error for the kinematic range $80 < W <$ 120 GeV and $\frac{M_Y^2}{-t} < 100$. 124
45 Tabulated values of the cross section ratio ψ/ρ, with statistical error (stat.), systematic uncertainty (syst.) and total error for the kinematic range $80 < W <$ 120 GeV and $\frac{M_Y^2}{-t} < 100$. 124

1 Introduction

Questions about the origin of life, the structure of matter, indivisible particles and the ultimate force ruling the world has been always asked by mankind. People as different as priests, philosophers, physicist or biologist are seeking answers to these questions. Starting from the nature-philosophers such as Democrit with his vision of *the atom* as the smallest, indivisible component of matter, the deep feeling that entire world, with its various forms, smells and tastes, is composed out of a few tiny particles was present in human minds. The discipline of "particle" or "high energy" physics tries to find these smallest particles and to answer the question which forces keep them together. Years of experimenting and hard work to understand and predict the experimental results led to extraordinary discoveries and theories of high energy physics in the last century. The road to our present understanding of elementary particles, elementary forces and their interactions has been long and full of false traces. Often the actual picture of the micro-world was trusted to be the final one. And, so far always, new phenomena or models would destroy or change the old schemes to built a *Brave New World*.

The Quantum Chromodynamics (QCD), being the quantized field theory of the strong interaction, (together with the electroweak theory) succeeded in describing many phenomena and features of the present high energy physics. However, there are still fields, where QCD is not applicable and different models and approaches are necessary to describe them. One of such regions is diffractive ep scattering. Diffractive physics is often seen as a transition region between "hard" physics described by perturbative QCD (pQCD) and "soft" physics, for which the strong coupling constant is too large for pQCD to be applicable. The domain presented in this thesis is the diffractive photoproduction of vector mesons, which is introduced in Sec. 2. The study of the exclusive diffractive ep scattering at HERA has shown that the large photon virtuality Q^2 or the big mass of the produced particle can provide a hard scale so that the process can be calculated in terms of pQCD [1, 2]. It is expected that for the diffractive vector meson photoproduction, the four-momentum transfer squared, t, in the proton vertex may also provide a hard scale, for values of $-t$ sufficiently large [3, 4]. The analysis presented in this thesis uses data collected by the ZEUS detector at the HERA collider (Sec. 3) to test this hypothesis by determining the main features of the proton-dissociative diffractive photoproduction of the ρ^0,ϕ and J/ψ vector mesons at high $-t$. The kinematic variables, their reconstruction and the selection of the vector meson candidates relevant for this analysis are presented in Sec. 4. Sec. 5 gives a detailed description of the used Monte Carlo models, the simulation of the global trigger condition used by the ZEUS experiment (Sec. 5.5) and the efficiency of the 44m tagger, dedicated for the high $-t$ studies (Sec. 5.6). Sources of systematic uncertainties affecting the final results are summarized in Sec. 6. The results of the differential cross section $d\sigma/dt$ measurement are described in Secs. 7.1, 7.2, 7.3 for the ρ^0,ϕ and J/ψ mesons, respectively, and the results of the measurement of the cross section ratios are presented in Sec. 7.4. In addition, the results are compared to the previous measurement at lower $-t$ [5], which gave indications of the transition character of the studied process. Together with the present analysis, which extends the covered t range significantly, this provides a possibility to study the transition between the soft, non-perturbative phenomena, and the hard, perturbative regime of QCD. In Sec. 8 the data are confronted with theoretical predictions based on pQCD models for light [6] and heavy [7] vector mesons. Studies of the onset of the characteristics of pQCD can improve the understanding of the soft phenomena in QCD and give important insight into the strong interactions. A summary with closing remarks is given in Sec. 9.

2 Diffractive Vector Meson Production in Positron-Proton Interaction

2.1 Positron-Proton Scattering

In positron-proton scattering the incoming positron[1] couples to the electroweak current carrying the four-momentum q. The intermediate boson can be either a virtual photon, γ^*, or one of the weak gauge bosons Z or $W^{\pm}$. Since the momentum transfer q used in this analysis is low, the contribution of the heavy, weak gauge bosons can be ignored. In Fig.1 a lowest order diagram for the one-photon-exchange is shown. P, P', k, k' denote the four momenta of the incoming proton, the outgoing hadronic system, the initial positron and the final positron, respectively.

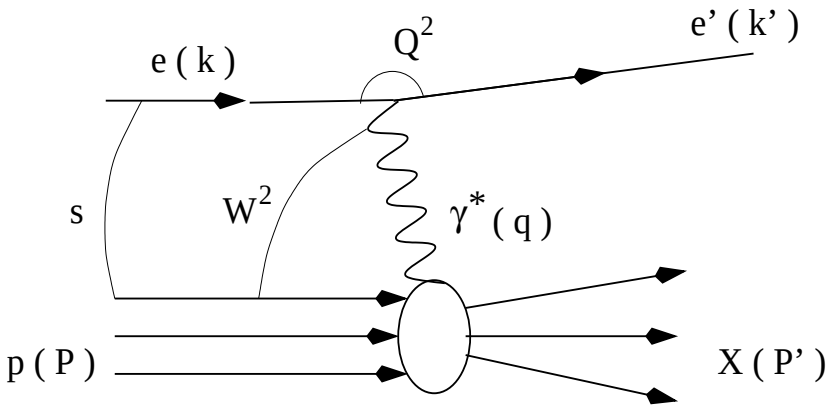

Figure 1: The schematic diagram of positron-proton scattering via one-photon exchange. The four-vectors of the particles are given in braces.

The scale of the interaction is set by the virtuality of the exchanged boson, because the spatial resolution is proportional to $1/|q|$. Using the notation from Fig.1 we define:

$$Q^2 \equiv -q^2 = -(k - k')^2 > 0, \tag{1}$$

being the negative square of the exchanged photon's four-momentum. Q^2 can take values between 0 and the square of the total center of mass energy, s. Neglecting the electron and proton masses, s is given by:

$$s = (k + p)^2 \simeq 4E_e E_p, \tag{2}$$

where E_e, E_p denote the electron and proton energies, respectively.

The kinematics of the inclusive scattering of unpolarized positrons and protons is described by s and any two of the following variables:

- the negative square of the four momentum of the exchanged photon Q^2,

[1]Since the present analysis does not depend on the charge of the lepton, electron and positron are used synonymously.

- the fraction of the positron energy transferred to the hadronic final state in the rest frame of the initial state proton

$$y \equiv \frac{p \cdot q}{p \cdot k}, \tag{3}$$

- or the center-of-mass energy of the photon-proton system

$$W^2 = (q + P)^2. \tag{4}$$

The differential cross section for the positron-proton interaction for $Q^2 \ll W^2$ can be expressed as:

$$\frac{d^2\sigma^{ep\to eX}}{dydQ^2} = \Gamma(y, Q^2)\left(\sigma_T^{\gamma^* p\to X} + \epsilon\sigma_L^{\gamma^* p\to X}\right), \tag{5}$$

where $\Gamma(y, Q^2)$ denotes the photon flux

$$\Gamma(y, Q^2) = \frac{\alpha}{2\pi Q^2}\left(\frac{1 + (1-y)^2}{y} - \frac{2(1-y)}{y}\frac{Q^2_{min}}{Q^2}\right), \tag{6}$$

and

$$\epsilon = \frac{2(1-y)}{1 + (1-y)^2 - 2(1-y)\frac{Q^2_{min}}{Q^2}}. \tag{7}$$

Q^2_{min} is the minimum possible value of Q^2, α in the fine-structure constant and the functions $\sigma_T^{\gamma^* p\to X}$ and $\sigma_L^{\gamma^* p\to X}$ are the photon-proton cross sections for transversely and longitudinally polarized photon, respectively. In a $Q^2 \to 0$ limit they satisfy

$$\lim_{Q^2\to 0} \sigma_T^{\gamma^* p\to X} = \sigma^{\gamma p\to X}(W), \tag{8}$$

$$\lim_{Q^2\to 0} \sigma_L^{\gamma^* p\to X} = 0. \tag{9}$$

If the virtuality of the exchanged photon is restricted to $Q^2 \lesssim 0.01$ GeV^2, $\sigma_L^{\gamma^* p\to X}$ and the Q^2-dependence of $\sigma_T^{\gamma^* p\to X}$ can be neglected and the differential cross section from Eq. 5 can be written as [8]:

$$\frac{d^2\sigma^{ep\to eX}}{dydQ^2} = \Gamma(y, Q^2)\sigma^{\gamma p\to X}(W). \tag{10}$$

Therefore a photon-proton cross section $\sigma^{\gamma p\to X}$ can be obtained from a measured positron-proton cross section $\sigma^{ep\to eX}$ by dividing the positron-proton cross section by the photon flux Γ integrated over the y and Q^2 range covered by the measurement.

2.2 Vector Meson Dominance Model

Photon-hadron interactions at high energies show similar behavior as hadron-hadron collisions. On a qualitative level this similarity can be understood in the following way. Due to the uncertainty principle a photon can fluctuate into a virtual $q\bar{q}$ state with the same quantum numbers as the photon ($J^{PC} = 1^{--}; Q = S = B = 0$), a vector meson, V. If the four

momentum of the photon is given in the proton rest frame by $q = (\nu, \vec{K})$, the fluctuation time is

$$t_f \simeq \frac{2\nu}{Q^2 + M_V^2}, \tag{11}$$

where M_V is the vector meson mass.

If the distance which the virtual meson can travel is much larger than the nuclear radius $r_h \simeq 1$ fm, then the photon fluctuates long before it hits the hadron and the interaction occurs between the vector meson and the hadron - see Fig.2.

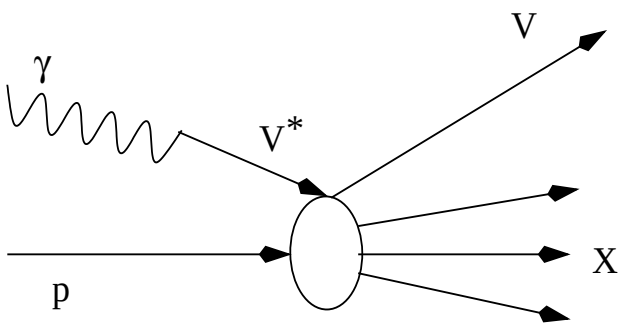

Figure 2: The vector meson production in the Vector Dominance Model, where the photon fluctuates into a vector meson, which then scatters off the proton.

Therefore the physical photon $|\gamma>$ can be considered as a superposition of a bare photon $|\gamma_B>$ and a hadronic component $\sqrt{\alpha}|h>$:

$$|\gamma> = \sqrt{Z_3}|\gamma_B> + \sqrt{\alpha}|h>, \tag{12}$$

where Z_3 gives the proper normalization.

The hadronic component of the photon is suppressed by $\sqrt{\alpha}$. However, for low Q^2 it dominates photon-proton interactions since the hadronic cross sections are very large. Photoproduction of the light vector mesons ρ^0, ω and ϕ suggests that they are a very important contribution to $|h>$. The hypothesis of the vector dominance model (VDM) considers only these vector mesons as the hadronic component and neglects the bare photon $|\gamma_B>$ contribution. The inclusion of more constituents to $|h>$ is referred to as the generalized vector dominance model (GVD). Reviews of these models can be found in [9, 10, 11] and [12].

As shown in the previous section, at very low $Q^2 \lesssim 0.01$ GeV^2, the electroproduction $ep \to X$ can be expressed in terms of the process $\gamma p \to X$ (Eq. 10). By the same arguments, the vector meson electroproduction $ep \to eVX$ can be written is terms of the real photoproduction $\gamma p \to VX$ as:

$$\frac{d^2\sigma^{ep\to eVX}}{dydQ^2} = \Gamma(y, Q^2)\sigma^{\gamma p\to VX}(W). \tag{13}$$

2.3 Diffraction

A name 'diffraction' was assigned, in analogy to optical diffraction, to a special class of events in hadron-hadron collisions, for example in $p\bar{p} \to pX$ scattering, in which the proton was detected at large values of rapidity and a gap in rapidity between the final proton and the final state X was observed. In hadron-hadron collisions three types of diffractive processes can be defined, which can be distinguished by the difference in the characteristic of the final states, as depicted in Fig. 3:

a) **elastic scattering**, where both incident hadrons stay intact after the collision,

b) **single dissociation**, where one of the initial hadrons breaks up into a multi-particle final state, which preserves the quantum numbers of this initial hadron,

c) **double dissociation**, where both of the initial hadrons dissociate, again ending up in the multi-particle final state, with the quantum numbers of the two interacting hadrons preserved.

Diffraction is most often described in terms of the exchange of an object carrying the quantum numbers of the vacuum at the proton vertex, called Pomeron (IP). Experimentally for diffractive events the lack of particles in a detector between the leading particle b or system Y and the system X is expected.

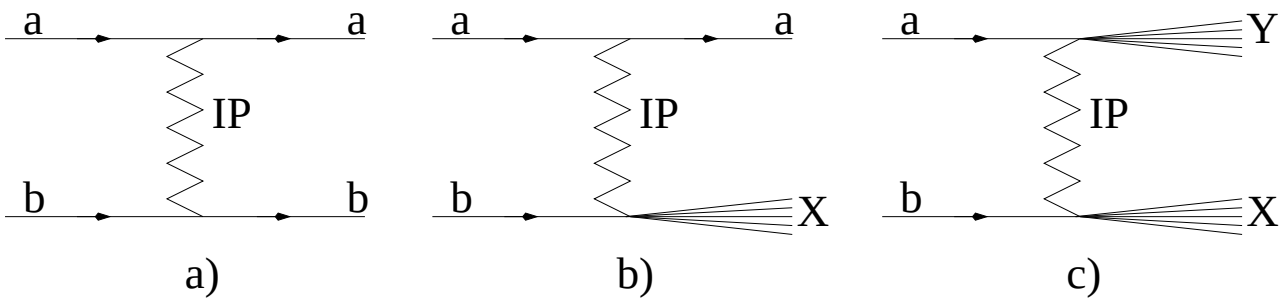

Figure 3: Three types of diffractive processes in hadron-hadron collisions: a) elastic scattering, b) single dissociation, c) double dissociation.

So far the theory is lacking a model that describes correctly all aspects of diffractive processes. The difficulty is connected to the fact that reactions of diffractive type belong mostly to the soft physics, mainly described by the phenomenological models only. One of the main available soft models, widely used to compare its predictions with measurements in diffractive physics, is Regge phenomenology. This model is outlined in the following section.

2.4 Diffraction in Terms of Regge Formalism

The Regge theory [13, 14, 15] is used to make predictions about the hadron-hadron scattering cross section and about leading particle production as a function of s. The interaction can be described by the exchange of a family of off-shell particles (Regge poles), where the relevant quantum numbers are conserved. One of the important features of these particles, which are

inherent to Regge theory, is the linear relation between the spin J and the square of the mass m. The correlation is described by the Regge trajectory:

$$\alpha(t) \;=\; \alpha(0) + \alpha' \cdot t, \tag{14}$$

where $\alpha = J$ and $t = m^2$. According to Regge theory, the behavior of the elastic hadron scattering amplitude is controlled by a sequence of Regge trajectories, which correspond to an exchange of families of particles with different spin. For a certain process, the contribution of all particle trajectories should be summed. In general, every Regge pole is called a Reggeon. In following, however, to distinguish between Pomeron and non-Pomeron exchange, the name Reggeon ($\mathbb{R}$) will be reserved for all Regge particles except the Pomeron, which correspond to the exchange of vacuum quantum numbers.

In the Regge limit ($-t \ll M^2 \ll s$) the total, elastic and single dissociative cross section formulae for the interaction of initial hadrons a and b can be written as:

$$\sigma_{tot}^{ab} \;=\; \sum_k \beta_{ak}(0)\beta_{bk}(0) s^{\alpha_k(0)-1}, \tag{15}$$

$$\frac{d\sigma_{el}^{ab}}{dt} \;=\; \sum_k \frac{\beta_{ak}^2(t)\beta_{bk}^2(t)}{16\pi} s^{2\alpha_k(t)-2}, \tag{16}$$

$$\frac{d^2\sigma_{sd}^{ab}}{dt dM^2} \;=\; \sum_{k,l} \frac{\beta_{ak}^2(t)\beta_{bl}^2(0) g_{kkl}(t)}{16\pi} \frac{1}{M^2} \left(\frac{s}{M^2}\right)^{2\alpha_k(t)-2} (M^2)^{\alpha_l(0)-1}, \tag{17}$$

where $\beta(t)$ and $g(t)$ are vertex functions and $\alpha(t)$ is the Regge trajectory. The sum runs over all Regge trajectories for which the quantum numbers are preserved. In principle for elastic and single dissociative processes $k = \mathbb{P}$, f and $l = \mathbb{P}, \mathbb{R}$. The $\mathbb{R}$ trajectory corresponds to the exchange of the mesons ρ, ω, a_2, f_2. The $\mathbb{P}$ trajectory dominates the elastic and diffractive cross section.

The elastic hadronic and photoproduction cross section was found to fall initially with increasing center-of-mass energy, but then levels off and show a slight rise - see Fig.4. The initial fall can be described by a Reggeon trajectory with intercept $\alpha_{\mathbb{R}}(0) = 0.55$ and slope $\alpha'_{\mathbb{R}} \simeq 1$ GeV^{-2}, while the rise can be fitted to a Pomeron trajectory [16]:

$$\alpha_{\mathbb{P}} = 1.08 + 0.25 \cdot t. \tag{18}$$

This growth of the cross section was first predicted by Pomeranchuk [17] and the trajectory was named after him.

2.5 Diffractive Photoproduction

Photoproduction processes are classified similar to hadron-hadron interactions. At high energies hard photoproduction is observed, characterized by events with a jet-like structure. However the cross section for hard photoproduction is very small. Most of the hadronic interactions are characterized by low transverse momenta and is referred to as soft processes. These processes are described phenomenologically by Regge theory (section 2.4). Soft diffractive photoproduction can be classified as follows:

- **elastic diffraction** ($\gamma p \to Vp, V = \rho^0, \omega, \phi$):
  In VDM this process is the analog to the elastic scattering in hadron-hadron collisions. The contribution of elastic diffraction to the total γp cross section is similar to the elastic scattering contribution in hadron-hadron interactions.

- **diffractive dissociation:**
  In this class of events at least one of the incoming particles dissociates into a higher mass state (Y for the proton or X for the vector meson, with $M_X > M_V$, $M_Y > M_p$). In diffractive dissociation three processes can be distinguished:

  - proton dissociation ($\gamma p \to VY$),
  - photon dissociation ($\gamma p \to Xp$),
  - double dissociation ($\gamma p \to XY$).

  At a given $W_{\gamma p}$ the cross section of the diffractive processes has been found to approximately follow:

$$\frac{d^2\sigma}{dtdM^2_{X(Y)}} \propto \frac{e^{bt}}{(M^2_{X(Y)})^a} \tag{19}$$

  with $a \simeq 1$ [18]. The slope parameter b depends on the mass of the dissociative system $M_{X(Y)}$. For single dissociation and masses above the resonance region, b is roughly half the value for elastic scattering.

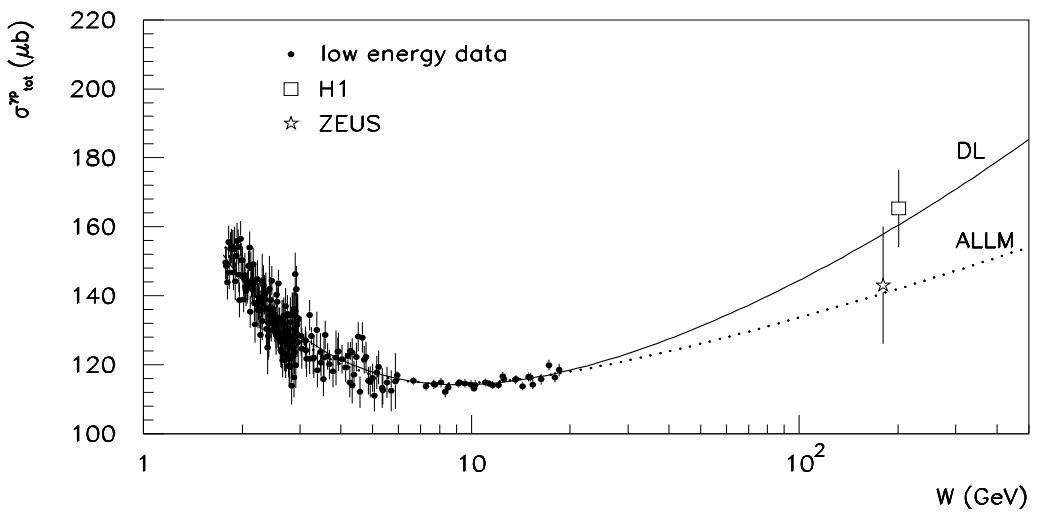

Figure 4: Total photoproduction cross section as a function of the center-of-mass energy W of the γp system. The lines correspond to Regge fits with $\alpha_{I\!P}(0) = 1.0808$ (solid) and $\alpha_{I\!P}(0) = 1.045$ (dotted).

2.6 Vector Meson Production

Fig.5 shows the elastic vector meson production $\gamma^* p \to Vp$ and the proton-dissociative process $\gamma^* p \to VN$, where in both cases vector meson decays into two charged particles, q^+ and q^-. The following variables, in addition to the ones presented in Sec. 2.1, can be introduces for these processes:

- the squared four-momentum transfer at the $\gamma^* V$ vertex

$$t = (q - v)^2 = (P - P')^2, \tag{20}$$

  where v is the four-momentum of the vector meson,

- the mass of the vector meson, M_V,

- the angles describing the production and decay of the vector meson,

- and for the proton-dissociative reaction, the mass M_Y of the diffractively produced state Y is relevant

$$M_Y^2 = (P')^2.$$

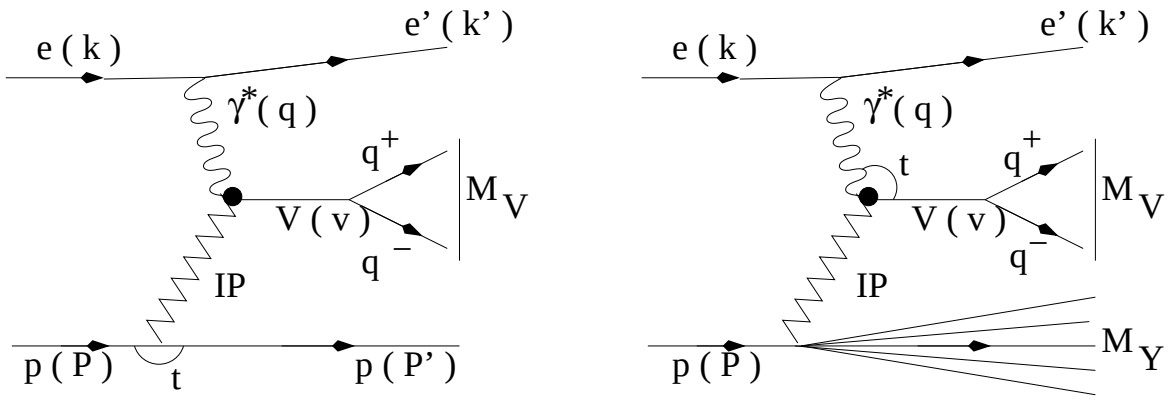

Figure 5: Sketch showing the kinematic variables describing vector meson elastic photoproduction (left) and proton-dissociative photoproduction (right).

Decay angular distribution

Some aspects of the production process require the knowledge of the vector meson spin. An example can be the spin dependent properties of the vector meson production, such as s-channel helicity conservation (SCHC), which issues a question, if the vector meson retains the helicity of the photon. The spin state of the produced vector meson might be measured from the angular distribution of its decay products, using the formalism developed in the dedicated publication [19].

For the purpose of the helicity analysis, the production and decay angles are usually defined in the s-channel helicity frame shown in Fig. 6 [20]. The s-channel helicity frame is defined as the rest frame of the vector meson in which the meson direction in the γp center-of-mass frame is taken as the quantization axis. The polar angle ϑ_h is the angle between the direction of the outgoing meson and the direction of the positively charged decay particle (by convention).

The azimuthal angle φ_h is defined as the angle between the vector meson decay plane and the meson production plane. The Φ angle is the angle between the meson production plane and the positron scattering plane.

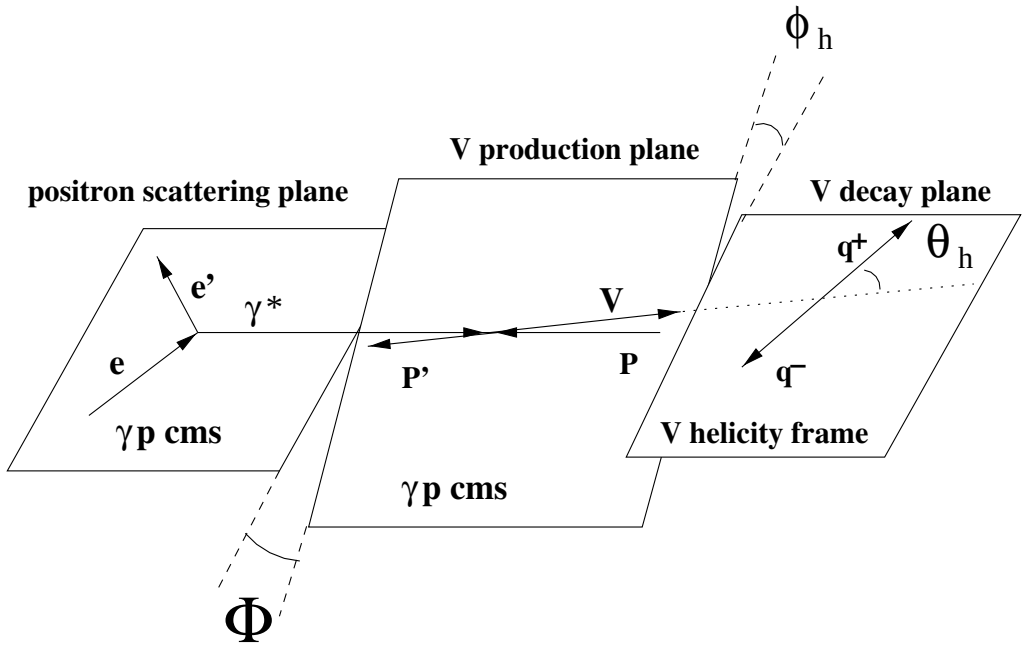

Figure 6: Definition of the planes and angles describing the decay of the vector meson V into two charged particles q^+ and q^-.

The full decay angular distribution is expressed as a function of all three angles $(cos\vartheta_h, \varphi_h, \Phi)$. The decay angular distribution integrated over the Φ angle, which is not measured in this analysis, has a following form for an unpolarized positron beam and for a decay into two spin-0 particles:

$$\begin{aligned} W\left(cos\vartheta_h, \varphi_h\right) = \; & \frac{3}{4\pi}\left[\frac{1}{2}\left(1 - r^{04}_{00}\right) + \frac{1}{2}\left(3r^{04}_{00} - 1\right) cos^2\vartheta_h \right. \\ & -\sqrt{2}Re\left(r^{04}_{10}\right) sin2\vartheta_h cos\varphi_h \\ & \left. -r^{04}_{1-1} sin^2\vartheta_h cos2\varphi_h\right], \end{aligned} \tag{21}$$

where r^{04}_{00}, r^{04}_{10} and r^{04}_{1-1} are the relevant vector meson spin density matrix elements. One-dimensional distributions are obtained by integration over $cos\vartheta_h$ or φ_h:

$$W\left(cos\vartheta_h\right) = \frac{3}{4}\left[1 - r^{04}_{00} + \left(3r^{04}_{00} - 1\right) cos^2\vartheta_h\right]. \tag{22}$$

$$W\left(\varphi_h\right) = \frac{1}{2\pi}\left(1 - r^{04}_{1-1} cos2\varphi_h\right), \tag{23}$$

The r^{04}_{00} element represents the probability that the vector meson is produced in a helicity zero state. The r^{04}_{10} element is related to the interference between helicity single flip (helicity changes by one unit) and helicity non-flip amplitudes and the element r^{04}_{1-1} is related to the interference between the helicity double flip (helicity changes by two units) and helicity non-flip amplitudes. If SCHC holds, r^{04}_{00}, r^{04}_{10} and r^{04}_{1-1} should be equal zero.

Eq. 21 is valid for a decay into two spin-0 particles (for example $\rho^0 \to \pi^+\pi^-$ and $\phi \to K^+K^-$). For a decay into two spin-1/2 particles ($J/\psi \to e^+e^-$ and $J/\psi \to \mu^+\mu^-$) the equation has a form:

$$\begin{aligned} W\left(cos\vartheta_h, \varphi_h\right) = \; & \frac{3}{4\pi}\left[\frac{1}{2}\left(1 + r_{00}^{04}\right) - \frac{1}{2}\left(3r_{00}^{04} - 1\right) cos^2\vartheta_h \right. \\ & + \sqrt{2} Re\left(r_{10}^{04}\right) sin2\vartheta_h cos\varphi_h \\ & \left. + r_{1-1}^{04} sin^2\vartheta_h cos2\varphi_h\right]. \end{aligned} \tag{24}$$

Integrating over $cos\vartheta_h$ or φ_h gives one-dimensional distributions:

$$W\left(cos\vartheta_h\right) = \frac{3}{4}\left[1 + r_{00}^{04} - \left(3r_{00}^{04} - 1\right) cos^2\vartheta_h\right], \tag{25}$$

$$W\left(\varphi_h\right) = \frac{1}{2\pi}\left(1 + r_{1-1}^{04} cos2\varphi_h\right). \tag{26}$$

2.6.1 Expectations of the Regge Phenomenology

The main predictions of the Regge theory for the vector meson production include a presence of shrinkage (i.e. the slope of the t-distribution depends on the energy) for both, the elastic and proton-dissociative cross sections, a dependence of the proton-dissociative cross section on M_Y and a lack of dependence of the ratio of $d\sigma/dt$ for elastic to proton-dissociative reaction on the type of vector meson and energy. In the following these features of the vector meson production are briefly derived from the Regge formalism introduced in Sec. 2.4.

For the diffractive vector meson photoproduction the Regge formulae 16 and 17 have a form:

$$\frac{d\sigma_{\gamma p \to Vp}}{dt} = \sum_k \frac{\beta_{Vk}^2(t)\beta_{pk}^2(t)}{16\pi}(W^2)^{2\alpha_k(t)-2}, \tag{27}$$

$$\frac{d^2\sigma_{\gamma p \to VY}}{dt dM_Y^2} = \sum_{k,l} \frac{\beta_{Vk}^2(t)\beta_{pl}^2(0) g_{kkl}(t)}{16\pi} \frac{1}{M_Y^2}\left(\frac{W^2}{M_Y^2}\right)^{2\alpha_k(t)-2}(M_Y^2)^{\alpha_l(0)-1}. \tag{28}$$

For these processes $k = I\!P, f$ and $l = I\!P, I\!R$. The ϕ and J/ψ mesons are pure $s\bar{s}$ and $c\bar{c}$ states, respectively, which couple only to $I\!P$. Therefore for the ϕ and J/ψ production the exchange of trajectory f is forbidden. For the ρ^0 production f trajectory is allowed, however, at large W^2, hight $-t$ and small M_Y^2/W^2 its contribution is expected to be negligible. To simplify the formulae, the f trajectory exchange is neglected also in the ρ^0 production.

Taking into account only the $I\!P$ exchange, the elastic and proton-dissociative cross section are given by equations:

$$\frac{d\sigma_{\gamma p \to Vp}}{dt} = f_V(t) \cdot (W^2)^{2\alpha_{I\!P}(t)-2}, \tag{29}$$

$$\frac{d^2\sigma_{\gamma p \to VY}}{dt dM_Y^2} = G^V_{I\!P I\!P I\!P}(t)\frac{1}{M_Y^2}\left(\frac{W^2}{M_Y^2}\right)^{2\alpha_{I\!P}(t)-2}\left[(M_Y^2)^{\alpha_{I\!P}(0)-1} + R(t)\cdot(M_Y^2)^{\alpha_{I\!R}(0)-1}\right], \tag{30}$$

where

$$f_V(t) = \frac{\beta_{VI\!P}^2(t)\beta_{pI\!P}^2(t)}{16\pi}, \tag{31}$$

$$G^V_{\mathbb{P}\mathbb{P}\mathbb{P}}(t) = \frac{\beta^2_{V\mathbb{P}}(t)\beta_{p\mathbb{P}}(0)g_{\mathbb{P}\mathbb{P}\mathbb{P}}(t)}{16\pi}, \quad (32)$$

$$G^V_{\mathbb{P}\mathbb{P}\mathbb{R}}(t) = \frac{\beta^2_{V\mathbb{P}}(t)\beta_{p\mathbb{R}}(0)g_{\mathbb{P}\mathbb{P}\mathbb{R}}(t)}{16\pi}, \quad (33)$$

$$R(t) = \frac{G^V_{\mathbb{P}\mathbb{P}\mathbb{R}}(t)}{G^V_{\mathbb{P}\mathbb{P}\mathbb{P}}(t)} = \frac{\beta_{p\mathbb{R}}(0)g_{\mathbb{P}\mathbb{P}\mathbb{R}}(t)}{\beta_{p\mathbb{P}}(0)g_{\mathbb{P}\mathbb{P}\mathbb{P}}(t)}. \quad (34)$$

$G^V_{\mathbb{P}\mathbb{P}\mathbb{P}}(t)$ and $G^V_{\mathbb{P}\mathbb{P}\mathbb{R}}(t)$ depend on the type of produced vector meson. $R(t)$ is the same for all vector mesons and is expected to be the same for all proton-dissociative reactions $ap \to aX$, independent of the initial hadron a.

Elastic cross section

If $f_V(t)$ is approximated by the single exponential function $f_V(t) \simeq e^{b^V_{0,el}\cdot t}$, which is the most often case, the elastic cross section is expressed by:

$$\frac{d\sigma_{\gamma p\to Vp}}{dt} \sim e^{(b^V_{0,el}+2\alpha'_{\mathbb{P}}ln(W^2))\cdot t}\cdot (W)^{4\alpha_{\mathbb{P}}(0)-4} \sim e^{b^V(W)\cdot t}\cdot (W)^{4\alpha_{\mathbb{P}}(0)-4}, \quad (35)$$

where

$$b^V(W) = b^V_{0,el} + 2\alpha'_{\mathbb{P}}\ln(W^2) \simeq b^V_{0,el}W^{4\alpha'_{\mathbb{P}}/b^V_{0,el}}. \quad (36)$$

Eq. 36 is an important prediction of the Regge theory. The existence of the non-zero $\alpha'_{\mathbb{P}}$ implies the fact that the slope of the t distribution depends on the energy, so the shrinkage is expected. The energy dependence of the elastic cross section can be derived from Eqs. 35 and 36; integration over t gives:

$$\sigma_{\gamma p\to Vp} \sim \frac{(W)^{4\alpha_{\mathbb{P}}(0)-4}}{b^V(W)} \simeq W^{0.2}. \quad (37)$$

Proton-dissociative cross section

Under assumptions that $G^V_{\mathbb{P}\mathbb{P}\mathbb{P}}(t) \sim e^{b^V_{0,pg}\cdot t}$ and $R(t) = R = const$ the proton-dissociative cross section is approximated by:

$$\frac{d^2\sigma_{\gamma p\to VY}}{dtdM^2_Y} \sim e^{\left(b^V_{0,pd}+2\alpha'_{\mathbb{P}}ln\left(\frac{W^2}{M^2_Y}\right)\right)\cdot t}\cdot\frac{1}{M^2_Y}\left(\frac{W}{M_Y}\right)^{4\alpha_{\mathbb{P}}(0)-4}\left[(M^2_Y)^{\alpha_{\mathbb{P}}-1} + R\cdot(M^2_Y)^{\alpha_{\mathbb{R}}(0)-1}\right] \quad (38)$$

For the proton-dissociative vector meson production b^V defined by:

$$b^V(W, M_Y) = b^V_{0,pd} + 2\alpha'_{\mathbb{P}}ln\left(\frac{W^2}{M^2_Y}\right) \quad (39)$$

depends both on the energy W and the proton dissociative mass M_Y. Similarly as for the elastic cross section the non-zero $\alpha'_{\mathbb{P}}$ in Eq. 39 indicates the existence of the shrinkage for the proton-dissociative cross section.

Ratio of the elastic to proton-dissociative cross section as a function of t

Without any assumptions about the t-dependence of the $G^V_{\mathbb{P}\mathbb{P}\mathbb{P}}(t)$, $R(t)$ and $f_V(t)$ the Regge theory prediction about the ratio of the elastic to proton-dissociative differential cross section

$d\sigma/dt$ has a form:

$$\frac{d\sigma_{\gamma p\to Vp}}{dt}/\frac{d\sigma_{\gamma p\to VY}}{dt} \;=\; F(t)\cdot I(t,M_Y^{max}), \tag{40}$$

where

$$F(t)=\frac{f_V(t)}{G^V_{\mathbb{P}\mathbb{P}\mathbb{P}}(t)} \;=\; \frac{\beta^2_{p\mathbb{P}}(t)}{\beta_{p\mathbb{P}}(0)g_{\mathbb{P}\mathbb{P}\mathbb{P}}(0)} \tag{41}$$

and

$$I(t,M_Y^{max}) \;=\; \int_0^{M_Y^{max}} \frac{(M_Y^2)^{2\alpha_{\mathbb{P}}(t)-1}}{(M_Y^2)^{\alpha_{\mathbb{P}}(0)-1}+R(t)\cdot(M_Y^2)^{\alpha_{\mathbb{R}}(0)-1}}\cdot dM_Y\,. \tag{42}$$

The ratio in Eq. 42 is independent of the vector meson involved in both, elastic and proton-dissociative processes, and does not depend on the energy W.

The predictions of the Regge theory has been extensively tested in various reactions that involve the vector meson production. The comparison of the Regge expectation with the vector meson photoproduction for $-t\lesssim 3$ GeV^2 can be found in the previous ZEUS measurement [5].

2.6.2 Expectations of the pQCD Models

Fig. 7 shows the diffractive photoproduction of the vector meson on the photon as seen in the framework of pQCD-based models [21]. The definition of the variables is the same as in Secs. 2.1 and 2.6.

When the photon energy is sufficiently big, three steps of the process can be distinguished:

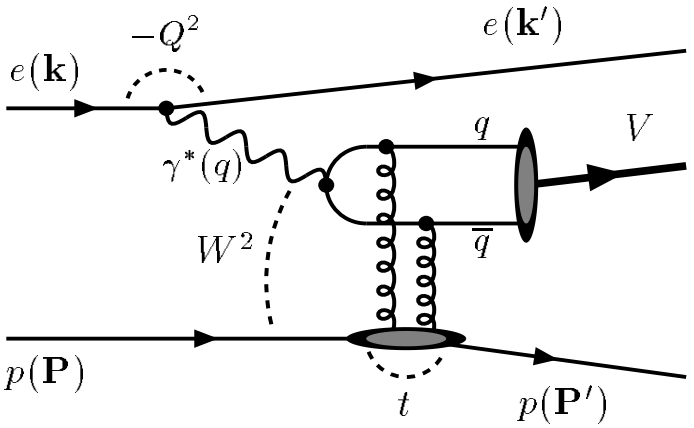

Figure 7: The diagram of the hard diffractive production of vector mesons described as two gluon exchange.

- Long before the interaction the photon fluctuates into $q\bar{q}$ state. The fluctuation is described by the photon wave-function derived from QCD [21].

- Then the $q\bar{q}$ pair scatters off the proton target. This interaction in a lowest order is described as the exchange of two gluons in a color singlet state. If treated by the leading logarithmic approximation (LLA), the interaction can be described by the exchange of a gluon ladder [22, 7, 23, 6]. The pQCD can be used to calculate this process only in the presence of a hard scale. In photoproduction, where $Q^2 \simeq 0$ GeV^2, the pQCD formalism can be applied only if the vector meson mass or the momentum transfer t is large enough to provide a hard scale.

- After the scattering off the proton the $q\bar{q}$ pair turns into a vector meson. This transition is a non-perturbative phenomenon and its description requires the knowledge of the vector meson wave-function. A determination of the meson wave-function is based on the lattice calculations and sum rules [24].

Soft and hard regimes are expected to differ significantly. The pQCD predictions for the diffractive vector meson photoproduction in a presence of the hard scale provided by the large $-t$, are different that the ones based on the Regge approach. Therefore the measured features of the process can be used to distinguish whether the vector meson photoproduction at high $-t$ exhibits characteristic of the soft or hard physics. Some of the expected signs of approaching the perturbative regime of the diffractive vector meson production are listed below.

1. The diffractive cross section, due to the gluon density in the proton, is expected to rise fast with W [22];

2. The differential cross section $d\sigma/dt$ is predicted to follow the power-like behavior [3, 4];

3. No W-dependence of the cross section and no shrinkage of the diffractive t-slope [23, 6] or weak W-dependence of the cross section [7] is predicted;

4. The pQCD calculations give the significant breaking of SCHC for light vector mesons production (helicity matrix elements (Eq. 21) differ from zero) [23, 6, 25]. At the asymptotic limit of very large $-t$ the maximal breaking is expected, which means that the mesons are produced in the helicity zero state independently of the initial photon helicity;

5. Approximate restoration of the flavor-independent production mechanism is predicted [26] (i.e. SU(3) and SU(4) for light and heavy vector mesons, respectively). The ratio of the production cross section, resulting from the quark charges and SU(3) or SU(4) symmetries, is expected to have a relative size of $9:1:2:8$ for ρ^0:ω:ϕ:J/ψ.

The hypothesis 2, 3 and 5 are tested in this thesis. An independent analysis based on the same data sample and event selection measures the helicity matrix elements [27]. Therefore the determination of main features of the diffractive photoproduction of the vector mesons at large $-t$ gives a perfect possibility of searching and studying the signatures of the hard scale.

Two recent theoretical models describing the diffractive vector meson photoproduction in terms of the pQCD [7, 6] are presented in more detail in Sec. 8. The predictions of these models are compared to the results of this analysis.

3 ZEUS - a Detector at the HERA Accelerator

3.1 HERA

The Hadron Electron Ring Accelerator (HERA) [28], shown in Fig. 8, located at DESY in Hamburg, is the first electron-proton collider in the world. HERA offers a unique possibility to study scattering between electrons (or positrons) of about 30 GeV and protons of 820 GeV. The HERA tunnel runs for most of its length of 6.3 km outside the site of DESY and 10 - 25 m deep under ground. There are four experimental halls, the two main experiments, H1 and ZEUS, are located in the north and south hall, respectively. The remaining two halls are occupied by experiments, that use the proton beam (HERA-B) or the electron beam (HERMES) only. HERA-B is designed to study CP violation in the $B^0\bar{B}^0$ system, using a wire target to produce B-mesons in the proton beam halo. HERMES is designed to investigate the spin structure of the nucleons by scattering of longitudinally polarized photons off polarized gas targets.

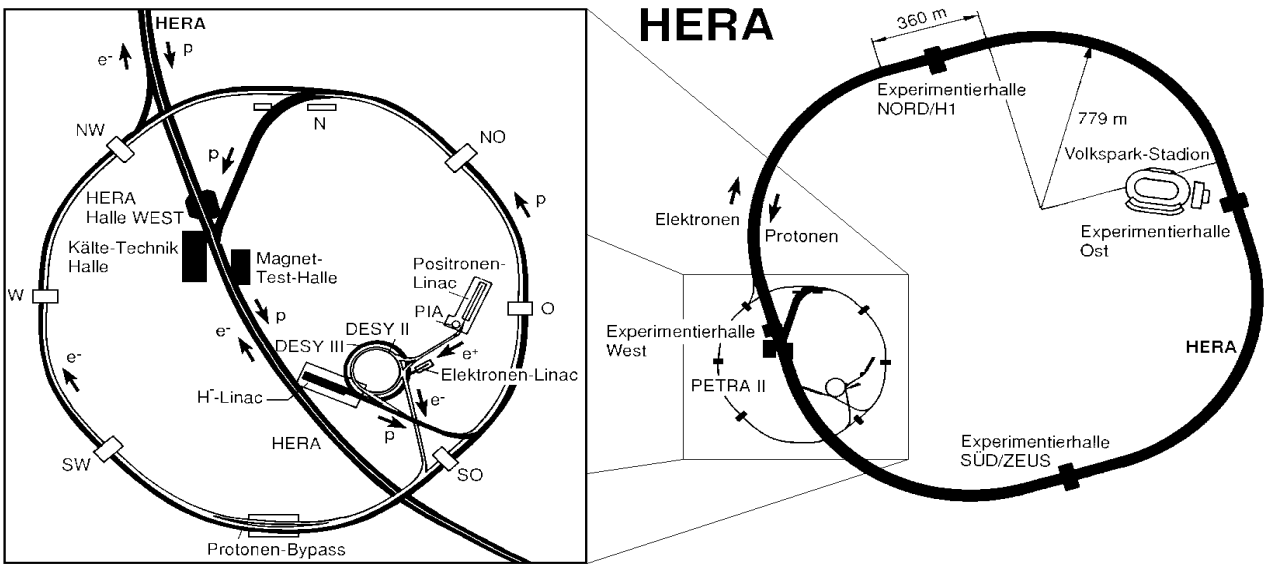

Figure 8: Hera collider with the four experimental halls and the preaccelerator system.

The two storage rings for the electron (e) and proton (p) beams are mounted on top of each other in the HERA tunnel. The magnets of the electron storage ring contain normal conductors and operate at room temperature. The energy lost by the electrons due to synchrotron radiation is compensated by the radiofrequency cavities, some of which are superconducting. The magnets of the proton storage ring need to produce a magnetic field of 4.68 Tesla for bending the high momentum proton beam in the ring area. To accomplish this, superconducting magnets operating at 4.4 K have been constructed. At nominal beam energies, the resulting center-of-mass energy, $\sqrt{s} = 314$ GeV, is equivalent to a 51 TeV electron beam colliding on a fixed proton target.

Some HERA design parameters [29] and the machine performance during the 1996 and 1997 data taking periods are summarized in Tab.1.

HERA parameters	**Design values**		**1996**		**1997**	
	e^-	p	e^+	p	e^+	p
Energy (GeV)	30	820	27.5	820	27.5	820
Instantaneous luminosity ($cm^{-2}s^{-1}$)	$1.7 \cdot 10^{31}$		$3.8 \cdot 10^{30}$		$5.6 \cdot 10^{30}$	
Specific luminosity ($cm^{-2}s^{-1}(mA)^{-2}$)	$3.9 \cdot 10^{29}$		$5.3 \cdot 10^{29}$		$5.7 \cdot 10^{29}$	
Integrated luminosity (pb^{-1})	35		17.6		36.35	
Magnetic Field (T)	0.165	4.65				
Current (mA)	58	163	23	60	30	75
Number of bunches	210		177+28	177+3	176+20	176+5
Beam σ_x (mm) at IP	0.30	0.27	0.27	0.18	0.27	0.18
Beam σ_y (mm) at IP	0.06	0.09	0.06	0.06	0.06	0.06
Beam σ_z (cm) at IP	0.8	0.11	0.8	0.11	0.8	0.11

Table 1: HERA design parameters and actual performance in 1996 and 1997. The luminosity values are typical values (specific) and typical peak values (instantaneous) towards the end of running periods.

The electrons and the protons are initially accelerated in the system of a few accelerators and injected into the HERA storage rings.

Electrons are injected into the LINAC I and accelerated to 220 MeV, from there they are passed into LINAC II and there accelerated to 450 MeV. The next step is filling the positron intensity accumulator (PIA) with a single bunch with an electron current up to 60 mA. Then the bunch is transferred to DESY II and accelerated up to 7.5 GeV. When passing the bunch to PETRA II (Positron-Elektron Tandem Ring Anlage), it is stretched, so that 70 bunches with 96 ns spacing are obtained. Then the electrons are accelerated to 14 GeV and passed to HERA. HERA is filled with up to 210 bunches and the electrons are accelerated to 27.5 GeV with a life time of about 8 hours (for positrons). Under standard operation, HERA is not filled with all bunches. Satellite (unpaired) bunches can be used to estimate beam related background rates. Empty bunches allow to study and estimate background rates due to cosmic rays. In the 1996 and 1997 data taking period, HERA operated with an average of 176 ep bunches, 20 electron and 5 proton bunches.

As the proton source serves hydrogen. The proton are accelerated up to 50 MeV in a linear accelerator. Then these protons are injected in the DESY III storage ring, which is filled with up to 11 proton bunches. The bunches in DESY III have already the same bunch spacing as HERA (96 ns) and are accelerated up to 7.5 GeV. Then the protons are transferred to PETRA where 70 bunches are accumulated and accelerated up to 40 GeV, and then passed to HERA. This process is repeated until HERA is filled up to 210 proton bunches. In HERA the protons are accelerated up to their final energy[2] of 820 GeV with a beam life time of a few days.

[2]In the 1998/99 running period, the proton energy in HERA was increased to 920 GeV.

The HERA Collider was commissioned in 1991 and first ep interactions were observed and recorded by H1 and ZEUS during spring 1992. Since then the integrated luminosity delivered by HERA has been continuously increased, what can be seen in Fig.9. This analysis uses the data taken during 1996 and 1997. Since between 1996 and 1997 there was only one short break, these years can be considered one complete data set.

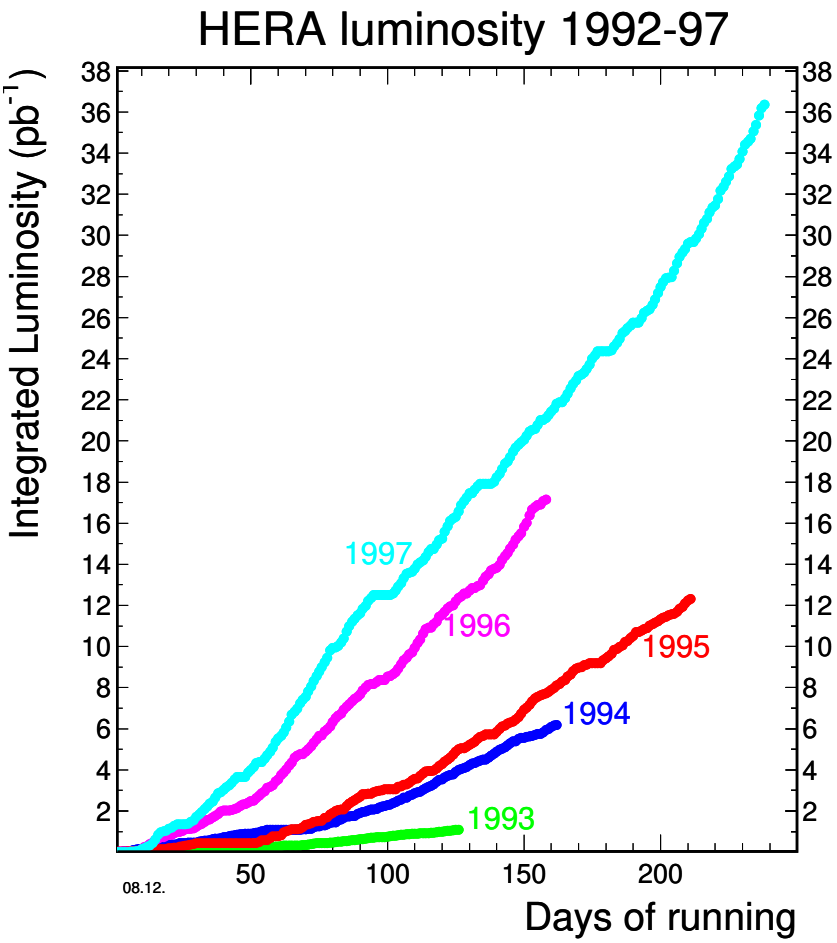

Figure 9: Integrated luminosity delivered by HERA during the data taking periods from 1993 to 1997.

3.2 The ZEUS Detector

The ZEUS collaboration joins over 450 physicists and an equal number of technicians and engineers from 51 institutes in 11 countries.

The goal of the ZEUS detector [30] (Fig. 10) is to determine with high precision, the energies, directions and nature of single particles and jets created in the interactions. It was designed to study various aspects of lepton-hadron scattering, including, for example, the photoproduction

of vector mesons and jets, the structure of the photon, proton and Pomeron, the production of leading neutrons or more exotic phenomena, like contact interactions and excited fermions. The design accounts for the large forward-backward asymmetry of the ep final state, which results from the big difference in the energies of the incoming particles and gives a center-of-mass system moving in the direction of the proton beam relative to the lab frame. The ZEUS detector is located in the South Hall of HERA. Its construction and installation was finished in fall 1991. Therefore, to accommodate the gain in physics and technical understanding by the collaboration over the years of data taking, several detector upgrades and additions have taken place.

The ZEUS coordinate system is defined as a right-handed orthogonal system, which origin (X=Y=Z=0) is at the nominal interaction point IP. The X-axis points towards the center of the HERA ring, the Y-axis is pointing upwards and the Z-axis is given by the proton beam direction. This corresponds to the polar angle, measured with respect to the positive Z-axis, of the proton and end electron equal 0° and 180°, respectively. The azimuthal angle is measure with respect to the X-axis.

The heart of the ZEUS detector is the Uranium Scintillator Calorimeter (UCAL) which measures energies and directions of particles and particle jets with high precision. The UCAL is divided in three sections: the Forward Calorimeter (FCAL), the Rear Calorimeter (RCAL) and Barrel Calorimeter (BCAL). In front of the RCAL and FCAL, Rear and Forward Presampler detectors (RPRES and FPRES) are installed, consisting of a single layer of scintillator plates. The calorimeter hermetically encloses the tracking detectors which measure the tracks of charged particles using wire chambers and which consist of: the Central Drift Chamber (CTD), Forward (FTD) and Backward (RTD) Drift Chambers and in the forward direction the Transition Radiation Detector (TRD) to identify high energy electrons. These chambers are surrounded by a thin superconducting solenoid producing an axial magnetic field of 1.8 Tesla for determining the momenta of charged particles from track curvature. The Vertex Detector (VXD), still shown in Fig. 10 was removed in the winter shutdown 1995/96.

Energy not fully absorbed in the UCAL is measured in the Backing Calorimeter (BAC) which uses the 7.3 cm thick iron plates of the return yoke as absorber and proportional tube chambers for observing penetrating particles.

Particles which are not absorbed in the material of the uranium, scintillator and backing calorimeter are typically identified as muons. Their tracks are measured before and after the iron yoke by limited streamer tube chambers, forward, barrel and rear muon chambers (FMUON, BMUO, RMUO). The muon momenta are determined by the deflections of their paths by the solenoid and by the iron yoke which is magnetized toroidally up to 1.6 Tesla by copper coils. In the forward direction magnetized iron toroids instrumented with limited streamer tubes and drift chambers measure very energetic muons (up to 150 GeV/c).

A small sampling calorimeter is installed near the beam pipe, just behind the RCAL module, to explore the low Q^2 region. This Beam Pipe Calorimeter (BPC) is accompanied by a small Beam Pipe Tracker (BPT). An iron wall equipped with two layers of scintillation counters (VETOWALL) is placed near the tunnel exit, at Z=−7.3 m, for detection of background particles produced upstream by the proton beam. Further down the electron beam direction (negative Z-axis) photons and electrons are detected in the luminosity monitor (LUMI), consisting of two lead-scintillator electromagnetic calorimeters, located at Z=−35 m (electron detector) and Z=−107 m (photon detector). At Z=−44 m, another lead-scintillator electromagnetic calorimeter, 44m tagger, is placed, designed to measure electrons from photoproduction

events.

In the forward direction, at Z=5.1, the Proton Remnant Tagger (PRT), a lead-scintillator counter, is installed around the beam pipe to obtain information about the hadronic final state (for example a dissociating proton) in the range of pseudorapidity[3] $4.3 < \eta < 5.8$. Between about 20 m to 90 m in positive Z-direction the 6 stations of silicon microstrip detectors of the Leading Proton Spectrometer (LPS) is installed in the beam line to measure forward scattered protons. The Forward Neutron Calorimeter (FNC) is a lead-scintillator sandwich calorimeter situated at Z=105 m.

The short time spacing of the *ep* bunches at HERA of 96 ns results in a nominal interaction rate of about 10 MHz. To reduce this rate to the level of a few Hz, at which the data can be handled by the data acquisition system, the three-level trigger is used in ZEUS. More information about the trigger can be found in Sec. 4.2.

Some of the components playing a key role for this analysis are described in more detail below.

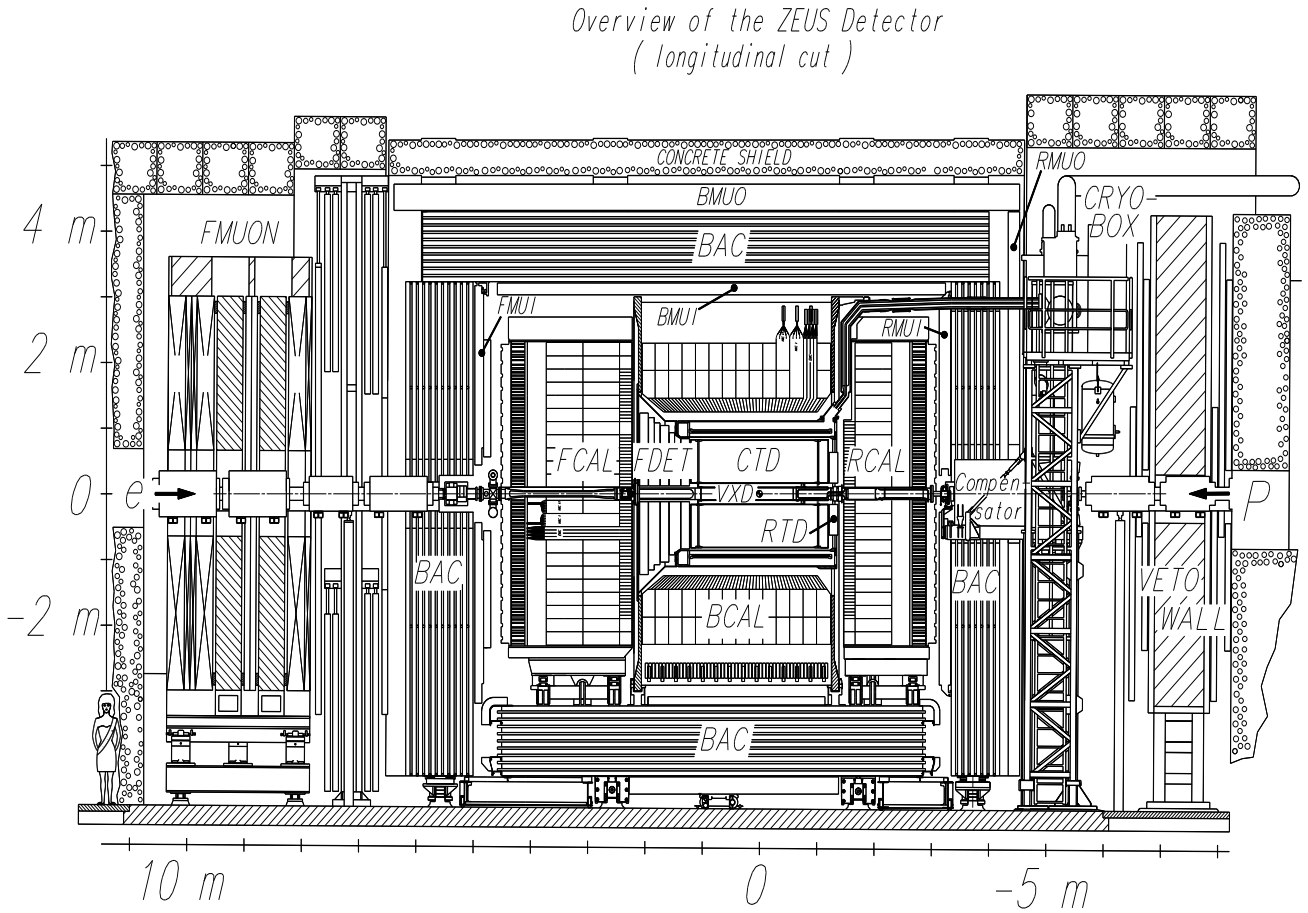

Figure 10: Schematic view of the ZEUS detector.

The Uranium Calorimeter (UCAL)

The UCAL [31] is segmented longitudinally into an electromagnetic and one or two hadronic

[3]The pseudorapidity η is defined as: $\eta = -\ln\ tan(\theta/2)$, where θ is the particle zenith angle.

sections and is divided into three part: BCAL [32], FCAL and RCAL [33], (Fig. 11), with 7, 5 and 4 absorption lengths, respectively. This forward-backward asymmetry of the calorimeter was chosen to account for the large forward-backward asymmetry of the ep final state due to the different energies of the incoming positrons and protons. The FCAL covers the polar angle between 2.2° and 39.9°, corresponding to $4.0 > \eta > 1.0$; the BCAL the polar angle θ from 36.7° to 129.1°, corresponding to $1.1 > \eta > -0.74$ and the RCAL, the polar angle from 128.1° to 176.5°, corresponding to $-0.72 > \eta > -3.49$. The UCAL is a sampling calorimeter and consists of plates of depleted uranium[4] interleaved with plastic scintillator[5] in order to achieve compensation (i.e. the same response of the calorimeter to electrons and hadron of equal energies) and the best possible energy resolution for hadrons. Under beam test conditions, the resolution of the calorimeter for hadrons was measured to be

$$\frac{\sigma(E)}{E} = \frac{0.35}{\sqrt{E}},$$

and for electrons

$$\frac{\sigma(E)}{E} = \frac{0.18}{\sqrt{E}},$$

with an impact energy of E in GeV.

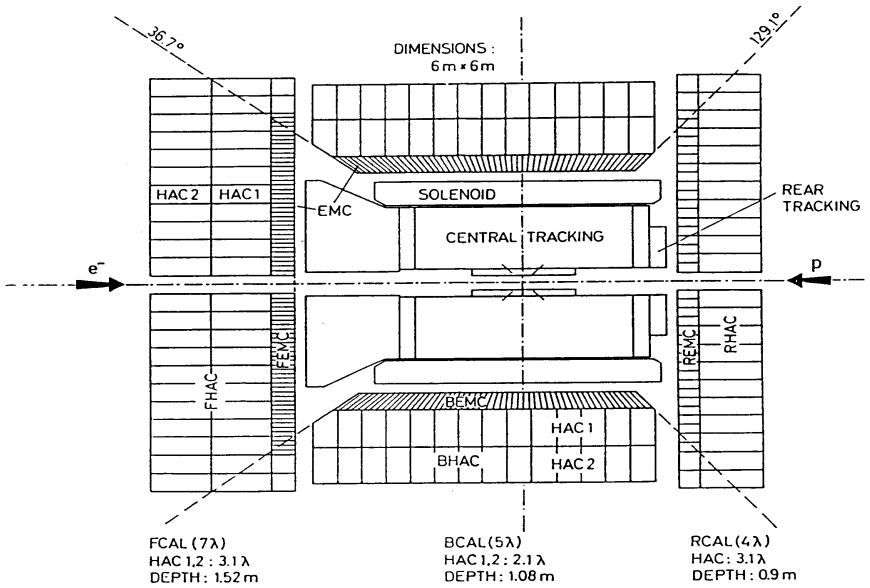

Figure 11: Cross sectional view of the ZEUS calorimeter along the beam direction.

The three section of the calorimeter are divided into modules, which are subdivided transversely into towers of dimension 20×20 cm^2. The towers are subdivided longitudinally into electromagnetic (EMC) and hadronic (HAC) parts. Every EMC section consists of four 5×20 cm^2 cells (two 10×20 cm^2 cells in RCAL). Each cell of the calorimeter is read out on two sides by wavelength shifters coupled to photomultiplier tubes (PMT). The longitudinal depth of the UCAL is chosen, so that 90% of the recorded jets lose a minimum of 95% of their energy in the UCAL.

[4] An alloy of 98.4% U^{238}, 1.4% Nb and $\leq 0.2\%$ U^{235}.
[5] SCSN-38

Beside its compensating effect, U^{238} provides an extremely valuable source of calibration and monitoring tool by its natural radioactivity. The precision of the inner calibration between cells is known to 1%. Despite the presence of the uranium activity, the calorimeter has very low noise, which is typically 10 and 20 MeV for EMC and HAC cells, respectively.

The Central Tracking Detector (CTD)

The momenta and direction of charged particles are measured with high precision by the CTD [34] in the magnetic field of the solenoid. The solenoid is 280 cm long and has an inner radius of 86 cm. Its total material thickness was minimized to be about 0.9 radiation lengths X_0 (equivalent to 8 cm of aluminum) in order to keep the loss of energy of electrons, photons and hadrons small. The influence of the magnetic field of the thin solenoid on the HERA beam dynamics is compensated by the super conducting solenoid (compensator) with a length of 120 cm and an inner radius of 18 cm creating a field of 5 Tesla. The additional information for particle identification is obtained from the mean energy loss dE/dx of charged particles within the gas chamber volume of the CTD.

The CTD is built as a cylindrical drift chamber with a length of 205 cm and an inner/outer radius of 18.2 cm/79.4 cm. This gives a coverage of the polar angle of $15° < \theta < 164°$ (corresponding to $2.04 > \eta > -1.96$ in pseudorapidity) and a full coverage in the azimuthal angle. The inner structure of the central tracking detector consists of 9 superlayers, with a total of 576 drift cells. Each cell has 8 sense wires, The chamber is presently operated with a gas mixture of $Ar:CO_2:C_2H_6$ (90:8:2). Its spatial resolution is 120 - 130 μm in the plane perpendicular to the beam. The interaction vertex is measured on an event-by-event basis with a typical resolution along and transverse to the beam axis of 0.4 and 0.1 cm, respectively.

The 44m Tagger

The 44m tagger is a small detector located at Z=–44 m and sensitive to positrons of energy 21-26 GeV, scattered under very small angles. The detector is an electromagnetic sampling calorimeter. It consists of twelve $70 \times 90 \times 7$ mm^3 tungsten plates interleaved with 3 mm thick scintillator layers. After the first three tungsten plates additional scintillator strips are installed. These 8 mm wide vertical strips are connected at the top end to plastic light guides. Signals from the strips can be used to apply fiducial cuts and select well contained electromagnetic showers within the tagger.

The energy resolution for 1-5 GeV electrons hitting the tagger centrally was measured in a test beam and is $0.25/\sqrt{E(\mathrm{Gev})}$. The calorimeter linearity is better then 1%.

The Luminosity Detector (LUMI)

The collider luminosity $\mathcal{L}$ measures the rate R of events per second for a given process with the cross section σ and is defined by:

$$R = \mathcal{L} \times \sigma.$$

The standard luminosity unit is cm^{-2}s^{-1}. An accurate determination of the luminosity is crucial for any direct measurement of cross sections. In ZEUS, the ep luminosity is measured

by studying the rate of the Bethe-Heitler bremsstrahlung process

$$ep \rightarrow e'\gamma p.$$

The cross section for this process is well understood and the theoretical calculations predicts its value to an accuracy of 0.5%.

The luminosity detector [35] consists of two components. The first is the lead-scintillator sampling calorimeter, located at Z=–107 m, which detects photons (LUMI_γ). After 3 X_0 a detector to measure shower position is inserted. Photon radiated at angles of $\Theta_\gamma < 0.5$ mrad with respect to the beam axis, exit the beam pipe through a copper/beryllium window at Z=–92 m. This window defines the aperture of the acceptance. The energy resolution of the photon calorimeter has been measured in a test beam to be $18\%/\sqrt{E(\mathrm{GeV})}$. To protect the calorimeter from the synchrotron radiation, a 3.5 X_0 carbon/lead filter was placed in front of the detector. The presence of the filter degradetes the energy resolution of the calorimeter to $25\%/\sqrt{E(\mathrm{GeV})}$.

The second component of the LUMI detector is an electron calorimeter (LUMI_e), located at Z=–35 m, behind a steel exit window. It is a 22 X_0 deep lead-scintillator sampling calorimeter with an electron position detector inserted at a depth of 7 X_0. It is sensitive to electrons with energies between 5 and 21 GeV. The energy resolution of the calorimeter is $18\%/\sqrt{E(\mathrm{GeV})}$.

In practice, the luminosity determination is performed with the measured photon flux in the LUMI photon calorimeter. The less accurate luminosity measurement obtained out of the coincidence of a photon in the LUMI_γ and positron in LUMI_e is used as a cross-check. A more important use for the LUMI electron calorimeter is the detection of positrons originating from photoproduction events, where the scattering angle is small due to small momentum transfer.

Fig.12 shows the general layout of the luminosity monitor and the 44m tagger with respect to the HERA beam line.

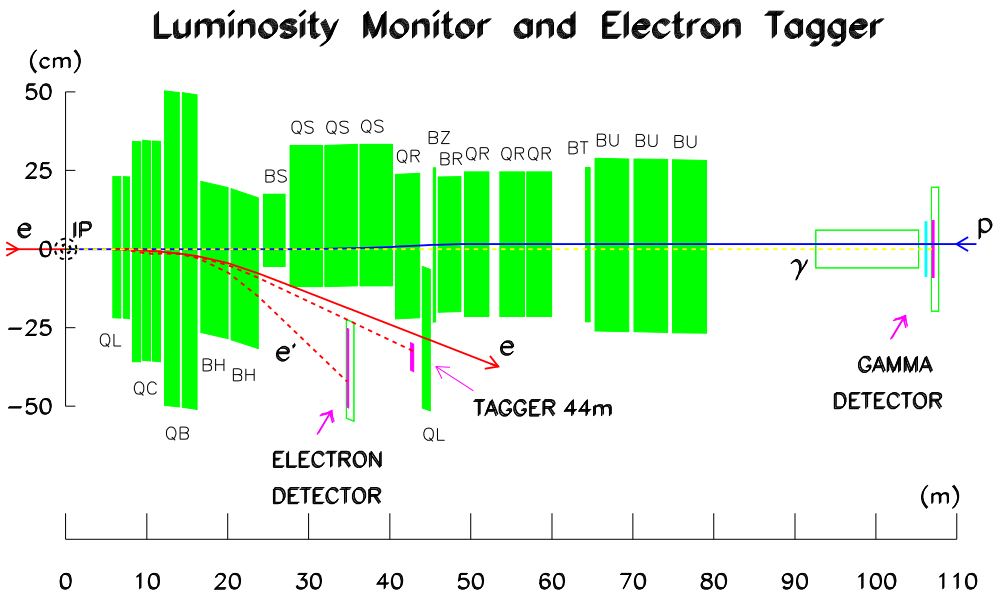

Figure 12: General layout of the ZEUS luminosity monitor and the 44m tagger.

4 Reconstruction and Event Selection

This chapter presents the reconstruction of the vector meson kinematic variables, the on-line trigger configuration and the final event selection. The accidental coincidences are briefly discussed. At the end, the method of calculating the cross section is described.

4.1 Reconstruction of the Kinematic Variables

The analysis presented in this thesis studies the production of vector mesons which decay into two charged particles. The statistical limitations, however, do not allow to collect enough events to perform a cross section measurement for the rare mesons, like $\rho'(1500-1700)$, ψ' or Υ. Therefore the results are limited to three vector mesons: ρ^0,ϕ, and J/ψ, decaying into $\pi^+\pi^-$, K^+K^-, and e^+e^- or $\mu^+\mu^-$, respectively.

The main features of the diffractive vector meson production in the ZEUS detector are shown in Fig. 13. Two well-measured tracks of opposite charge, coming from the common vertex observed in the CTD are required. An invariant mass of the meson is reconstructed from the track momenta, assuming that the particle mass of the track is equal to the π, K and e mass for ρ^0,ϕ and J/ψ, respectively. The scattered positron is detected in the 44m tagger. It ensures that the virtuality of the photon is low and allows the precise measurement of the momentum transfer. The UCAL was used to reconstruct additional particles. Events which had an energy deposit in the calorimeter not associated with the tracks were excluded from the analysis; the exception was the FCAL, where the energy deposits originate from the proton dissociative system Y. This condition suppresses the photon-dissociative background and fulfills the experimental definition of the diffraction, which requires a gap of at least two units in pseudorapidity between the tracks and system Y (so called 'rapidity gap').

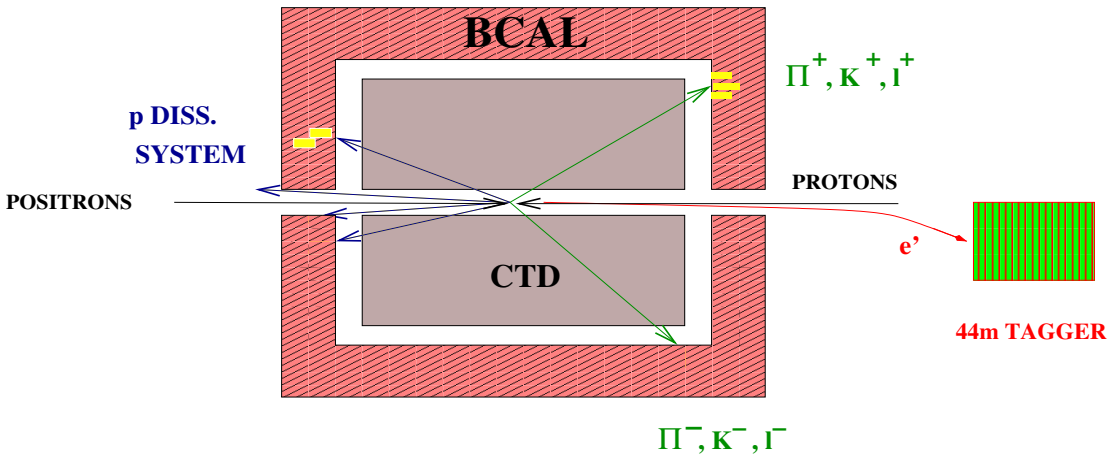

Figure 13: The diffractive vector meson production signatures in the ZEUS detector with two tracks in the CTD, energy deposit in the FCAL from the proton dissociated system Y and the scattered positron detected in the 44m tagger.

The CTD tracks and the primary vertex are reconstructed using the package VCTRAK [36]. The track finding and reconstruction can be performed in two ways - either using only the CTD information or including other components (SRTD and RTD) in the procedure. The analysis presented here is based on the CTD information alone, which reduces the uncertainties of the

acceptance and efficiency. The track finding and reconstruction starts in the outer part of the CTD and goes inward. The interaction vertex is reconstructed after all track candidates are found using information only from the tracks which originate from the beam pipe (so called 'vertexed tracks'). This analysis uses vertexed tracks to reconstruct the kinematic variables, which are assumed to come from the decay of a vector meson.

The 44m tagger detects positrons of energy between 21 and 26 GeV, scattered under very small angles. A hit in the 44m tagger is defined as an energy deposit in the detector greater than 1 GeV, which is well above noise. The hit in the 44m tagger is required in the trigger. To reconstruct the energy in the 44m tagger a fiducial cut selecting electromagnetic showers well contained in the detector is needed. It reduces the number of observed vector meson candidates by 30-50% and increases the systematic error of the tagging efficiency. Additionally, the photon energy reconstructed from the vector meson momentum measured in the CTD has a much better resolution. Therefore no information from the 44m tagger except the hit was used in this measurement.

The energy deposit in the RCAL, coming from the tracks, is used in the *High Lumi* trigger definition (see Sec. 5.5). The deposits in the FCAL are used in the study of the M_Y distribution (see Sec. 5.7.1). The energy distribution of all cells had been monitored for all runs used in this analysis and the cells with the noise above average or with faulty PMTs were removed from the data sample [37].

Kinematic variables

Except the UCAL energies only the three-momenta of the decay particles are measured. The kinematic variables are reconstructed only from the track momenta of the vector meson decay particles and the energy deposit in the UCAL. Neither the energy of the scattered positron nor the angle between the vector meson production plane and the scattering plane are directly determined. In tagged photoproduction, the Q^2 of the event varies from the kinematic minimum $Q^2_{min} \approx 10^{-9}$ GeV^2 to the maximum value at which the scattered positron is detected in the 44m tagger $Q^2_{max} \approx 0.015$ GeV^2. For $Q^2 > 0.015$ GeV^2 the 44m tagger acceptance is very small. The typical Q^2 is very small (with a median $Q^2 \approx 10^{-7}$ GeV^2) and therefore it can be neglected in the reconstruction of the kinematic variables, simplifying the used formulae. The γp center-of-mass energy W and the squared four-momentum transfer$t$ are given by [5]:

$$W^2 \approx 2E_p \cdot (E - p_z), \tag{43}$$

$$t \approx -p_T^2, \tag{44}$$

where E, p_z and p_T are the energy, longitudinal and transverse momentum of the produced vector meson in the laboratory frame, respectively and E_p is the incoming proton energy. This approximation is valid for M_Y, the meson mass M_V and p_T much smaller than W. In the reconstruction of the helicity angles ϑ_h and φ_h the virtual photon direction was approximated by the direction of the incoming positron. The direction opposite to that of the nucleonic state Y was approximated by that of the produced meson. Since the angle of the scattered positron is not measured, the helicity angle Φ cannot be determined and the three-dimensional angular distribution had to be averaged over Φ. Therefore the photon helicities states $+1$ and -1 could not be distinguished.

4.2 Trigger Configuration

Since the bunch crossing time in HERA of 96 ns corresponds to a rate of $\approx 10^7$ events/second, an efficient trigger and data acquisition system is necessary. Rates of the positron-proton interactions are much smaller than rates of the background processes, such as collisions of the proton with the residual gas in the beam pipe, cosmic rays events and electron beam-gas interactions. Out of a total interaction rate of about 10-100 kHz, the true ep scattering rate is only a few Hz. Therefore, to efficiently select physics events and cope with such rate of the background interactions, the ZEUS three-level trigger system [38] is used.

For each component, a hardware First Level Trigger (FLT) is designed in order to reduce the events rate to below 1 kHz. Its decision is based on the global properties of the event recorded in the component, such ass energy sums, timing information or signals in the veto counters. This information is passed to the Global First Level Trigger (GFLT), which issues a global trigger decision, determined from the component's trigger input.

Events accepted by the GFLT are passed to the Second Level Trigger (SLT), which for each component is a software-based trigger and runs on a network of transputers. The main task of the SLT is to identify and reject the background events. It reduces the input rate to below 100 Hz. The Global Second Level Trigger (GSLT) combines the information from the component SLTs and issues the final decision.

The next step is the software Third Level Trigger (TLT). It enables advanced selection of interesting events based on part of the ZEUS off-line reconstruction code. The TLT reduces the input rate to a few Hz, which contain ep physics events. Events which are accepted by the TLT are then written to tape and are available for off-line analyzes.

To suppress the background, the ZEUS experiment runs on-line in two trigger modes, the so called *High Lumi* and *Low Lumi* configurations. The detailed description of these triggers and their efficiency is presented in Sec. 5.5.

4.2.1 Trigger for High t Vector Mesons

The three levels of the trigger specially designed to study photoproduction of vector mesons at large t are described below.

1. At the FLT level the coincidence between a signal above 1 GeV in the 44m tagger and a good track candidate in the CTD is required. Additionally, to suppress random overlays with the bremsstrahlung events, an upper limit of 1 GeV on the energy deposited in the LUMI photon and electron detectors was imposed (LUMI_VETO). A detailed description of the efficiency of the 44m tagger can be found in Sec. 5.6.

2. The SLT restricts the number of tracks to below 4 and imposes a cut on the z position of the vertex, $|v_z| < 60$ cm, if the vertex is found. In addition, to efficiently select events with large $-t$, the transverse momentum of at least one track candidate is required to be greater than 0.8 GeV.

3. The TLT requires one vertex located within the bound of the nominal IP ($|v_z| < 60$ cm) and exactly two tracks pointing to the vertex.

4.2.2 Accidental Coincidences

The trigger requires a coincidence of signals and vetoes in various ZEUS components. For some events the trigger decision can be falsified by a random overlay of signals/vetoes in any of the triggering detector components. These so called accidental coincidences may either remove a valid event or add a random event to the data sample. Since it is impossible to distinguish such events from the real ones, they cannot be rejected from the data sample on the event-by-event basis. Therefore the fraction of events removed or added to the sample was studied using the data collected by the random trigger. When this fraction is known, it can be statistically subtracted or added to the data sample, for the enriched or depleted statistics, respectively.

Events removed from the data sample

For the trigger used in this analysis there are two possibilities to loose events due to the accidental coincidences. In one case good events which fulfill requirements of the FLT but have an accidental particle detected in the LUMI photon calorimeter are rejected from the sample. The fraction of discarded events was estimated to be $+7.1\%$ of the randomly collected events. The second possibility is an accidental signal in the LUMI electron detector, without any energy deposit in the LUMI photon calorimeter, which removes such event from the data sample. This contribution is much smaller than the one for the signal in the photon detector and was evaluated to be on the level of $+0.2\%$.

Events added to the data sample

One class of false events can be added to the selected data sample using the trigger configuration described above. These events mimic the trigger by an accidental hit in the 44m tagger, not accompanied by an energy deposit in any of the LUMI detectors. The fraction of such events in the random sample was estimated to be -1.3%.

The random trigger studies were performed separately for the *Low* and *High Lumi* triggers but no significant difference in the results was observed. Therefore for the fractions mentioned above, the combined data sample was used. The global correction factor, f_{AC}, resulting from the random trigger studies and estimating the overall fraction of events wrongly triggered due to accidental overlays of the component trigger signals, is

$$f_{AC} = 7.1\% + 0.2\% - 1.3\% = +6\%.$$

The final results have to account for the accidental coincidences which change the number of observed events. Therefore the measured cross section was multiply by the factor 1.06. Due to large statistics of the events collected by the random trigger and used to above studies, the error of the f_{AC} is very small, on the level of 0.1%, and therefore was not included in the systematic uncertainty of the cross section calculation.

4.3 Event Selection

For the vector meson candidate selection, the output from the ZEUS off-line reconstruction software package was used. At this point, the final calibration for all components is available,

as well as miscellaneous information such as bad running periods or bad channel lists. A reduced event record, which contains enough information to determined the entire kinematics is written to Data Summary Tables (DSTs). For the final selection the following requirements were applied to the DSTs.

- **General selection**

  1. Distinction between *Low Lumi* and *High Lumi* trigger (see Sec. 5.5). *Low Lumi* trigger was active only in 1997, runs numbered 25918 and higher were used. *High Lumi* trigger was active in 1996 and 1997. In 1996 runs starting from 22233 were used, and in 1997 runs starting from 25204.

  2. Runs with any problem with the photoproduction tagger or other essential components were excluded. The 44m tagger was modified and placed closer to the beam pipe in the middle of 1996. Therefore only the data taken with the tagger in the new position are used in this analysis.

- **Tracks Selection**

  3. Two tracks with opposite charges coming from one vertex were required.

  4. To restrict the measurement to a region were the detector performance and the trigger efficiency are well known, the following quality cuts were applied to each track with transverse momentum p_T and pseudorapidity η:

  $p_T > 0.15$ GeV for ρ^0
  $p_T > 0.40$ GeV for ϕ $\qquad |\eta| < 2.1$ GeV for all three vector mesons
  $p_T > 0.50$ GeV for J/ψ

  5. The vertex was constrained to be around the interaction point:

  $$|v_Z| < 40 \text{ cm}, \quad \sqrt{v_X^2 + v_Y^2} < 0.7 \text{ cm}$$

  6. To reduce the non-diffractive background, a cut on the maximum energy E_{max} of the calorimeter cell in RCAL or BCAL not associated with the tracks was applied:

  $$E_{max} < 250 \text{ MeV}.$$

  E_{max} was determined by applying a matching routine TRAKCLU [39] using a cone algorithm with a nominal cone angle $a = 0.2$ rad. This cut was not required for the FCAL, where the energy from proton remnants can be deposited.

  7. The trigger conditions and event selection impose different efficient cuts on the pseudorapidity of the most backward track in the FCAL, η_{min}, for neutral and charged particles. For neutral particles $\eta_{min} > 1$ and for charged particles $\eta_{min} \gtrsim 2.3$. Therefore to have symmetric cuts for charged and neutral particles, an explicit cut on η_{min} was applied:

  $$\eta_{min} > 2.1.$$

  In addition, this cut reduces the non-resonant background of the vector meson production and ensures that the rapidity gap between the vector meson and system Y fulfills the definition of diffraction (see Fig. 15).

- **The kinematic cuts**

  8. The W range was restricted to the region where the 44m tagger acceptance is well understood:

  $$80 < W < 120 \text{ GeV}.$$

9. The identification of the vector meson candidates was performed using the cuts on the invariant mass of the tracks measured in the CTD, assuming that the observed particles were pions ($M_{\pi\pi}$), kaons (M_{KK}) or electrons (M_{ee}) for the ρ^0, ϕ and J/ψmeson, respectively:

$$\begin{array}{lcccl} 0.55 & < & M_{\pi\pi} & < & 1.10 \text{ GeV} \quad \text{and} \quad M_{KK} > 1.075 \text{ GeV} \quad \text{for } \rho^0 \\ 0.99 & < & M_{KK} & < & 1.06 \text{ GeV} \quad \text{for } \phi \\ 2.98 & < & M_{ee} & < & 3.13 \text{ GeV} \quad \text{for } J/\psi \end{array}$$

The cut on $M_{\pi\pi}$ suppresses the contamination from decays of other vector mesons ($\omega \to \pi^+\pi^-\pi^0$, $\rho^{'}(1500) \to \pi^+\pi^-$ and $\phi \to K^+K^-$). The mass windows for ϕ and J/ψ have widths of three typical mass resolution around the reconstructed mass in order to reduce the non-resonant background.

10. The statistical limitations and the trigger conditions restricted the t range of the analysis to:

$$\begin{array}{lcccl} 1.2 & < & -t & < & 10 \text{ GeV}^2 \quad \text{for } \rho^0 \\ 1.2 & < & -t & < & 6.5 \text{ GeV}^2 \quad \text{for } \phi \\ 1.2 & < & -t & < & 6.5 \text{ GeV}^2 \quad \text{for } J/\psi \end{array}$$

11. The selection cuts described above and the trigger conditions restricted the M_Y range to:

$$M_Y \lesssim 25 \text{ GeV}.$$

The final number of events after all selection cuts is 19268, 2286 and 123 for the ρ^0, ϕ and J/ψ meson, respectively. The pseudorapidity η^+ and transverse momentum p_T^+ of the positive track, W, helicity angles φ_h and $\cos\vartheta_h$, the pseudorapidity of the vector meson η_{VM} and the pseudorapidity gap RG between the nucleonic state Y and the tracks are compared between the data and EPSOFT Monte Carlo in Figs. 14 and 15. The vertical lines indicate the applied selection cuts. For EPSOFT to reproduce the data distributions as shown in Figs. 14 to 15, it had to be reweighted according to the procedure described in the Sec. 5.

4.4 Cross Section Evaluation

The differential cross sections $d\sigma/dv$ ($v = t$ or M_V) for the proton-dissociative diffractive photoproduction of the ρ^0,ϕ and J/ψ mesons are calculated according to the formula:

$$\frac{d\sigma}{dv}(\gamma p \to VY) = \frac{N_{data} \cdot C_{res}}{A \cdot \Phi_\gamma \cdot \Delta v \cdot C_{br} \cdot \mathcal{L}}, \tag{45}$$

where N_{data} is the number of observed vector meson candidates after all selection cuts in v bin of the width Δv, C_{res} is the resonant contribution in this bin, A the overall acceptance in the bin, Φ_γ is the photon flux integrated over the y and Q^2 range covered in the analysis, $\mathcal{L}$ the integrated luminosity and C_{br} the branching ratio for the particular vector meson decay mode. The effective photon flux for $Q^2 < 0.015$ GeV^2 and $80 < W < 120$ GeV (corresponding to $0.0709 < y < 0.1595$) is $\Phi_\gamma = 0.0259$. The integrated luminosity of the sample is $\mathcal{L} = 24.14$ pb^{-1}. The branching ratios are 1, 0.5 and 0.12 for the ρ^0, ϕ and J/ψ mesons, respectively.

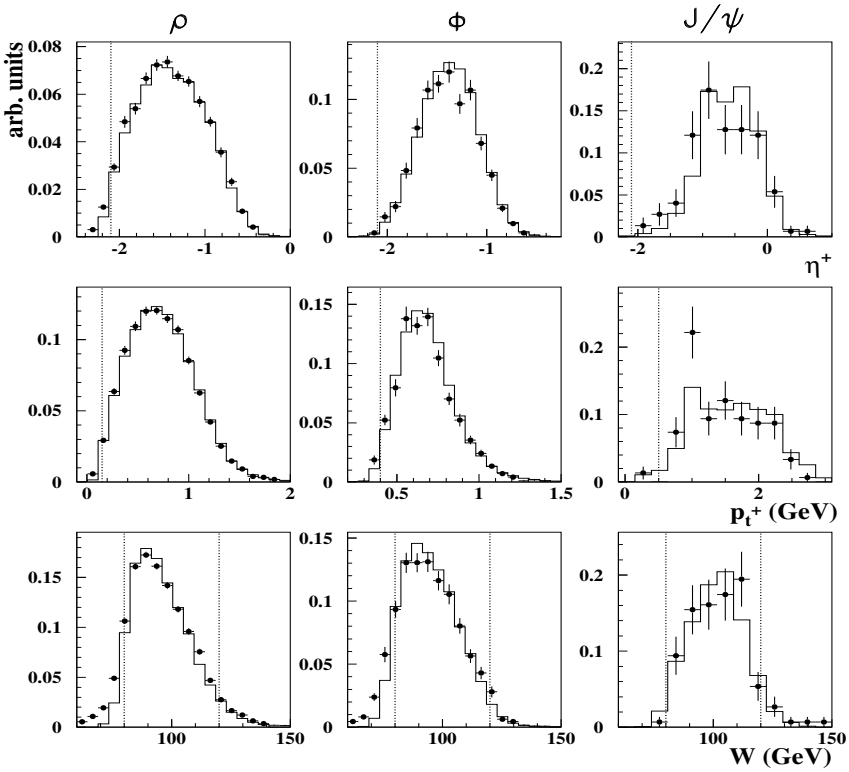

Figure 14: Comparison between the data (dots) and the EPSOFT MC (histograms) of the measured pseudorapidity η^+ and transverse momentum p_t^+ of the positive track and the center-of-mass energy W for ρ^0,ϕ and J/ψ. The dotted lines correspond to the selection cuts.

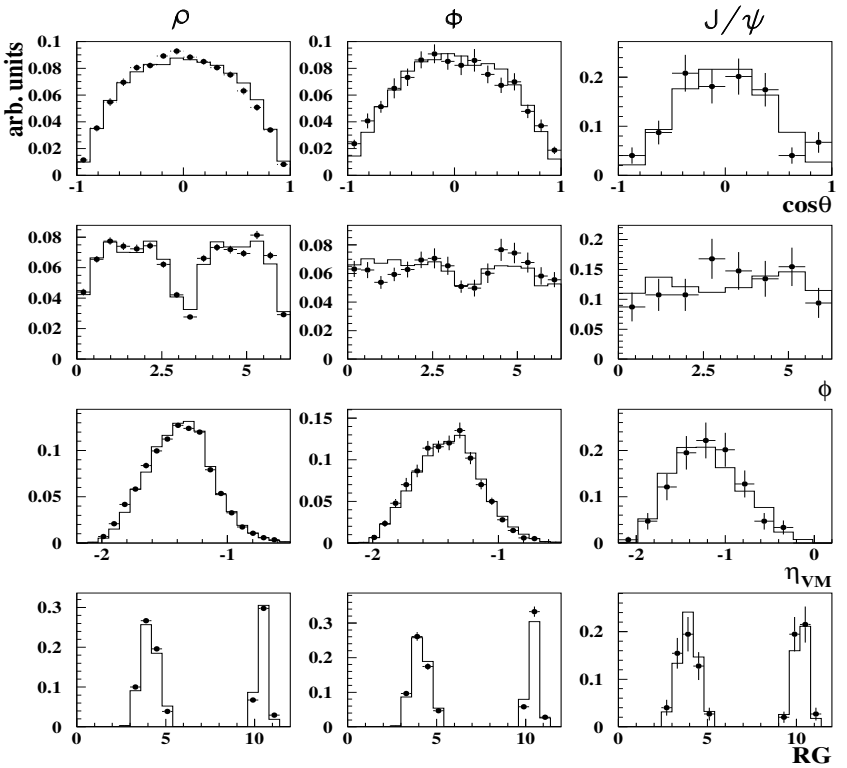

Figure 15: Comparison between the data (dots) and the EPSOFT MC (histograms) of the helicity angles ϑ_h and φ_h, the vector meson pseudorapidity η_{VM} and the rapidity gap RG (the difference between the vector meson pseudorapidity and the rapidity of the most backward track in the FCAL) for ρ^0,ϕ and J/ψ.

In order to compare the differential cross section $d\sigma/dt$ with the theoretical calculations, the kinematic range for the measurement was restricted to the region of the models validity:

$$x = \frac{-t}{M_Y^2 - t} > 0.01, \tag{46}$$

where x can be interpreted as the fraction of the proton momentum carried by the struck parton. Eq. 46 corresponds to the kinematic range $\frac{M_Y^2}{-t} < 100$ used in this analysis. The previous ZEUS results for lower $-t$ [5] were evaluated for the kinematic range $\frac{M_Y^2}{W^2} < 0.01$. For $t \approx 1$ GeV^2 and $W \approx 100$ GeV, the two conditions are numerically equivalent and therefore the results of this analysis and the previous measurement can be directly compared.

5 Monte Carlo Simulation

The analysis presented here is the measurement of the diffractive proton-dissociative photoproduction of vector mesons for large values of $-t$, $1.2 < -t < 10$ GeV^2. A previous measurement [5] was restricted to $-t$ values up to ~ 3 GeV^2, mostly due to statistical limitations and a trigger configuration. The chapter presents Monte Carlo samples used in the analysis and describes the ZEUS Monte Carlo simulation.

5.1 EPSOFT MC Generator

To simulate the proton-dissociative reaction $\gamma p \to VY$, the EPSOFT [40] generator was used. EPSOFT1.0 has been developed in the framework of HERWIG 5.8 [41]. Non-diffractive γp collisions as well as the $\mathbb{P}p$ and $\mathbb{P}\gamma$ scattering in diffractive events are treated as soft hadron-hadron collisions. The program has been tuned to ZEUS photoproduction data but works correctly also for $Q^2 \gg 0$.

Samples for all three mesons were generated according to the s-channel helicity conservation (all spin density matrix elements (Eq. 21, 24) are equal zero). The mass of the ρ^0 vector meson was assumed to have a relativistic Breit-Wigner shape, while the ϕ and J/ψ masses are fixed constants.

Electron Vertex

Kinematic variables y and Q^2 are generated according to the cross section formula:

$$\frac{d^2\sigma(ep)}{dydQ^2} = \frac{\alpha}{2\pi}\frac{1}{Q^2}\left\{\frac{(1+(1-y)^2)}{y}\sigma_{T\,ALLM}(\gamma p) + \frac{2(1-y)}{y}\sigma_{L\,ALLM}(\gamma p)\right\}, \qquad (47)$$

where $\sigma_{T\,ALLM}(\gamma p)$ and $\sigma_{L\,ALLM}(\gamma p)$ are the cross sections for scattering of transverse and longitudinal photons on protons, respectively, calculated from the ALLM parameterization [42]. It relies on triple–Regge type of considerations and has been fitted to the available photoproduction and Deep Inelastic Scattering (DIS) data. It also provides a smooth transition between the two kinematic regions.

Once the cross section is evaluated and the electron vertex is generated, the emitted photon collides hadronically with the proton. The diffractive dissociation (photon dissociation ($\gamma p \to Xp$), proton dissociation ($\gamma p \to VN$) and double dissociation ($\gamma p \to XN$)) is modeled as an exchange of the Pomeron. $\mathbb{P}$ is assumed to behave as a hadron, so the diffractive dissociation is treated as a collision of two hadrons: the dissociating particle and $\mathbb{P}$. For the $\mathbb{P}p$ interaction the transverse momenta (with respect to the $\mathbb{P}$p collision axis) of the final state hadrons are assumed to be produced entirely from thermal motion. The longitudinal momenta are generated with the flat rapidity distribution. Hadrons multiplicities, transverse and longitudinal momenta with respect to the $\mathbb{P}$p collision axis do not depend on t. Large transverse momentum of the $\mathbb{P}$ in the ZEUS frame results only in a change of the $\mathbb{P}$p collision axis.

Particle multiplicity of the proton dissociative system

In this analysis the multiplicity of particles coming from the proton dissociation cannot be measured because about 70% of the proton dissociated system is lost through the forward

beam pipe for $\eta < -3.5$. In the 1996 and 1997 data taking period used in this measurement no forward detector covered this region. Therefore the simulation of the multiplicity distributions in the Monte Carlo is based on results from other measurements.

The EPSOFT version 1.1 (EPSOFT1.1), developed by Leszek Adamczyk [20], is based on the standard EPSOFT1.0 but improved using a knowledge from the ZEUS 95 high $-t$ data [20]. The difference between these two versions is a simulation of the particle multiplicity of a proton dissociative system.

EPSOFT1.0 uses a parameterization of the average particle multiplicity $\langle n \rangle$ with dispersion D as a function of the mass M_Y of the proton dissociated system Y, obtained from the fit to the ZEUS photon-dissociative photoproduction data and to hadron-hadron results [40]. However, it was found that this parameterization does not reproduce the multiplicity distributions measured in $pp \to pN$ experiments in the low M_Y region, which was essential for the ZEUS 95 analysis [5]. Therefore the modeling of the proton dissociation in EPSOFT1.1 was improved, using results obtained in [43]. The multiplicity distributions for charged and neutral hadrons from the decay of the system Y at a fixed mass M_Y are assumed to be Gaussian

$$P(n) \sim \frac{1}{D} \exp\left(-\frac{(n - \langle n \rangle)^2}{2D^2}\right), \tag{48}$$

where $n = 1, 3, ...$ is the multiplicity of charged hadrons, $n = 0, 1, 2, ...$ the multiplicity of neutral hadrons and

$$\langle n \rangle = \langle n \rangle_{ch} = 2\sqrt{(M_Y - M_P)} \text{ for charged hadrons,} \tag{49}$$

$$\langle n \rangle = \langle n \rangle_{n} = \sqrt{(M_Y - M_P)} \text{ for neutral hadrons,} \tag{50}$$

$$\langle n \rangle / D = 2. \tag{51}$$

EPSOFT1.1. was used to correct data for acceptance.

5.2 DIFFVM MC generator

To study the dependence of the final results on a different MC approach with a different proton fragmentation, the MC generator DIFFVM [44] was used.

The DIFFVM generator simulates diffractive processes in electron-proton scattering in the framework of Regge phenomenology [13, 14, 15] and the Vector Dominance Model (VDM) [9, 10, 11]. In this approach the electron emits a photon which fluctuates into a virtual vector meson, which then interacts diffractively with a proton. Both, the vector meson and the proton may either dissociate diffractively or emerge intact from the interaction. For the elastically produced vector mesons, the s-channel helicity is conserved. The generator features a detailed description of the proton-dissociative final state, includes N^* resonance production and the continuum. It uses a parameterization of the proton dissociation data from the reaction $pD \to XD$ [45, 46].

In DIFFVM $\mathbb{P}$ scatters off a single parton in a proton, which is either quark or antiquark. The fraction x of the longitudinal momentum of the incoming proton carried by the struck quark is defined by

$$x = \frac{-t}{M_Y^2 - t - M_p^2}. \tag{52}$$

The di-quark, which forms the p remnant carries a momentum fraction $1-x$.

However, pQCD calculations suggest that hard $\mathbb{P}$ mostly couples to a gluon (see Sec. 8). Therefore, DIFFVM was modified to allow the $\mathbb{P}$ to scatter off a gluon. The proton remnant was assumed to be a quark-diquark system, where the quark carries the fraction $\frac{1}{3}\cdot(1-x)$ and the diquark $\frac{2}{3}\cdot(1-x)$ of the incoming proton momentum. Further studies (see Sec. 5.7) confirmed that this approach describes the data better and was therefore used for systematic checks.

The fragmentation is then modeled by JETSET [47], using the LUND string model [48]. In the case of the $\mathbb{P}$ scattering off a quark (in the following denoted 'DIFFVM-q'), the struck quark and the proton remnant are connected by a string (q-string-qq). If the $\mathbb{P}$ scatters of a gluon (in the following denoted 'DIFFVM-g') the struck gluon and proton remnant are connected by two strings (q-string-$gluon$-string-qq).

5.3 Radiative Corrections

The EPSOFT or DIFFVM MC generators simulate events without any radiative corrections. To account for the radiative corrections, which can influence the measured process, an independent estimation of their effect was used. The interacting positron can emit photons in the initial (ISR) or final state (FSR). Since on the FLT level, events with an energy deposition in the LUMI photon detector greater than 1 GeV were removed from the data sample, only ISR events can affect the cross section measurement. In this case the positron energy decreases due to the photon emission. Since the efficiency of the 44m tagger depends on the positron energy (see Sec. 5.6), therefore ISR events can be removed from the data sample.

The effect of the radiative corrections for the vector meson photoproduction was studied for the low t region [49] and assumed to be constant with t [5]. The overall correction originating from ISR was estimated to be on the level of $\pm 2\%$ and is treated as a source of systematic uncertainty for the final results of the cross section calculation.

5.4 ZEUS Monte Carlo Simulation

After generating events with the Monte Carlo generators, they are passed through the simulation of ZEUS detector and trigger to obtained so called 'reconstructed events', which are later treated by the reconstruction and analysis code the same way as the data.

The ZEUS detector simulation uses the GEANT [50] package and takes into account the geometry, position and material of every component, and the actual knowledge of the detector response from various test beams and physics analyzes. The MOZART package [51] was used to lead the particles through the entire detector taking into account physics processes, such as particle decays, energy loss and multiple scattering. Part of MOZART is a software package ZGANA [52] which is used to simulate the ZEUS trigger decision, based on signals from the individual detector components. The information from all components about the simulated detector response is stored in the same tables as real data. In addition, the true Monte Carlo event information is available.

Two crucial ZEUS components for this analysis, the *High Lumi* trigger and the 44m tagger, are not properly simulated in MOZART. Therefore, the simulation of these components had to be modified. The detailed description of the *High Lumi* trigger and 44m tagger acceptance studies can be found in Sec 5.5 and 5.6, respectively.

5.5 REMC Trigger Efficiency

A significant source of background originates from the collision of a proton with residual gas in the beam pipe which usually happens outside the interaction point region. Particles, which emerged from the interaction, spray in the forward direction. To suppress this background, the ZEUS experiment runs on-line in two trigger modes, the so called *High Lumi* and *Low Lumi* configurations. In the beginning of every run, when rates and luminosity is high and therefore the probability of the p-gas collision big, the *High Lumi* trigger is required, later, after the luminosity goes below a certain value, the *Low Lumi* configuration is switched on. The *High Lumi* trigger requires an energy deposition greater then 464 MeV in any of four zones of the electromagnetic part of the RCAL, to ensure that particles were produced in the rear direction. This cut is called REMC (Rear ElectroMagnetic Calorimeter) trigger. For the *Low Lumi* trigger configuration, this requirement is removed because the probability of the background interaction is smaller. Tab. 2 shows how much luminosity was collected for the 96-97 high t vector mesons photoproduction in both trigger configurations.

To make use of the maximum available luminosity for the running period 1996-97, it is necessary to combine the data taken with the two trigger configurations. To do this, the REMC trigger has to be well simulated in the Monte Carlo. This simulation is done using the MOZART program but results of the measurement presented in this chapter prove that it was not good enough for the purpose of the current analysis.

year	*High Lumi*	*Low Lumi*
1996	3.3 pb^{-1}	-
1997	13.2 pb^{-1}	7.6 pb^{-1}
total	16.5 pb^{-1}	7.6 pb^{-1}

Table 2: Integrated luminosity collected with the high $-t$ VM trigger in 96-97.

5.5.1 Data - Monte Carlo Comparison

The *Low Lumi* sample can be used to study the REMC trigger behavior. Since here no REMC cuts were applied on-line, events, which would have passed also the *High Lumi* trigger can be selected by requiring the so called REMC trigger bit ($E_{REMC} > 464$ MeV). This can be done both in the data and the MC to compare efficiencies for different kinematic variables.

Fig. 16 shows such as a comparison for the distribution of the electromagnetic energy of one arbitrarily chosen RCAL quadrant. The plots for the three other sections look very similar. The MC simulation of the trigger around the threshold of $E = 464$ MeV does not agree with the data, most likely due to a wrong simulation of the RCAL energy distribution on the FLT level. This leads to discrepancies between data and Monte Carlo for Low and *High Lumi* samples in the case of the ρ^0 and ϕ mesons. The J/ψ sample suffers from small statistics. However, within these large statistical uncertainties, no discrepancy between the data and the MC was seen. Therefore it was assumed that the REMC trigger simulation is correct for the J/ψ vector meson. An example of the bad simulation is shown in Fig. 17, where the trigger efficiency as a function of t, W and the two kaon invariant mass M_{KK} is compared for the

ϕ data and MC. The observed discrepancy is big (greater then 10%) and the standard REMC trigger simulation, performed by MOZART, cannot be used for the analysis.

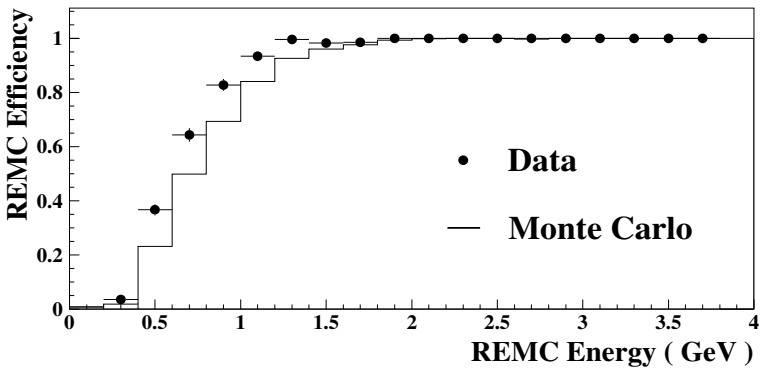

Figure 16: Comparison of the REMC trigger efficiency between the data (dots) and the MC (histogram) as a function of electromagnetic energy in one section of the RCAL.

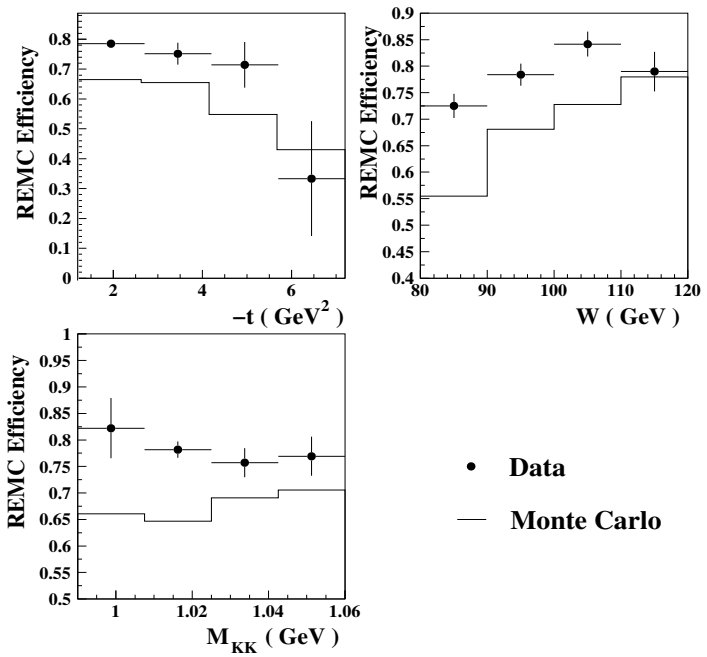

Figure 17: Comparison of the REMC trigger efficiency as a function of $-t$, W and M_{KK} between the data (dots) and the MC (histogram) for the ϕ meson using the standard REMC trigger simulation.

5.5.2 REMC Trigger Efficiency Parameterization

To improve the situation an independent simulation of the REMC trigger was done, based on a method developed for the 95 data [53].

The energy deposition in the electromagnetic part of the RCAL results from the decay products of the ρ^0, ϕ and J/ψ mesons. As a natural consequence the trigger efficiency was

parameterized as a function of the track momenta, using *Low Lumi* data. The data sample was divided into two categories: 1) both tracks hit the same RCAL quadrant; 2) at least one track hits the RCAL and is not contained in 1). Events in which none of the two tracks hits the RCAL were excluded from the analysis. These events amount is less the 1% of the sample. In the first case, the REMC efficiency was parameterized as a function of sum of the track momenta. In the second case, the parameterization was done separately for positive and negative track momentum. A function of the form [53]:

$$\mathcal{E} = a \cdot \left(1 - e^{(p_{tr}-b)\cdot c}\right) \tag{53}$$

was fitted separately to the ρ^0 and ϕ data. a, b and c are the fit parameters and p_{tr} stands for the sum of the track momenta (category 1) or for the positive/negative track momentum (category 2), respectively.

Fig. 18 shows the REMC efficiency for the ρ^0 meson as a function of the track momenta together with the fitted function (Eq. 53).

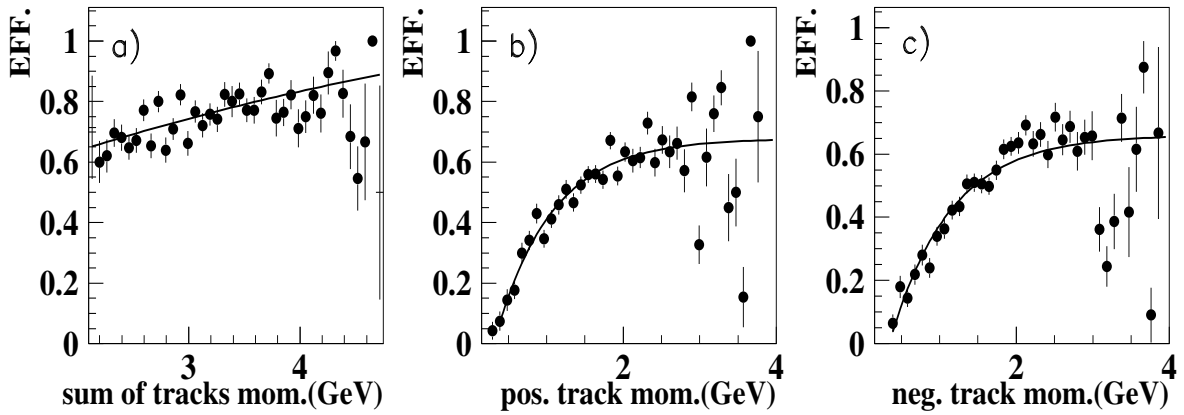

Figure 18: REMC efficiency for the ρ^0 meson a function of: a) sum of tracks momenta, b) positive track momentum, c) negative track momentum, together with fitted parameterization according to Eq. 53.

For the ϕ meson, in about 70% of the events both tracks were matched to the same RCAL quadrant, so the statistics for the second case was very limited. Therefore for the parameterization of positive and negative tracks, the shape of the function (b, c in Eq. 53) was taken from the ρ^0 fit and only the normalization was fitted to the data. To include the REMC trigger efficiency into the MC simulation, these parameterizations were used to apply a weight to every track.

Fig. 19 shows a comparison between the data and the EPSOFT Monte Carlo efficiencies for the ϕ meson, as a function t, W and M_{KK}. The agreement between data and MC with REMC simulation is good. Since this method of parameterization of the REMC trigger in the MC gave satisfactory results for all relevant kinematic variables it was used in the analysis presented in this thesis.

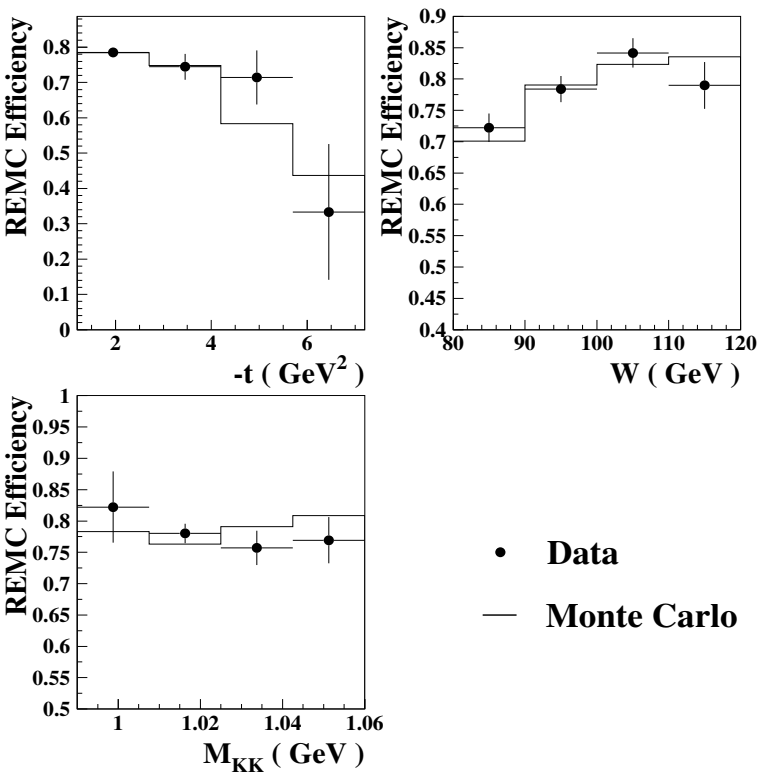

Figure 19: Comparison of the efficiency for ϕ between data (dots) and EPSOFT MC (histograms) with the REMC trigger efficiency parameterization according to Eq.53, as a function of different kinematic variables of $-t$, W and M_{KK}.

5.6 44m Tagger Acceptance

An event is triggered by the 44m tagger if the scattered positron deposits an energy greater that 1 GeV in the tagger. Due to this low threshold the tagging efficiency is determined mostly by geometrical acceptance of the tagger. The evaluation of the 44m acceptance was performed in two steps, using both data and Monte Carlo simulation. The chapter presents the method of studying the 44m tagger efficiency and the results of this analysis.

5.6.1 Bremsstrahlung Process

In the first step, Bethe-Heitler bremsstrahlung process, $ep \to e^{'}\gamma p$ was studied. The basic idea of the tagger efficiency measurement is illustrated in Fig. 20. For events where the bremsstrahlung γ is measured in the LUMI photon calorimeter the number of events is counted for which the associated positron is recorded in the 44m tagger. The acceptance A_B of the 44m tagger can then be defined as the ratio of events with a coincidence of the 44m tagger and the LUMI detector to all events recorded in the LUMI photon calorimeter. Since the 44m tagger does not measure the scatter positron energy, this acceptance is studied as a function of the photon energy. The information about the energy of the tagged scattered positron $E_{e'}$ can be extracted from the relation: $E_{e'} = E_e - E_\gamma$, where E_e and E_γ are the energies of the positron beam and radiated photon, respectively. For the data the 1996 and 1997 bremsstrahlung events were selected and corrected for background originating from electron-beam gas interactions.

The photon energy in the LUMI detector is measured in ADC channels. It is then transformed

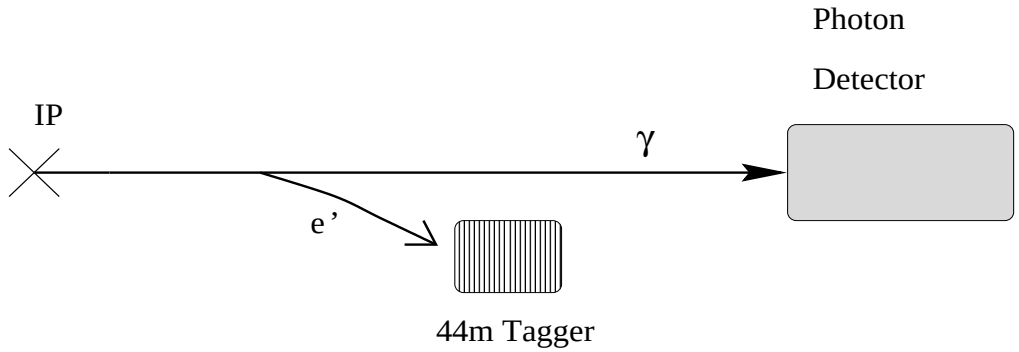

Figure 20: Overview of the tagging system for the photon and the electron/positron scattered under small angle.

into GeVs using the following parameterization of the average detector response, $\overline{ADC_\gamma}$, as a function of the 'true' photon energy E_γ [54]:

$$\overline{ADC_\gamma} = c_\gamma \left[1 + f_{nl}(E_e - E_\gamma)\right](E_\gamma - E_{filter}) + ADC_\gamma^{ped}, \tag{54}$$

where c_γ is a conversion constant from GeV to ADC counts, f_{nl} is the global non-linearity parameter, ADC_γ^{ped} is the pedestal and E_{filter} is the parameter accounting for energy loss in the carbon filter of the LUMI photon detector. To account for the sampling fluctuations in the LUMI calorimeter the photon 'true' energy is smeared by a Gaussian function with the resolution σ_0. The parameters $c_\gamma, f_{nl}, E_{filter}$ and σ_0 are obtained from the fits to the data and their values vary between 1996 and 1997.

Fig. 21 shows the bremsstrahlung photon energy spectrum in the LUMI photon detector for the run 26462 as a function of ADC counts, for all events and for events tagged in the 44m

tagger, together with the acceptance A_B as a function of ADC channels. The right tail of the acceptance distribution results from multiple bremsstrahlung scattering. The level of the tail indicates the amount of the multiple events, depending mainly on the beam rates.

The positron, after the interaction and before it reaches the 44m tagger, travels through the

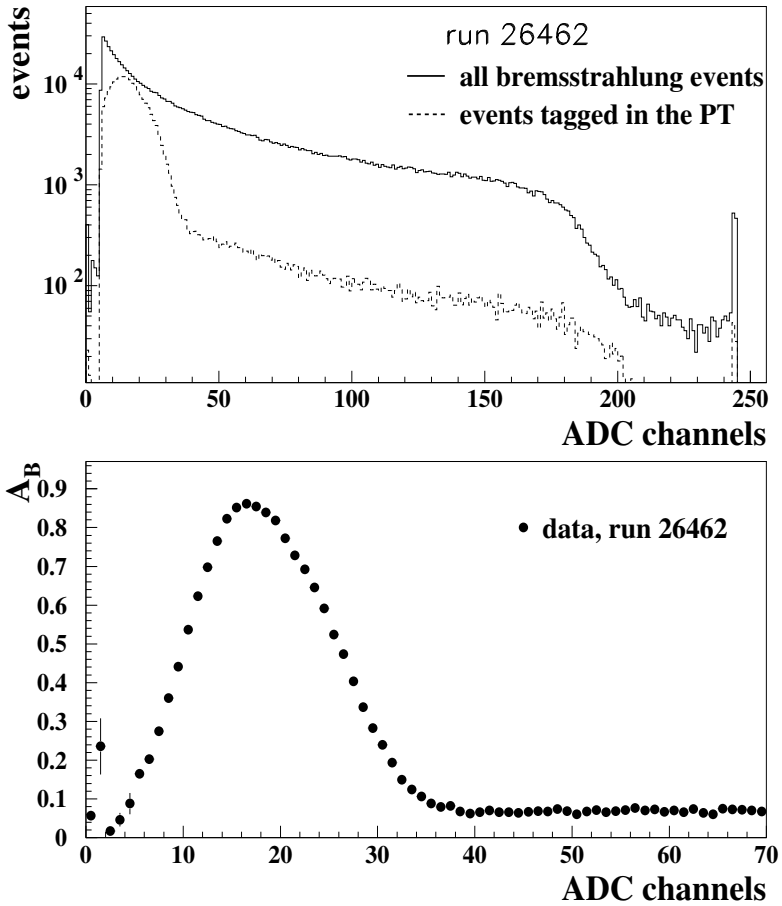

Figure 21: Run 26462, the bremsstrahlung γ energy distribution in the LUMI photon calorimeter as a function of ADC counts for all events (solid histogram, up) and for events tagged in the 44m tagger (dashed histogram, up), together with the tagging efficiency A_B (dots, down).

beam line, consisting of several magnets (dipoles and quadrupoles) and the vacuum beam pipe. The positron has a chance to trigger the event only when, after passing through the magnets, it hits the face of the 44m tagger. The main variables determining the path of the scatter positron is the scattering angle, $E_{e'}$ and the interaction vertex distribution. Due to the parameters of the beam line optics only the changes of the x position of the vertex, v_x, affect the acceptance of the 44m tagger. Effects of variation of the v_y and v_z on the efficiency are negligible. Three features of the trigger efficiency A_B shape presented in Fig. 21 were studied run-by-run for all runs included in this analysis: a maximal acceptance A_{max}, a width of the A_B distribution A_w and an energy E_{max} which corresponds to A_{max}. A_{max} and A_w were found to be constant as a function of the run number and independent of the vertex position. In contrast, E_{max} varies strongly with the run number and is correlated with the distribution of v_x. Fig. 22 shows v_x measured in the CTD, v_x^{CTD}, plotted versus E_{max} for the bremsstrahlung data in the run range 25204-26086 (1997). Each dot correspond to one run. The errors are not displayed. They are of the order of the dot's size or smaller. E_{max} was measured in GeV, using Eq. 54. The linear

correlation between the two variables is observed. Therefore it is clear that the v_x distribution plays an important role in the 44m tagger acceptance shape and should be well reproduced in the MC used to evaluate the acceptance.

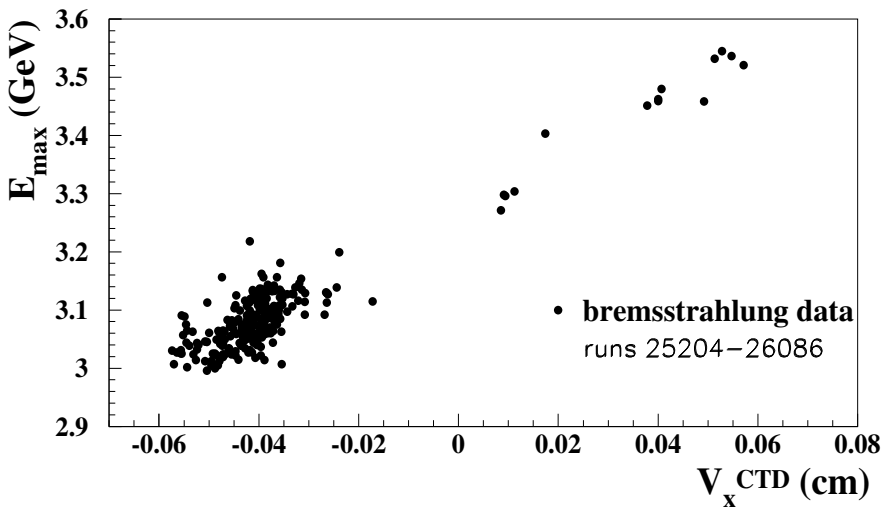

Figure 22: The v_x measured in the CTD, v_x^{CTD} versus E_{max} for the bremsstrahlung data in the run range 25204-26086. Each dot corresponds to one run. The errors are not drawn.

For the Monte Carlo studies the sample of Bethe-Heitler events was generated using the BREMGE MC generator [55]. These events were passed through a stand-alone Fortran program simulating the beam optics from the interaction point to the 44m tagger. As discussed above, the x position of the vertex is a crucial parameter for the tracking code. Other free parameters of this stand-alone program were position and geometry of the tagger, the number of multiple bremsstrahlung events and the spatial resolution of the beam σ_b. The position and geometry of the 44m tagger, v_x and σ_b affect the shape of the A_B distribution and the value of E_{max}. The amount of the multiple events controls the level of the right tail of the distribution and the maximal acceptance A_{max}. Since v_y and v_z do not influence the 44m tagger acceptance, they were set to the nominal value of zero in the simulation. All these parameters (except v_y and v_z) were tuned to give the best description of the data for chosen runs which have the biggest statistics in the running period considered. Their values were constrained by the ones measured in the reality (with big uncertainties). In order to compare data and MC the generated scattered photon energy was first smeared to account for the sampling fluctuations and then translated to the ADC counts using Eq. 54. Fig 23 shows the comparison between the bremsstrahlung data and the MC with the tuned parameters for run 22151. The agreement is satisfactory. The simulation describes well all aspects of the A_B distribution, assuring that all parameters were properly chosen.

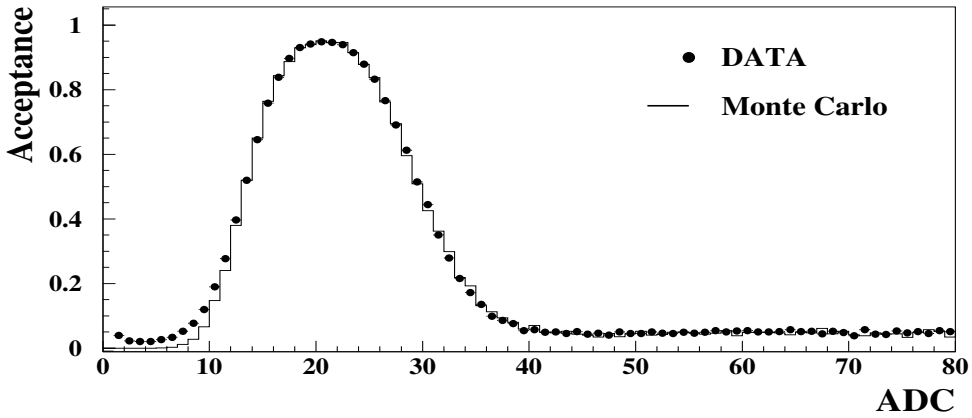

Figure 23: Comparison of the 44m tagger acceptance A_B between the bremsstrahlung data from the run 22151 and the MC with the tuned parameters as a function of ADC channels in the LUMI photon calorimeter.

5.6.2 Photoproduction Acceptance

The 44m tagger efficiency for photoproduction A_{Ph} was calculated using photoproduction events for $Q^2 < 0.015$ GeV^2, which were passed through the HERA beam simulation described above. For larger Q^2 the acceptance in negligible. The stand-alone simulation parameters such as the position and geometry of the tagger and σ_b were taken from the MC bremsstrahlung studies. As the v_x distribution the x position of the vertex measured in every analyzed run was used. Fig. 24 shows the acceptance A_{Ph} of the 44m tagger as a function of W. The shaded band reflects the systematic uncertainty of the acceptance calculation. The average acceptance for the W range $80 < W < 120$ GeV, indicated by the vertical lines in Fig. 24, is 80% $\pm$ 4%.

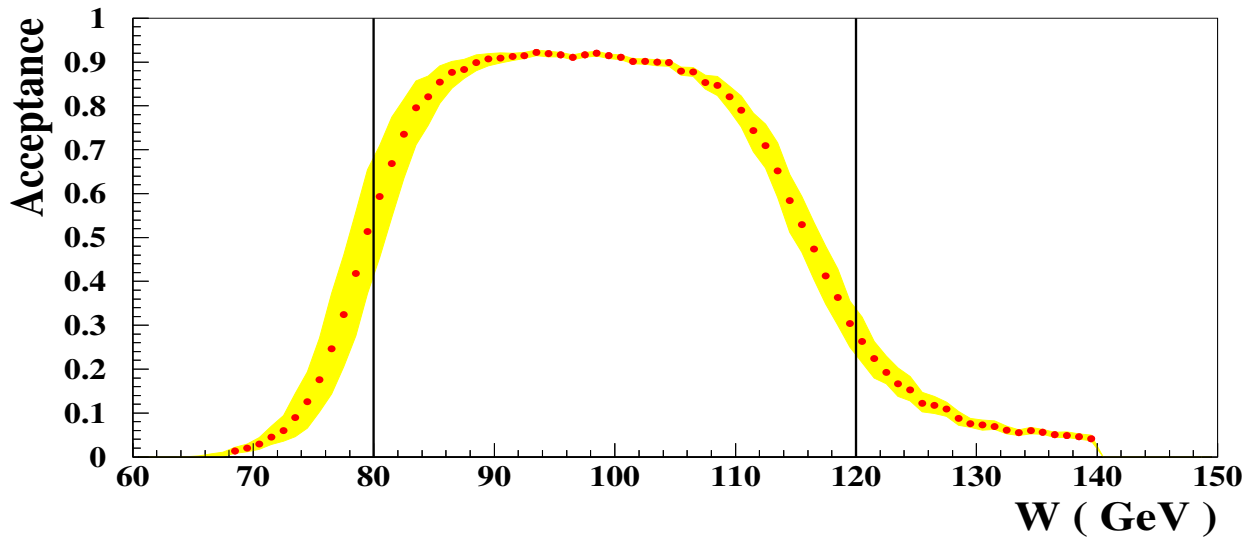

Figure 24: The acceptance of the 44m tagger as a function of the collision energy W for the photoproduction events. The shaded band corresponds to the systematic uncertainty of the tagger acceptance. The vertical lines indicate the W range used in the analysis.

Systematic error

The sources of systematic uncertainties for the evaluation of the 44m tagger acceptance were the following: the LUMI photon detector calibration, the position and geometry of the tagger, the error on the spatial beam resolution and the error of the v_x distribution measurement. Main contribution to the total error have the position and geometry of the 44m tagger and the uncertainties of the v_x evaluation. The biggest systematic uncertainties appear for W between 70 and 90 GeV and between 110 and 140 GeV, on the falling edges of the A_{Ph} distribution. There the acceptance is strongly influenced by v_x and the position and geometry of the 44m tagger. A plateau of A_{Ph} for $90 < W < 110$ GeV has a very small error. The W range of the analysis was chosen to fulfill two aims: to maximize the possible statistics and to restrict the measurement to the region, where the 44m tagger acceptance is well understood.

In the analysis, to account for the 44m tagger acceptance, the reconstructed EPSOFT MC was reweighted using the measured function $A_{Ph}(W)$, displayed in Fig. 24. The error of the $A_{Ph}(W)$ evaluation was taken into account in the systematic uncertainties of the final results.

5.7 Reweighting of the Monte Carlo

The Monte Carlo generators used in the analysis and the standard ZEUS MC simulation were presented in Sec. 5. The modification of the trigger simulation and the evaluation of the 44m tagger acceptance are described in Secs. 5.5 and 5.6, respectively. Since the MC model EPSOFT (Sec. 5) which was used to correct the data for acceptance and resolution effects does not describe the data at high values of $-t$, it had to be modified by the so called "reweighting". This chapter explains how the generated events were reweighted in order to describe the data. Also a comparison between the EPSOFT and DIFFVM generators is presented.

5.7.1 M_Y evolution with $-t$

The mass spectrum of the nucleonic system Y resulting from the dissociation of the p was simulated according to a phenomenological formula inspired by the Regge model (Eq. 30):

$$\frac{d\sigma}{\mathrm{d}M_Y^2} \sim \left(\frac{1}{M_Y^2}\right)^{\beta}, \tag{55}$$

where β is the intrinsic parameter of a generator and can be changed either using steering cards or by reweighting. The EPSOFT and DIFFVM samples used in this study assume that β is constant (i.e. there is no M_Y evolution with t), with a value equal 1 for EPSOFT and 0.5 for DIFFVM. However, results from proton-dissociative experiments [56, 57] and measurement in this analysis show, that this is not sufficient to describe the data for large values of $-t$.

Since most of the proton dissociative system Y is lost through the forward beam pipe for the 96-97 data ($\eta < -3.5$), only about 30% of the mass M_Y is contained in the detector. M_Y was reconstructed from the deposits in the forward calorimeter using formula:

$$M_Y^2 = \left(\sum_i E_i\right)^2 - \left(\sum_i p_i\right)^2, \tag{56}$$

where the sum runs over all cells in the FCAL, E_i is the energy and p_i the momentum associated with the cell i. Fig. 25 shows the EPSOFT generated proton dissociated mass M_Y^{GEN} versus the reconstructed mass M_Y^{REC} for the ρ^0 sample.

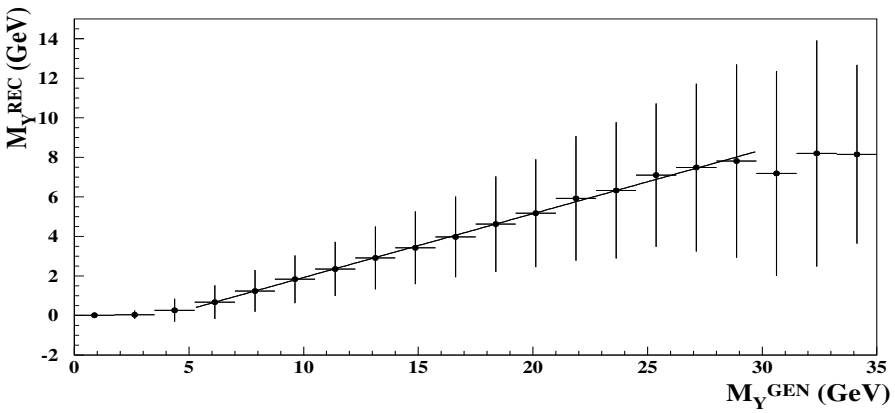

Figure 25: The generated proton dissociative mass M_Y^{GEN} versus the reconstructed mass M_Y^{REC} for the ρ^0 EPSOFT MC. The solid line indicates a result of the linear fit in the M_Y^{GEN} range $5 < M_Y^{GEN} < 30$.

For masses between 5 and 30 GeV the reconstructed mass M_Y^{REC} is a linear function of the generated mass M_Y^{GEN} but with a very large correction factor:

$$M_Y^{REC} = 0.32 \cdot M_Y^{GEN} - 1.31 \tag{57}$$

Dissociative masses below $\sim$ 5 GeV are not reconstructed at all. For $M_Y^{GEN} > 30$ GeV the dependence saturates and again the mass can not be reconstructed properly.

Due to the large correction factors involved, any results using these corrections would strongly depend on how the proton fragmentation is modeled in the Monte Carlo. Therefore, reconstructing M_Y according to Eq. 57 is not sufficient to perform direct studies of the M_Y distribution.

A better variable for this aim is the energy deposition, E_{FCAL}, of the fragments of the nucleonic system Y in the FCAL. It is correlated with the proton dissociative mass distribution and reflects changes of the generated $d\sigma/dM_Y^2$ function.

Fig. 26 shows a comparison between the data and two MCs for the energy distribution in the FCAL, in different t bins, for the ρ^0, ϕ and J/ψ mesons, with $\beta = 1$ for EPSOFT and 0.5 for DIFFVM-g (ρ^0 only). The mean values on the plot correspond to the data. The lower bound of $E_{FCAL} > 3$ GeV selects events with a substantial energy deposit in the calorimeter, the upper one of $E_{FCAL} < 60$ GeV removes bins with low statistics.

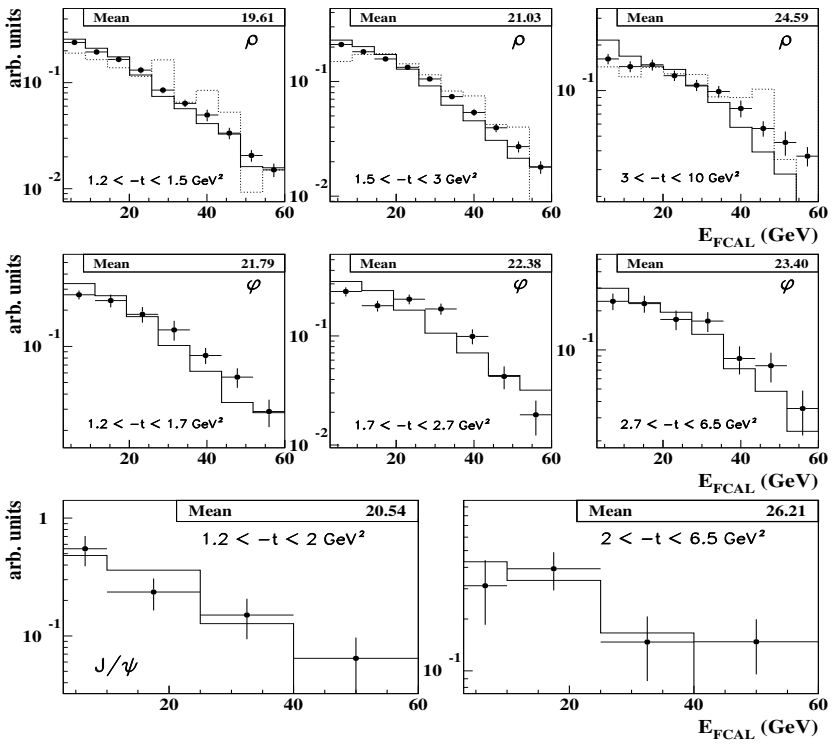

Figure 26: Comparison between the data (dots), EPSOFT MC (solid histograms) and DIFFVM (dotted histogram, only ρ^0) for the E_{FCAL} distributions in different t bins. The histograms are normalized to the total number of events in the histogram. Quoted mean values correspond to the data.

A clear evolution with t of the E_{FCAL} distribution is visible in the data, manifested in a rise of the mean energy value with increasing momentum transfer. The MCs do not reproduce

the data, especially for high t bins. Therefore the M_Y distribution in the Monte Carlo had to be reweighted to follow the t-dependence of the E_{FCAL} distribution seen in the data.

A reason for this discrepancy can be either the wrong shape of the M_Y distribution assumed in the generator or a fact that β changes with t. Results from the ISR experiment [56] suggest the latter possibility. The ISR measured the invariant cross section $d^2\sigma/dtdM_Y^2$ in the p-dissociative process for $0.15 < -t < 2.95$ GeV^2. These results were fitted with Eq. 55 to determine β for different values of the momentum transfer [20]. This parameterization described the ISR data very well and β was found to depend on t. Therefore in this analysis the shape of the $\mathrm{d}\sigma/\mathrm{d}M_Y^2$ distribution was assumed to follow Eq. 55 and the possibility of the t-dependent β was tested.

It should be stressed, however, that there is no direct proof of this assumption and distribution (55) might fail for the high momentum transfer. Other possible ways to account for the differences between data and MC are:

- the shape of the $\mathrm{d}\sigma/\mathrm{d}M_Y^2$ follows a formula:

$$\frac{d\sigma}{\mathrm{d}M_Y^2} \sim \left(\frac{1}{M_Y^2 + |t|}\right)^{\beta},$$

  which is suggested both by Regge formalism (Finite Mass Sum Rule) and pQCD calculations (e.g. [6]);

- the proton parton density functions (PDFs) need to be taken properly into account. This is the approach used in pQCD calculations (Eq. 87, Sec. 8). The differential cross section $\frac{d^2\sigma(\gamma p \to VX)}{dtdx}$ is expressed in terms of the parton cross sections and the PDFs which, being a function of x and t, define the M_Y distributions by the equation $x = -t/(M_Y^2 - t)$.

Effects of both these possibilities on the final results were studied. The assumption of Eq. 55 was applied in this analysis because it was successfully used before and β can be directly measured with our sample. A t-dependent $\beta = \beta(t)$ was extracted to reweight EPSOFT.

To extract the parameterization for $\beta(t)$, the E_{FCAL} distribution in the data was compared in each t bin to the MC distributions obtained for different β values. The parameter β best describing the data was found by minimizing the χ^2 function, defined for a given t bin as:

$$\chi^2(\beta') = \sum_i \frac{(d_i - m_i(\beta'))^2}{\sigma_i}, \tag{58}$$

where the sum runs over all bins in E_{FCAL}, d_i is the number of data, m_i is the number of MC events for $\beta = \beta'$ in bin i. The distributions in each t bin were normalized to the number of events in this bin. σ_i is the error assigned to the number of events in bin i. The error σ_i was evaluated according to:

$$\sigma_i^2 = (\sigma_i^d)^2 + (\sigma_i^m)^2,$$

where σ_i^d and σ_i^m are the errors from the normalized number of entries in bin i for the data and the MC, respectively. Tables 3, 4 and 5 show results of the minimizing procedure performed in few t bins, for the ρ^0,ϕ and J/ψ mesons respectively. The errors on β', $\delta_{\beta'}$, quoted in the tables correspond to one standard deviation of the χ^2 distribution. Due to the limited statistics the procedure for J/ψ was performed only in one t bin.

For the ρ^0 and ϕ mesons β' clearly depends on the momentum transfer. The results above lead to the following parameterization of β:

$$\beta = \exp(-0.077 - 0.114 \cdot t) \quad \text{for } \rho^0, \tag{59}$$

$$\beta = \exp(-0.065 - 0.186 \cdot t) \quad \text{for } \phi, \tag{60}$$

$$\beta = 0.73 \quad \text{for J}/\psi. \tag{61}$$

$-t$ range (GeV^2)	$\langle t \rangle$ (GeV^2)	β'	$\delta_{\beta'}$
1.2 - 1.4	1.30	0.81	0.09
1.4 - 2.0	1.66	0.76	0.09
2.0 - 3.0	2.42	0.70	0.08
3.0 - 5.0	3.72	0.59	0.11
5.0 - 10.	6.45	0.47	0.16

Table 3: Fit results for β' for the ρ^0 meson.

$-t$ range (GeV^2)	$\langle t \rangle$ (GeV^2)	β'	$E_{\beta'}$
1.2 - 1.5	1.35	0.62	$\pm$ 0.28
1.5 - 2.0	1.72	0.72	$\pm$ 0.18
2.0 - 3.0	2.72	0.64	$\pm$ 0.25
3.0 - 6.5	3.85	0.43	$\pm$ 0.16

Table 4: Fit results for β' for the ϕ meson.

$-t$ range (GeV^2)	$\langle t \rangle$ (GeV^2)	β'	$E_{\beta'}$
1.2 - 6.5	2.45	0.73	$\pm$ 0.37

Table 5: Fit results for β' for the J/ψ meson.

The hypothesis of factorization of the photon and proton vertices can be tested using the results of the above studies. In the presence of factorization, the M_Y distribution should be independent of the vector meson considered. Therefore the same $\beta(t)$ should be able to describe the M_Y distribution for the ρ^0,ϕ and J/ψ meson, respectively. (Proton dissociates in the same way, doesn't matter which vector meson is produced in the photon vertex.)

Fig. 27 shows the β' values determined for all three mesons. Within the (large) errors, factorization is confirmed.

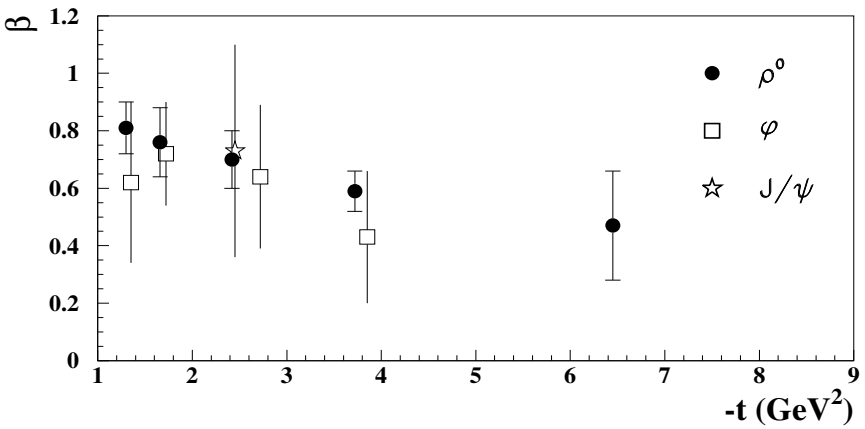

Figure 27: Comparison of β' values for different vector mesons.

Since the data are not in contradiction with the factorization assumption, the same M_Y distribution was taken for all three particles under study, i.e. the same $\beta(t)$ was used to reweight the EPSOFT MC sample for ρ^0, ϕ and J/ψ. Because the ρ^0 sample has the highest statistics, $\beta(t)$ from the ρ^0 studies (Eq. 59) was taken as a nominal parameterization. For ϕ and J/ψ the results for $\beta(t)$ following Eqs. 60 and 61, respectively, were taken into account in the systematic uncertainties.

Fig. 28 shows a comparison of the E_{FCAL} between the data and the EPSOFT MC reweighted using the same $\beta(t)$ for ρ^0, ϕ and J/ψ mesons, given by Eq. 59. The quoted mean values in Fig. 28 correspond to the MC events and should be compared to the data mean values in Fig 26. After reweighting, the EPSOFT Monte Carlo describe the E_{FCAL} distribution well.

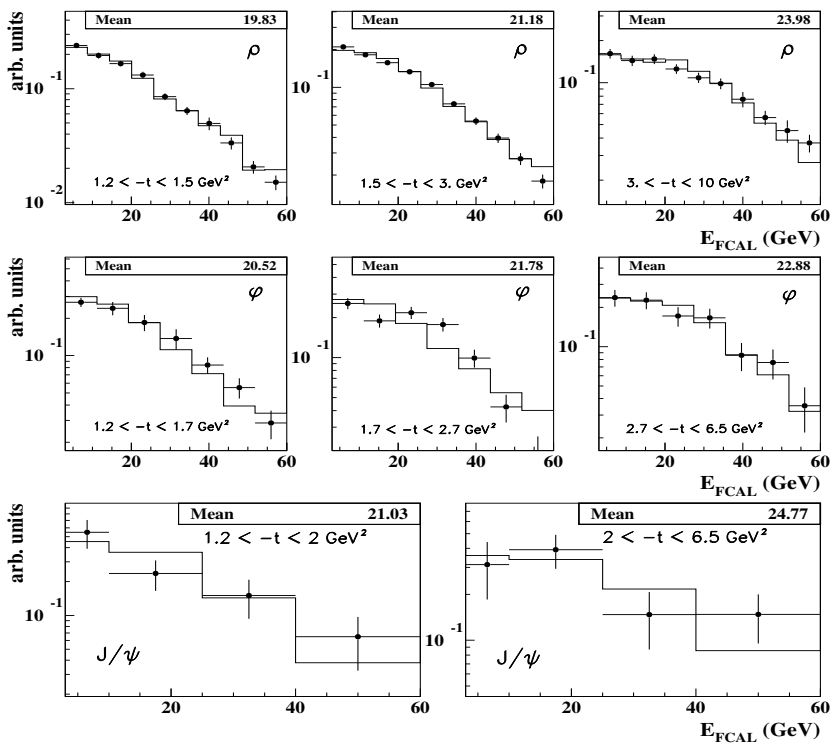

Figure 28: Comparison between the data (dots) and the reweighted EPSOFT MC (histograms) for the E_{FCAL} distributions in few t bins. Quoted mean values correspond to the Monte Carlo.

For the reweighting of the ρ^0 DIFFVM sample two method can be used:

1. the same method as described above for the EPSOFT MC;

2. the M_Y distribution in the MC is reweighted according to the parton (quarks and gluons) densities (PDFs) in the proton.

Method 1 failed completely for the DIFFVM sample with IP scattering off a quark (DIFFVM-q). The minimal χ^2 method described above gave $\chi^2/NDF \sim 15$ and was not sufficient to find a β parameterization describing the data. In this case only the reweighting according to PDFs was possible.

Both methods were applied for the DIFFVM-g sample, where IP scatters off a gluon. Method 1 resulted here in reasonable χ^2/NDF (0.1 - 1.6 in different t bins) and gave t-independent $\beta = 0.715 \pm 0.082$

Fig. 29 shows the distributions of E_{FCAL} in three t bins for DIFFVM-q and DIFFVM-g reweighted using parton densities compared to data. The DIFFVM-g sample is able to describe the data. The agreement is limited to the E_{FCAL} up to $\sim$ 60 GeV. DIFFVM-q does not reproduce the energy distribution in the FCAL.

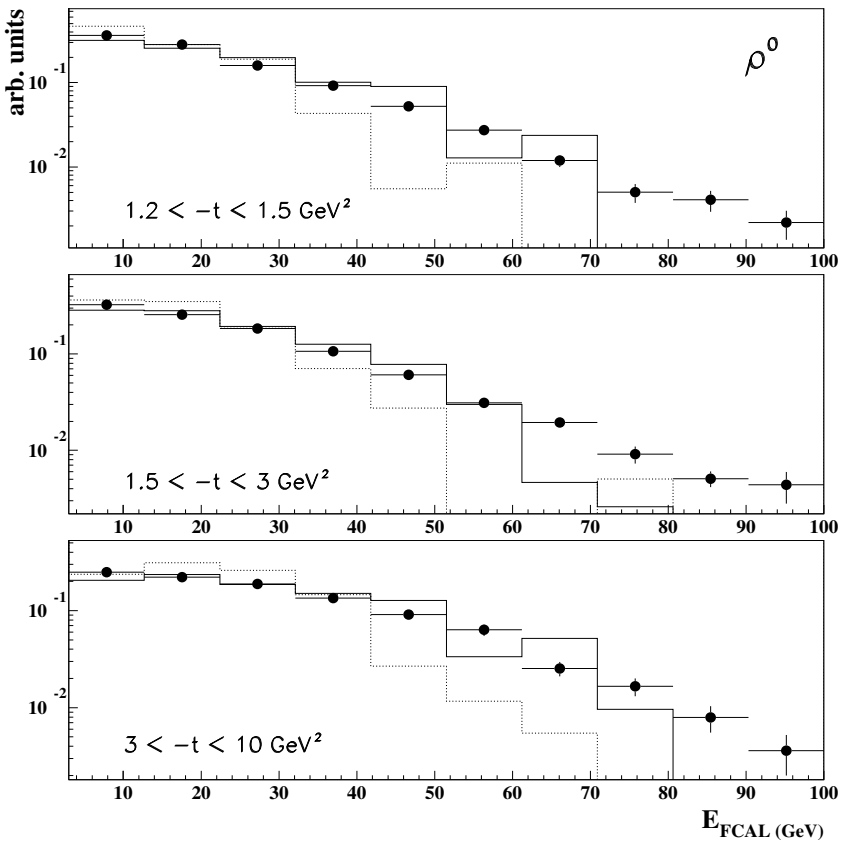

Figure 29: Comparison in three t bins of the E_{FCAL} distributions between the ρ^0 data (dots), DIFFVM-g (solid histogram) and DIFFVM-q (dotted histogram), both MC samples with the M_Y distribution reweighted according to the PDFs.

Fig. 30 shows the comparison between the data and these MC samples, which were found to give a reasonable description of the data, namely EPSOFT and DIFFVM-g reweighted using method 1 and 2. Both reweighting methods for DIFFVM give similar results. For energies up to $\sim$ 60 GeV the agreement between the data and the DIFFVM MC is satisfactory. But for $E_{FCAL} > 60$ GeV there is almost no energy deposited in the FCAL in the DIFFVM sample, contrary to the data. EPSOFT gives a reasonable description of the data in the whole FCAL energy range.

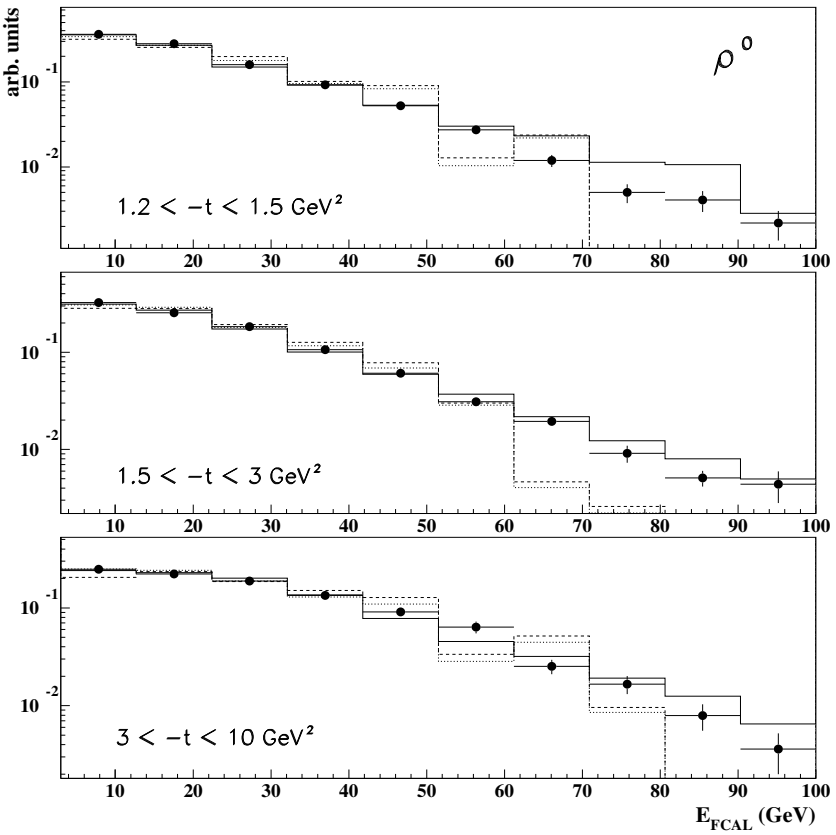

Figure 30: Comparison in three t bins between the ρ^0 data (dots) and three reweighted MC samples for the E_{FCAL} distributions. The solid histograms correspond to EPSOFT and the dashed and dotted once to DIFFVM, reweighted according to PDFs (dashed) and to describe the measured E_{FCAL} (dotted).

5.7.2 Forward Energy Flow

A good variable to compare a description of the data by different Monte Carlo models is the energy flow $dE/d\eta$ in the FCAL, defined for a certain pseudorapidity range η_k as:

$$dE/d\eta|_k = 1/N \cdot \sum_i E_i, \tag{62}$$

where the sum runs over all cells of the FCAL within the pseudorapidity window η_k with the energy above the noise threshold of 300 MeV. N is a total number of events. The energy flow is sensitive to the proton dissociation and fragmentation modeling and can be used as an additional test to establish how well a given MC model describes the forward energy distribution.

Fig. 31 shows a comparison between the energy flow for $E_{FCAL} > 3$ GeV observed in the data and simulated with EPSOFT, DIFFVM-g and DIFFVM-q. The comparison is done in the whole momentum transfer range and for three different t bins. The pseudorapidity window of the energy flow distribution is limited for low η by the selection cut of $\eta_{min} > 2.1$ and for high η by the edge of the FCAL. The description given by EPSOFT and DIFFVM-g is reasonable in all t bins. DIFFVM-q fails to describe the data in the whole pseudorapidity range and for all values of the momentum transfer.

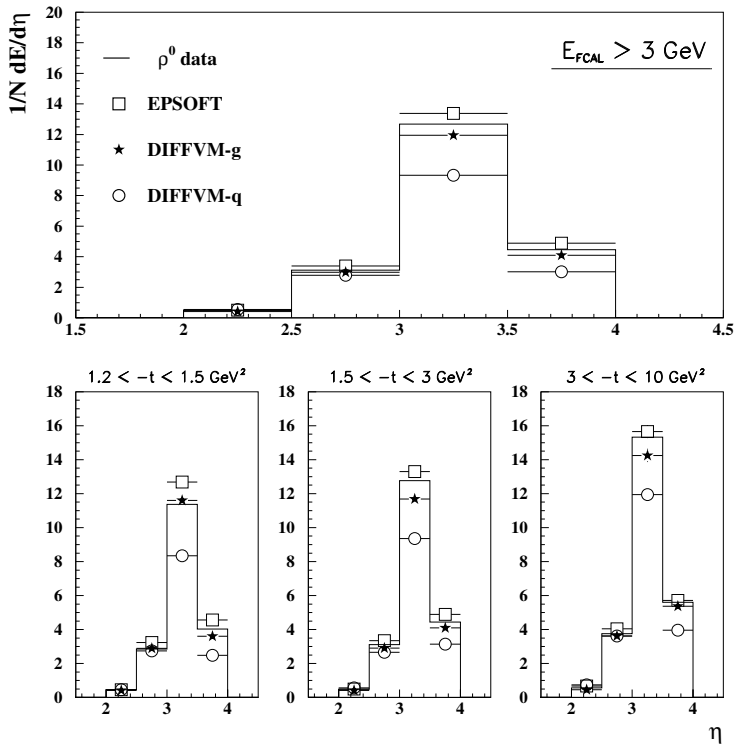

Figure 31: The normalized energy flow distribution as a function of the pseudorapidity η for the EPSOFT MC sample (squares), DIFFVM-g (stars), DIFFVM-q (open circles) and the data (histogram) for the FCAL energy > 3 GeV in the entire t range $1.2 < -t < 10$ GeV^2 (up) and in three t bins (down).

Fig. 29 showed that DIFFVM-g describes the FCAL energy distributions in the limited E_{FCAL} range, up to ~ 60 GeV. It is therefore interesting to check if limiting E_{FCAL} to this value for the energy flow comparison helps to achieve a better agreement with the data. The comparison is shown in Fig 32 . Again the comparison is done in the whole momentum transfer range and for three different t bins. The agreement between the data and both MC samples improves. Both, EPSOFT and DIFFVM-g give similar results for the full E_{FCAL} range and for $E_{FCAL} < 60$ GeV. It is impossible to determined from the energy flow only, which generator better describes the data. However, the DIFFVM generator does not predict the energy distribution in the FCAL for $E_{FCAL} > 60$ GeV.

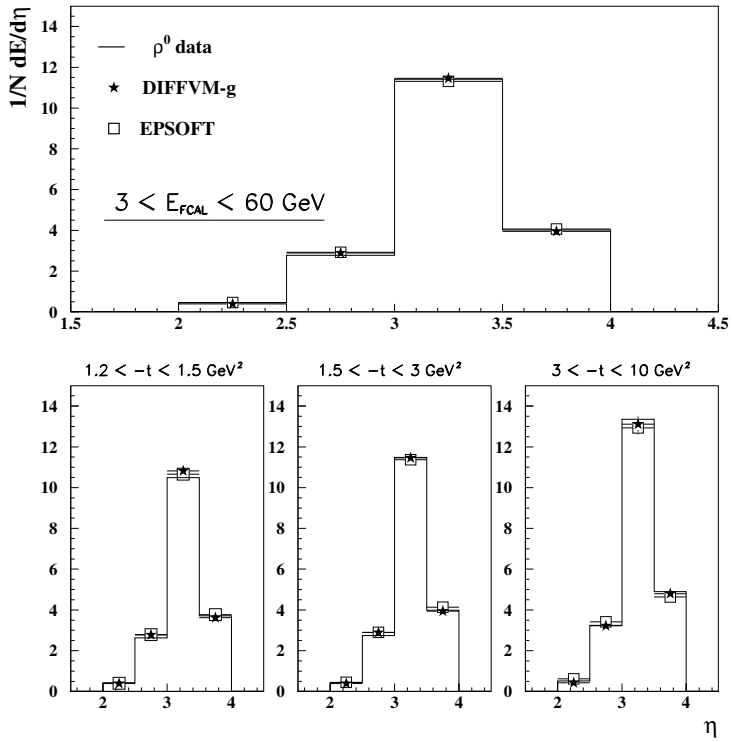

Figure 32: The normalized energy flow distribution as a function of the pseudorapidity η for the EPSOFT MC sample (squares), DIFFVM-g (stars) and the data (histogram) in the FCAL energy range $3 < E_{FCAL} < 60$ GeV in the entire t range $1.2 < -t < 10$ GeV^2 (up) and in three t bins (down).

Another possible bias in these distributions might originate from the fact, that the cut $E_{FCAL} > 3$ GeV may not correspond to the same minimal M_Y in data and for the MC samples. Since only a small fraction of the proton dissociated mass M_Y is reconstructed (see sec. 5.7.1), it is impossible to ensure that the same range in M_Y is selected in data and MC.

A strong conclusions from the energy flow comparison could only be drawn, if the same M_Y window in the data and the MC is selected. Then $dE/d\eta$ does not depend on the shape of the distribution of the proton dissociative mass or on the acceptance but is sensitive to the fragmentation approach only.

Since both MC samples, EPSOFT and DIFFVM-g are able to describe the forward energy flow but only the reweighted EPSOFT MC agrees with the measured E_{FCAL} distribution in the full E_{FCAL} range covered by the data, the EPSOFT MC is used in the following analysis. The DIFFVM- sample with $\mathbb{P}$ scattering off a quark was excluded by above studies. The dependence of the measured cross section $d\sigma/dt$ on the different MC approach was studied for the ρ^0 meson using the DIFFVM-g sample.

5.7.3 Separation of Elastic and Proton-dissociative Events

From the previous high $-t$ measurement [5] it is known that the contribution of elastic events falls exponentially with t and the ratio of the elastic to proton-dissociative cross section was estimated to be less than 10% for $-t > 1$ GeV^2.

When the proton breaks in an interaction, fragments of the nucleonic system Y can deposit

energy in the forward detectors - FCAL or Proton Remnant Tagger (see Sec. 3.2). In the elastic case, the proton travels undetected down the beam pipe and no energy is observed in the forward detectors. Therefore these detectors can be used to distinguish between elastic and proton-dissociative events. Separation of the p-dissociative sample is achieved either by requiring a hit in the PRT or energy deposit in the FCAL, both ensuring that the proton has broken.

Fig. 33 shows the comparison of the ratio of the the number of events tagged in the PRT to all events for the ρ^0, ϕ and J/ψ data and the EPSOFT MC. The ratio was studied in the same t bins that the cross sections were evaluated. The shaded area reflects the systematic error for the MC coming from the reweighting of the M_Y distribution (Eq. 55). The band is the statistic and systematic uncertainties of the MC added in quadrature. The MC samples used in this analysis contain only proton-dissociative events. Therefore the ratio for the EPSOFT shows the efficiency of the tagger, as simulated in MOZART [51]. For the ρ^0 and ϕ mesons the efficiency saturates and is around 90% for $-t > 4$ GeV^2. For lower $-t$ it is smaller and equal $\sim 80\%$ at $-t \sim 1.2$ GeV^2. For J/ψ, on the other hand, the ratio is flat in the whole t range and at the level of $\sim 85\%$.

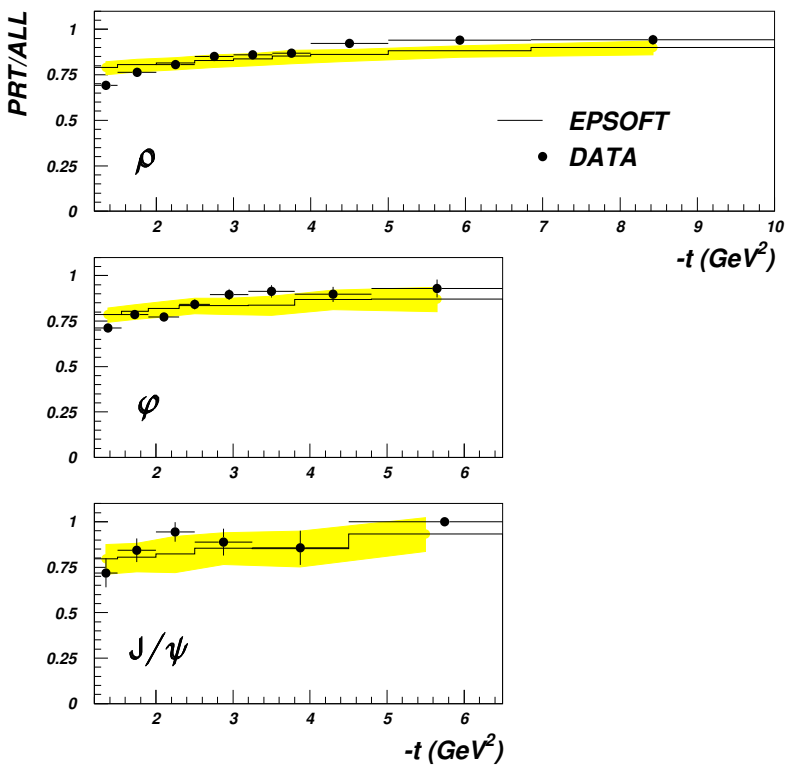

Figure 33: Comparison of the ratio of the number of events tagged in the PRT to all events between the data (dots) and the EPSOFT MC (histograms). The shaded band reflects the uncertainty of the M_Y distribution reweighting in the EPSOFT MC.

The overall agreement between data and EPSOFT MC is good, except for the few lowest bins of $-t \lesssim 2.5$ GeV^2, where the data points lie below the p-dissociative MC. This means that the data show some contamination of elastic events, where the proton emerged intact from the interaction and was undetected in the PRT. However, this contamination is not large, and

always below 12%.

Because the efficiency of the PRT is between 80 and 90% (see Fig. 33), using the hit in the tagger to separate elastic and dissociative samples would mean loosing $\sim 15\%$ of the statistics. Since the ratio for the data and EPSOFT MC agree within 12%, no proton dissociation requirement was applied to maximize the statistics. Following the above MC studies, the sample was assumed to contain mostly proton-dissociative events, except for the low $-t$ region, where results were corrected for the elastic contribution. The differential cross section $\mathrm{d}\sigma/\mathrm{dt}$ in the 3 first t bins for the ρ^0 and ϕ meson and the first bin for the J/ψ meson are multiplied by a factor coming from the observed difference in the ratios between the data and the MC.

5.7.4 Reweighting of the MC for the ρ^0 meson

Table 6 summarizes informations from the Particle Data Group (PDG) about the ρ^0, ϕ and J/ψ vector mesons.

	ρ^0	ϕ	J/ψ
I^G	1^+	0^-	0^-
J^{PC}	1^{--}	1^{--}	1^{--}
M (MeV)	769.3 ± 0.8	1019.413 ± 0.008	3096.88 ± 0.04
Γ (MeV)	150.2 ± 0.8	4.43 ± 0.06	0.87 ± 0.05
decay mode	$\pi^+\pi^-$ ~ 100 %	K^+K^- 49.1 ± 0.8 %	e^+e^- 6.02 ± 0.19 %
			$\mu^+\mu^-$ 6.02 ± 0.19 %

Table 6: PDG summary for the ρ^0, ϕ and J/ψ mesons.

The ρ^0 sample was generated according to SCHC. The spin density matrix elements were not determined in this analysis. However, another analysis, based on the same data sample and even selection, measures the spin density matrix elements r^{04}_{00}, $\mathrm{Re}(r^{04}_{10})$ and r^{04}_{1-1} [27]. It was found, that for ρ^0 photoproduction, the elements $\mathrm{Re}(r^{04}_{10})$ and r^{04}_{1-1} related to the single helicity-flip and the double helicity-flip, respectively, differ significantly from zero and depend on t. The t-evolution of the matrix elements was parameterized in the following way:

$$r^{04}_{1-1} = -0.114 - 0.0162 \cdot (-t), \tag{63}$$

$$Re(r^{04}_{10}) = 0.052, \tag{64}$$

$$r^{04}_{00} = 0.0147 \cdot (-t). \tag{65}$$

To account for observed deviation from SCHC, the ρ^0 Monte Carlo sample was reweighted using the helicity angular distribution of Eq. 21 and the above parameterization of the spin density matrix elements.

The ρ^0 mass peak in original EPSOFT was generated with the Breit-Wigner shape without any background [40]. In reality there is a contamination from the non-resonant $\pi^+\pi^-$ pair production under the ρ^0 signal and a background from the diffractive photon dissociation reaction $\gamma p \to XY$. MC had to be reweighted to describe the data.

The differential cross section $d\sigma/dM_{\pi\pi}$ can be described by a parameterization from the Söding model [58], where the p-wave relativistic Breit-Wigner shape is distorted by the interference with the non-resonant $\pi\pi$ production:

$$\frac{d\sigma}{dM_{\pi\pi}} = A^2 \left[\left| \frac{\sqrt{M_{\pi\pi} M_\rho \Gamma_\rho}}{M_{\pi\pi}^2 - M_\rho^2 + i M_\rho \Gamma_\rho} + B/A \right|^2 + f \right], \tag{66}$$

where M_ρ is the ρ^0 mass and Γ_ρ is the momentum dependent width:

$$\Gamma_\rho(M_{\pi\pi}) = \Gamma_0 \left(\frac{q}{q_0} \right)^3 \frac{M_\rho}{M_{\pi\pi}}.$$

Γ_0 is the ρ^0 width, q is the π momentum in the $\pi\pi$ rest frame and q_0 is the value of the q for $M_{\pi\pi} = M_\rho$. A is the normalization of the resonant amplitude, B denotes the M_ρ-independent non-resonant amplitude and f reflects the background from the photon dissociation and is assumed to be of the form [53]:

$$f = A_f(1 + 1.5 \cdot M_{\pi\pi}). \tag{67}$$

To evaluate the differential cross section $\mathrm{d}\sigma/\mathrm{dM}_{\pi\pi}$, a fit to the acceptance corrected invariant mass spectra was performed in 9 t bins using Eq. 66. The free parameters of fit were M_ρ, Γ_ρ, A, B/A and A_f. The fit was done in the invariant mass range: $0.55 < M_{\pi\pi} < 1.3$ GeV. The same t bins were chosen to calculate differential cross section $d\sigma/dt$ in Sec. 7.1

The iterative method was used. First for a mass-dependent correction of the data the EPSOFT MC sample with only the Breit-Wigner function for the ρ^0 peak was used. In next steps MC was reweighted according to fit results (with the background included). The procedure was repeated until the fit parameters converged, i.e. until the parameterization in the MC was the same for i and $i+1$ step within the fit errors.

Tab. 7 shows the result of the Söding fit after the last iteration. The χ^2/NDF for all bins is satisfactory. The fitted values of the M_ρ and Γ_ρ do not depend on $-t$ and are within the statistical errors close to the values quoted by the PDG (Tab. 6). Therefore to minimize the uncertainties of the fit parameters, the final results for B/A and A_f were obtained using Eq. 66 with the ρ^0 mass and width set to the PDG values. The results from the final fits are summarized in Tab. 8. Both background contributions (B/A and A_f) depend on t.

B/A decreases with $-t$, meaning that the skewing of the Söding function decreases as the momentum transfer increases. For reweighting the EPSOFT MC, the t-dependence of B/A was parameterized as:

$$B/A = k_S \cdot e^{b_s \cdot t}, \tag{68}$$

where k_S and b_S were free parameters. For a better estimation of k_S and b_S, the results from the previous ZEUS analysis for B/A at lower $-t$ were also used [20]. The fit results of $k_S = 0.76 \pm 0.14$ (stat.) $^{+0.04}_{-0.06}$ (syst.) GeV$^{-1/2}$ and $b_S = 1.29 \pm 0.17$ (stat.) $^{+0.18}_{-0.19}$ (syst.) GeV^{-2} are consistent with [20].

-t (GeV^2)	M_ρ (MeV)	Γ_ρ (MeV)	B/A (GeV$^{-1/2}$)	A_f (GeV^{-1})	χ^2/NDF
1.20 - 1.50	772. $\pm$ 4.	149. $\pm$ 7.	0.155 $\pm$ 0.039	0.093 $\pm$ 0.024	0.7
1.50 - 2.00	773. $\pm$ 3.	133. $\pm$ 7.	0.133 $\pm$ 0.036	0.141 $\pm$ 0.026	1.6
2.00 - 2.50	772. $\pm$ 4.	141. $\pm$ 11.	0.081 $\pm$ 0.049	0.137 $\pm$ 0.043	1.4
2.50 - 3.00	769. $\pm$ 6.	142. $\pm$ 14.	0.038 $\pm$ 0.072	0.199 $\pm$ 0.072	0.4
3.00 - 3.50	782. $\pm$ 13.	196. $\pm$ 32.	0.054 $\pm$ 0.120	0.025 $\pm$ 0.083	1.7
3.50 - 4.00	771. $\pm$ 10.	129. $\pm$ 18.	-0.037 $\pm$ 0.108	0.230 $\pm$ 0.105	0.3
4.00 - 5.00	782. $\pm$ 17.	164. $\pm$ 35.	0.134 $\pm$ 0.169	0.139 $\pm$ 0.127	0.9
5.00 - 6.85	753. $\pm$ 22.	135. $\pm$ 36.	-0.093 $\pm$ 0.200	0.133 $\pm$ 0.183	0.8
6.85 - 10.0	783. $\pm$ 26.	81. $\pm$ 93.	-0.027 $\pm$ 0.283	0.319 $\pm$ 0.312	0.3

Table 7: Results for the fits to the Söding parameterization (Eq. 66) for ρ^0 in different t bins. The fit was performed in the mass range $0.55 < M_{\pi\pi} < 1.3$ GeV.

-t (GeV^2)	A^2 (nb)	B/A (GeV$^{-1/2}$)	A_f (GeV^{-1})	χ^2/NDF
1.20 - 1.50	59.9 $\pm$ 1.5	0.133 $\pm$ 0.022	0.082 $\pm$ 0.016	0.7
1.50 - 2.00	44.0 $\pm$ 1.2	0.080 $\pm$ 0.021	0.085 $\pm$ 0.017	2.0
2.00 - 2.50	19.0 $\pm$ 0.7	0.046 $\pm$ 0.029	0.102 $\pm$ 0.026	1.3
2.50 - 3.00	8.5 $\pm$ 0.5	0.030 $\pm$ 0.042	0.169 $\pm$ 0.044	0.4
3.00 - 3.50	5.1 $\pm$ 0.4	-0.019 $\pm$ 0.066	0.081 $\pm$ 0.052	1.8
3.50 - 4.00	9.7 $\pm$ 0.7	-0.064 $\pm$ 0.053	0.147 $\pm$ 0.061	0.4
4.00 - 5.00	3.0 $\pm$ 0.3	0.038 $\pm$ 0.089	0.134 $\pm$ 0.075	0.7
5.00 - 6.85	1.8 $\pm$ 0.2	0.023 $\pm$ 0.111	0.142 $\pm$ 0.102	0.6
6.85 - 10.0	1.3 $\pm$ 0.3	-0.200 $\pm$ 0.138	0.018 $\pm$ 0.160	0.6

Table 8: Results for the fits to the Söding parameterization (Eq. 66) for the ρ^0 meson in 9 t bins. The fit was performed in the mass range $0.55 < M_{\pi\pi} < 1.3$ GeV. The values of M_ρ and Γ_ρ were fixed to the DPG values (Tab. 6). Only the statistical errors are shown.

The background contribution from the diffractive photon dissociative events grows with increasing $-t$. It was parameterized as:

$$A_f = n_f \cdot \log(d_f \cdot (-t)), \tag{69}$$

where n_f and d_f were free parameters and their final values are: $n_f = 0.06 \pm 0.01$ (stat.) ± 0.01 (syst.) GeV^{-2} and $d_f = 3.0 \pm 1.0$ (stat.) $^{+0.4}_{-0.6}$ (syst.) GeV^{-2}. Also in this fit, for a better estimation of the fit parameters, the results from the previous ZEUS measurement for A_f at lower $-t$ were used [20]. Fig. 34, 35 present results of the fits.

After determining the background contribution under the ρ^0 mass peak, the minimal χ^2 method was used to find optimal values of M_ρ and Γ_0 in the Monte Carlo. Both, the mass and the width of the ρ^0 were assumed to be t-independent and found equal

$$M_\rho = 772 \pm 2 \text{ MeV} \quad \text{and} \quad \Gamma_0 = 151 \pm 4 \text{ MeV}.$$

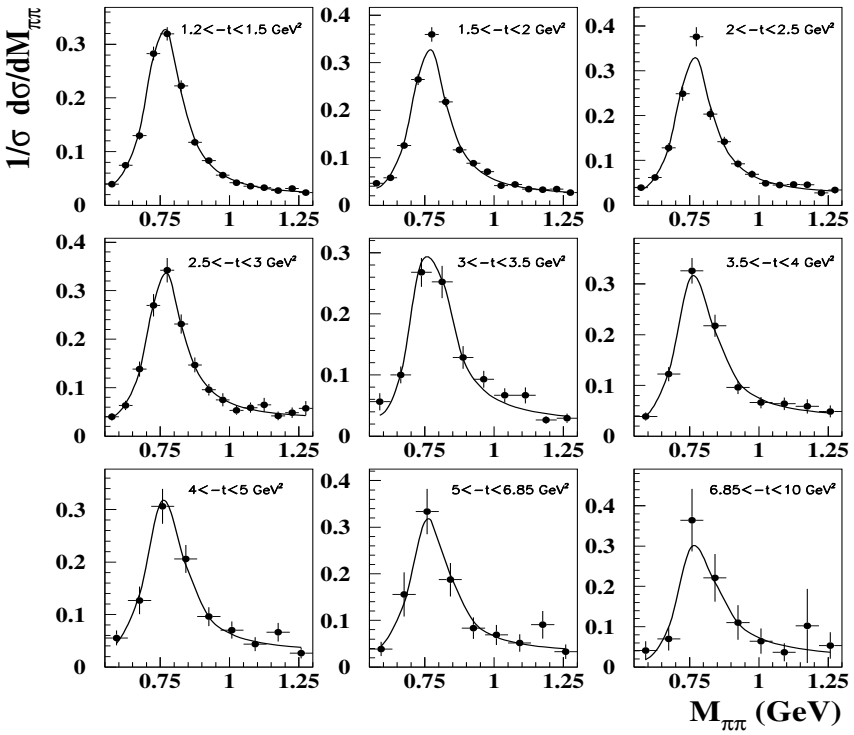

Figure 34: The differential cross section $\mathrm{d}\sigma/\mathrm{dM}_{\pi\pi}$ in different t bins. The solid line is the result of the fit using the Söding parameterization of Eq. 66. Only the statistical errors are shown.

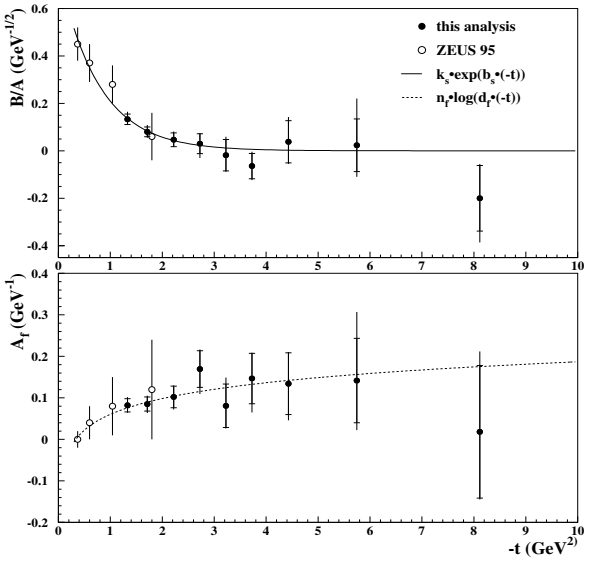

Figure 35: The ration B/A and the diffractive photon dissociation background A_f as a function of $-t$. Dots represent this analysis and open circles the ZEUS 95 measurement. The inner error bars indicate the statistical uncertainties, the outer ones statistical and systematic errors added in quadrature. Lines are the parameterization of B/A (solid) and A_f (dashed), given by Eq. 68 and 69, respectively.

For the final reweighting the $M_{\pi\pi}$ distribution was assumed to follow the Söding parameterization (66) with M_ρ and Γ_0 equal the optimal values of 772 and 151 MeV, respectively, and the non-resonant and photon-dissociative backgrounds described by Eqs. 68 and 69. To account for observed SCHC breaking in the reweighting procedure, the helicity angular distribution (Eq. 21) with the parameterization of the helicity matrix elements given by Eqs. 63,64 and 65. Table 9 summarizes the final reweighting parameters for the ρ^0 MC. Values marked with a star were not measured in this analysis but are from [27]. The errors on M_ρ and Γ_0 correspond to one standard deviation. The t distribution in the Monte Carlo was reweighted to match the data.

parameter	optimal value	error
M_ρ	772 MeV	$\pm$ 2 MeV
Γ_ρ	151 MeV	$\pm$ 4 MeV
k_S	0.76 GeV$^{-1/2}$	$\pm$ 0.14 GeV$^{-1/2}$
b_S	1.29 GeV^{-2}	$\pm$ 0.17 GeV^{-2}
n_f	0.06 GeV^{-2}	$\pm$ 0.01 GeV^{-2}
d_f	2.99 GeV^{-2}	$\pm$ 1.04 GeV^{-2}
r_{00}^{04} *	$0.0147 \cdot t$	$\pm$ 0.0065
Re(r_{00}^{04}) *	0.052	$\pm$ 0.008
r_{1-1}^{04} *	$-0.114 - 0.0162 \cdot t$	-0.114$\pm$0.027, -0.0162$\pm$ 0.0053

Table 9: The final parameters of the ρ^0 MC reweighting procedure.

Fig. 36 shows the comparison between the ρ^0 data and reweighted EPSOFT MC for $-t$, W, $M_{\pi\pi}$, as well as for p_t and η of the positive track in 4 arbitrary chosen t ranges. For each variable (except t) the data and MC samples have all cuts described in Sec. 4.3 applied, except for the one on the variable shown. For the t distribution all cuts are applied. These cuts are indicated on the plot by dotted lines. The agreement between data and MC in all variables is good.

5.7.5 Reweighting of the MC for the ϕ meson

The spin density matrix element r_{1-1}^{04} for the ϕ meson was found to differ from zero and to depend on the momentum transfer [27]. Its t-dependence was parameterized according to:

$$r_{1-1}^{04} = -0.0339 \cdot t \tag{70}$$

and used in the MC reweighting procedure.

The original ϕ EPSOFT MC sample was generated without any background. Studies of the ϕ mass distribution shows that the non-resonant background under the ϕ mass peak is big and cannot be neglected in the analysis. For the reweighting procedure, the data with the background subtracted have to be used.

The acceptance as a function of the invariant mass M_{KK} is flat in the resonance region [20] so the non-resonant background was determined by fitting uncorrected mass spectra in 8 t bins. A relativistic Breit-Wigner distribution for the ϕ signal convoluted with a Gaussian for the finite tracing resolution was fitted to the data together with a function describing the background.

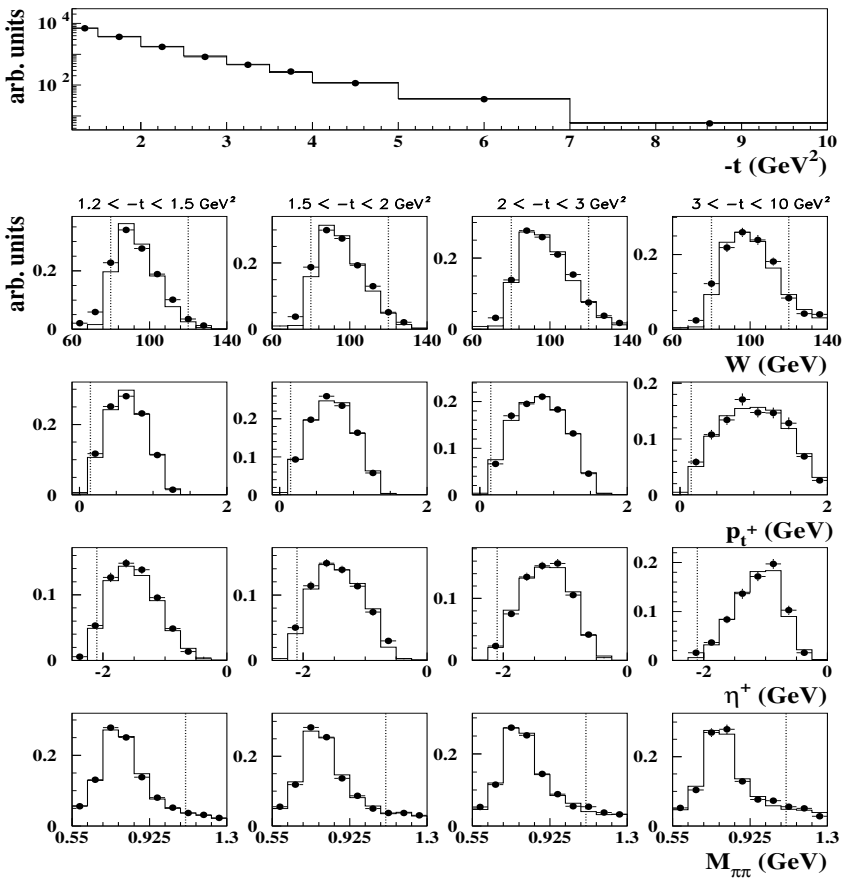

Figure 36: Comparison between the ρ^0 data (dots) and reweighted EPSOFT MC (histogram) for $-t$ (top), W, $M_{\pi\pi}$ and for p_t and η of the positive track in different t bins. Dashed lines indicate the selection cuts applied to the displayed variable. On all other variables the final selection cuts are imposed (Sec. 4.3).

The non-resonant background under the ϕ mass peak is mostly due to a diffractive ρ^0 production, where a ρ^0 event was reconstructed with a kaon mass. To parameterize this contribution as a function of M_{KK}, the invariant mass distribution of the ρ^0 MC events were studied, by assigning the kaon mass to the two pions. The shape of this background (BG) can be described by the equation:

$$BG = N_{BG} \cdot (M_{KK} - 2M_K)^{\delta}, \tag{71}$$

where the normalization of the background N_{BG} and δ are parameters determined by the fit.

In the fits to the ϕ mass spectra, the width of the Breit-Wigner function was set to 4.43 MeV, while the free parameters of the fit were: the normalization, M_ϕ, N_{BG} and δ. The fit was performed in the 8 t bins listed in Tab. 10. The same bins were chosen for the cross section evaluation.

The results of the fit for the ϕ mass are in very good agreement with the PDG, namely 1020 ± 0.5, 1020 ± 0.5, 1021 ± 0.6, 1019 ± 1.2, 1020 ± 0.2, 1020 ± 0.6 MeV, 1019 ± 7.6, 1020 ± 1.3 MeV for increasing t bins. To have a better estimation of the background contribution, the ϕ mass was fixed at the PDG value of 1019.413 MeV for the final fits.

The results of the fit are summarized in Tab. 10. All fits were performed in the mass range of $0.99 < M_{KK} < 1.14$ GeV and the background fraction was determined in the mass window of $0.99 < M_{KK} < 1.06$ GeV. The agreement between the resolution in data (5 MeV, see Sec. 5.8, Tab. 13) and in MC is satisfactory.

-t (GeV^2)	χ^2/NDF	backg. (%)	δ	resolution (MeV)
1.2-1.55	1.1	24.5 $\pm$ 2.1	0.4 $\pm$ 0.1	5.7 $\pm$ 0.4
1.55-1.9	1.7	15.3 $\pm$ 2.1	0.9 $\pm$ 0.2	6.0 $\pm$ 0.5
1.9-2.3	2.5	13.3 $\pm$ 1.7	1.1 $\pm$ 0.2	5.6 $\pm$ 0.4
2.3-2.7	1.0	14.2 $\pm$ 2.5	1.0 $\pm$ 0.3	5.1 $\pm$ 0.7
2.7-3.2	0.7	20.3 $\pm$ 3.2	0.7 $\pm$ 0.3	3.5 $\pm$ 1.5
3.2-3.8	0.9	10.1 $\pm$ 2.6	1.2 $\pm$ 0.6	3.5 $\pm$ 1.4
3.8-4.8	0.1	2.7 $\pm$ 1.7	2.8 $\pm$ 0.8	3.1 $\pm$ 2.7
4.8-6.5	0.7	2.3 $\pm$ 0.8	2.5 $\pm$ 1.2	4.1 $\pm$ 1.7

Table 10: The fit results for the M_{KK} spectra. The fit was performed in the range $0.99 < M_{KK} < 1.14$ GeV. The background was evaluated in the region $0.99 < M_{KK} < 1.06$ GeV.

Fig. 37 shows the M_{KK} mass spectra. The solid curve is the final fit with the parameters summarized in Tab. 10. The dashed line represents the fitted background.

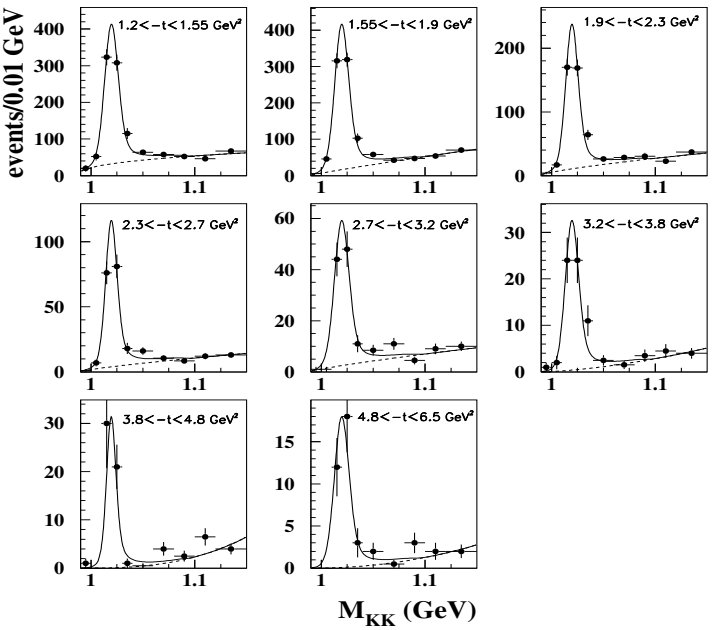

Figure 37: Two kaon invariant mass distribution for ϕ in eight t bins. The solid line is a result of fit to the sum of the Breit-Wigner function convoluted with the Gaussian and the background of the form of Eq.71. The dashed line indicates fitted background.

The t distribution is not properly generated in the MC, so it had to be reweighted to describe the data. For the reweighting the minimal χ^2 method was used.

Fig. 38 shows comparison between the ϕ data and the reweighted EPSOFT for $-t$, W, p_t and η of the positive track in four arbitrary chosen t bins for the ϕ sample. The overall agreement between data and modified EPSOFT is good.

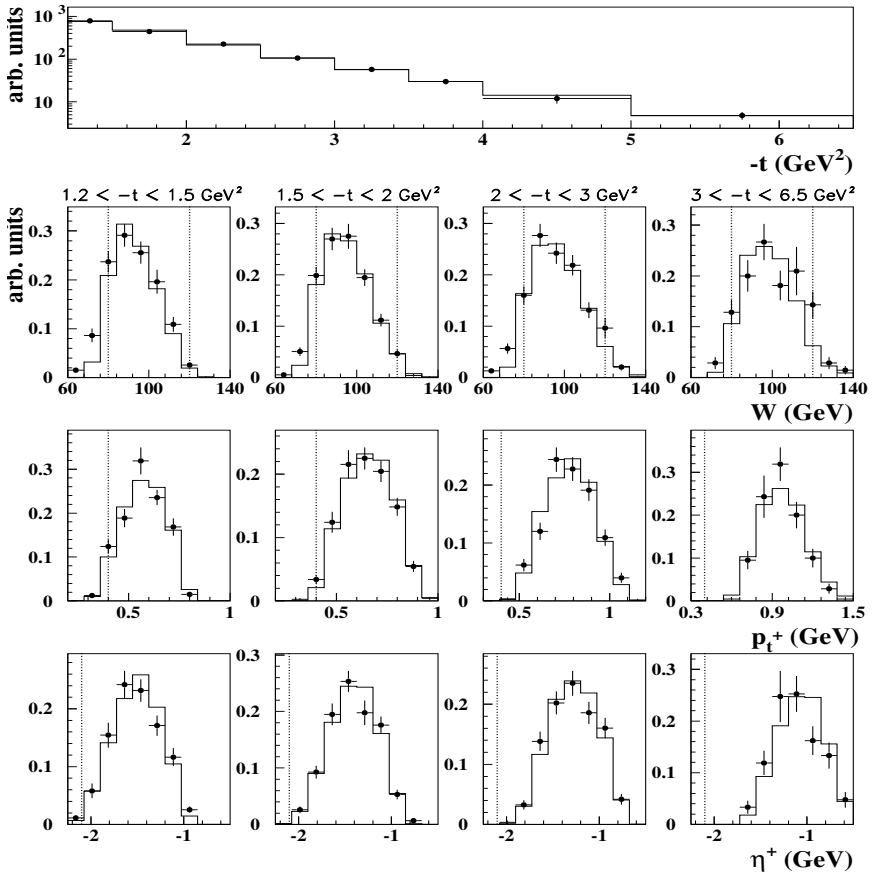

Figure 38: Comparison of the ϕ data (dots) and reweighted EPSOFT MC (histogram) for $-t$ (up) and W, p_t^+ and η^+ in four t bins. Dashed lines indicate the selection cuts applied to the displayed variable. On all other variables the final selection cuts are imposed (Sec. 4.3).

5.7.6 Reweighting of the MC for the J/ψ meson

The spin density matrix elements r^{04}_{1-1} and r^{04}_{00} are consistent with zero for J/ψ photoproduction [27]. Therefore, in the case of the J/ψ Monte Carlo sample no reweighting of the helicity angles distributions was applied.

The original J/ψ Monte Carlo sample was generated without contribution from any background sources. Studies of the background in J/ψ photoproduction show that the background does not depend on t within statistical errors. Therefore, no background subtraction was applied for the reweighting procedure.

The non-resonant background under the J/ψ mass peak was determined by fitting the observed mass distributions in the data without mass dependent corrections. Due to the limited statistic of the J/ψ data sample, the analysis was performed in only 3 t bins. A sum of the bremsstrahlung function convoluted with the Gaussian (electron decay channel) and the Gaussian function (muon decay channel) with equal weights was fitted to the data over a linear

background (BG) of the form [5]:

$$BG = A_{BG} \cdot (1 + \delta M_{ee}). \tag{72}$$

The free parameters of the fit were $M_{J/\psi}$, resolution, normalization, A_{BG} and δ. The fit was performed in the mass range: $2.6 < M_{ee} < 3.4$ GeV. The background contribution was derived for $2.98 < M_{ee} < 3.13$ GeV.

The results of the fit are summarized in Tab. 11. The resolution determined for the EPSOFT MC is 25 MeV (Tab. 13, Sec. 5.8). The values determined for $M_{J/\psi}$ from the fit are in agreement with the values quoted by the PDG. Within the statistical errors the resolutions derived from the data and MC sample (25 MeV, see Tab. 13, Sec. 5.8) agree.

-t (GeV^2)	χ^2/NDF	$M_{J/\psi}$ (MeV)	backg. (%)	resolution (MeV)
1.2 - 1.65	0.4	3080 $\pm$ 10	8.0 $\pm$ 4	30 $\pm$ 9
1.65 - 2.5	0.6	3101 $\pm$ 11	8.7 $\pm$ 2	29 $\pm$ 7
2.5 - 6.5	0.1	3086 $\pm$ 24	8.6 $\pm$ 2	38 $\pm$ 20

Table 11: Result of the fit to the M_{ee} mass spectra of the J/ψ data. The fit was performed in the M_{ee} range of $2.6 < M_{ee} < 3.4$ GeV. The background contribution was derived in the mass window $2.98 < M_{ee} < 3.13$ GeV.

Fig. 39 shows the distribution of the two electron invariant mass M_{ee} in three t bins of the data together with the fit results.

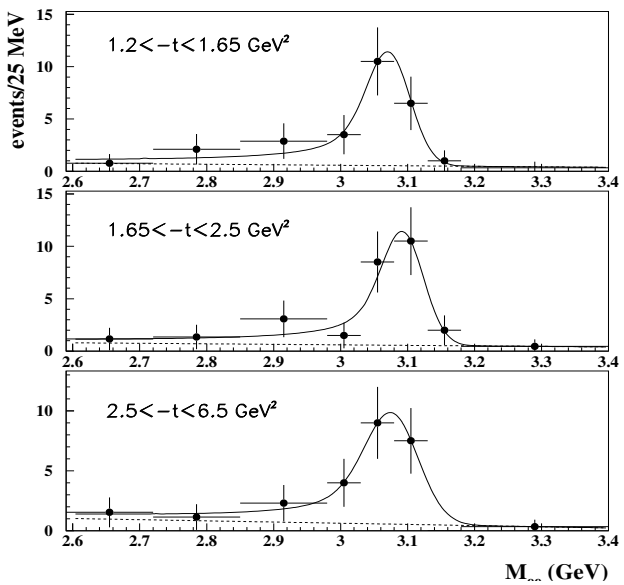

Figure 39: The M_{ee} mass distribution for J/ψ in three t bins (dots). The solid line is the result of the fit to the sum of Gaussian (muon decay channel) and the bremsstrahlung function convoluted with th Gaussian (electron decay channel) with equal weight and a linear background. The dotted line corresponds to the fitted background described by Eq. 72.

Since the non-resonant background does not depend on t, to improve its estimation for the final results, the background was evaluated in the entire t range. Fig. 40 shows the results of the fit to the M_{ee} integrated over the full t range. The fit parameters are quoted in Tab. 12. The value obtained for $M_{J/\psi}$ is within the error consistent with the value quoted by the PDG. Also the resolution agrees with the one observed in the Monte Carlo (25 MeV, Sec. 5.8).

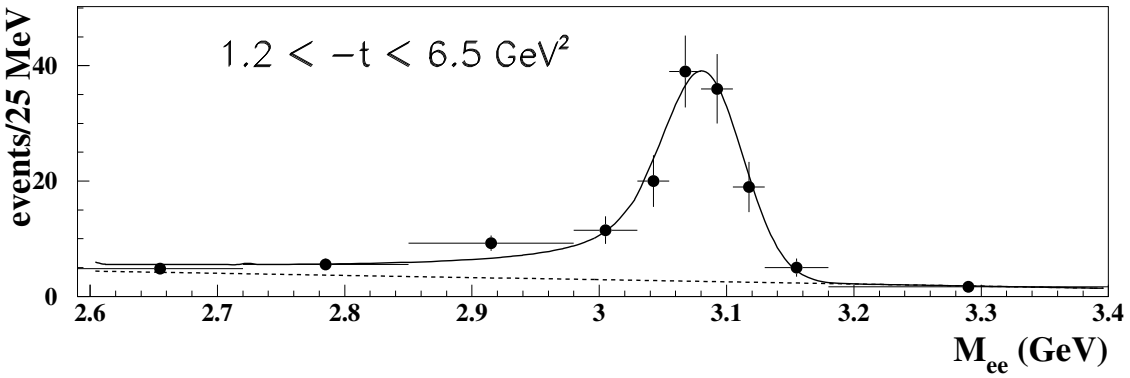

Figure 40: The two electron invariant mass distribution for J/ψ meson (dots). The solid line is the result of the fit to the sum of the Gaussian (muon decay channel) and the bremsstrahlung function convoluted with the Gaussian (electron channel) with equal weights over the linear background. The dashed like indicates fitted non-resonant background, given by Eq. 72.

$-t$ (GeV^2)	$M_{J/\psi}$ (MeV)	resolution (MeV)	background (%)	χ^2/NDF
1.2 - 6.5	3089 $\pm$ 4	26 $\pm$ 5	9.8 $\pm$ 0.7 (stat.) +5.8 -3.3 (syst.)	0.3

Table 12: The results for the fit to M_{ee} shown in Fig. 40. The fit range is 2.6 < M_{ee} < 3.4 GeV. The fraction of background was estimated in the mass window 2.98 < M_{ee} < 3.13 GeV.

The systematic uncertainty for the non-resonant background was calculated using checks 1-7 described in Sec. 6. The main sources for the systematic error of the background are the following: no η_{min} cut imposed (check 6b), resulting in the background of 14.9%, calculating the background in narrowed and widened two-electron invariant mass range (checks 7a and 7b, respectively), the looser cut for the maximum energy of the calorimeter cell not associated with the tracks (check 4b) and the wider cut for the transverse momentum p_T of the track (check 2b).

Since the original EPSOFT MC was not generated with the correct t distribution, it had to be reweighted to describe the data. The minimum χ^2 method was used to determine the parameters of the reweighting function.

Fig. 41 presents the comparison between the data and the reweighted EPSOFT Monte Carlo in two t bins. Dotted lines on the figure correspond to the selection cuts. The overall agreement is good.

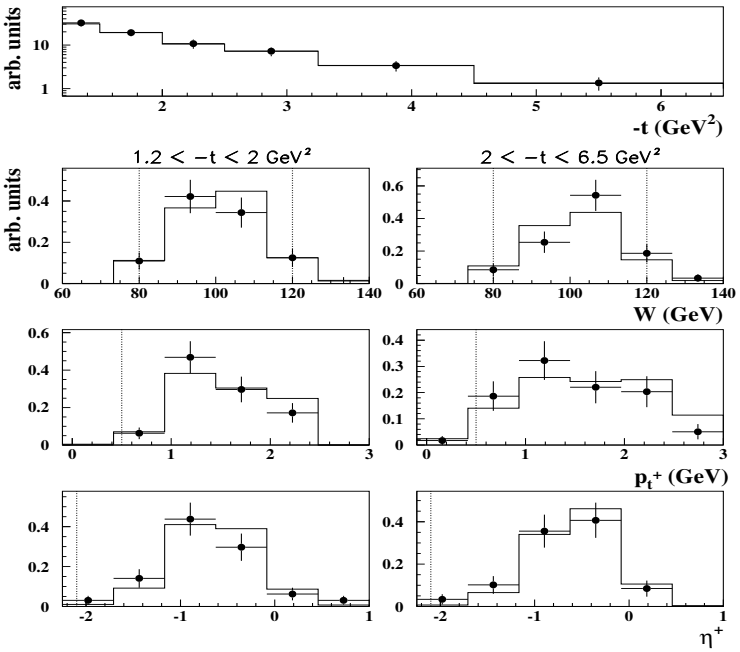

Figure 41: Comparison between the J/ψ data (dots) and reweighted EPSOFT (histogram) for $-t$ (up), W, p_t^+ and η^+ in two bins of $-t$ (down). The vertical lines show selection cuts applied to the variable shown.

5.8 Resolution

The resolution of a kinematic variable v is determined from the root-mean-square (RMS) of a distribution:

$$r_v = v^{gen} - v^{rec}, \tag{73}$$

where v^{gen} and v^{rec} is a generated and reconstructed value of the variable v, respectively. The mean of the distribution of r_v is used to determine if there is any systematic shift between the generated and reconstructed values of the variable v. The resolution of the kinematic variables t, W, M_V and helicity angles $\cos\vartheta_h$ and φ_h was studied as a function of the reconstructed momentum transfer t_{rec}, using the EPSOFT MC. Since the reconstruction of t and W for large values of $-t$ is affected by large values of M_Y, the resolution study was restricted to region $M_Y < 10$ GeV.

Fig. 42 shows the mean and RMS of r_v, for $v = -t, W, \cos\vartheta_h$ and φ_h as a function of reconstructed value of t for the ρ^0, ϕ and J/ψ meson. Tab. 13 summarizes typical resolutions for the different variables. In general the resolution improves with increasing $-t$. This a result of a fact that with increasing $-t$, the angle between the tracks and Z-axis increases and both tracks cross more CTD superlayers which leads to an improvement of the track momenta reconstruction. As described in Sec. 4.1, all kinematic variables (except the calorimeter energy deposits) are reconstructed from the tracks momenta measured with the CTD. Therefore, improving the tracks reconstruction has a big impact on the resolution of the kinematic variables. The angular resolution depends strongly on the opening angles between the meson decay products. For the ϕ meson the opening angle between the two kaons is smaller than the angle between the two pions for ρ^0 or the two leptons for J/ψ. Therefore the angular resolution for ϕ signif-

icantly deteriorates compared to the ρ^0 and J/ψ cases. There is no systematic shift between the generated and reconstructed variables. Exception in the invariant mass distribution for the J/ψ meson. In a magnetic field, electrons radiate photons. This energy lose causes a systematic shift of 50 MeV in the reconstruction of the J/ψ mass for the electron decay channel.

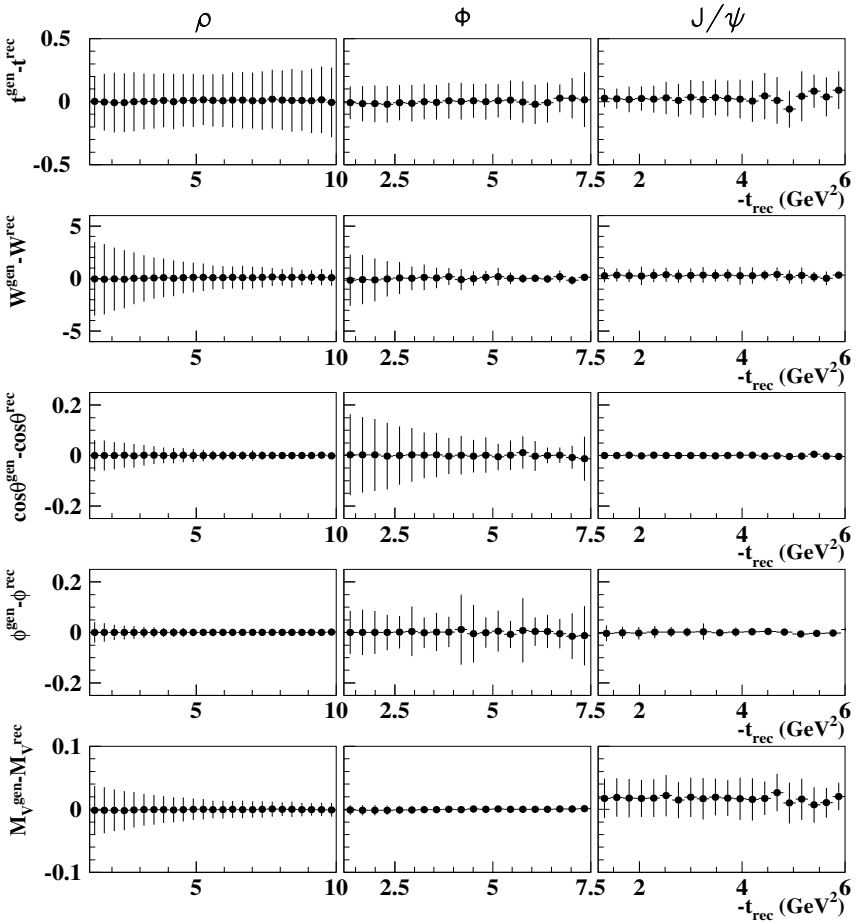

Figure 42: The distribution $r_v = v^{gen} - v^{rec}$ for $v = -t, W, \cos\vartheta_h$ and φ_h with the RMS reflecting the resolution of the variable v, as a function on the reconstructed momentum transfer t_{rec} for the ρ^0,ϕ and J/ψ meson.

	typical resolution		
variable	ρ^0	ϕ	J/ψ
t (GeV^2)	0.20	0.10	0.10-0.20
W (GeV)	4-1	2.5-1	1
$cos\vartheta_h$	0.06-0.01	0.15-0.05	0.01
φ_h (rad)	0.05-0.01	0.1	0.5
M_V (MeV)	50	5	25

Table 13: The typical resolution of the kinematic variables t, W, M_V and helicity angles $cos\vartheta_h$ and φ_h for the ρ^0,ϕ and J/ψ meson.

For the further analysis bins in all relevant variables were chosen to be wider than the considered variable resolution. This suppresses the probability of migrations between neighboring bins and lowers a correlation between statistical errors.

5.9 Acceptance

To obtained corrected distributions for a particular variable, the data had to be corrected for the acceptance of the ZEUS detector, the trigger configuration and the selection cuts. The acceptance is estimated from MC generated events by the ratio of the number of reconstructed and accepted events to the number of generated events in the selected kinematic range. The acceptance determined in this way accounts for the detector and reconstruction efficiencies, the geometrical acceptance, the detector resolution and the trigger efficiency.

The simulation of the 44m tagger acceptance and the *High Lumi* trigger efficiency was performed separately for the need of this analysis and is presented in Secs. 5.5 and 5.6, respectively. Since the overall acceptance has to account for all detector features, in the studies described below the 44m tagger acceptance and the *High Lumi* trigger simulations are included.

Fig.43 shows the acceptance as a function of different kinematic variables estimated with EPSOFT MC, reweighted as described above, for the three vector mesons ρ^0,ϕ and J/ψ.

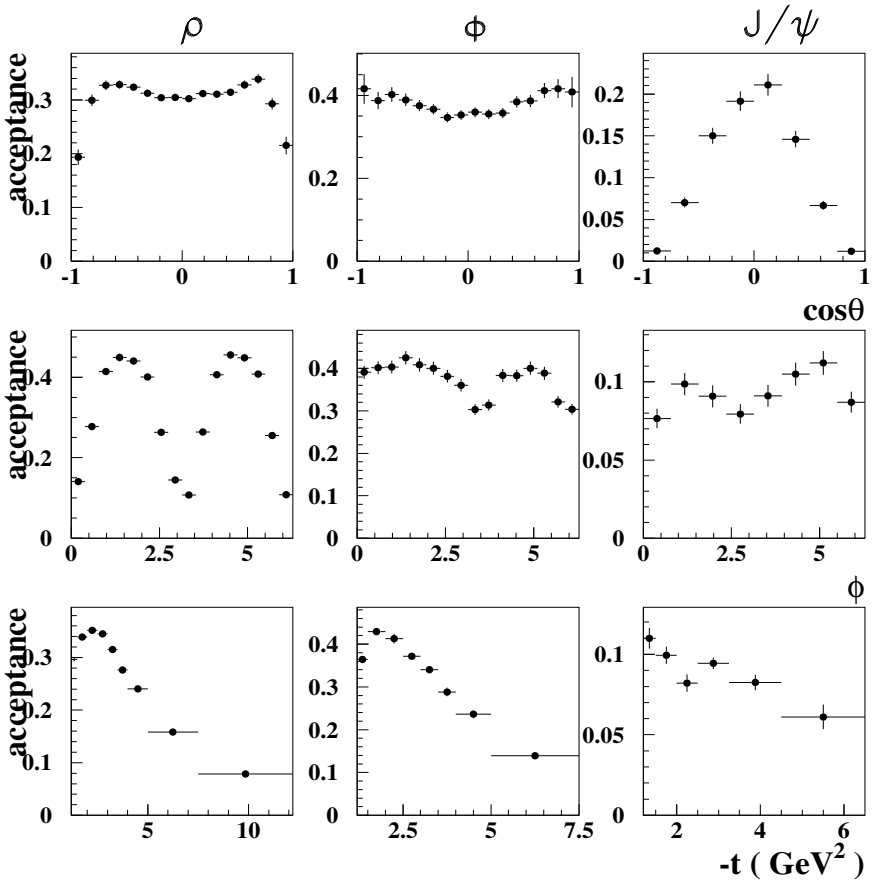

Figure 43: The overall acceptance as a function of $cos\vartheta_h$, φ_h and $-t$ for the ρ^0 (left column), ϕ (middle column) and J/ψ (right column) vector mesons.

Inefficiencies at low $-t$ for ρ^0 and ϕ and a strong variation of the φ_h angle acceptance is caused by the small opening angle of the decay particles, which results in many backward tracks outside the geometrical acceptance of the CTD. The average acceptance as a function of t varies from 10 to 40% for ρ^0 and ϕ, and from 5 to 10% for the J/ψ meson. An inefficiency at high $-t$ is cause by the trigger conditions and selection cuts.

6 Systematic Checks

There are three sources of the systematic uncertainties. One is the change of selection cuts imposed on the data and the MC sample. The other is the uncertainty reflecting the used models and parameterizations in the MC reweighting procedures. To the third class belong uncertainties coming from the global corrections applied to the final measurement. All systematic checks performed for this analysis are described below. The total systematic uncertainty of the measurement was estimated by using three classes of the checks. First, the effect of varying the selection cuts imposed on the data and the MC (according to the resolution of the variable) was studied. The second class of checks reflects the uncertainty of the MC models and the parameterization of the reweighting procedure. Finally, the global errors affecting the normalization of the measurement, like luminosity estimation uncertainty, radiative corrections or uncertainty of estimating the accidental coincidences, were applied.

Changes in the cuts described in Sec. 4.3

1. the pseudorapidity of the track $|\eta|$ ($|\eta| < 2.1$) was changed to

   a) $|\eta| < 2.0$ and

   b) $|\eta| < 2.2$

2. the transverse momentum p_T of the track ($p_T > 0.15$, $p_T > 0.4$ and $p_T > 0.5$ for ρ^0,ϕ and J/ψ, respectively) was selected with

   a) $p_T > 0.1$ GeV and

   b) $p_T > 0.2$ GeV for ρ^0

   a) $p_T > 0.3$ GeV and

   b) $p_T > 0.5$ GeV for ϕ

   a) $p_T > 0.4$ GeV and

   b) $p_T > 0.6$ GeV for J/ψ

3. the selection criteria for the vertex ($|v_Z| < 40$ cm, $\sqrt{v_X^2 + v_Y^2} < 0.7$ cm) were varied according to

   a) $|v_Z| < 35$ cm and

   b) $|v_Z| < 45$ cm

   c) $\sqrt{v_X^2 + v_Y^2} < 0.5$ cm and

   d) $\sqrt{v_X^2 + v_Y^2} < 1.0$ cm

4. the maximum energy of the calorimeter cell not associated with the tracks ($E_{max} < 250$ GeV) was changed to

   a) $E_{max} < 200$ GeV and

b) $E_{max} < 300$ GeV

5. the angle of the cone algorithm ($a = 0.2$ rad), used in determination of the calorimeter cell not associated with the tracks was varied according to

   a) $a = 0.15$ m and

   b) $a = 0.25$ m

6. the η_{min} cut ($\eta_{min} > 2.1$) was modified to

   a) $\eta_{min} > 2.3$ and

   b) no η_{min} cut imposed

7. the invariant mass window used in the analysis was narrowed and widened according to

   a) $0.6 < M_{\pi\pi} < 1.05$ GeV and

   b) $0.5 < M_{\pi\pi} < 1.15$ GeV for ρ^0

   a) $1 < M_{KK} < 1.05$ GeV and

   b) $0.98 < M_{KK} < 1.07$ GeV for ϕ

   a) $3 < M_{ee} < 3.11$ GeV and

   b) $2.96 < M_{ee} < 3.13$ GeV for J/ψ

Changes in the MC reweighting [6]

8. The parameterization of the function $\beta(t)$ (Sec. 5.7.1, Eq. 59) was changed according to the fit errors of the direct measurement for each vector meson:

   a) $\beta = \exp(-0.222 - 0.114 \cdot (-t))$ and

   b) $\beta = \exp(0.068 - 0.114 \cdot (-t))$

   c) $\beta = \exp(-0.077 - 0.175 \cdot (-t))$ and

   d) $\beta = \exp(-0.077 - 0.053 \cdot (-t))$, for ρ^0

9. In case of the ϕ and J/ψ mesons additionally the β parameterization from the direct measurement was used

   a) $\beta = \exp(0.461 - 0.448 \cdot t)$ for ϕ

   a) $\beta = 0.73$ for J/ψ

10. For the W-dependence study of the ρ^0 and ϕ vector mesons, instead of the check 8, the β parameterization determined in each W bin (using the ρ^0 data) was varied according to the errors of the fitted parameters (Sec. 7.1.2)

[6] For the final version of the paper the systematic uncertainty concerning the reweighting of the M_Y distribution (see checks 8-11 below) is calculated in a way described in the additional document.

a) $\beta = \exp(0.259 - 0.221 \cdot (-t)$

b) $\beta = \exp(-0.181 - 0.221 \cdot (-t)$

c) and $\beta = \exp(0.039 - 0.087 \cdot (-t)$

d) $\beta = \exp(0.039 - 0.355 \cdot (-t)$, for $80 < W < 90$ GeV

a) $\beta = \exp(0.229 - 0.100 \cdot (-t)$

b) $\beta = \exp(-0.329 - 0.100 \cdot (-t)$

c) and $\beta = \exp(-0.05 + 0.025 \cdot (-t)$

d) $\beta = \exp(-0.05 - 0.225 \cdot (-t)$, for $90 < W < 100$ GeV

a) $\beta = \exp(0.418 - 0.204 \cdot (-t)$

b) $\beta = \exp(0.095 - 0.068 \cdot (-t)$

c) and $\beta = \exp(0.095 - 0.068 \cdot (-t)$

d) $\beta = \exp(0.095 - 0.338 \cdot (-t)$, for $100 < W < 120$ GeV

11. Additionally for the W-dependence study of the ϕ meson the β parameterization from the direct ϕ measurement in three W bins was used

a) $\beta = 0.41$ for $80 < W < 90$ GeV

a) $\beta = 0.89$ for $90 < W < 100$ GeV

a) $\beta = 0.54$ for $100 < W < 120$ GeV

12. Systematic error of the 44m tagger acceptance, see Sec. 5.6

a) the outer contour of the acceptance systematic uncertainty was used

b) the inner contour of the acceptance systematic uncertainty was used

c) the acceptance was shifted by +1.5 GeV

d) the acceptance was shifted by -1.5 GeV

13. The slope of the t-distribution was varied by

a) $+0.04\ GeV^{-2}$ and

b) -0.04 GeV^{-2} for ρ^0

a) $+0.14\ GeV^{-2}$ and

b) -0.14 GeV^{-2} for ϕ

a) $+0.2\ GeV^{-2}$ and

b) -0.2 GeV^{-2} for J/ψ

14. The error of the REMC trigger simulation was imposed by varying the normalization of the REMC efficiency according to the uncertainties of the fitted parameterization (Sec. 5.5) by

    a) +6% and

    b) -6% for ρ^0 and ϕ

15. The parameters of the ρ^0 mass shape reweighting (Sec. 5.7.4, Tab. 9) were changed to the values

    a) $M_\rho = 774$ MeV and

    b) $M_\rho = 770$ MeV

    c) $\Gamma_\rho = 155$ MeV and

    d) $\Gamma_\rho = 147$ MeV

    e) $k_S = 0.90$ GeV$^{-1/2}$ and

    f) $k_S = 0.62$ GeV$^{-1/2}$

    g) $b_S = 1.46$ GeV^{-2} and

    h) $b_S = 1.12$ GeV^{-2}

    i) $n_f = 0.07$ GeV^{-2} and

    j) $n_f = 0.05$ GeV^{-2}

    k) $d_f = 4.03$ GeV^{-2} and

    l) $d_f = 1.95$ GeV^{-2}

16. For the ρ^0 and ϕ meson the SCHC was assumed

17. For the ϕ meson the background in each t bin was varied according to the errors of the background estimation (Tab. 10, Sec. 5.7.5)

    a) $BG + \Delta BG$ in each t bin

    b) and $BG - \Delta BG$ in each t bin

18. For the W-dependence study of the ϕ mesons the background determined from the ϕ data in three W bins was varied according to the errors of the fit parameters (Eqs. 77, Sec. 7.1.2)

    a) $BG = \exp(-1.23 - 0.41 \cdot (-t)$

    b) $BG = \exp(-1.23 - 0.53 \cdot (-t)$

    c) and $BG = \exp(-1.12 - 0.47 \cdot (-t)$

    d) $BG = \exp(-1.34 - 0.47 \cdot (-t)$, for $80 < W < 90$ GeV

    a) $BG = \exp(-1.14 - 0.20 \cdot (-t)$

    b) $BG = \exp(-1.14 - 0.28 \cdot (-t)$

    c) and $BG = \exp(-1.05 - 0.24 \cdot (-t)$

d) $BG = \exp(-1.23 - 0.24 \cdot (-t)$, for $90 < W < 100$ GeV

a) $BG = \exp(-1.03 - 0.16 \cdot (-t)$
b) $BG = \exp(-1.03 - 0.24 \cdot (-t)$
c) and $BG = \exp(-0.95 - 0.20 \cdot (-t)$
d) $BG = \exp(-1.11 - 0.20 \cdot (-t)$, for $100 < W < 120$ GeV

Global effects

19. For the J/ψ meson the resonant contribution C_{res} was changed, according to the results of the background estimation (Tab. 12, Sec. 5.7.6), to the values

    a) $C_{res} = 0.909$ and
    b) $C_{res} = 0.895$

20. For the J/ψ meson W studies the resonant contribution C_{res} was changed, according to the results of the background estimation (Tab. 24, Sec. 7.3.2), to the values

    a) $C_{res} = 0.790$ and
    b) $C_{res} = 0.942$ for $80 < W < 100$ GeV

    a) $C_{res} = 0.921$ and
    b) $C_{res} = 0.947$ for $100 < W < 120$ GeV

21. The luminosity of the data sample was varied by

    a) $+1.7$ % and
    b) -1.7 %

22. The uncertainty due to the radiative correction was applied, equal

    a) $+2$ % and
    b) -2 %

To account for the differences of the modeling the proton dissociation and fragmentation approaches the second MC, DIFFVM-g, was used to evaluate cross section $d\sigma/dt$ for the ρ^0 meson. The difference between this cross section and the nominal one was found to be less then 5%. It was treated as a model-dependence of the results and was not includes in the systematic uncertainty.

For the systematic checks 6 and the DIFFVM-g correction the entire analysis, starting from the $\beta(t)$ parameterization evaluation was repeated. For the systematic checks 1-18 the full analysis, starting from the EPSOFT MC reweighting procedure (excluding the $\beta(t)$ estimation, nominal parameterization of $\beta(t)$ was used), was performed. The checks 19-20 were applied as the uncertainty of the normalization to the final result.

Information about the systematic error for the measured cross section is summarized in Tables 27-43 in Appendix A.

7 Experimental Results

7.1 ρ^0 Photoproduction

The ρ^0 studies were performed in nine t bins in which the differential cross sections $d\sigma/\mathrm{dM}_{\pi\pi}$ and $d\sigma/\mathrm{d}t$ were evaluated. The detailed description of the $d\sigma/\mathrm{dM}_{\pi\pi}$ measurement and the bin boundaries are presented in Sec. 5.7.4.

7.1.1 Differential Cross Section $d\sigma/\mathrm{d}t$

The differential cross section $d\sigma/\mathrm{d}t$ in the proton-dissociative reaction $\gamma p \to \rho^0 Y$ was measured in the kinematic range $1.2 < -t < 10$ GeV^2, $80 < W < 120$ GeV and $\frac{M_Y^2}{-t} < 100$. The number of acceptance corrected resonance events (factor $\frac{N \cdot C_{res}}{A}$ in Eq. 45) in each t bin was obtained from the fits to the two pion invariant mass spectra (Sec. 5.7.4). The cross section $d\sigma/dt$ was corrected for the contamination from elastic events in the final data sample (Sec. 5.7.3) and for the accidental coincidences on the trigger level, changing the number of expected events (Sec. 4.2.2).

A hard production mechanism [3, 4] predicts a power dependence of $d\sigma/dt$ on t. To check this assumption the measured cross section was fitted with the function:

$$A \cdot (-t)^{-n}, \tag{74}$$

where A and n were free parameters. Perturbative QCD calculations give for an asymptotically large momentum transfer t a value of n of around 4 [6].

In Fig. 44 the differential cross section $d\sigma/\mathrm{d}t$ is displayed together with the previous ZEUS 95 measurement [5]. The solid line corresponds to the fitted function (Eq. 74). The measurement at large $-t$ matches well with the low $-t$ results from 1995. The data presented in this analysis have much higher precision and cover a much larger region of the momentum transfer, up to 10 GeV^2.

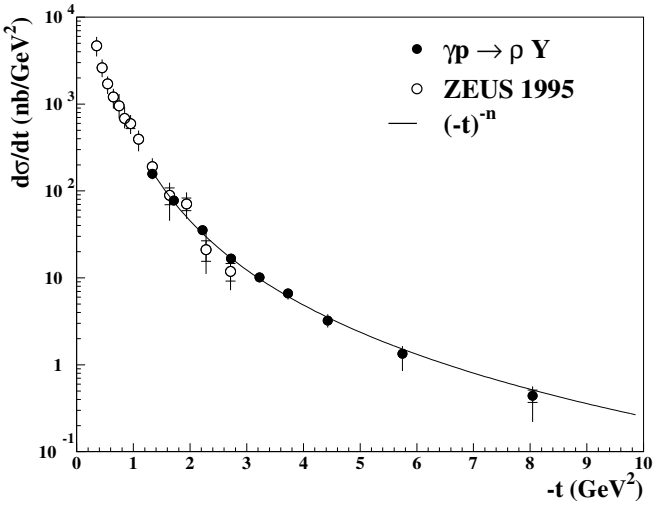

Figure 44: The differential cross section $d\sigma/\mathrm{d}t$ in the kinematic range $80 < W < 120$ GeV and $\frac{M_Y^2}{-t} < 100$. The results of this measurement (dots) are compared to the ZEUS results using 1995 data (open circles). The solid line is the result of the fit to the power-like function of Eq. 74. The inner error bars indicate the statistical error, the outer ones the statistical and systematic uncertainties added in quadrature.

The cross section is well described by the power-like dependence. The fit using the whole t range gives $n = 3.22 \pm 0.04$ (stat.) $^{+0.19}_{-0.15}$ (syst.) with a $\chi^2 = 2.1$. To check, if χ^2 and the power n depend on the $-t$ region in which the fit is performed, the procedure was repeated in four restricted ranges of the momentum transfer. In each case the fit range was limited by excluding one more t bin, starting with the lowest. $-t_0$ corresponds to the average $-t$ value in the first bin of the fit. Tab. 14 and Fig. 45 summarize these studies.

t range (GeV^2)	$n \pm$ stat.	syst.	total error	χ^2
$1.2 < -t < 10$	3.22 ± 0.04	+0.19 -0.15	+0.19 -0.16	2.1
$1.5 < -t < 10$	3.32 ± 0.05	+0.24 -0.16	+0.25 -0.17	0.9
$2.0 < -t < 10$	3.40 ± 0.10	+0.32 -0.19	+0.33 -0.21	0.6
$2.5 < -t < 10$	3.37 ± 0.20	+0.36 -0.21	+0.41 -0.29	0.7
$3.0 < -t < 10$	3.50 ± 0.17	+0.50 -0.26	+0.53 -0.31	0.7

Table 14: Results of the fits of the differential cross section $d\sigma/dt$ with the power-like function $A \cdot (-t)^{-n}$ in different t ranges.

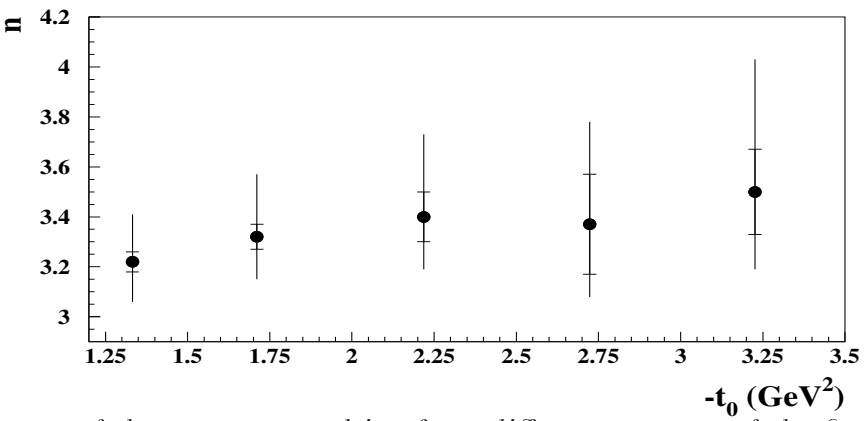

Figure 45: Changes of the power n resulting from different t ranges of the fit, as a function of the fit starting point $-t_0$. The inner error bars indicate the statistical uncertainty, the outer ones the statistical and systematic errors summed in quadrature.

The χ^2 improves with increasing t_0, to $\chi^2 = 0.6$. The central values of the fitted power n grows with increasing t_0 and saturates at the level of ~ 3.4 However, with the statistical and systematic uncertainties, the distribution of n as a function of $-t_0$ is flat, except for the lowest value of $-t_0$.

To compare results of the power-like fit with the ϕ and J/ψ meson in the same t range, the fit was also performed in for $1.2 < -t < 6.85$ GeV^2, which is the range available for all three vector mesons. The result of this fit is $n = 3.20 \pm 0.04$ (stat.), $^{+0.17}_{-0.15}$ (syst.), which is in perfect agreement with the value obtained for the entire t range.

Since the low $-t$ data [5] start at $-t = 0.35$ GeV^2, it is interesting to check if the power-like function (Eq. 74) describes the measured cross section $d\sigma/dt$ in the whole available t range $0.35 < -t < 10$ GeV^2. Therefore the data from this analysis were combined with the ZEUS 95 results and the power-like fit was repeated. Since the measurement presented here has a much higher precision in the region where the two results overlap, only the cross section values for $-t < 1.2$ GeV^2 from 1995 were included in the fit. They correspond to the first eight

open circles in Fig. 44. Fig. 46 shows the comparison between the results of the power-like function fitted to the data from this analysis and the fit to the combined measurement in the t range $0.35 < -t < 10$ GeV^2. Only the points used in the combine fit are drawn. The power dependence does not describe the data in the t range $0.35 < -t < 10$ GeV^2. The fit result is a power $n = 2.92 \pm 0.02$ (stat.) with a large $\chi^2 = 11$.

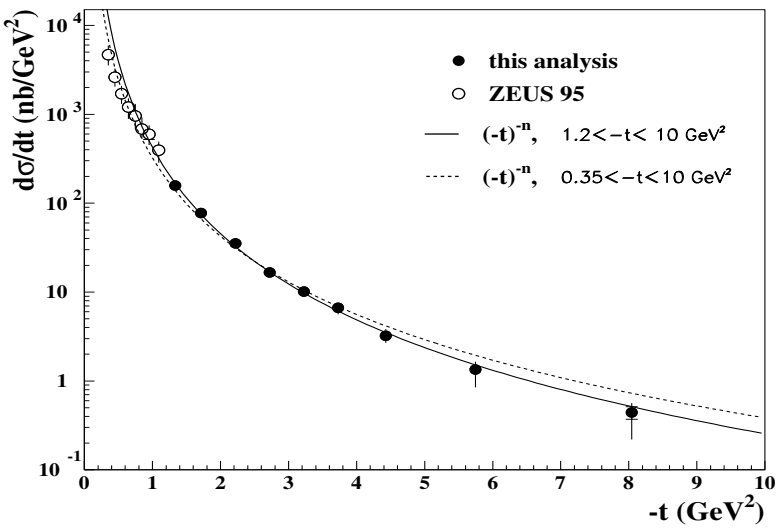

Figure 46: Power-like fit of Eq. 74 to the results of this analysis (dots) alone (solid line) and to the combined data set including ZEUS 1995 data (open circles, fit as broken line). For 1995, only points included in the fit are shown.

The systematic uncertainty of the differential cross section $d\sigma/dt$ varies between 10-20%, increasing with increasing $-t$, except for the last two t bins, where the negative systematic error is 33% and 45%, respectively. For a detailed list of all checks performed (with reference to the check index) see Sec. 6. The major contributions to the total systematic uncertainty are:

a) errors connected to the proton-dissociation modeling in the MC (checks 6, 8): 5-20%,

b) the uncertainty of the REMC trigger efficiency parameterization (check 14): 3-20%,

c) the error coming from the assumption of SCHC (check 16): 4-5%,

d) the uncertainty of the 44m tagger acceptance evaluation (check 12): 4%,

e) the error coming from widening the angle of the cone algorithm (check 5b): 3%,

f) the uncertainty resulting from narrowing the vertex criteria (check 3c): 3%, caused by the differences in the vertex distributions for the data and the EPSOFT MC.

The overall normalization uncertainty of the measured cross section, originating from the checks 21 and 22, is 2.6%.

For the power-like fit to $d\sigma/dt$, the systematic error of the power n is dominated by the uncertainties coming from the proton-dissociation modeling in the EPSOFT MC (checks 6, 8), changing the slope of the t distribution (check 11) and changes of the ρ^0 width Γ_ρ in the MC reweighting (checks 13c, 13d).

Tables containing tabulated values of the ρ^0 differential cross section $d\sigma/dt$ and values of the systematic uncertainties for all applied checks can be found in Appendix A.

7.1.2 W-dependence of the Cross Section

The W dependence of the cross section was studied in three W bins: $80 < W < 90$ GeV (W_1), $90 < W < 100$ GeV (W_2) and $100 < W < 120$ GeV (W_3) and in the momentum transfer range $1.2 < -t < 8.5$ GeV^2. For each center-of-mass energy bin, W_1, W_2 and W_3, the whole analysis was repeated, starting from the MC reweighting procedure. The methods described in detail in Sec. 5 and 7.1.1 were used. The results of the helicity angle analysis [27], the REMC trigger studies (Sec. 5.5) and the amount of incidental coincidences (Sec. 4.2.2) were assumed to be independent of W.

M_Y Evolution with t in W bins. The study of the energy deposition, E_{FCAL}, in the FCAL showed that the $\beta(t)$ parameterization of the generated M_Y distribution (Eq. 55) depends on the center-of-mass energy W. Therefore, a separate $\beta(t)$ was used for each W bin. Fig 47 shows β values evaluated in five t bins for every W range. The errors on β are big but even within these uncertainties the results cannot be parameterized by one $\beta(t)$ for all W ranges. Therefore, for each bin of the center-of-mass energy, a separate β parameterization was applied:

$$\beta_1 = \exp(0.039(\pm 0.200) - 0.220(\pm 0.134) \cdot (-t)), \quad \text{for } W_1 \tag{75}$$

$$\beta_2 = \exp(-0.050(\pm 0.279) - 0.100(\pm 0.125) \cdot (-t)), \quad \text{for } W_2 \tag{76}$$

$$\beta_3 = \exp(0.095(\pm 0.323) - 0.203(\pm 0.135) \cdot (-t), \quad \text{for } W_3 \tag{77}$$

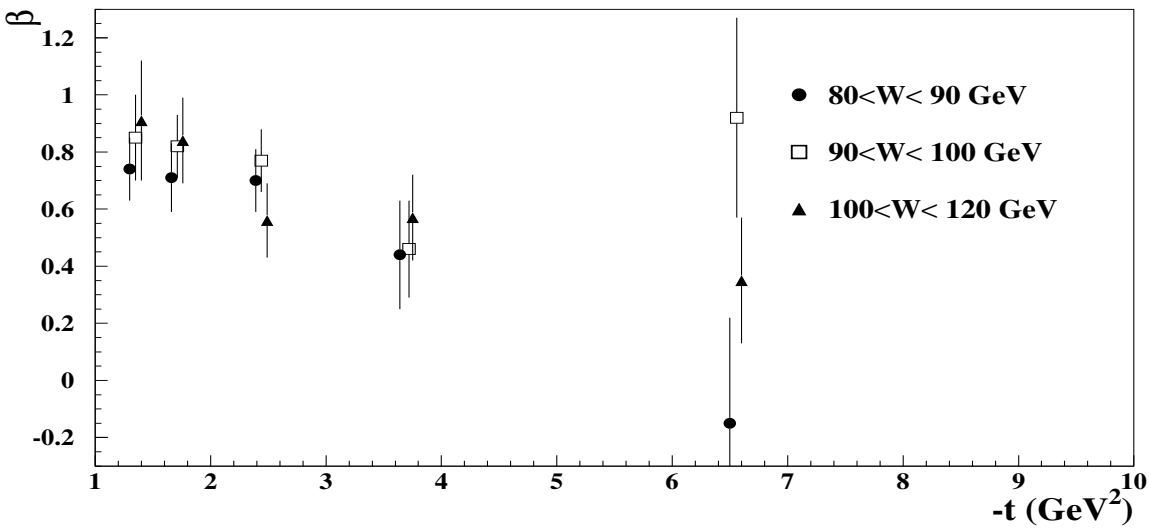

Figure 47: Results of the study of the β parameter in the generated M_Y distribution (Eq. 55) as a function of $-t$ for three W bins. Circles, squares and triangles correspond to the W ranges $80 < W < 90$ GeV, $90 < W < 100$ GeV and $100 < W < 120$ GeV, respectively. For displaying reasons, the points for W_2 and W_3 they were shifted by 0.05 and 0.1 GeV^2, respectively.

Mass Distributions in W bins. In each of the W ranges W_1, W_2 and W_3, the differential cross section $d\sigma/dM_{\pi\pi}$ was derived in six t bins by fitting the Söding function (Eq. 66) to the acceptance corrected two pion invariant mass spectra. To improve the estimation of the background, the ρ^0 mass M_ρ, and width Γ_0, were set to the PDG values. Tab. 15 summarizes the results of the fit. Fig. 48 shows the ratio $-B/A$ and the photon dissociative background A_f as a function of the momentum transfer for three W bins together with the fitted parameterization of Eqs. 68 and 69. The photon dissociative background in the W region $100 < W < 120$ GeV is t-independent and was fitted with the constant function. The results of the fit for $-B/A$ and A_f can be found in Tab. 16. Both background contributions from photon-dissociation and non-resonant ρ^0 production, respectively, depend on W. The bottom row on Fig. 48 compares the non-resonant and photon dissociative background for different center-of-mass energies.

$80 < W < 90$ GeV				
t range (GeV^2)	$\langle t \rangle$ (GeV^2)	B/A (GeV$^{-1/2}$)	A_f (GeV^{-1})	χ^2/NDF
1.2 - 1.5	1.33	0.056 ± 0.030	0.050 ± 0.027	1.8
1.5 - 2.0	1.71	0.042 ± 0.034	0.092 ± 0.032	1.4
2.0 - 2.6	2.26	-0.006 ± 0.048	0.134 ± 0.048	1.7
2.6 - 3.5	2.98	-0.067 ± 0.069	0.287 ± 0.090	0.6
3.5 - 5.0	4.09	-0.035 ± 0.102	0.154 ± 0.092	1.0
5.0 - 8.5	6.21	-0.250 ± 0.220	0.132 ± 0.134	0.3
$90 < W < 100$ GeV				
t range (GeV^2)	$\langle t \rangle$ (GeV^2)	B/A (GeV$^{-1/2}$)	A_f (GeV^{-1})	χ^2/NDF
1.2 - 1.5	1.33	0.109 ± 0.038	0.030 ± 0.029	0.3
1.5 - 2.0	1.71	0.024 ± 0.034	0.083 ± 0.034	0.6
2.0 - 2.6	2.25	0.061 ± 0.052	0.079 ± 0.046	1.5
2.6 - 3.5	2.97	0.019 ± 0.069	0.096 ± 0.058	1.3
3.5 - 5.0	4.07	-0.022 ± 0.085	0.199 ± 0.106	0.9
5.0 - 8.5	6.22	-0.172 ± 0.146	0.175 ± 0.152	0.6
$100 < W < 120$ GeV				
t range (GeV^2)	$\langle t \rangle$ (GeV^2)	B/A (GeV$^{-1/2}$)	A_f (GeV^{-1})	χ^2/NDF
1.2 - 1.5	1.33	0.194 ± 0.062	0.117 ± 0.043	1.3
1.5 - 2.0	1.71	9.153 ± 0.045	0.073 ± 0.037	1.4
2.0 - 2.6	2.26	0.197 ± 0.036	0.032 ± 0.036	2.2
2.6 - 3.5	2.97	0.087 ± 0.060	0.155 ± 0.059	0.8
3.5 - 5.0	4.10	-0.017 ± 0.069	0.113 ± 0.074	0.6
5.0 - 8.5	6.17	-0.114 ± 0.086	0.026 ± 0.088	0.7

Table 15: Results for the fits to the Söding parameterization (Eq. 66) for the ρ^0 meson in three W bins and six $-t$ bins. The fit was performed in the mass range $0.55 < M_{\pi\pi} < 1.3$ GeV. The values of M_ρ and Γ_ρ were fixed to the DPG values (Tab. 6). Only statistical errors are shown.

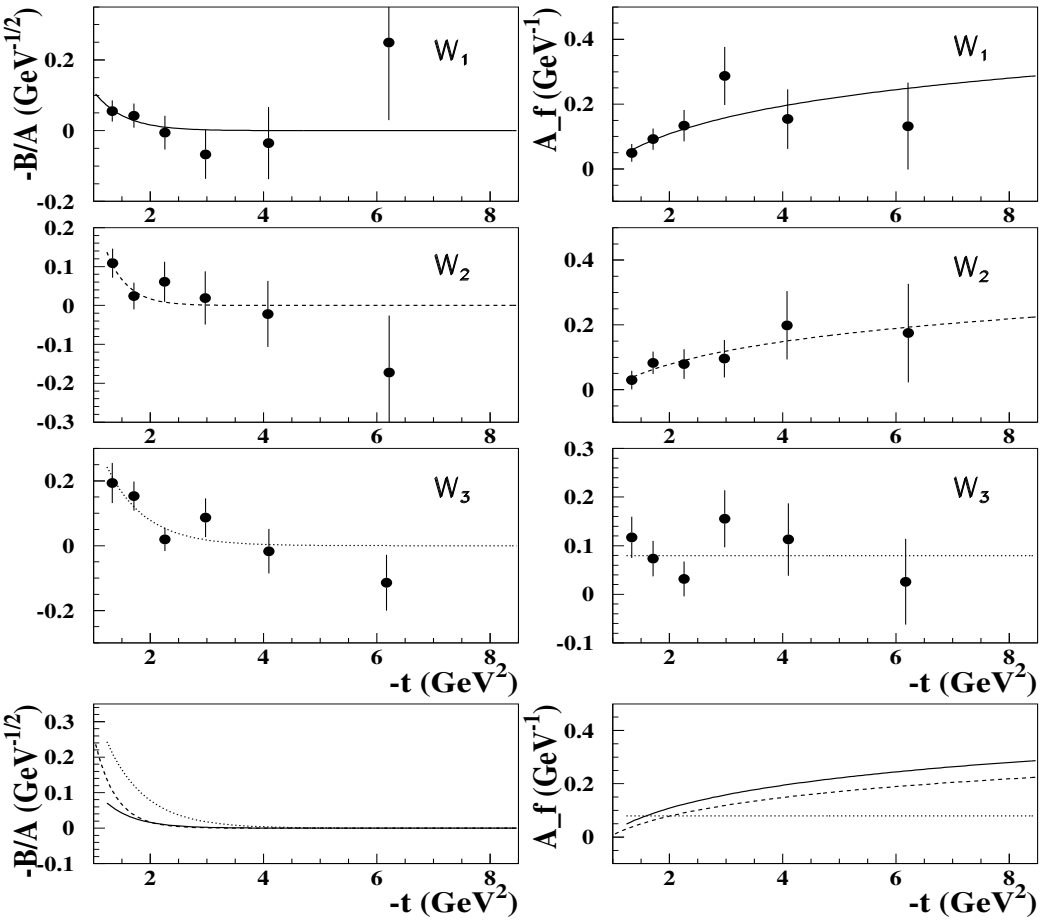

Figure 48: The ratio B/A (left) and the diffractive photon dissociation background A_f (right) as a function of $-t$ in three W ranges together with the parameterization of Eq. 68 and 69, respectively. In the bottom row, the parameterizations for B/A and A_f are directly compared for W_1 (solid line), W_2 (broken line) and W_3 (dotted line).

$B/A = k_S exp(b_s\|t\|)$	$80 < W < 90$ GeV	$90 < W < 100$ GeV	$100 < W < 120$ GeV
k_S (GeV$^{-1/2}$)	0.76 ± 0.35 (stat.)	3.93 ± 1.31 (stat.)	1.53 ± 0.33 (stat.)
b_S (GeV^{-1})	-1.93 ± 0.33 (stat.)	-2.72 ± 0.24 (stat.)	-1.49 ± 0.65 (stat.)
$A_f = n_f \cdot log(d_f \cdot \|t\|)$			
n_f (GeV^{-2})	0.12 ± 0.06 (stat.)	0.10 ± 0.06 (stat.)	–
d_f (GeV^{-2})	1.20 ± 0.47 (stat.)	1.09 ± 0.48 (stat.)	–
$A_f = const$	–	–	0.08 ± 0.02

Table 16: Results of the fits of the differential cross section $d\sigma/dt$ with the power-like function $A \cdot (-t)^{-n}$ in different W bins.

Separating of Elastic and Proton-dissociative Events in W bins. As discussed in Sec. 5.7.3, the analyzed data sample consists of proton-dissociative events, except the low t bins, $-t \lesssim 2.5$ GeV^2, where a contamination of elastic events was observed. Therefore it is necessary to study the W-dependence of the elastic admixture. Fig. 49 shows the comparison of the ratio of the number of events tagged in the PRT to all events for data and the proton dissociative EPSOFT MC in three W bins. The overall agreement is good, except for the low t bins where the data have a contamination from elastic events. The amount of the non-dissociative contribution in the first t bins is of the order of $4-12\%$. Within the errors, there is no significant dependence on W. As for the results obtained for the full W range, no PRT tag was used to select proton-dissociative events. Instead, the data were corrected for the elastic admixture to obtain the final results. As suggested by Fig. 49, in the first two W bins the correction was applied in the lowest two t bins, in the last W bin the first three t bins were corrected.

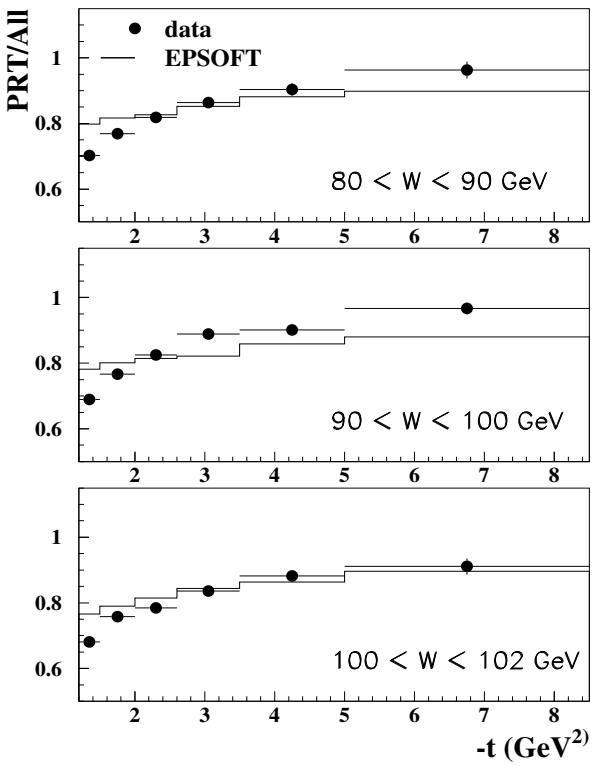

Figure 49: The ratio of events tagged in the PRT to all events for the data (dots) and the proton-dissociative EPSOFT MC (histogram) in three W bins of $80 < W < 90$ GeV, $90 < W < 100$ GeV and $100 < W < 120$ GeV.

Differential Cross Section $d\sigma/dt$ in W bins. In the three W bins W_1, W_2 and W_3, the differential cross section $d\sigma/dt$ was determined in six $-t$ bins for $\frac{M_V^2}{-t} < 100$. Fig. 50 shows the cross section in the three W bins together with the curve obtained as a fit to the power-like function (Eq. 74) compared with $d\sigma/dt$ calculated in the full W range. Within the errors, the normalization of the measurement for different center-of-mass energy bins agrees with the data in the full W range. The cross sections are well described by the fit to Eq. 74. The results

of the power-like fit are summarized in Tab. 17. Within the errors, there is no W dependence of the power n and the values obtained in each W bin agree with the n fitted to the full data sample with $80 < W < 120$ GeV. As predicted by pQCD assuming the 2-gluon exchange [6], the global shape of the t distribution does not depend on center-of-mass energy.

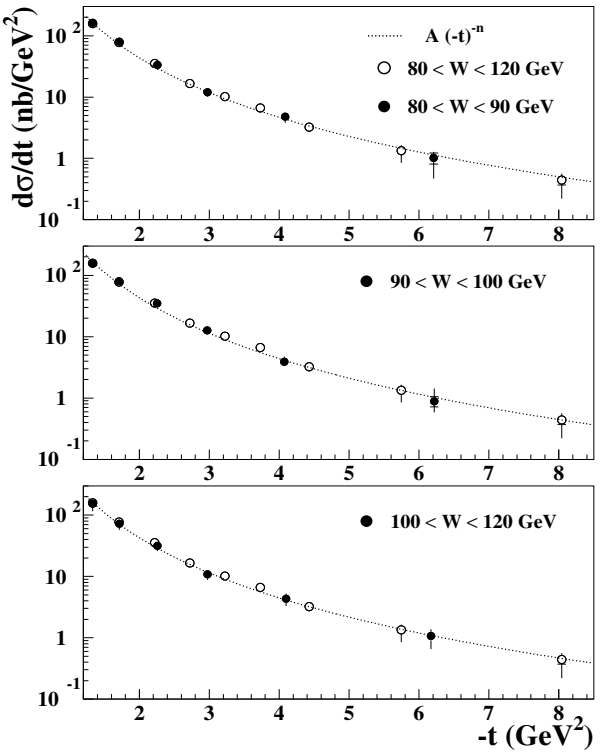

Figure 50: The differential cross sections $d\sigma/dt$ of the ρ^0 meson in the three W bins of $80 < W < 90$ GeV, $90 < W < 100$ GeV and $100 < W < 120$ GeV for $\frac{M_V^2}{-t} < 100$ (dots), together with the result of the fit to the power-like function (Eq. 74) (dotted line) compared with the cross section measured in the full W range (open circles). The inner error bars indicate the statistical error, the outer ones the statistical and systematic uncertainties added in quadrature.

W range (GeV)	power n	stat. error	syst. error	χ^2/ndf
$80 < W < 90$	3.22	$\pm$ 0.07	+0.20 -0.14	1.2
$90 < W < 100$	3.30	$\pm$ 0.07	+0.08 -0.18	1.6
$100 < W < 120$	3.26	$\pm$ 0.08	+0.21 -0.39	0.9

Table 17: Results of the power-like fit of Eq. 74 to the differential cross section $d\sigma/dt$ in the three W bins.

The 44m tagger acceptance depends strongly on the center-of-mass energy. It is flat for W between $\sim$ 90 and 110 GeV but changes steeply outside this window (Sec. 5.6). Also the uncertainties of the 44m tagger acceptance depends on W. Therefore, to be free from this

uncertainty, the studies of the differential cross section as a function of W were performed for the normalized cross sections $(d\sigma/dt)^i_N$ in five t bins. The normalized differential cross section $(d\sigma/dt)^i_N$ in bin i of the momentum transfer is defined as:

$$\left(\frac{d\sigma}{dt}\right)^i_N = \left(\frac{d\sigma}{dt}(t_i)\right) / \left(\frac{d\sigma}{dt}(t_1)\right), \tag{78}$$

where $d\sigma/dt(t_1)$ is the cross section in the first t bin. Normalizing the cross section to the first t bin was the natural choice because for this bin the statistical error, which propagates to $(d\sigma/dt)^i_N$, is smallest.

The normalized cross section $(d\sigma/dt)_N$ in each t bin was fitted with the function inspired by the Regge phenomenology:

$$\left(\frac{d\sigma}{dt}\right)^i_N = A \cdot W^{\delta}, \tag{79}$$

where A and δ are free parameters of the fit. Fig. 51 shows the normalized cross section $(d\sigma/dt)_N$ as a function of W in five t bins together with the fit to Eq. 79. The $-t$ values quoted on the plots are the average values in the t bin considered. Only the statistical errors are plotted. The results of the fit for δ as a function of $-t$ are summarized in Tab. 18 and displayed in Fig. 52.

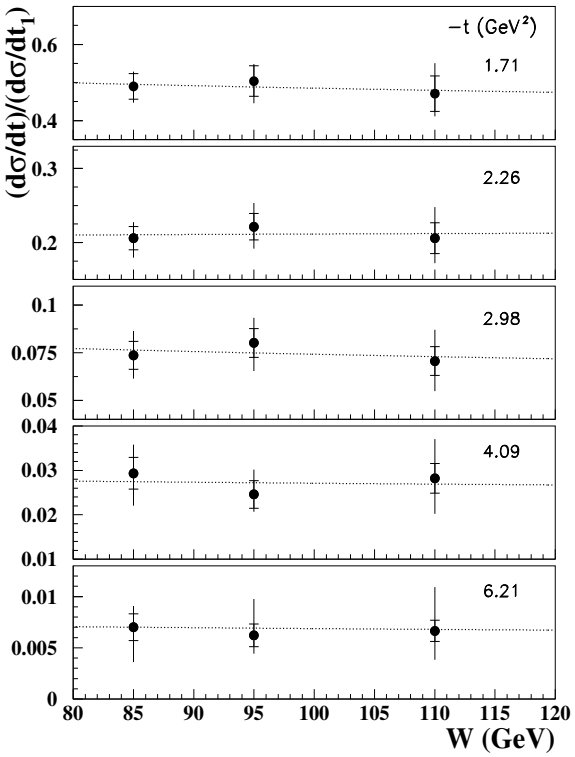

Figure 51: The measured normalized cross sections $(d\sigma/dt)_N$ as a function of W in five t bins together with the results of the fit to Eq. 79. The $-t$ values quoted on the plots are the average values in the t bin considered. The inner error bars show the statistical error, the outer ones the statistical and systematic uncertainties added in quadrature.

The uncertainties are very big but within the errors no dependence of δ on the momentum transfer is observed. The results of the analysis are consistent with $\delta = 0$ in the entire t range.

The fit of a constant function to the measured values of $\delta = -0.033 \pm 0.048$ (stat.) and is consistent with zero.

t range (GeV^2)	δ	stat. error	syst. error	χ^2/ndf
$1.5 < -t < 2.0$	-0.126	$\pm$ 0.089	+0.51 -0.24	0.2
$2.0 < -t < 2.6$	0.029	$\pm$ 0.062	+0.68 -0.29	0.5
$2.6 < -t < 3.5$	-0.179	$\pm$ 0.233	+0.47 -0.54	0.7
$3.5 < -t < 5.0$	-0.077	$\pm$ 0.222	+0.90 -0.51	1.1
$5.0 < -t < 8.5$	-0.122	$\pm$ 0.131	+1.66 -1.23	0.3

Table 18: Results of the fit of Eq. 79 to the normalized cross section $(d\sigma/dt)_N$ for different t bins.

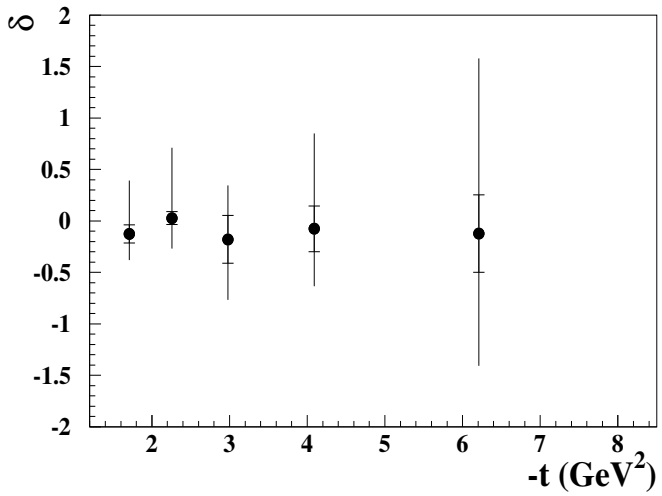

Figure 52: The parameter δ fitted to Eq. 79 as a function of the momentum transfer. The inner error bars indicate the statistical error, the outer ones the statistical and systematic uncertainties added in quadrature.

The systematic uncertainty of the cross section evaluation is strongly dominated by the modeling of the proton-dissociation. For the W bins $80 < W < 90$ GeV and $100 < W < 120$ GeV the uncertainty in the determination of the 44m tagger acceptance is biggest and causes the systematic uncertainty of 5-8%. The other check which influences the final results of the cross section evaluation on the level of 10-15% is the assumption of SCHC.

The overall normalization uncertainty of the measured cross section, originating from the checks 21 and 22, is 2.6%.

The Regge model predicts a shrinkage of the W dependence of the cross section, i.e. δ grows with increasing t. The 2-gluon exchange calculations [6] don't predict any changes of the cross section with the center-of-mass energy. The results of the measurement in the different W bins, W_1, W_2 and W_3, do not show any W-dependence within the errors and therefore support the pQCD prediction.

Tables containing tabulated values of the ρ^0 differential cross section $d\sigma/dt$ in three W bins and values of the systematic uncertainties for all applied checks can be found in Appendix A.

7.2 ϕ Photoproduction

7.2.1 Differential Cross Section $d\sigma/\mathrm{d}t$

The differential cross section $d\sigma/\mathrm{d}t$ for the diffractive proton-dissociative photoproduction of the ϕ vector meson was measured in eight t bins in the kinematic range $1.2 < -t < 6.5$ GeV^2, $80 < W < 120$ GeV and $\frac{M_Y^2}{-t} < 100$. Since the background is t-dependent (Sec. 5.7.5), it was statistically subtracted from the data. In each t bin, the background was fitted and the fraction of resonant events calculated according to:

$$C_{res}^i = 1 - BG^i, \tag{80}$$

where BG^i is the background in bin i of the momentum transfer t.

Fig. 53 shows the differential cross section $d\sigma/\mathrm{d}t$ together with the previous ZEUS 95 measurement [5]. The agreement between the new and the old results is good. The measured cross section was fitted with a power-like function (Eq. 74). The data are well described by this parameterization in the full t range. The result of the fit is $n = 2.75 \pm 0.07$ (stat.), $^{+0.20}_{-0.21}$ (syst.) with $\chi^2 = 2.1$.

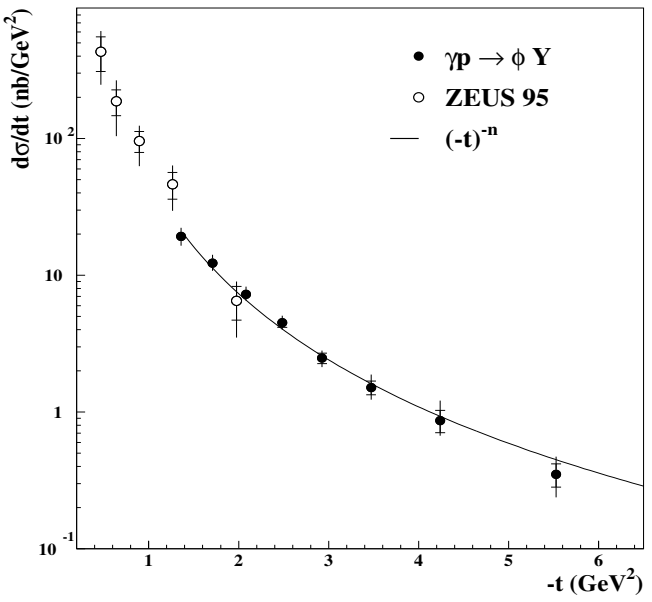

Figure 53: The differential cross section $d\sigma/\mathrm{d}t$ for the ϕ meson in the kinematic range $80 < W < 120$ GeV and $\frac{M_Y^2}{-t} < 100$ (dots). The solid line is the result of the fit to the power-like function. The inner error bars indicate the statistical error, the outer once the statistical and systematic uncertainties added in quadrature. Also shown are ZEUS results obtained for 1995.

The procedure was repeated in two restricted ranges of the momentum transfer. In each case the fit range was limited by excluding one more t bin, starting with the lowest t bin. The value of $-t_0$ corresponds to the average $-t$ value in the first bin of the fit. Tab. 19 and Fig. 54 summarize these studies. The power n increases with increasing t_0 and the χ^2 decreases but uncertainties are to big too draw any strong conclusions.

t range (GeV^2)	$n \pm$ stat.	syst.	total error	χ^2
$1.20 < -t < 6.5$	2.75 ± 0.07	+0.20 -0.21	+0.21 -0.22	2.1
$1.55 < -t < 6.5$	2.98 ± 0.11	+0.26 -0.27	+0.28 -0.29	0.4
$1.90 < -t < 6.5$	3.09 ± 0.20	+0.30 -0.34	+0.36 -0.39	0.2

Table 19: Results of the fits of the differential cross section $d\sigma/dt$ with the power-like function $A \cdot (-t)^{-n}$ in different t ranges.

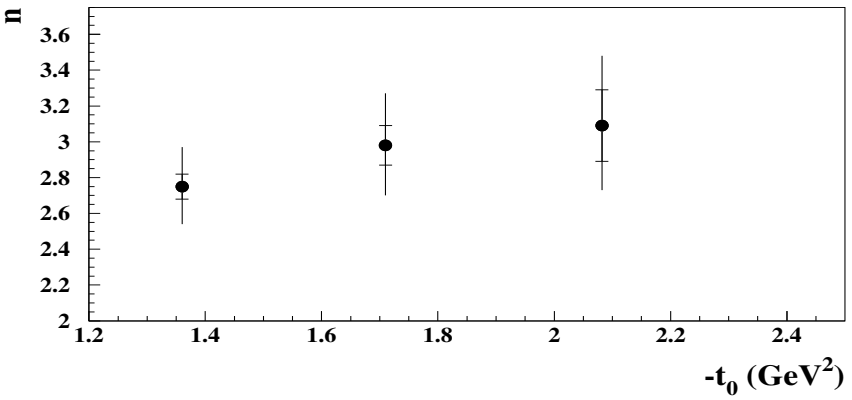

Figure 54: Changes of the power n resulting from different t ranges of the fit, as a function of the fit starting point $-t_0$, for the ϕ meson. The inner error bars show the statistical uncertainty, the outer ones the statistical and systematic errors summed in quadrature.

Since the low $-t$ data [5] start at $-t = 0.45$ GeV^2, it was checked if the power-like function (Eq. 74) describes the measured cross section $d\sigma/dt$ in the whole available t range $0.45 < -t < 6.5$ GeV^2. Therefore, the data from this analysis were combined with the ZEUS 95 results and the power-like fit was repeated. Since the measurement presented here has a much higher precision in the region where the two results overlap, only the cross section values for $-t < 1.2$ GeV^2 from 1995 were included in the fit. They correspond to the first four open circles in Fig. 53. The result of the fit to the combined measurement in the t range $0.45 < -t < 6.5$ GeV^2 is shown in Fig. 55. Only the points used in the combine fit are drawn. The power dependence describes the data well in the t range $0.45 < -t < 6.5$ GeV^2. The fit results is a power $n = 2.79 \pm 0.04$ (stat.) with $\chi^2 = 1.9$, which is in agreement with the value measured in this analysis for the t range $1.2 < -t < 6.5$ GeV^2.

The systematic uncertainty of the differential cross section $d\sigma/dt$ varies between 10-25%, increasing with increasing $-t$. See Sec. 6 for a complete list of all checks performed. The major contributions to the total systematic uncertainty come from:

a) the proton-dissociation modeling in the MC (checks 6, 8, 9a): $\sim 10 - 20\%$,

b) the uncertainty resulting from narrowing the vertex criteria (check 3c): 6%, caused by the differences in the vertex distributions for the data and the EPSOFT MC,

c) the uncertainty of the 44m tagger acceptance evaluation (check 12): 4%,

d) the uncertainty of the REMC trigger efficiency parameterization (check 14): 3 %.

The overall normalization error of the differential cross section evaluation, resulting from checks 17, 21 and 22, is equal $\pm 4\%$.

For the power-like fit to $d\sigma/dt$, the systematic error of the power n is dominated by the uncertainties coming from the proton-dissociation modeling in the EPSOFT MC (checks 6, 8, 9a, 14).

Tabulated values of the differential cross section $d\sigma/dt$ for the ϕ meson and values of the systematic uncertainties for all applied checks can be found in Appendix A.

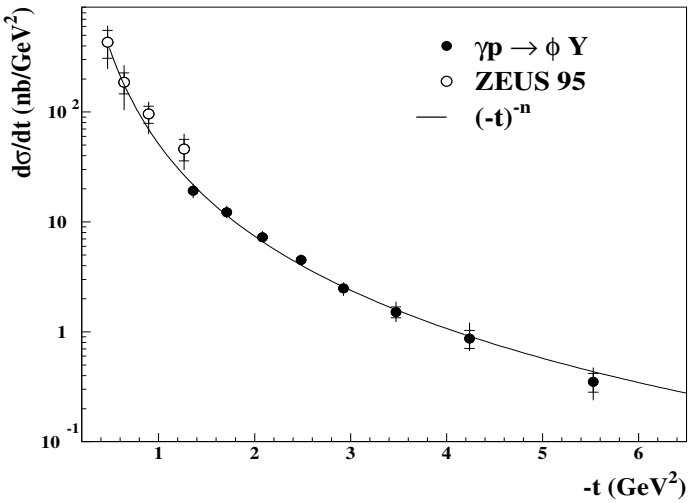

Figure 55: Power-like fit of Eq. 74 (solid line) to the combined ϕ data set including this analysis (dots) and ZEUS 1995 data (open circles). For 1995, only points included in the fit are shown.

7.2.2 W-dependence of the Cross Section

The W dependence of the cross section was studied in three W bins: $80 < W < 90$ GeV (W_1), $90 < W < 100$ GeV (W_2), $100 < W < 120$ GeV (W_3) and in the momentum transfer range $1.2 < -t < 6.5$ GeV^2. For each center-of-mass energy bin, W_1, W_2 and W_3, the whole analysis was repeated, starting from the MC reweighting procedure. The methods described in detail in Sec. 5 and 7.1.1 were used. The results of the helicity angle analysis [27], the REMC trigger studies (Sec. 5.5) and the amount of incidental coincidences (Sec. 4.2.2) were assumed to be independent of W.

M_Y Evolution with t in W bins. The parameterization of β of the proton-dissociative energy distribution of Eq. 55 was found to depend on W, as was the case for the ρ^0 meson. Due to the limited statistics, β could be studied only in three t bins in every W bin. Fig. 56 shows the values of β in different t bins for each W range. For comparison, the β parameters obtained for ρ^0 in the same W bins are also shown. Within the errors, the results for ϕ and ρ^0 are in agreement in all W ranges. Since the ρ^0 parameterization has better accuracy and the data are not in contradiction with a universal β (factorization) also for different W bins, the nominal β parameterization was taken from the ρ^0 analysis. The results for the ϕ meson were parameterized:

$$\beta_1 \;=\; 0.41 \pm 0.16, \quad \text{for} \quad W_1 \tag{81}$$

$$\beta_2 = 0.89 \pm 0.18, \quad \text{for } W_2 \tag{82}$$
$$\beta_3 = 0.54 \pm 0.17, \quad \text{for } W_3 \tag{83}$$

and used as systematic checks for the cross section calculation.

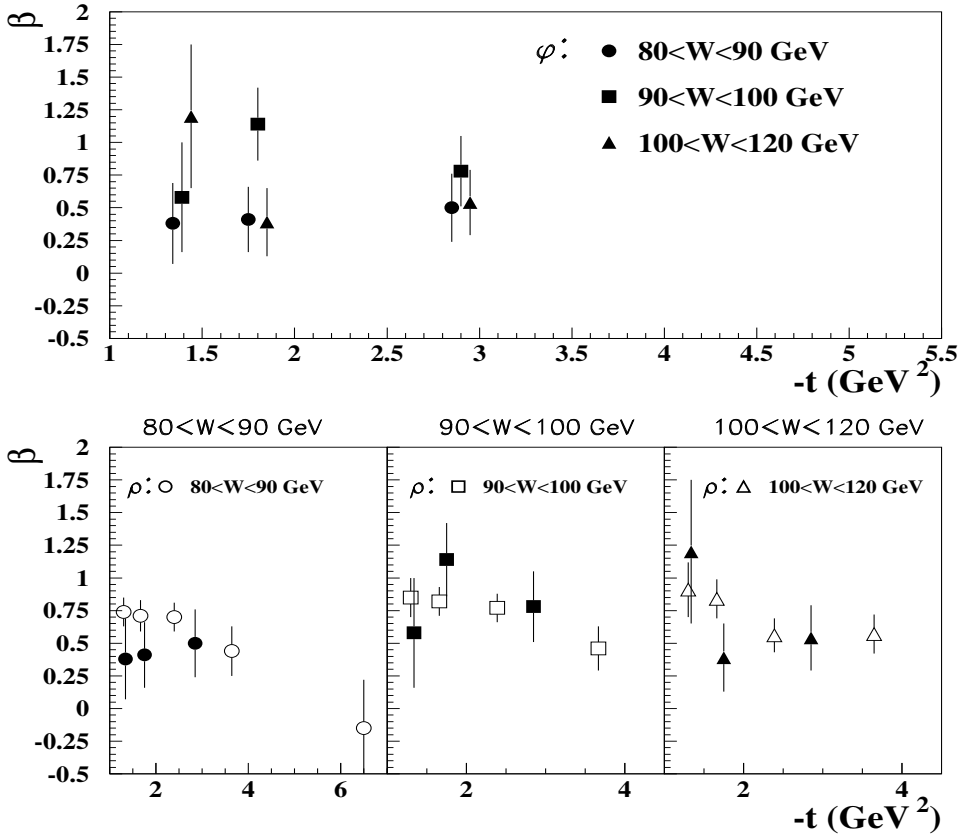

Figure 56: Results of the study of the β parameter in the generated M_Y distribution (Eq. 55) as a function of $-t$ for three W bins. Full circles, squares and triangles on the upper plot correspond to the ϕ meson and W ranges $80 < W < 90$ GeV, $90 < W < 100$ GeV and $100 < W < 120$ GeV, respectively. For displaying reasons, the points for W_2 and W_3 they were shifted by 0.05 and 0.1 GeV^2, respectively. The lower plot shows the comparison between the β values as a function of $-t$ for ϕ (full symbols) and ρ^0 (empty symbols) in three W ranges W_1, W_2 and W_3.

Mass Distributions in W bins. The background under the ϕ mass peak was found to increase with increasing W. Therefore the W-dependence of the background had to be taken into account for the EPSOFT MC reweighting procedure. Due to the statistical limitations when binning also in W, the background could not be calculated in the same t bins, in which the differential cross section$d\sigma/dt$ was evaluated in Sec. 7.2.1. Therefore, the background was fitted in three t bins per W region. Results were parameterized as a function of t for each W bin and these parameterizations were used in the reweighting procedure of the EPSOFT MC. Tab. 20 summarizes the studies of the ϕ mass distribution in three W bins.

$80 < W < 90$ GeV				
t range (GeV^2)	$\langle t \rangle$ (GeV^2)	background (%)	resolution (MeV)	χ^2/NDF
1.2 - 1.5	1.34	16.8 $\pm$ 2.5	0.050 $\pm$ 0.027	1.8
1.5 - 2.1	1.72	11.6 $\pm$ 2.0	0.092 $\pm$ 0.032	1.4
2.1 - 6.5	2.77	8.8 $\pm$ 2.5	0.134 $\pm$ 0.048	1.7
background parameterization :		$BG = \exp(-1.23(\pm 0.11) - 0.47(\pm 0.06) \cdot (-t))$		
$90 < W < 100$ GeV				
t range (GeV^2)	$\langle t \rangle$ (GeV^2)	background (%)	resolution (MeV)	χ^2/NDF
1.2 - 1.5	1.34	22.4 $\pm$ 3.8	0.030 $\pm$ 0.029	0.3
1.5 - 2.1	1.74	21.7 $\pm$ 2.8	0.083 $\pm$ 0.034	0.6
2.1 - 6.5	2.89	15.8 $\pm$ 2.7	0.079 $\pm$ 0.046	1.5
background parameterization :		$BG = \exp(-1.14(\pm 0.09) - 0.24(\pm 0.04) \cdot (-t))$		
$100 < W < 120$ GeV				
t range (GeV^2)	$\langle t \rangle$ (GeV^2)	background (%)	resolution (MeV)	χ^2/NDF
1.2 - 1.6	1.41	28.7 $\pm$ 3.6	0.117 $\pm$ 0.043	1.3
1.6 - 2.3	1.93	22.0 $\pm$ 3.3	0.073 $\pm$ 0.037	1.4
2.3 - 6.5	3.22	19.6 $\pm$ 3.4	0.032 $\pm$ 0.036	2.2
background parameterization :		$BG = \exp(-1.03(\pm 0.08) - 0.20(\pm 0.04) \cdot (-t))$		

Table 20: Results of the fits to the two-kaon invariant mass spectra for the ϕ meson in three W bins and three $-t$ bins, together with the background parameterization as a function of t for each W range. The fits were performed in the mass range $0.99 < M_{KK} < 1.14$ GeV and the background was evaluated in the mass window $0.99 < M_{KK} < 1.06$ GeV. The values of M_ϕ and Γ_ϕ were fixed to the DPG values (Tab. 6). Only statistical errors are shown.

Separating of Elastic and Proton-dissociative Events in W bins. As discussed in Sec. 5.7.3, the analyzed data sample consists of proton-dissociative events, except the low t bins, $-t \lesssim 2.5$ GeV^2, where a contamination of elastic events was observed. Therefore the amount of the elastic admixture was studied in three W bins used to calculate the differential cross section. Fig. 57 shows the comparison of the ratio of the number of events tagged in the PRT to all events for data and the proton dissociative EPSOFT MC in three W bins. The overall agreement is good, except for the low t bins where the data have a contamination from elastic events. Within the errors, there is no significant dependence on W. As for the results obtained for the full W range, no PRT tag was used to select proton-dissociative events. Instead, the data were corrected for the elastic admixture to obtain the final results. In the first W bin the correction was applied in the lowest two t bins, in the middle and last W bins only the first t bin was corrected.

Differential Cross Section $d\sigma/dt$ in W bins. In each of the W bins W_1, W_2 and W_3, the differential cross section $d\sigma/dt$ was determined in five $-t$ bins for $\frac{M_Y^2}{-t} < 100$. In Fig. 58 the cross section measured in the three W bins, together with the curve obtained as a fit to the power-like function (Eq. 74), is compared with $d\sigma/dt$ calculated in the entire W range.

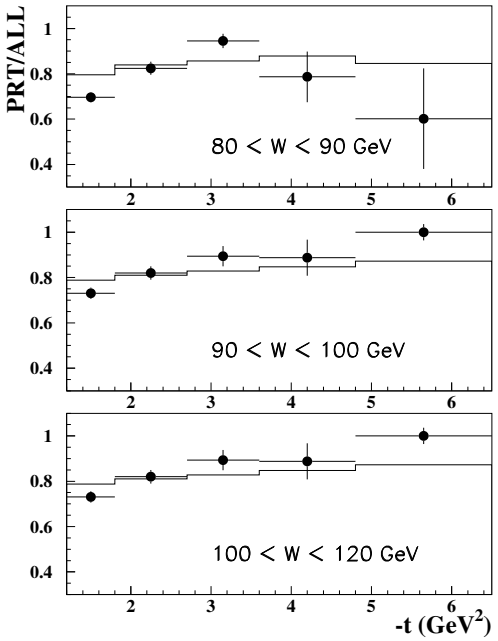

Figure 57: The ratio of events tagged in the PRT to all events for the ϕ data (dots) and the proton-dissociative EPSOFT MC (histogram) in three W bins of $80 < W < 90$ GeV, $90 < W < 100$ GeV and $100 < W < 120$ GeV.

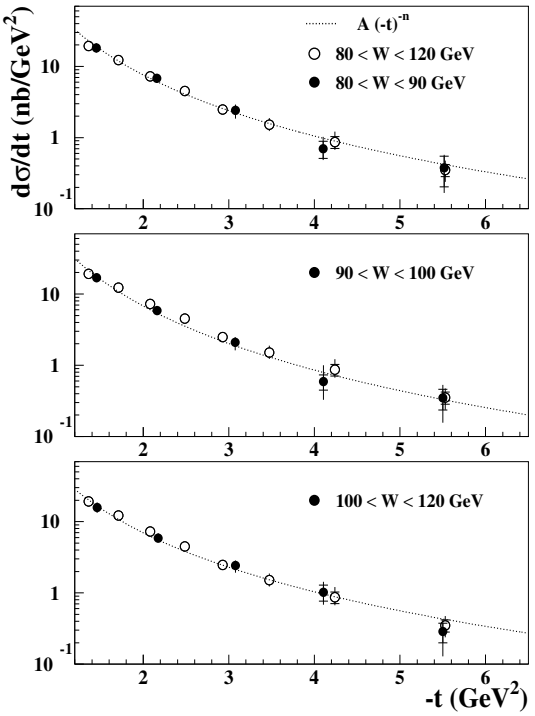

Figure 58: The differential cross sections $d\sigma/dt$ for the ϕ meson in the three W bins of $80 < W < 90$ GeV, $90 < W < 100$ GeV and $100 < W < 120$ GeV for $\frac{M_V^2}{-t} < 100$ (dots), together with the result of the fit to the power-like function (Eq. 74) (dotted line) compared with the cross section measured in the full W range (open circles). The inner error bars show the statistical error, the outer ones the statistical and systematic uncertainties added in quadrature.

The normalization of the measurement for different center-of-mass energy bins agrees with the data in the full W range. The cross sections are well described by the fit to Eq. 74. The results of the power-like fit are summarized in Tab. 21. Within the errors, no W dependence of the power n is observed and the values obtained in each W bin agree with n fitted to the full data sample with $80 < W < 120$ GeV. As expected from pQCD predictions with the two-gluon exchange [6], the global shape of the t distribution does not depend on center-of-mass energy.

W range (GeV)	power n	stat. error	syst. error	χ^2/ndf
$80 < W < 90$	2.85	$\pm$ 0.14	+0.22 –0.17	1.5
$90 < W < 100$	2.99	$\pm$ 0.14	+0.29 –0.28	1.3
$100 < W < 120$	2.75	$\pm$ 0.14	+0.32 –0.21	1.6

Table 21: Results of the power-like fit of Eq. 74 to the differential cross section $d\sigma/dt$ in the three W bins.

Fig. 59 shows the normalized cross section $(d\sigma/dt)_N$ (Eq. 78, Sec. 7.1.2) as a function of W in five t bins together with the fit to Eq. 79. The $-t$ values quoted on the plots are the average values in the t bin considered. Only the statistical errors are plotted. The results of the fit for δ as a function of $-t$ are summarized in Tab. 22 and displayed in Fig. 60. Within the total error the results of the analysis are consistent with $\delta = 0$ except for the δ value at $-t = 4.1$ GeV^2. For this point the difference is on the level of 2σ.

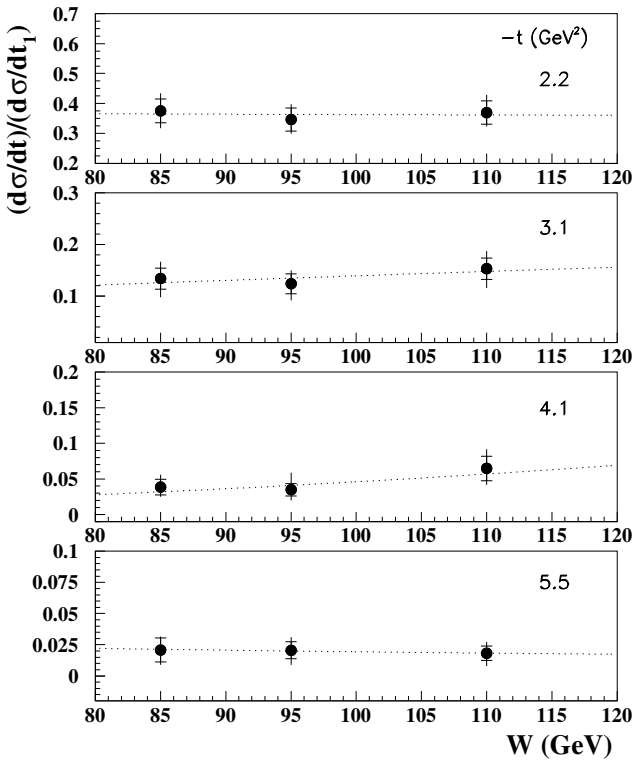

Figure 59: The measured normalized cross sections $(d\sigma/dt)_N$ for ϕ as a function of W in four t bins together with the results of the fit to Eq. 79. The $-t$ values quoted on the plots are the average values in the t bin considered. The inner error bars indicate the statistical error, the outer ones the statistical and systematic uncertainties added in quadrature.

t range (GeV^2)	δ	stat. error	syst. error	χ^2/ndf
$1.8 < -t < 2.7$	-0.01	$\pm$ 0.11	+0.60 –0.14	0.5
$2.7 < -t < 3.6$	0.62	$\pm$ 0.29	+0.69 –0.47	0.8
$3.6 < -t < 4.8$	2.21	$\pm$ 0.53	+1.29 –0.25	1.0
$4.8 < -t < 6.5$	-0.54	$\pm$ 0.70	+1.28 –1.50	0.3

Table 22: Results of the fit of Eq. 79 to the normalized cross section $(d\sigma/dt)_N$ of the ϕ meson for different t bins.

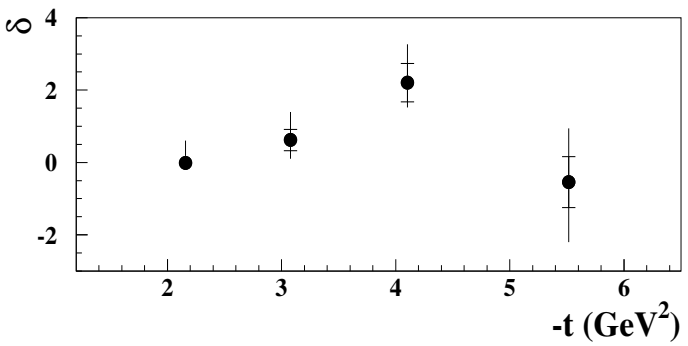

Figure 60: The parameter δ for the ϕ meson fitted to Eq. 79 as a function of the momentum transfer. The inner error bars indicate the statistical error, the outer ones the statistical and systematic uncertainties added in quadrature.

The systematic uncertainty of the cross section calculation in different W ranges is strongly dominated by the modeling of the proton-dissociation and by the uncertainty in the 44m tagger acceptance, especially for W_1 and W_3 bins. For $80 < W < 90$ GeV and $100 < W < 120$ GeV the acceptance of the 44m tagger has big systematic uncertainty, which results in the systematic error of the cross section calculations of 5 and 10% for W_1 and W_2, respectively. The overall normalization error of the differential cross section evaluation, originating from checks 21 and 22, is equal $\pm$2.6%.

Tables containing tabulated values of the ϕ differential cross section $d\sigma/dt$ in three W bins and values of the systematic uncertainties for all applied checks can be found in Appendix A.

7.3 J/ψ Photoproduction

7.3.1 Differential Cross Section $d\sigma/dt$

The differential cross section $d\sigma/dt$ for the diffractive proton-dissociated photoproduction of the J/ψ vector meson in the kinematic range $1.2 < -t < 6.5$ GeV^2 $80 < W < 120$ GeV and $\frac{M_Y^2}{-t} < 100$ was calculated using Eq. 45. Since the non-resonant background under the mass peak does not depend on the momentum transfer (Sec. 5.7.6), the fraction of resonant events C_{res} for every $-t$ bin i was determined according to the equation:

$$C_{res}^i = 1 - bg,$$

where bg corresponds to the background fitted in the full $-t$ range ($bg = 9.8 \pm 0.7$).

Fig. 61 displays the measured differential cross section $d\sigma/dt$ of J/ψ meson photoproduction in six $-t$ bins together with the previous ZEUS 95 data for lower $-t$. The agreement between the low $-t$ results and the results obtained in this analysis is good, however the errors of the earlier measurement are large. The solid line shows a power-like function (Eq. 74) fitted to the measured cross section. The fit describes the data well in the entire range of the momentum transfer and yields $n = 1.8 \pm 0.2$ (stat.) ± 0.2 (syst.) with $\chi^2 = 0.1$.

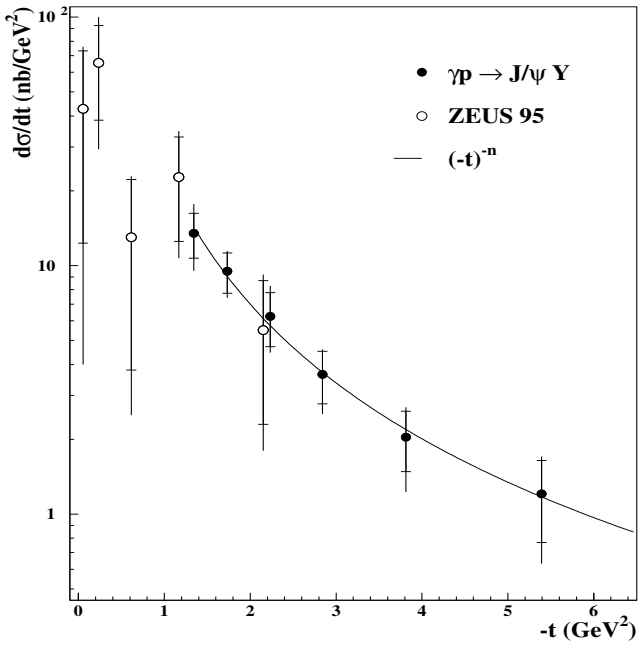

Figure 61: The differential cross section $d\sigma/dt$ for the process $\gamma p \to J/\psi Y$ in the kinematic range $80 < W < 120$ GeV and $\frac{M_Y^2}{-t} < 100$. The full points represent results from this analysis, open dots show the result of the ZEUS 95 high $-t$ measurement. The solid line corresponds to the power-like fit according to Eq. 74. The inner error bars show the statistical error, the outer once the statistical and systematic uncertainties added in quadrature.

The systematic uncertainty on the differential cross section $d\sigma/dt$ is $\sim 20\%$ and is on the level of the statistical errors. The systematic uncertainty is dominated by

a) errors connected to the proton-dissociation modeling in the MC (checks 6, 8, 9): 10-15%,

b) errors resulting from changing the invariant mass window in the event selection (check 7): $\sim 10\%$,

c) the uncertainty of the 44m tagger acceptance (check 12): 5%.

The error resulting from the global normalization (checks 18, 20, 21) is $\sim 3\%$. Due to the small number of events, for some checks in single bins the systematic uncertainty can fluctuate and be $> 3\%$. However, in most cases the systematic error is less then 3%.

The systematic error of the power n comes mostly from the parameterization of $\beta(t)$, varying the invariant mass window in the selection cuts and changing the maximum energy in the calorimeter not associated with the tracks.

Tabulated values of the J/ψ differential cross section $d\sigma/dt$ and values of the systematic uncertainties for all applied checks can be found in Appendix A.

For all three vector mesons, ρ^0,ϕ and J/ψ, the power-like function (Eq. 74) fitted to the measured cross section $d\sigma/dt$ describes the data well. Tab. 23 summarizes the values of the power n for ρ^0,ϕ and J/ψ in the restricted t range for all three mesons. The power differs significantly between different vector mesons, decreasing with the increasing mass of the meson. The result is shown in Fig. 62.

meson	VM mass (GeV)	t range (GeV^2)	$n \pm$ stat.	total error
ρ^0	0.769	$1.2 < -t < 6.85$	3.20 ± 0.04	+0.17 -0.16
ϕ	1.019	$1.2 < -t < 6.5$	2.75 ± 0.07	+0.21 -0.22
J/ψ	3.097	$1.2 < -t < 6.5$	1.8 ± 0.2	± 0.3

Table 23: The results of the fit to the measured cross section $d\sigma/dt$ with the power-like function of Eq. 74 for three vector mesons in the same t ranges, $1.2 < -t < 6.85$ GeV^2, $1.2 < -t < 6.5$ GeV^2 and $1.2 < -t < 6.5$ GeV^2, for ρ^0,ϕ and J/ψ, respectively.

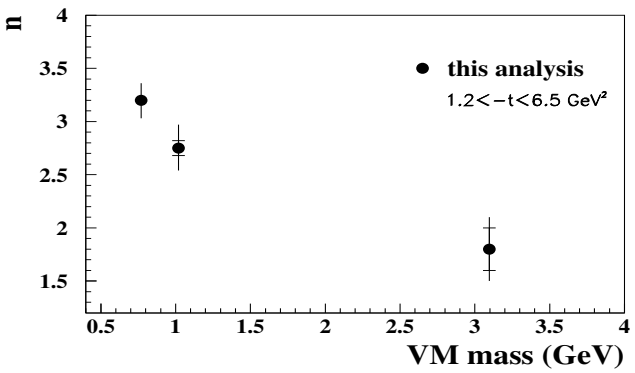

Figure 62: The power n from the fit of $d\sigma/dt$ to power-like function (Eq. 74) (dots) as a function of the vector meson mass. The fits were performed in the similar t range for all three vector mesons, $1.2 < -t < 6.85$ GeV^2, $1.2 < -t < 6.5$ GeV^2 and $1.2 < -t < 6.5$ GeV^2, for ρ^0,ϕ and J/ψ, respectively. The inner error bars indicate the statistical error, the outer once the statistical and systematic uncertainties added in quadrature.

7.3.2 W-dependence of the Cross Section

The differential cross section $d\sigma/dt$ in different W regions was determined employing the procedure used to extract the cross section for the entire W range. Since the J/ψ sample has only a small number of events, the following restrictions were imposed on the analysis:

- the analysis was performed in two W bins:
  $W_1: \quad 80 \quad < \quad W \quad < \quad 100 \quad \text{GeV}$
  $W_2: \quad 100 \quad < \quad W \quad < \quad 120 \quad \text{GeV},$
  chosen so to have an equal number of events in both bins;
- a study of the energy distribution in the FCAL was not possible,due to the statistical limitations, so that the β parameterization was assumed to be the same as for the entire W region (Eq. 59);
- the measurement of the cross section was performed in four bins for the momentum transfer between $1.2 < -t < 5$ GeV^2.

The J/ψ Monte Carlo was reweighted as described in Sec. 5.7.6.

Mass Distribution in W bins. The measured two electron invariant mass distributions were fitted in the full t range, assuming that the non-resonant background is t-independent. Fig. 63 shows the two electron invariant mass spectra in two W bins. The solid curve represents the results of the fit, the dashed line indicates the non-resonant background. The results of the fit are summarized in Tab. 24. The values obtained for $M_{J/\psi}$ are in agreement with the PDG. There is no significant difference in the fit results between the two W ranges, however the lower W bin have a bigger background, estimated with a large uncertainty.

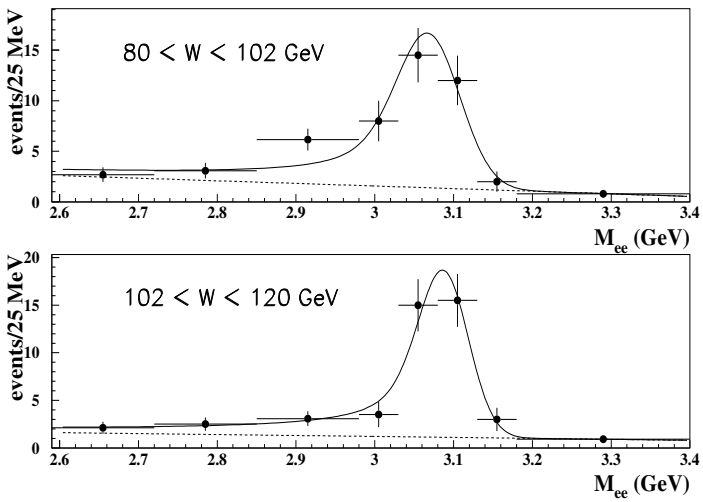

Figure 63: The two electron invariant mass distributions for the J/ψ meson in two W regions: $80 < W < 100$ GeV and $100 < W < 120$ GeV. The solid line is the result of the fit to the sum of the Gaussian (muon decay channel) and the bremsstrahlung function convoluted with the Gaussian (electron channel) with equal weights over the linear background. The dashed line shows fitted non-resonant background.

W range (GeV)	$M_{J/\psi}$ (MeV)	resolution (MeV)	backg. (%)	χ^2/NDF
$80 < W < 100$	3084 ± 6	24 ± 7	13.4 ± 7.6	0.5
$100 < W < 120$	3092 ± 5	26 ± 7	7.1 ± 0.8	0.1

Table 24: The results of the fit to the two electron invariant mass spectra for the J/ψ meson for two W bins. In each case the fit range was $2.6 < M_{ee} < 3.4$ GeV. The background fraction was calculated in the region $2.98 < M_{ee} < 3.13$ GeV. Quoted errors are the statistical uncertainties only.

Differential Cross Section $d\sigma/dt$ in W bins. Fig. 64 shows the comparison between the differential cross sections $d\sigma/dt$ in the entire center-of-mass energy region and in the two W ranges, W_1 and W_2, together with the results of a power-like function (Eq. 74). Since within the errors the PRT ratio for data and MC were in agreement, no correction due to elastic contamination was applied to the measured cross sections. The differential cross sections, as well as the results of the power-like fit, for the W regions $80 < W < 100$ GeV and $100 < W < 120$ GeV are consistent with the measurement in the full W range. They are summarized in Tab. 25. Within the errors the measured cross section does not show any W-dependence.

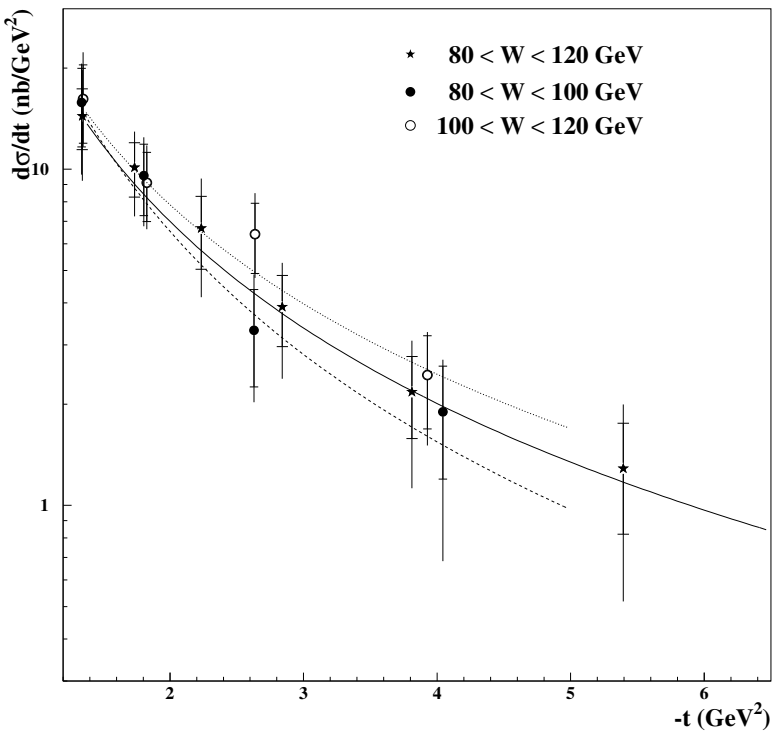

Figure 64: The comparison of the differential cross section $d\sigma/dt$ for the process $\gamma p \to J/\psi Y$ in the three kinematic ranges $80 < W < 100$ GeV (dots), $100 < W < 120$ GeV (open circles) and the entire W region of $80 < W < 120$ GeV (stars). The solid line corresponds to the power-like fit according to Eq. 74 for the full W range, the dashed and dotted lines indicate the same fit in the W range $80 < W < 100$ GeV and $100 < W < 120$ GeV, respectively. The inner error bars indicate the statistical error, the outer ones the statistical and systematic uncertainties added in quadrature.

W range (GeV)	n ($\pm$ tot.)	stat. error	syst. error	χ^2/NDF
$80 < W < 120$	1.8 ± 0.3	$\pm$ 0.2	± 0.2	0.1
$80 < W < 100$	$2.1^{+0.6}_{-0.5}$	$\pm$ 0.4	$^{+0.5}_{-0.3}$	0.3
$100 < W < 120$	$1.7^{+0.5}_{-0.4}$	$\pm$ 0.4	$^{+0.3}_{-0.1}$	0.4

Table 25: The results of the power-like fit of Eq. 74 to the differential cross sections $d\sigma/dt$ in the whole W range $80 < W < 120$ GeV (Sec. 7.3.1) and in the two W bins of $80 < W < 100$ GeV and $100 < W < 120$ GeV (Sec. 7.3.2).

For both W ranges, $80 < W < 100$ GeV and $100 < W < 120$ GeV, the systematic uncertainty of the cross section calculation is $\sim 20\%$ and is of the order of the statistical errors.

For $80 < W < 100$ GeV the main sources of the systematic uncertainty are:

a) varying the invariant mass range used in the analysis (check 7): 15%,

b) changing the cuts for the p_t of the track (check 2): $\sim 10\%$,

c) uncertainty of the β parameterization (checks 6, 8, 9): $\sim 5\%$, except for the last two t bins, where this uncertainty is 16 and 48%, respectively,

d) and the uncertainty of the 44m tagger acceptance evaluation (check 12): 3%.

The overall acceptance uncertainty resulting from checks 19-20 is 9%, mostly due to the big error of the background estimation.

For $100 < W < 120$ GeV the main sources of the systematic uncertainty are:

a) uncertainty of the β parameterization (checks 6, 8, 9): $\sim 5 - 20\%$,

b) varying the invariant mass range used in the analysis (check 7): 5-10%,

c) and the uncertainty of the 44m tagger acceptance evaluation (check 12): 8%.

The uncertainty originating from the estimation of the 44m tagger is greater for the second W bin due to the 44m tagger acceptance shape and its systematic uncertainty (Fig. 24, Sec. 5.6). The overall acceptance uncertainty resulting from checks 19-20 is 3%. For other checks caused by the limited statistics, the systematic uncertainty is usually below 3%.

The systematic uncertainty of the power n for both W bins is dominated by the uncertainty of the proton-dissociation modeling (checks 6, 8, 9), varying the invariant mass range used in the analysis (check 7) and changing the cuts for the calculation of the maximal energy in the calorimeter not associated with the tracks (checks 4 and 5).

Tabulated values of the J/ψ differential cross section $d\sigma/dt$ in two W bins and values of the systematic uncertainties for all applied checks can be found in Appendix A.

7.4 Cross Sections Ratios

Under three assumptions the cross section ratios of the ρ^0, ω,ϕ and J/ψ mesons is predicted to behave as $9:1:2:8$. These assumptions are natural for hard processes: 1) the photon fluctuates into a $q\bar{q}$ par, 2) a vector meson quark composition is described by SU(3) or SU(4) symmetries (for ρ^0,ϕ and J/ψ, respectively) and 3) flavor independent production mechanism is present. Therefore, the expectations for the cross section rations $\frac{d\sigma}{dt}(\gamma p \to \phi N)/\frac{d\sigma}{dt}(\gamma p \to \rho^0 N)$ and $\frac{d\sigma}{dt}(\gamma p \to J/\psi N)/\frac{d\sigma}{dt}(\gamma p \to \rho^0 N)$ (in the following denoted ϕ/ρ and ψ/ρ) are 2/9 and 8/9,respectively. This chapter presents the results of this measurement.

The ratios of the differential cross section ϕ/ρ and ψ/ρ were calculated in the kinematic range $1.2 < -t < 6.5$ GeV^2, $80 < W < 120$ GeV and $\frac{M_V^2}{-t} < 100$ in eight and six t bins, respectively. To obtain the ratios ϕ/ρ and ψ/ρ, the cross sections for ρ^0 and ϕ and for ρ^0 and J/ψ were calculated in the same t bins and then divided. The mean $-t$ values, $\langle t \rangle$, are similar for different vector mesons with differences up to $\Delta \simeq 0.01$ GeV^2. Therefore the results for the cross sections ratios are measured for a particular $-t$ bin and not for the mean $-t$ value in this bin. For display purposes, the cross sections ratios are plotted at $\langle t \rangle$ obtained for the ρ^0 meson. Since for all three vector mesons, the power-like function (Eq. 74) describes the data well in the entire $-t$ range, the results of the fits were used to obtain the so called 'fitted ratios'. They are a result of dividing the power-like functions fitted to the differential cross sections $d\sigma/dt$ for ϕ/ρ and ψ/ρ ratios, respectively.

Fig. 65 shows the measured cross section ratios ϕ/ρ and ψ/ρ, the 'fitted ratios' for this analysis and previous ZEUS results [5]. The shaded bands correspond to the errors of the cross section fits.

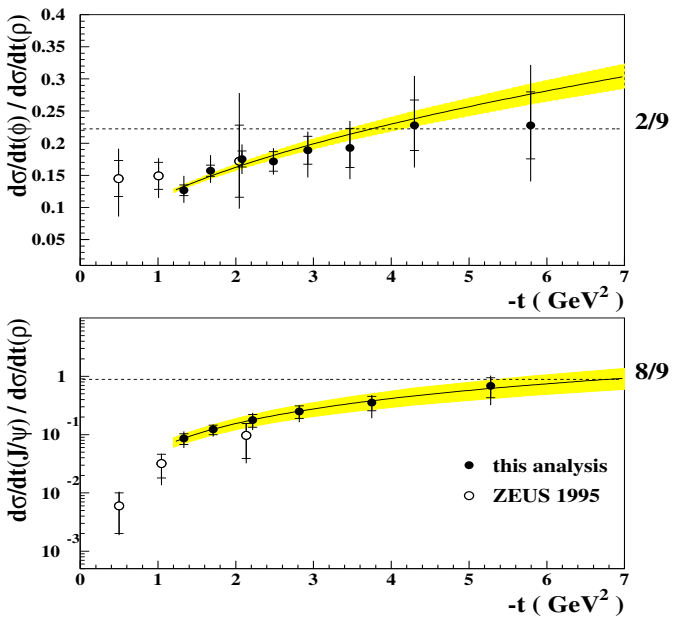

Figure 65: The ratios of the cross sections $d\sigma/dt$ for ϕ to ρ^0 (top) and J/ψ to ρ^0 (bottom) for this measurement (dots) and the low $-t$ data (open circles) together with the 'fitted ratios' (solid line) obtained by dividing the results of the fit to the power-like function (Eq. 74). The shaded bands show the uncertainties of the fits to the cross sections. The dashed lines correspond to the SU(4) predictions. The inner error bars indicate the statistical error, the outer bars the statistical and systematic uncertainties added in quadrature.

The low and high t data match well. A rise of the ϕ/ρ ratio up to $-t \approx 4$ GeV^2 is observed, where it approaches the SU(3) value of 2/9. The 'fitted ratios' also show a rise with increasing $-t$ but they indicate that the ϕ/ρ ratio might not saturate at the SU(3) value but keeps growing. A clear increase of the ψ/ρ ratio with increasing $-t$ is observed and the ratio approaches within the errors the SU(4) value of 8:9 for $t \simeq 5.4$ GeV^2. The 'fitted ratio' confirms this observation, indicating the agreement with the flavor independent production mechanism for J/ψ photoproduction at high $-t$.
Tabulated values of the cross section ratios and their uncertainties can be found in Appendix A. The biggest uncertainty for ϕ/ρ and ψ/ρ originates from the proton-dissociation modeling: $\sim 5-20\%$ for both ratios.

It is interesting to compare the t and Q^2 dependences of the cross section ratios for vector meson production. Fig. 66 shows the results from Fig. 65 as a function of $-t$ together with measurements of the cross section ratios as a function of Q^2 obtained by the ZEUS and H1 Collaborations [63]. At large Q^2, the ϕ/ρ^0 ratio approaches the SU(3) value for $Q^2 \geq 7$ GeV^2, while in photoproduction it does so already for $-t > 4$ GeV^2. For $-t \approx Q^2 \approx 3.5$ GeV^2, the ψ/ρ^0 ratios are significantly smaller than the SU(4) prediction and the photoproduction ratio is a factor of five larger than for DIS. Since the cross section ratios grow faster with $-t$ than with Q^2, it is implied that $-t$ and Q^2 cannot be treated as equivalent scales.

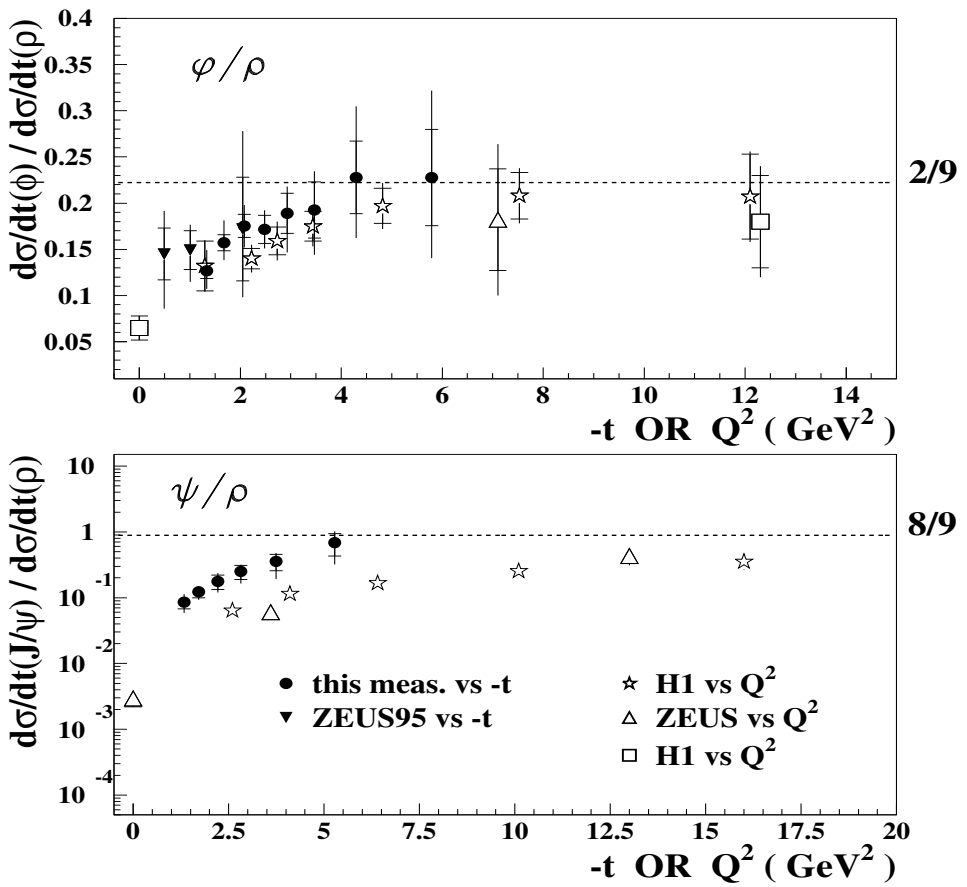

Figure 66: The ratios of the cross sections $d\sigma/dt$ for ϕ to ρ^0 (top) and J/ψ to ρ^0 (bottom) for this measurement (dots) and low $-t$ data (triangles) as a function of $-t$ together with the results of measurements as a function of Q^2 (open symbols). The inner error bars show the statistical error, the outer bars the statistical and systematic uncertainties added in quadrature.

An attempt to establish a linear relationship between the $-t$ and Q^2 was done. The most accurate measurement of the cross section ratio [63] as a function of Q^2 (open stars in Fig. 66) were fitted using the parameterization:

$$\mathcal{R} = A \cdot log(B \cdot Q^2), \tag{84}$$

where A and B were parameters of the fit and $\mathcal{R}$ denotes the cross section ratios ϕ/ρ and ψ/ρ. The results of the fit are shown in Fig. 67 for ϕ/ρ and ψ/ρ are summarized in Tab. 26. For the fitting procedure only the statistical errors of the ratios were taken into account.

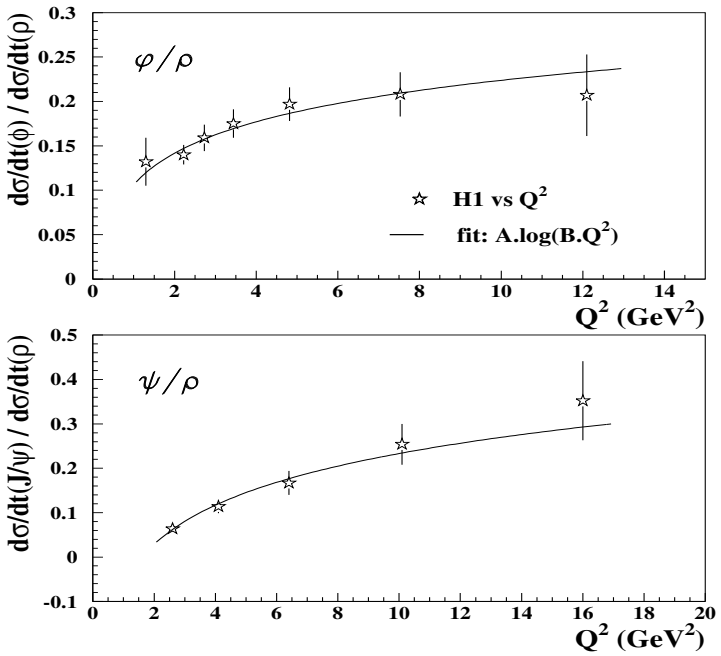

Figure 67: The results of the fit of Eq. 84 (solid line) to the cross section ratios ϕ/ρ (top) and ψ/ρ (bottom) as a function of Q^2. Only the statistical errors are shown.

$A \cdot log(B \cdot Q^2)$	ϕ/ρ	ψ/ρ
A	0.051 ± 0.003	0.127 ± 0.009
B	8.04 ± 1.04	0.627 ± 0.033
χ^2/NDF	0.3	0.3

Table 26: The results of the fit of Eq. 84 to the cross section ratios ϕ/ρ and ψ/ρ as a function of Q^2. Only the statistical errors are quoted.

The results of the fits were used to estimate the scale $\mathcal{S}$ between $-t$ and Q^2 using the minimal χ^2 method. The χ^2 function for each cross section ratio was defined as:

$$\chi^2(\mathcal{S}) = \sum_i \frac{(\mathcal{R}_i^t - \mathcal{R}_i(\mathcal{S}))^2}{\sigma_i}, \tag{85}$$

where the sum runs over all t bins, $\mathcal{R}_i^t$ is value of the cross section ratio measured in this analysis in bin i with an average t of $\langle t \rangle$, and $\mathcal{R}_i(\mathcal{S})$ is the value of Eq. 84 for $Q^2 = \mathcal{S} \cdot \langle t \rangle$. σ_i is the error assigned to bin i and was calculated according to:

$$\sigma_i^2 = \left(\sigma_t^i\right)^2 + \left(\sigma_{Q^2}^i\right)^2 ,$$

where σ_t^i is the statistical uncertainty of the cross section ratio evaluated in this analysis and $\sigma_{Q^2}^i$ is obtained from errors on the fit parameters (Tab. 26). The value of $\mathcal{S}$ for which χ^2 is minimal determines the linear correspondence between the two scales t and Q^2. The minimizing of χ^2 (Eq. 85) yields a values of $\mathcal{S}$ equal 1.47 ± 0.21 and 2.58 ± 0.31 for ϕ/ρ and ψ/ρ, respectively. The errors on $\mathcal{S}$ correspond to one standard deviation. The values of $\mathcal{S}$ for ϕ/ρ and ψ/ρ differ significantly, the scaling factor of t needed for the ψ/ρ ratio is much bigger than the one for the ϕ/ρ ratio and therefore there is no simple universal linear relationship between t and Q^2.

Fig. 68 shows a comparison of the cross section ratios ϕ/ρ and ψ/ρ as a function of Q^2 and as a function of scaled t, $t_S = \mathcal{S} \cdot \langle t \rangle$, as measured in this analysis. The values of $\mathcal{S}$ derived above were used. The agreement between the measurements as a function of Q^2 and t_S is satisfactory, as expected from the minimal χ^2 method.

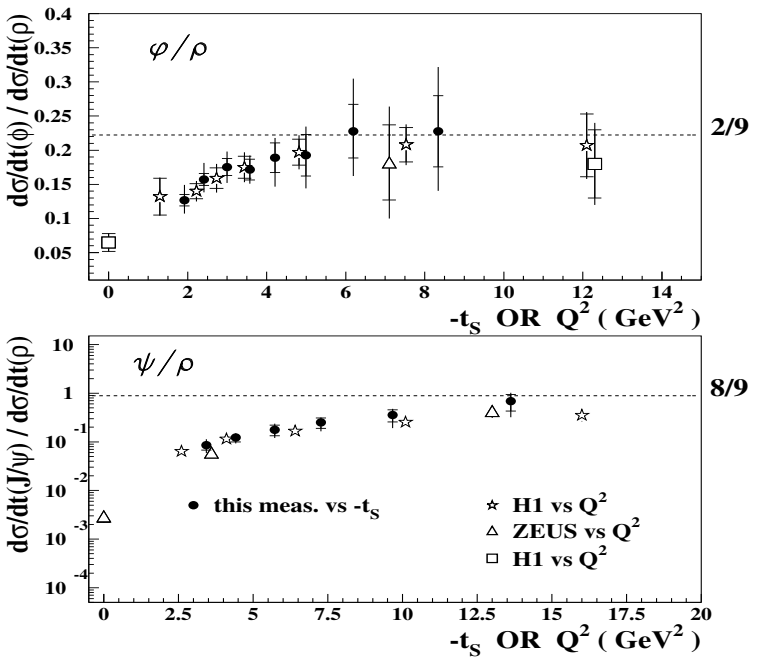

Figure 68: The ratios of the cross sections $d\sigma/dt$ for ϕ to ρ^0 (top) and J/ψ to ρ^0 (bottom) for this measurement (dots) as a function of $t_S = t \cdot \mathcal{S}$ together with the results of measurements as a function of Q^2 (open symbols). The inner error bars show the statistical error, the outer bars the statistical and systematic uncertainties added in quadrature.

8 Comparison of the Results with Theoretical Predictions

This chapter gives s brief description of two theoretical pQCD models that try to predict cross sections and helicity matrix elements for the high $-t$ vector meson photoproduction. The theoretical calculations are compared to the results of this analysis.

8.1 Light Vector Mesons

The precise description of a new QCD mechanism of the light vector meson photoproduction at large $-t$ is presented in [6]. The studied process

$$\gamma p \to V + Y, \tag{86}$$

where V is a vector meson and Y denotes the products of the proton dissociation, is depicted in Fig. 69. The interaction of the Pomeron with the vector meson is treated as a two-gluon exchange, where the gluons couple to a single parton in the proton. Soft interactions of the vector meson and system Y in the final state are neglected.

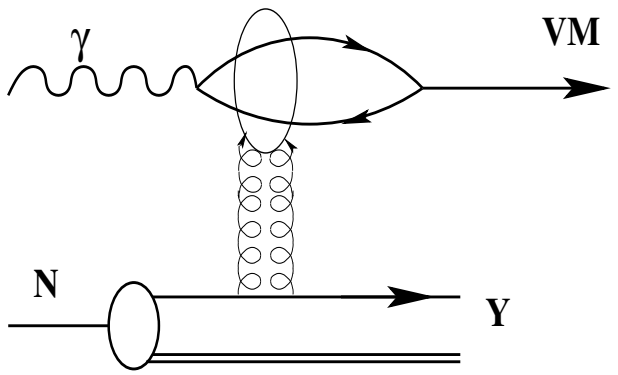

Figure 69: The proton-dissociative photoproduction of vector meson.

The cross section of the reaction (86) is related to the photoproduction cross section of a vector meson off a parton in the proton by [64, 7, 25, 23]:

$$\frac{d^2\sigma(\gamma p \to VY)}{dtdx} = \sum_f (q(x,t) + \bar{q}(x,t)) \cdot \frac{d\sigma(\gamma q \to Vq)}{dt} + G(x,t) \cdot \frac{d\sigma(\gamma G \to VG)}{dt}, \tag{87}$$

where $(\bar{q})q(x,t)$ is the (anti-)quark and and $G(x,t)$ the gluon density of the proton. x can be expressed in terms of the rapidity η_0 between the struck parton and the produced vector meson by:

$$x = \frac{4p_\perp^2}{s} cosh^2 \frac{\eta_0}{2}, \tag{88}$$

with $p_\perp$ being the struck quark transverse momentum and s the cms collision energy.

The vector meson parton photoproduction cross sections are related to each other by:

$$d\sigma(\gamma q \to Vq) = d\sigma(\gamma \bar{q} \to V\bar{q}) \tag{89}$$

$$d\sigma(\gamma G \to VG) = \frac{81}{16} d\sigma(\gamma q \to Vq) \tag{90}$$

All independent helicity amplitudes of the process (86) can be predicted by pQCD by introducing a new mechanism [6]: within usual perturbation theory a photon can split only into a chiral-even massless quark-antiquark pair (i.e. the helicities of the quark and the antiquark are antiparallel). The violation of the chiral symmetry, being the well known soft QCD phenomenon, generates a non-perturbative chiral-odd component of the real photon wave-function (the helicities of the quark and the antiquark are parallel). The authors show that the chiral-odd configuration in the quark loop shown in Fig. 69 gives a very important contribution for t not asymptotically large. The interaction of this additional chiral contribution can be described in pQCD since quark-dipole scattering at high $-t$ prefers a $q\bar{q}$ configuration with small transverse interquark distances. As a result the chiral-odd contribution can be factorized into two non-perturbative photon and vector meson light-cone wave-functions and the hard scattering amplitude.

The calculations predict that s-channel helicity is broken by the chiral-odd amplitudes. However the helicity non-flip amplitude is dominant. Taking into account the dominant helicity non-flip amplitudes, the following dependence of the differential cross section $d\sigma/dt$ on t is obtained:

$$\frac{d\sigma}{dt} \sim \frac{\alpha_s^4 \left(-t/4\right)}{(-t)^4}, \tag{91}$$

where α_s is the running coupling constant. The helicity-flip amplitudes introduce components proportional to $(-t)^5$ to the cross section. This approach does not predict any W-dependence of the differential cross section $d\sigma/dt$.

The previous high $-t$ measurement by ZEUS of the angular distribution of ρ^0 meson decay products from the process $\gamma p \to \rho^0 p$ at $-t \approx 2$ GeV^2 has demonstrated the dominance of the helicity non-flip amplitude in this t range [5]. However, the precision of this data is low and the only conclusion, that could be drawn, was about the relative sign between the amplitudes, and that the helicity-flip contributions are small. This is in agreement with the evaluations presented here [6].

The analysis presented in this thesis does not cover the decay angle distributions. They are measured with much higher precision than previously using the same data set and selection cuts used in this analysis [27]. The results of the high $-t$ helicity angles analysis agree semi-quantitatively with the theoretical predictions.

Comparison with the Measured Cross Section

The pQCD prediction was directly compared with the results of this analysis for the ρ^0 and ϕ vector mesons (Sec. 7.1 and 7.2). The theoretical parton cross section was evaluated according to the equation:

$$\frac{d\sigma}{dt}(\gamma \mathcal{P} \to V\mathcal{P}) = \frac{1}{16\pi} \cdot \frac{1}{s^2} \sum_i |\mathcal{M}|^2, \tag{92}$$

where $\mathcal{P}$ denotes partons (quarks or gluons), s is the center-of-mass energy and $\mathcal{M}$ is the sum of the dominant even and odd non-flip helicity amplitudes derived from formulae given in [6].

The differential cross section $d\sigma/dt(\gamma p \to VY)$ was obtained by convoluting the parton cross section (Eq. 92) with the PDF using the GRV94HO parameterization [59]. This particular parton density function was chosen from the wide selection offered by the PDFLIB [60] because it matches the kinematic range of this measurement. Other PDFs were also applied but the effect of different parameterizations was negligible.

In Fig. 70 the measured cross sections $d\sigma/dt$ for the ρ^0 and ϕ mesons are compared with the theoretical calculations for the light vector mesons. The measured and theoretical cross section do not agree, neither in the normalization nor in the shape of the distribution for both mesons. The prediction overshoots the data by a factor $\simeq 50$ and $\simeq 30$ for ρ^0 and ϕ, respectively. If the theoretical calculation for the ρ^0 meson is fitted with the power-like function (Eq. 74) a value of $n \simeq 5.5$ is determined for the momentum transfer range $1.2 < -t < 10$ GeV^2, compared to a value of $n = 3.22 \pm 0.04\ ^{+0.19}_{-0.15}$ measured in this analysis. If the theoretical calculation for the ϕ meson is fitted with the power-like function a value of $n \simeq 4.8$ is obtained for the t range $1.8 < -t < 6.5$ GeV^2, compared to $n = 2.75 \pm 0.07^{+0.20}_{-0.21}$.

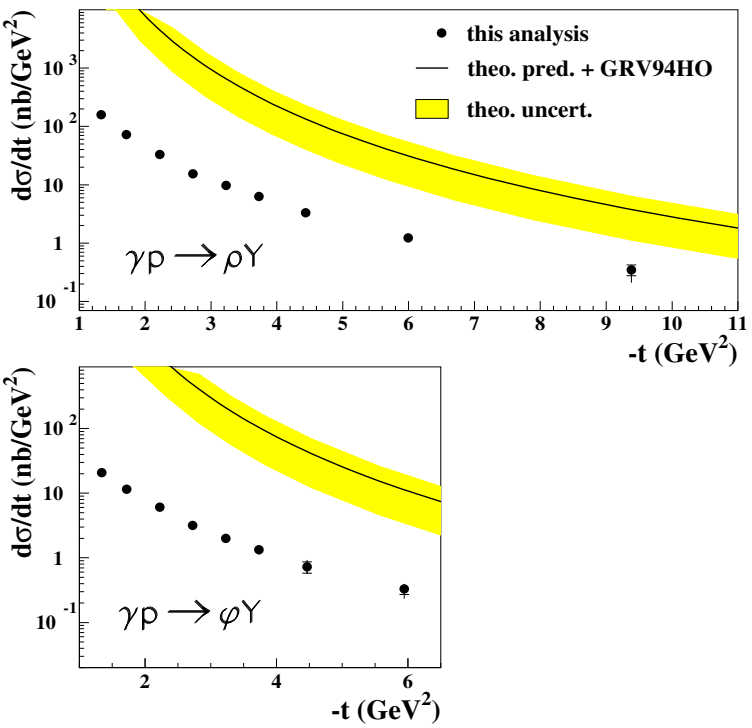

Figure 70: The comparison between the differential cross section dσ/dt for the process $\gamma p \to \rho Y$ (top) and $\gamma p \to \phi Y$ (bottom), in the kinematic range $80 < W < 120$ GeV and $\frac{M_V^2}{-t} < 100$ measured in this analysis (dots), and the theoretical calculation of these processes (solid line). The theoretical error (shaded band) comes from the uncertainties of the model parameters. The inner error bars show the statistical error, the outer ones the statistical and systematic uncertainties added in quadrature.

8.2 Heavy Vector Mesons

The detailed description of the theoretical predictions for the heavy vector mesons (e.g. J/ψ and Υ) was given by Bartels et al. [7].

The process (86) is analyzed within the Regge limit assuming a large momentum transfer, $s \gg -t \gg Q_0^2$, where Q_0^2 is the typical hadronic scale of the order of ~ 1 GeV^2. The cross section for the diffractive scattering of a virtual photon off a proton is written in terms of the parton-photon cross section and the parton densities in the proton (Eq. 87). The calculations are done in terms of the scaling variable $\tau = -t/(Q^2 + m_V^2)$, where Q^2 is the photon virtuality and m_V^2 is the vector meson mass. Note, that Q^2 can be zero. For the coupling of the IP to the proton, treated as an exchange of a gluon ladder, the Mueller-Tang prescription [4] is used, where the IP couples to a single parton. This is justified if the size of the IP,$\sim (\frac{1}{\sqrt{-t}})$, is smaller than the size of the proton ($\sim \frac{1}{Q_0^2}$), which leads to the condition $-t > 1$ GeV^2 [65]. The coupling of the BFKL-Pomeron to gluons is the same as the coupling to quarks except for a constant color factor $\frac{81}{16}$ (Eq. 90).

The approximation for the light-cone wave-function of the vector meson is simplified and assumed to be a δ-function, which partitions the light-cone momenta and the transverse momenta of the quark-antiquark pair from the photon equally. This non-relativistic approach is appropriate for heavy vector mesons. For the light vector mesons, the relativistic wave-functions should be used.

The calculation leads to the following form of the differential cross section:

$$\frac{d\sigma}{dt} \sim \frac{\alpha_s^4}{t^4} \cdot \mathcal{F}(\tau, s), \tag{93}$$

where s is the Mandelstam variable representing the γp center-of-mass energy and $s = xW^2$, with W being the total hadronic energy. The function $\mathcal{F}$, which needs to be derived numerically, introduces the W-dependence of the differential cross section and softens the t-dependence. In the calculations strong coupling constant α_s is taken constant, $\alpha_s = 0.2 \pm 0.02$. The power-like function (Eq. 74) fitted to the theoretical $d\sigma/dt$ yields a value of $n = 1.8$.

The approximation used in the presented model does not include any helicity-flip amplitude, so that s-channel helicity is by definition conserved.

Comparison with the Measured Cross Section

Fig. 71 shows the comparison of the measured cross section $d\sigma/dt$ for the J/ψ meson (Sec. 7.3) with the theoretical prediction by Bartels et al. for the heavy vector mesons [7]. The theoretical uncertainties reflects the uncertainties in the model parameters, mainly due to uncertainties in α_s and in center-of-mass energy W. The agreement between the measured and predicted cross section is very good but the theoretical calculations have large uncertainties. However, the data favor the nominal values of the theoretical parameters. Both, the normalization and the shape of the distribution are very well reproduced.

The presented calculations predict a weak dependence of the differential cross section dσ/dt on W, resulting from the form of the function $\mathcal{F}$ in Eq. 93. At fixed t, the cross section increases with increasing center-of-mass energy. Fig. 72 shows the measured differential cross section in four t bins as a function of W (Sec. 7.3.2) compared to the model prediction. The $-t$ values quoted on the plots are the average values in the $-t$ bin considered. Within the errors, the

measured cross sections do not show any W-dependence. The agreement between the data and theory is fairly good, however both, statistical and theoretical uncertainties are large.

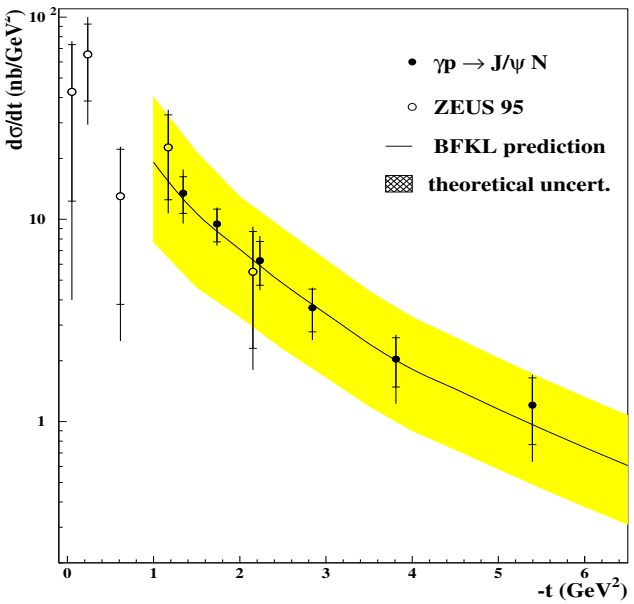

Figure 71: The comparison between the measured differential cross section $d\sigma/dt$ for the process $\gamma p \to J/\psi Y$ (dots) and the theoretical calculation of this process (solid line) in the kinematic range $80 < W < 120$ GeV and $\frac{M_Y^2}{-t} < 100$. The full points represent results from this analysis, open dots show the result of the ZEUS 95 measurement. The inner error bars give the statistical error, the outer once the statistical and systematic uncertainties added in quadrature.

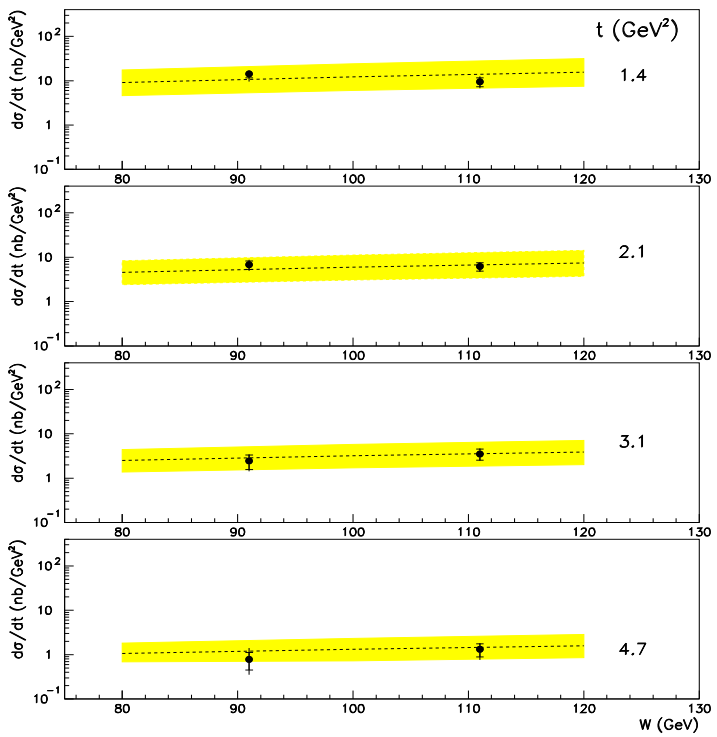

Figure 72: The comparison between the measured and predicted differential cross section $d\sigma/dt$ for two W as a function of W in different t bins. The $-t$ values quoted on the plots are the average values in the t bin considered. Dashed lines represent the theoretical calculations. The inner error bars show the statistical error, the outer ones the statistical and systematic uncertainties added in quadrature.

8.3 Discussion

The difficulty in the interpretation of the results presented in this thesis is the lack of a pQCD model describing the measured differential cross sections $d\sigma/dt$ for ρ^0 and ϕ. The basic idea of the pQCD prediction [6] for the light vector mesons is that the evaluated amplitudes have two contributions: a hard component, which can be calculated in pQCD and a soft component, which can be treated in the framework of pQCD and decreases with increasing t. In contrast, the pQCD predictions [7] for heavy vector mesons assume only hard contributions in the calculations. The main obstacle to perform the same evaluations for the light vector mesons is the assumed form of the meson wave-function. The J/ψ wave-function has a very simple, non-relativistic form, which is justified by the large mass of the meson. For lighter mesons, like ρ^0 or ϕ, the used meson wave-function should be relativistic and most likely of the more complicated form. However, it is interesting, despite the over-simplified meson wave-function, to compare the prediction of pQCD model for heavy vector mesons [7] applied to the ρ^0 and ϕ mesons, with the measured ρ^0 and ϕ cross sections. Fig. 73 shows the results of the theoretical calculations compared to the ρ^0 and ϕ data.

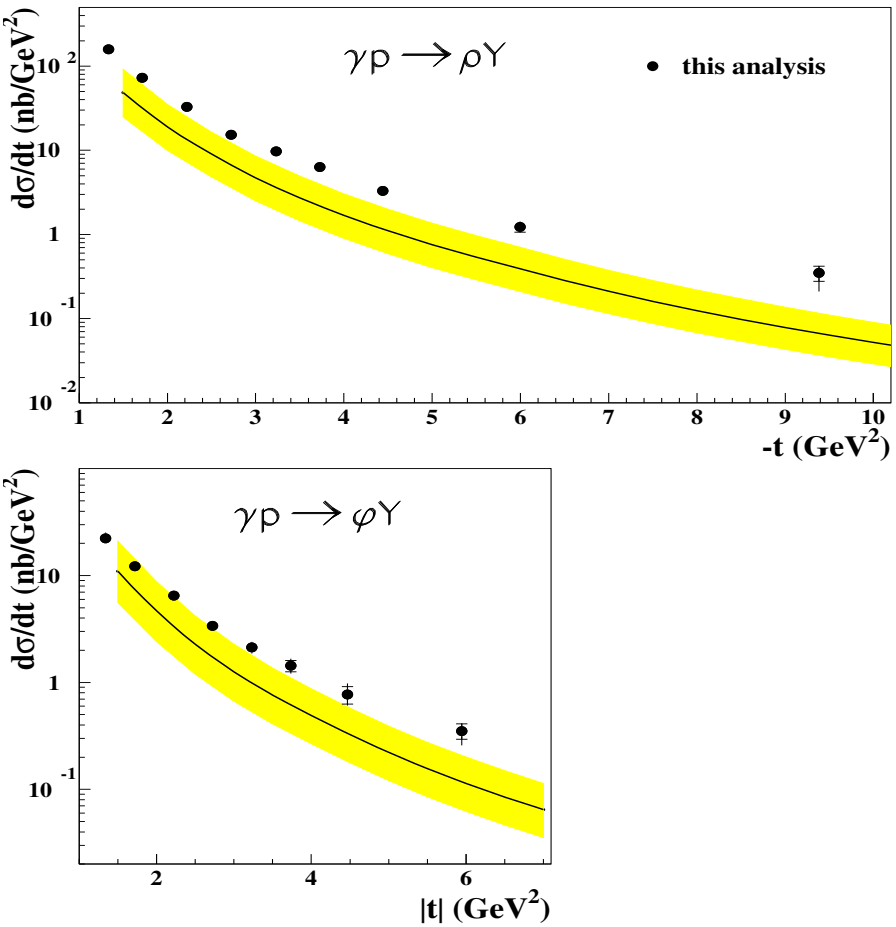

Figure 73: The comparison between the heavy mesons theoretical predictions evaluated for ρ^0 and ϕ with the measured cross sections $d\sigma/dt$. The shaded band corresponds to the uncertainty of the theoretical calculations, coming form the uncertainty of α_S and of the center-of-mass energy.

The theoretical calculations do not reproduce the measured cross sections but the disagreement decreases with the increasing mass of the meson. This fact might be a consequence of the meson wave-function form, which is valid only for a large vector meson mass. The difference between the data and the prediction based on the heavy vector mesons model, however, is smaller than that for the light vector meson model [6] (Fig. 70). This may suggest that the approach proposed in the heavy meson model could be, after a proper implementation of the meson wave-function, used to predict the differential cross sections also for ρ^0 and ϕ. The model for the heavy vector meson, if used for ρ^0 and ϕ, would have to cope with one more aspect of the studied process, namely with the results of the helicity angle analysis. The model predicts that SCHC holds for the J/ψ meson, which is consistent with the results of the helicity matrix elements measurement for high $-t$ photoproduction [27]. The same analysis measures also a weak SCHC breaking for the ρ^0 and ϕ mesons. If the approach presented in the heavy meson prediction is to describe the large $-t$ photoproduction of the light vector mesons, it has to account for the observed deviations from the SCHC.

The model for the light vector mesons [6] does not describe the data, neither in the normalization nor in the shape of the t distribution. The model predicts no W-dependence of the differential cross section consistent with the data. Also the SCHC breaking is predicted in this model, and the semi-quantitatively calculations for the helicity matrix elements agree with the measured values [27]. Two different effects, not taken into account in these calculations, could lead to a lower theoretical predictions of the calculations [6] for the cross sections $d\sigma/dt$.

First effect is that the pQCD $\mathbb{P}$ can interact with more than one parton in the proton. When x decreases, the gluon density in the proton increases. Therefore the interaction of $\mathbb{P}$ with the proton, depicted in Fig. 69 as gluon lines, can take place with more than one gluon in the proton, causing a decrease of the theoretical cross section, due to a destructive interference of the amplitudes.

A second possible effect, which might be considered in this case, is proposed by the Björken mechanism of filling the rapidity gap in hard processes by soft interactions of spectators [66]. In the approach used in the calculations for the light vector mesons presented in Sec. 8.1, the interactions in the final state are neglected. However, these accompanying soft interactions of the spectators produce usually hadrons, which fill the rapidity gap and effectively decrease the hard cross section. The magnitude of this reduction, given by the so called survival probability of the rapidity gap, was estimated to be between 0.015 and 0.15, with the central value of ~ 0.05 [66]. However, the author suggests that the best way to obtain this probability, it to measure it experimentally, for example in the highly inelastic double diffraction at large $-t$. If we evaluate the survival probability of the rapidity gap from the process $\gamma p \to VY$ measured in this analysis at high $-t$, the obtained value of ~ 0.02 and ~ 0.03 for the ρ^0 and ϕ mesons, respectively, is consistent with the above estimation.

9 Summary and Conclusions

The earlier vector meson measurement for lower $-t \lesssim 3$ GeV^2 [5] generally exhibits the features of a soft diffractive process. However, some indications of the transition character of this data were observed, such as non-zero values of the helicity matrix element r^{04}_{1-1} and the increase of the ratios of cross sections ϕ/ρ and ψ/ρ towards the expectations from the SU(4) symmetry.

The results of this analysis are a continuation of the previous measurement and show agreement with the previous results, in the $-t$ range covered by both measurements. The factor of twelve increase in the integrated luminosity with respect to the earlier analysis resulted in an extension of the measurement to much higher $-t$ values, up to $-t = 10$ GeV^2 and a much better precision of present data.

The diffractive photoproduction of the ρ^0, ϕ and J/ψ mesons was studied for $80 < W < 120$ GeV in the $-t$ range $1.2 < -t < 10$ GeV^2, $1.2 < -t < 6.5$ GeV^2 and $1.2 < -t < 6.5$ GeV^2, respectively.

The amount of proton-dissociative events in the data sample was estimated by comparing the tagging efficiency of the PRT for the data and for the proton-dissociative EPSOFT MC. These studies showed that the data sample consists mostly of proton-dissociative events, except for the low $-t$ range, $-t \lesssim 2.5$ GeV^2 where a contamination from elastic events on the level of $\sim 10\%$ is observed.

Different possible proton fragmentation approaches were tested using soft (EPSOFT) and hard (DIFFVM-g and DIFFVM-q) Monte Carlo models. The FCAL energy distribution E_{FCAL}, reflecting the M_Y distribution, and the forward energy flow $dE/d\eta$ were compared between the data and different MC samples. These studies showed that EPSOFT describes both, the E_{FCAL} and $dE/d\eta$ distributions in the data. DIFFVM-g, with $\mathbb{P}$scattering off a gluon, matches the forward energy flow distributions in the data but the measured FCAL energy distribution is properly described only for $E_{FCAL} > 3$ GeV . DIFFVM-q, where $\mathbb{P}$scatters off a quark, fails to reproduce the measured E_{FCAL} and $dE/d\eta$ distribution.

The factorization assumption was tested by comparing the $\beta(t)$ parameterizations of the M_Y distribution given by Eq. 55 for different vector mesons. Within the large errors, the data are consistent with the hypothesis of factorization.

The differential cross section $d\sigma/dM_{\pi\pi}$ was measured in nine $-t$ bins. The non-resonant background B/A and the photon-dissociative background A_f as a function of $-t$ were determined. Both are in agreement with the previous results at low $-t$ [5]. However, the results presented in this thesis extend the t range significantly. The skewing of the Söding distribution B/A decreases with increasing $-t$ and is described by an exponential dependence $k_S \cdot e^{b_S \cdot (-t)}$. The combined fit to this measurement and low $-t$ results gave $k_S = 0.76 \pm 0.14$ (stat.) $^{+0.04}_{-0.06}$ (syst.) GeV$^{-1/2}$ and $b_S = 1.29 \pm 0.17$ (stat.) $^{+0.18}_{-0.19}$ (syst.) GeV^{-2}, which is consistent with the previous measurement [5]. A_f grows with $-t$. The parameterization $n_f \cdot \log(d_f \cdot t)$ gave for the combined fit $n_f = 0.06 \pm 0.01$ (stat.) ± 0.01 (syst.) GeV^{-2} and $d_f = 3.0 \pm 1.0$ (stat.) $^{+0.4}_{-0.6}$ (syst.) GeV^{-2}.

The background under the ϕ mass peak was found to depend on t, decreasing with the increasing momentum transfer. For the J/ψ meson, the non-resonant background was measured to be t-independent.

The differential cross section $d\sigma/dt$ for $\frac{M_Y^2}{-t} < 100$ was obtained for the ρ^0,ϕ and J/ψ meson. The results agree with the previous measurement at low $-t$ in the overlap region. For all three vector mesons the cross section is well described by a power-like dependence $\sim (-t)^{-n}$, with

the power n decreasing with increasing meson mass: $n = 3.22 \pm 0.04$ (stat.) $^{+0.19}_{-0.15}$ (syst.) for ρ^0, $n = 2.75 \pm 0.07$ (stat.) $^{+0.20}_{-0.21}$ (syst.) for ϕ and $n = 1.8 \pm 0.2$ (stat.) ± 0.2 (syst.) for J/ψ, respectively. For the ρ^0 and ϕ mesons the theoretical calculations [6] do not describe the data, neither in the normalization, nor in the shape of the t distribution. For the J/ψ meson the pQCD predictions [7] agree with the measured $d\sigma/dt$ within the big theoretical uncertainties. The data favor the nominal theoretical parameters of the model.

The differential cross section $d\sigma/dt$ was measured in three W bins of $80 < W < 90$ GeV, $90 < W < 100$ GeV and $100 < W < 120$ GeV for ρ^0 and ϕ and in two W bins $80 < W < 100$ GeV and $100 < W < 120$ GeV for J/ψ. Due to the statistical limitations the $-t$ range of this analysis was restricted to $1.2 < -t < 8.5$ GeV^2 for the ρ^0 meson. Within the large statistical and systematic uncertainties, no dependence on W of the cross sections, normalized cross sections (Eq. 78) and of the fitted powers n was observed. The results of the W-dependence are consistent with the theoretical predictions and for the light [6] and heavy vector [5] mesons, respectively.

The ratios of the measured cross sections of ϕ/ρ and ψ/ρ agree with the earlier ZEUS measurement [5] in the lower $-t$ region. A rise of the ϕ/ρ cross section ratio up to $-t \approx 3$ GeV^2 is observed. For higher $-t$ the data are compatible with the value of 2/9 predicted by SU(3). An increase of the ψ/ρ cross section ratio with increasing $-t$ is observed up to $-t \approx 5$ GeV^2, where it reaches the SU(4) value of 8/9, taking into account the statistical and systematic uncertainties. Compared to the cross section ratios determined for DIS, the ratios grow faster with t than with Q^2, indicating that the momentum transfer and photon virtuality cannot be treated as equivalent scales.

In conclusion, a complete picture of vector meson production at large $-t$ is still lacking. The measurements of the J/ψ differential cross section, the vector meson cross section ratios and the agreement between the W-dependence and theoretical predictions based on the pQCD models indicate, that large $-t$ can provide a suitable hard scale for pQCD. This is further supported by the results of the decay angle analysis based on the same data sample and event selection [27]. However, the available pQCD calculations do not describe the results for light vector mesons cross sections quantitatively, so the definite conclusion is not possible at the moment.

Some aspects of the measured process, such as the dependence of the cross section $d\sigma/dt$ on M_Y or the W-dependence studied in much wider range of the center-of-mass energy, could add information to the global pictures of the vector meson photoproduction at large $-t$. The determination of $d\sigma/dt$ in different bins of M_Y was not possible for 1996-97 data due to the fact, that most of the proton-dissociative system Y was lost in the beam pipe and the M_Y reconstruction had a very big correction factor. The installation of the Forward Proton Calorimeter (FPC) in 1998, which allows a much more precise measurement of the proton remnant, may enable the determination of the cross section behavior with M_Y. On the other hand, an independent measurement of J/ψ photoproduction tagged in the LUMI electron detector (placed 35 m from the interaction point), extends the accessible W range to $120 \lesssim W \lesssim 240$ GeV [67]. A study of J/ψ photoproduction using results from the two detectors could be used to extend the W range of this analysis.

Appendix

A Tables of Data

t range (GeV^2)	$\langle t \rangle$ (GeV^2)	$\frac{d\sigma}{dt}(\gamma p \to \rho Y)$ (nb/GeV^2)	Stat. (nb/GeV^2)	Syst. (nb/GeV^2)	Total (nb/GeV^2)
1.20 - 1.50	1.332	157.68	5.30	+19.68 –20.87	+20.38 –21.53
1.50 - 2.00	1.711	77.54	2.35	+7.64 –8.55	+8.00 –8.87
2.00 - 2.50	2.218	35.37	1.33	+3.45 –3.35	+3.70 –3.60
2.50 - 3.00	2.723	16.63	0.84	+1.45 –1.74	+1.68 –1.93
3.00 - 3.50	3.226	10.16	0.66	+0.87 –1.25	+1.09 –1.41
3.50 - 4.00	3.728	6.64	0.56	+0.72 –0.86	+0.91 –1.03
4.00 - 5.00	4.430	3.23	0.26	+0.73 –0.57	+0.77 –0.63
5.00 - 6.85	5.746	1.34	0.14	+0.34 –0.51	+0.37 –0.53
6.85 - 10.0	8.042	0.44	0.07	+0.16 –0.23	+0.17 –0.24

Table 27: Tabulated values of $\frac{d\sigma}{dt}(\gamma p \to \rho Y)$ with statistical error (stat.), systematic uncertainty (syst.) and total error for the kinematic range $80 < W < 120$ GeV and $\frac{M_Y^2}{-t} < 100$.

Systematic uncertainty of $\frac{d\sigma}{dt}(\gamma p \to \rho Y)$ (nb/GeV^2)									
	t range (GeV^2)								
Check	1.2 - 1.5	1.5 - 2.0	2.0 - 2.5	2.5 - 3.0	3.0 - 3.5	3.5 - 4.0	4.0 - 5.0	5.0 - 6.85	6.85 - 10
1a	–0.68	–0.18	–0.34	–0.21	–0.12	–0.05	–0.03	0.00	0.00
1b	0.21	0.29	–0.27	–0.05	0.07	–0.07	0.01	0.00	0.00
2a	0.61	–0.46	–0.25	–0.09	–0.16	–0.05	0.05	–0.06	0.00
2b	0.96	0.10	0.07	–0.08	–0.11	–0.02	–0.07	–0.01	0.00
3a	–0.34	–0.57	–0.33	0.05	0.00	–0.05	0.04	–0.03	–0.01
3b	–0.17	–0.19	–0.27	–0.01	–0.14	–0.02	0.00	–0.02	–0.01
3c	6.79	2.86	1.47	0.40	0.28	0.25	0.12	0.05	0.00
3d	–3.07	–1.85	–0.58	–0.35	–0.13	–0.10	0.01	0.02	–0.01
4a	0.19	–1.11	1.24	0.11	–0.05	–0.08	–0.07	–0.10	–0.03
4b	0.52	–0.34	0.62	–0.19	–0.21	–0.22	–0.04	0.01	0.00
5a	–1.40	–0.90	–0.77	–0.60	0.09	0.15	–0.14	–0.07	–0.03
5b	6.41	3.25	1.65	0.94	0.18	0.28	0.17	0.15	0.01
6a	–0.79	–0.29	–0.76	–0.67	–0.43	–0.06	–0.33	–0.21	–0.10
6b	6.30	1.05	0.99	0.52	0.48	0.37	0.63	0.22	0.13
7a	0.24	–0.15	–0.06	–0.08	–0.08	–0.06	–0.02	0.00	0.00
7b	–0.30	–0.18	–0.19	–0.07	–0.07	–0.05	–0.02	0.00	0.00
8a	–9.17	–3.27	–0.81	0.23	0.25	0.19	0.12	0.06	0.02
8b	10.51	3.64	0.66	–0.45	–0.46	–0.34	–0.17	–0.08	–0.03
8c	–5.64	–2.51	–0.79	0.24	0.35	0.31	0.22	0.14	0.06
8d	5.68	2.50	0.61	–0.48	–0.60	–0.50	–0.30	–0.19	–0.09
12a	6.98	2.71	1.16	0.50	0.29	0.17	0.10	0.05	0.01
12b	–6.04	–2.50	–1.24	–0.54	–0.37	–0.24	–0.12	–0.04	–0.02
12c	5.24	1.39	0.38	0.04	0.00	–0.03	–0.03	–0.02	–0.01
12d	–3.78	–1.04	–0.41	–0.07	–0.04	–0.03	0.02	0.02	0.01
13a	0.10	–0.01	–0.10	–0.06	–0.07	–0.05	0.00	0.12	0.05
13b	–0.72	–0.39	–0.25	–0.10	–0.09	–0.06	–0.04	–0.11	–0.04
14a	–4.98	–2.55	–1.25	–0.59	–0.40	–0.26	–0.14	–0.20	–0.09
14b	4.74	2.36	0.98	0.48	0.27	0.17	0.07	–0.16	–0.08
15a	–0.77	–0.40	–0.29	–0.12	–0.09	–0.06	–0.02	0.00	0.00
15b	0.12	–0.01	–0.07	–0.03	–0.06	–0.05	–0.02	0.00	0.00
15c	–0.49	–0.34	–0.20	–0.07	–0.08	–0.06	–0.02	0.00	0.00
15d	–0.17	–0.08	–0.16	–0.08	–0.07	–0.05	–0.02	–0.25	–0.11
15e	–1.04	–0.47	–0.26	–0.09	–0.08	–0.06	–0.02	0.00	0.00
15f	0.40	0.07	–0.09	–0.06	–0.07	–0.05	–0.02	0.00	0.00
15g	0.29	0.08	–0.08	–0.05	–0.07	–0.05	–0.02	0.00	0.00
15h	–1.06	–0.54	–0.30	–0.11	–0.09	–0.06	–0.02	0.00	0.00
15i	–0.22	–0.20	–0.21	–0.10	–0.08	–0.06	–0.02	0.00	0.00
15j	–0.38	–0.18	–0.13	–0.06	–0.07	–0.05	–0.02	0.00	0.00
15k	–0.19	–0.18	–0.19	–0.09	–0.08	–0.06	–0.02	0.00	0.00
15l	–0.45	–0.21	–0.15	–0.06	–0.07	–0.05	–0.02	0.00	0.00
16	–14.51	–5.54	–1.82	–0.80	–0.46	–0.30	–0.15	–0.06	–0.02
21a	2.68	1.32	0.60	0.28	0.17	0.11	0.05	0.02	0.01
21b	–2.68	–1.32	–0.60	–0.28	–0.17	–0.11	–0.05	–0.02	–0.01
22a	3.15	1.55	0.71	0.33	0.20	0.13	0.06	0.03	0.01
22b	–3.15	–1.55	–0.71	–0.33	–0.20	–0.13	–0.06	–0.03	–0.01

Table 28: Tabulated values of the systematic uncertainties of $\frac{d\sigma}{dt}(\gamma p \to \rho Y)$ for systematic checks listed in Sec. 6 under the same indexes.

$80 < W < 90$ GeV					
t range (GeV^2)	$\langle t \rangle$ (GeV^2)	$\frac{d\sigma}{dt}(\gamma p \to \rho Y)$ ($\mathrm{nb/GeV}^2$)	Stat. ($\mathrm{nb/GeV}^2$)	Syst. ($\mathrm{nb/GeV}^2$)	Total ($\mathrm{nb/GeV}^2$)
1.20 - 1.50	1.332	162.96	7.97	+22.36 −25.22	+23.74 −26.45
1.50 - 2.00	1.712	79.83	3.80	+8.79 −11.23	+9.57 −11.86
2.00 - 2.60	2.257	33.53	1.99	+3.73 −5.24	+4.23 −5.61
2.60 - 3.50	2.975	12.00	1.03	+1.56 −1.66	+1.87 −1.95
3.50 - 5.00	4.088	4.78	0.53	+0.67 −1.05	+0.85 −1.17
5.00 - 8.50	6.211	1.01	0.21	+0.21 −0.52	+0.30 −0.56
$90 < W < 100$ GeV					
t range (GeV^2)	$\langle t \rangle$ (GeV^2)	$\frac{d\sigma}{dt}(\gamma p \to \rho Y)$ ($\mathrm{nb/GeV}^2$)	Stat. ($\mathrm{nb/GeV}^2$)	Syst. ($\mathrm{nb/GeV}^2$)	Total ($\mathrm{nb/GeV}^2$)
1.20 - 1.50	1.333	158.53	9.33	+17.87 –23.51	+20.16 –25.29
1.50 - 2.00	1.711	79.88	4.29	+6.52 –10.65	+7.80 –11.48
2.00 - 2.60	2.254	35.09	1.93	+3.66 –3.35	+4.13 –3.87
2.60 - 3.50	2.971	12.71	0.94	+0.85 –1.61	+1.27 –1.87
3.50 - 5.00	4.074	3.90	0.44	+0.72 –0.32	+0.84 –0.54
5.00 - 8.50	6.218	0.89	0.17	+0.53 –0.25	+0.55 –0.30
$100 < W < 120$ GeV					
t range (GeV^2)	$\langle t \rangle$ (GeV^2)	$\frac{d\sigma}{dt}(\gamma p \to \rho Y)$ ($\mathrm{nb/GeV}^2$)	Stat. ($\mathrm{nb/GeV}^2$)	Syst. ($\mathrm{nb/GeV}^2$)	Total ($\mathrm{nb/GeV}^2$)
1.20 - 1.50	1.332	162.25	12.48	+23.70 –34.89	+26.79 –37.05
1.50 - 2.00	1.712	76.42	4.77	+10.48 –14.04	+11.51 –14.83
2.00 - 2.60	2.258	33.42	2.21	+4.63 –5.09	+5.13 –5.55
2.60 - 3.50	2.974	11.46	0.85	+1.34 –1.77	+1.59 –1.96
3.50 - 5.00	4.097	4.58	0.42	+0.84 –0.92	+0.94 –1.01
5.00 - 8.50	6.169	1.13	0.14	+0.26 –0.38	+0.30 –0.41

Table 29: Tabulated values of $\frac{d\sigma}{dt}(\gamma p \to \rho Y)$ with statistical error (stat.), systematic uncertainty (syst.) and total error for the kinematic range $\frac{M_Y^2}{-t} < 100$ and three W bins $80 < W < 90$ GeV, $90 < W < 100$ and $100 < W < 120$ GeV.

Systematic uncertainty of $\frac{d\sigma}{dt}(\gamma p \to \rho Y)$ (nb/GeV^2) $80 < W < 90$ GeV						
	t range (GeV^2)					
Check	1.2 - 1.5	1.5 - 2.0	2. - 2.6	2.6 - 3.5	3.5 - 5.0	3.5 - 8.5
1a	–3.62	–0.96	–0.86	0.06	–0.03	0.02
1a	–1.90	–1.68	–1.00	–0.10	–0.04	0.02
2a	–1.65	–1.66	–0.93	0.04	0.04	0.01
2b	–1.44	–1.54	–0.68	0.09	–0.07	–0.03
3a	–1.55	–1.04	–0.95	0.00	–0.01	0.00
3b	–1.34	–1.50	–0.96	–0.06	0.04	0.00
3c	3.49	0.41	–0.22	–0.19	0.08	0.01
3d	–4.41	–2.54	–1.22	–0.14	0.12	0.04
4a	–3.25	–1.97	–0.95	0.03	–0.03	–0.16
4b	2.92	–0.40	–0.30	0.09	–0.07	0.00
5a	–6.08	–1.34	–1.32	–0.32	0.04	–0.04
5b	5.42	2.33	0.83	0.69	0.05	0.09
7a	–0.68	–1.10	–1.07	0.19	–0.17	–0.19
7b	–3.57	–2.98	–1.85	0.02	–0.33	–0.09
10a	4.21	0.10	–0.74	–0.55	–0.30	–0.04
10b	–7.42	–1.69	0.05	0.34	0.19	0.06
10c	3.82	0.31	–0.93	–1.00	–0.79	–0.22
10d	–6.67	–1.97	0.01	0.57	0.42	0.13
12a	13.38	5.46	2.34	0.77	0.29	0.08
12b	–11.19	–4.73	–2.00	–0.65	–0.26	–0.03
12c	14.24	5.73	2.49	0.81	0.31	0.08
12d	–10.63	–4.44	–1.87	–0.61	–0.24	–0.02
13a	–0.79	–0.42	–0.16	–0.05	–0.04	0.01
13b	–0.61	–0.29	–0.12	–0.04	–0.05	0.00
14a	–5.64	–2.86	–1.19	–0.42	–0.20	–0.28
14b	4.19	2.11	0.89	0.33	0.08	–0.26
15a	–0.95	–0.43	–0.20	–0.06	–0.03	0.02
15b	–0.91	–0.50	–0.18	–0.06	–0.03	0.02
15c	–1.04	–0.49	–0.18	–0.06	–0.03	0.02
15d	–0.81	–0.45	–0.20	–0.06	–0.03	0.02
15e	–1.16	–0.47	–0.18	–0.06	–0.03	0.01
15f	–0.67	–0.48	–0.18	–0.06	–0.03	0.01
15g	–0.80	–0.48	–0.18	–0.06	–0.03	0.01
15h	–1.11	–0.45	–0.18	–0.06	–0.03	0.01
15i	–0.93	–0.47	–0.20	–0.06	–0.03	0.01
15j	–0.89	–0.49	–0.16	–0.06	–0.04	0.01
15k	–0.90	–0.51	–0.21	–0.06	–0.03	0.01
15l	–0.97	–0.40	–0.12	–0.05	–0.03	0.01
16	–11.43	–5.22	–1.48	–0.40	–0.19	0.00
21a	2.77	1.36	0.57	0.20	0.08	0.02
21b	–2.77	–1.36	–0.57	–0.20	–0.08	–0.02
22a	3.26	1.60	0.67	0.24	0.10	0.02
22b	–3.26	–1.60	–0.67	–0.24	–0.10	–0.02

Table 30: Tabulated values of the systematic uncertainties of $\frac{d\sigma}{dt}(\gamma p \to \rho Y)$ for $80 < W < 90$ GeV, for systematic checks listed in Sec. 6 under the same indexes.

Systematic uncertainty of $\frac{d\sigma}{dt}(\gamma p \to \rho Y)$ (nb/GeV^2) $90 < W < 100$ GeV						
	t range (GeV^2)					
Check	1.2 - 1.5	1.5 - 2.0	2. - 2.6	2.6 - 3.5	3.5 - 5.0	3.5 - 8.5
1a	–1.03	–1.06	0.03	–0.06	0.01	0.00
1b	–0.63	–0.08	0.18	0.08	0.00	0.00
2a	–1.26	–0.98	–0.16	–0.05	0.05	0.02
2b	–1.21	–0.26	0.25	–0.06	–0.01	–0.02
3a	–1.50	–0.96	0.10	0.06	0.04	0.03
3b	–1.74	–0.73	–0.01	–0.22	–0.02	–0.01
3c	7.10	1.97	1.13	0.33	0.10	0.03
3d	–4.62	–2.51	–0.26	–0.13	–0.04	–0.01
4a	1.46	–2.95	1.29	0.37	0.01	0.01
4b	–2.37	–1.28	0.34	0.11	–0.06	0.02
5a	3.32	–3.01	–0.20	0.02	0.01	–0.05
5b	3.18	2.36	2.49	0.39	0.31	0.06
7a	5.69	2.85	–1.17	–0.47	0.54	0.10
7b	–0.63	–0.97	–2.10	–1.18	0.20	0.05
10a	–9.40	–3.82	–0.83	0.26	0.15	0.04
10b	7.46	2.87	1.07	–0.42	–0.16	–0.05
10c	11.28	2.98	0.65	–0.11	0.13	0.11
10d	–11.89	–3.81	–0.52	–0.01	–0.13	–0.14
12a	0.49	0.01	0.32	0.04	0.03	0.01
12b	–3.37	–1.48	–0.24	–0.15	–0.02	–0.01
12c	–0.13	–0.31	0.14	–0.02	0.01	0.00
12d	–2.60	–1.07	–0.06	–0.08	0.00	0.00
13a	–0.89	–0.45	–0.21	–0.07	0.04	0.42
13b	–1.98	–0.61	–0.19	–0.06	0.03	0.25
14a	–6.29	–3.19	–1.08	–0.46	–0.14	–0.14
14b	3.49	1.82	1.20	0.37	0.13	–0.12
15a	–2.04	–0.89	–0.02	–0.06	0.00	0.00
15b	–1.19	–0.71	0.05	–0.06	0.00	0.00
15c	–1.83	–0.81	0.00	–0.06	0.00	0.00
15d	–1.43	–0.78	0.03	–0.06	0.00	0.00
15e	–2.43	–0.68	–0.21	–0.06	0.00	0.00
15f	0.77	–0.13	–0.14	–0.06	0.00	0.00
15g	0.22	–0.21	–0.14	–0.06	0.00	0.00
15h	–2.25	–0.69	–0.23	–0.06	0.00	0.00
15i	–0.76	–0.44	–0.21	–0.07	0.00	0.00
15j	–0.89	–0.39	–0.11	–0.05	0.00	0.00
15k	–0.60	–0.42	–0.16	–0.06	0.00	0.00
15l	–1.30	–0.40	–0.20	–0.06	0.00	0.00
16	–13.45	–5.59	–1.40	–0.57	–0.15	–0.04
21a	2.69	1.36	0.60	0.22	0.07	0.02
21b	–2.70	–1.36	–0.60	–0.22	–0.07	–0.02
22a	3.17	1.60	0.70	0.25	0.08	0.02
22b	–3.17	–1.60	–0.70	–0.25	–0.08	–0.02

Table 31: Tabulated values of the systematic uncertainties of $\frac{d\sigma}{dt}(\gamma p \to \rho Y)$ for $90 < W < 100$ GeV, for systematic checks listed in Sec. 6 under the same indexes.

Systematic uncertainty of $\frac{d\sigma}{dt}(\gamma p \to \rho Y)$ (nb/GeV^2) $100 < W < 120$ GeV						
	t range (GeV^2)					
Check	1.2 - 1.5	1.5 - 2.0	2. - 2.6	2.6 - 3.5	3.5 - 5.0	3.5 - 8.5
1a	4.07	–1.39	–0.83	–0.22	–0.02	0.00
1b	–2.72	0.57	–0.25	0.14	0.03	0.00
2a	0.39	–1.17	–0.14	–0.21	0.06	–0.06
2b	3.14	–0.57	0.13	–0.12	–0.04	0.01
3a	–0.28	–0.83	–0.51	0.07	0.01	–0.03
3b	–0.94	–0.92	–0.20	–0.09	0.02	–0.02
3c	9.88	5.37	2.85	0.65	0.34	0.08
3d	–3.10	–3.40	–1.10	–0.23	–0.05	0.03
4a	0.77	–0.79	1.60	0.13	–0.17	–0.09
4b	–2.44	–1.11	0.29	–0.15	–0.11	–0.04
5a	–5.37	0.09	–1.49	–0.20	–0.03	–0.09
5b	7.03	2.84	1.12	0.60	0.29	0.15
7a	–6.17	5.05	1.58	0.08	0.33	0.06
7b	–3.36	0.75	0.84	–0.27	0.03	0.04
10a	–1.51	–3.14	–2.29	–0.80	–0.39	–0.10
10b	–1.47	1.15	1.57	0.47	0.29	0.07
10c	16.79	4.69	–0.04	–0.99	–0.71	–0.30
10d	–13.44	–4.63	–0.68	0.48	0.42	0.15
12a	2.59	1.50	0.83	0.33	0.19	0.05
12b	–4.78	–2.35	–1.12	–0.41	–0.15	–0.05
12c	–4.73	–2.48	–1.26	–0.49	–0.20	–0.06
12d	3.11	1.86	1.07	0.47	0.25	0.08
13a	–0.56	–0.30	–0.09	–0.10	–0.02	0.00
13b	0.19	0.21	0.19	0.16	0.11	0.07
14a	–5.98	–2.87	–1.20	–0.42	–0.15	–0.10
14b	3.76	2.02	0.87	0.32	0.15	–0.06
15a	–2.59	–1.12	–0.46	–0.13	–0.01	0.00
15b	–0.11	0.03	0.04	0.00	0.01	0.00
15c	–1.71	–0.81	–0.22	–0.06	0.00	0.00
15d	–1.00	–0.30	–0.21	–0.07	0.01	0.00
15e	–4.61	–1.53	–0.40	–0.10	0.00	0.00
15f	2.77	0.95	0.12	–0.03	0.01	0.00
15g	7.04	2.91	0.61	0.05	0.02	0.00
15h	–15.77	–7.68	–2.27	–0.45	–0.05	0.00
15i	–0.80	–0.23	–0.17	–0.08	0.00	0.00
15j	–0.93	–0.30	–0.11	–0.04	0.01	0.00
15k	2.76	1.30	0.57	0.19	0.08	0.02
15l	–2.76	–1.30	–0.57	–0.19	–0.08	–0.02
16	–23.43	–7.74	–2.23	–0.52	–0.20	–0.05
21a	3.25	1.53	0.67	0.23	0.09	0.02
21b	–3.25	–1.53	–0.67	–0.23	–0.09	–0.02
22a	3.17	1.60	0.70	0.25	0.08	0.02
22b	–3.17	–1.60	–0.70	–0.25	–0.08	–0.02

Table 32: Tabulated values of the systematic uncertainties of $\frac{d\sigma}{dt}(\gamma p \to \rho Y)$ for $100 < W < 120$ GeV, for systematic checks listed in Sec. 6 under the same indexes.

t range (GeV^2)	$\langle t \rangle$ (GeV^2)	$\frac{d\sigma}{dt}(\gamma p \to \phi Y)$ (nb/GeV^2)	Stat. (nb/GeV^2)	Syst. (nb/GeV^2)	Total (nb/GeV^2)
1.20 - 1.55	1.360	19.26	1.00	$+2.83-2.66$	$+3.00-2.84$
1.55 - 1.90	1.710	12.27	0.66	$+1.74-1.36$	$+1.86-1.51$
1.90 - 2.30	2.082	7.26	0.46	$+0.91-0.61$	$+1.02-0.76$
2.30 - 2.70	2.484	4.51	0.34	$+0.46-0.40$	$+0.57-0.53$
2.70 - 3.20	2.927	2.48	0.22	$+0.26-0.28$	$+0.34-0.36$
3.20 - 3.80	3.472	1.51	0.17	$+0.33-0.22$	$+0.37-0.28$
3.80 - 4.80	4.239	0.87	0.16	$+0.31-0.12$	$+0.35-0.20$
4.80 - 6.50	5.527	0.35	0.07	$+0.10-0.09$	$+0.12-0.11$

Table 33: Tabulated values of $\frac{d\sigma}{dt}(\gamma p \to \phi Y)$ with statistical error (stat.), systematic uncertainty (syst.) and total error for the kinematic range $80 < W < 120$ GeV and $\frac{M_Y^2}{-t} < 100$.

Systematic uncertainty of $\frac{d\sigma}{dt}(\gamma p \to \phi Y)$ (nb/GeV^2)								
	t range (GeV^2)							
Check	1.2 - 1.55	1.55 - 1.9	1.9 - 2.3	2.3 - 2.7	2.7 - 3.2	3.2 - 3.8	3.8 - 4.8	4.8 - 6.5
1a	−0.610	−0.083	−0.005	−0.004	−0.003	0.000	0.000	0.000
1b	0.237	−0.035	−0.009	0.000	−0.003	0.000	0.000	0.000
2a	−0.547	−0.333	−0.085	−0.005	−0.003	0.000	0.000	0.000
2b	0.991	0.576	0.221	0.079	0.021	−0.001	−0.001	0.001
3a	−0.008	−0.107	−0.074	0.035	−0.006	0.016	−0.002	0.005
3b	0.080	0.074	0.001	0.019	−0.061	−0.014	−0.011	−0.002
3c	1.396	1.047	0.404	0.037	0.101	0.064	0.031	0.033
3d	−0.276	−0.235	−0.115	−0.061	−0.043	0.016	0.008	0.006
4a	0.492	0.274	0.046	−0.132	0.023	−0.066	0.067	−0.065
4b	0.113	0.035	−0.205	−0.011	−0.003	−0.002	0.066	0.032
5a	−0.604	−0.571	−0.161	−0.223	0.021	−0.006	0.043	0.009
5b	0.371	0.304	0.076	0.147	0.057	0.047	0.075	0.025
6a	−1.296	0.165	−0.077	0.045	−0.097	−0.163	−0.066	−0.028
6b	0.433	0.366	0.031	0.210	−0.129	0.272	0.252	0.049
7a	0.707	0.181	0.197	0.148	−0.090	−0.037	−0.008	0.000
7b	0.042	−0.187	0.020	0.048	0.041	0.035	0.023	0.007
8a	−1.078	−0.516	−0.202	0.069	0.067	0.049	0.035	0.018
8b	1.314	0.647	0.255	−0.087	−0.078	−0.056	−0.040	−0.020
8c	−0.658	−0.395	−0.186	0.062	0.075	0.066	0.058	0.040
8d	0.738	0.463	0.226	−0.081	−0.091	−0.081	−0.070	−0.048
9	−1.174	−0.644	−0.286	0.093	0.109	0.092	0.078	0.052
12a	0.720	0.453	0.465	0.170	0.093	0.056	0.030	0.013
12b	−0.557	−0.321	−0.016	−0.137	−0.075	−0.046	−0.025	−0.011
12c	0.370	0.174	0.248	0.022	0.007	−0.002	−0.007	−0.006
12d	−0.173	−0.020	0.222	0.018	0.014	0.014	0.014	0.009
13a	0.007	0.006	0.002	0.000	0.000	0.000	0.000	0.000
13b	−0.007	−0.006	−0.002	0.000	0.000	0.000	0.000	0.000
14a	−0.635	−0.395	−0.248	−0.153	−0.082	−0.050	−0.029	−0.010
14b	0.688	0.428	0.270	0.166	0.089	0.054	0.031	0.011
16	−0.080	−0.029	−0.012	−0.010	−0.007	−0.006	−0.001	−0.002
17a	−0.535	−0.319	−0.143	−0.132	−0.100	−0.044	−0.015	−0.003
17b	0.535	0.290	0.143	0.132	0.100	0.044	0.015	0.003
21a	0.327	0.209	0.123	0.077	0.042	0.026	0.015	0.006
21b	−0.327	−0.209	−0.123	−0.077	−0.042	−0.026	−0.015	−0.006
22a	0.385	0.245	0.145	0.090	0.050	0.030	0.017	0.007
22b	−0.385	−0.245	−0.145	−0.090	−0.050	−0.030	−0.017	−0.007

Table 34: Tabulated values of the systematic uncertainties of $\frac{d\sigma}{dt}(\gamma p \to \phi Y)$ for systematic checks listed in Sec. 6 under the same indexes.

$80 < W < 90$ GeV					
t range (GeV^2)	$\langle t \rangle$ (GeV^2)	$\frac{d\sigma}{dt}(\gamma p \to \phi Y)$ (nb/GeV^2)	Stat. (nb/GeV^2)	Syst. (nb/GeV^2)	Total (nb/GeV^2)
1.20 - 1.80	1.453	18.10	1.24	+2.80−2.22	+3.06−2.54
1.80 - 2.70	2.158	6.79	0.54	+0.70−0.60	+0.89−0.81
2.70 - 3.60	3.077	2.42	0.33	+0.35−0.46	+0.48−0.57
3.60 - 4.80	4.103	0.70	0.19	+0.26−0.11	+0.32 -0.22
4.80 - 6.50	5.517	0.38	0.17	+0.09−0.12	+0.19−0.21
$90 < W < 100$ GeV					
t range (GeV^2)	$\langle t \rangle$ (GeV^2)	$\frac{d\sigma}{dt}(\gamma p \to J/\phi Y)$ (nb/GeV^2)	Stat. (nb/GeV^2)	Syst. (nb/GeV^2)	Total (nb/GeV^2)
1.20 - 1.80	1.454	16.93	1.21	+2.21−1.93	+2.52−2.28
1.80 - 2.70	2.161	5.86	0.50	+0.72−0.64	+0.88−0.81
2.70 - 3.60	3.073	2.09	0.28	+0.28−0.39	+0.40−0.48
3.60 - 4.80	4.106	0.59	0.14	+0.39−0.22	+0.41−0.26
4.80 - 6.50	5.500	0.35	0.11	+0.14−0.15	+0.18−0.19
$100 < W < 120$ GeV					
t range (GeV^2)	$\langle t \rangle$ (GeV^2)	$\frac{d\sigma}{dt}(\gamma p \to J/\phi Y)$ (nb/GeV^2)	Stat. (nb/GeV^2)	Syst. (nb/GeV^2)	Total (nb/GeV^2)
1.20 - 1.80	1.459	15.83	1.19	+2.61−2.23	+2.87−2.53
1.80 - 2.70	2.173	5.85	0.43	+0.99−0.56	+1.08−0.70
2.70 - 3.60	3.079	2.42	0.27	+0.33−0.41	+0.43−0.49
3.60 - 4.80	4.106	1.02	0.26	+0.32−0.22	+0.41−0.34
4.80 - 6.50	5.499	0.29	0.09	+0.10−0.13	+0.14−0.16

Table 35: Tabulated values of $\frac{d\sigma}{dt}(\gamma p \to \phi Y)$ with statistical error (stat.), systematic uncertainty (syst.) and total error for the kinematic range $\frac{M_Y^2}{-t} < 100$ and three W bins $80 < W < 90$ GeV, $90 < W < 100$ and $100 < W < 120$ GeV.

Systematic uncertainty of $\frac{d\sigma}{dt}(\gamma p \to \phi Y)$ (nb/GeV^2) $80 < W < 90$ GeV					
	t range (GeV^2)				
Check	1.2 - 1.8	1.8 - 2.7	2.7 - 3.6	3.6 - 4.8	4.8 - 6.5
1a	0.000	0.000	0.000	0.000	0.000
1b	0.000	0.000	0.000	0.000	0.000
2a	0.459	0.036	0.000	0.000	0.002
2b	1.582	0.011	0.000	−0.001	0.004
3a	−0.173	0.043	0.024	0.009	0.006
3b	−0.080	−0.007	0.024	−0.010	−0.004
3c	1.072	0.234	0.033	0.051	0.039
3d	−0.398	−0.170	−0.007	−0.020	−0.008
4a	−0.254	−0.192	0.138	−0.011	−0.057
4b	0.660	0.072	0.092	0.095	0.057
5a	−0.398	−0.095	−0.017	0.075	−0.046
5b	0.250	0.180	0.165	0.163	−0.015
6a	−0.133	−0.180	−0.385	−0.027	−0.009
6b	0.566	0.244	0.088	0.136	−0.016
7a	0.681	0.232	0.056	−0.026	0.010
7b	0.040	−0.216	−0.004	0.025	−0.001
10a	0.456	−0.083	−0.091	−0.028	−0.021
10b	0.392	−0.064	−0.073	−0.023	−0.017
10c	0.460	−0.090	−0.179	−0.080	−0.080
10d	−0.570	0.006	0.108	0.046	0.051
11	−1.675	0.039	0.094	0.009	−0.026
12a	0.785	0.289	0.099	0.027	0.013
12b	−0.579	−0.214	−0.073	−0.020	−0.010
12c	0.821	0.303	0.103	0.029	0.013
12d	−0.487	−0.179	−0.061	−0.017	−0.008
13a	−0.004	0.000	0.000	0.000	0.001
13b	0.004	0.000	0.000	0.000	−0.001
14a	−0.593	−0.228	−0.079	−0.021	−0.006
14b	0.643	0.248	0.086	0.022	0.006
16	−0.035	−0.026	−0.009	0.001	−0.009
18a	−0.284	−0.111	−0.037	−0.009	−0.003
18b	0.260	0.097	0.031	0.007	0.002
18c	−0.369	−0.093	−0.022	−0.004	−0.001
18d	0.331	0.084	0.019	0.003	0.001
21a	0.308	0.116	0.041	0.012	0.006
21b	−0.308	−0.116	−0.041	−0.012	−0.006
22a	0.362	0.136	0.048	0.014	0.008
22b	−0.362	−0.136	−0.048	−0.014	−0.008

Table 36: Tabulated values of the systematic uncertainties of $\frac{d\sigma}{dt}(\gamma p \to \phi Y)$ for $80 < W < 90$ GeV, for systematic checks listed in Sec. 6 under the same indexes.

Systematic uncertainty of $\frac{d\sigma}{dt}(\gamma p \to \phi Y)$ (nb/GeV^2) $90 < W < 100$ GeV					
	t range (GeV^2)				
Check	1.2 - 1.8	1.8 - 2.7	2.7 - 3.6	3.6 - 4.8	4.8 - 6.5
1a	0.000	0.000	0.000	0.000	0.000
1b	0.000	0.000	0.000	0.000	0.000
2a	0.198	0.000	0.000	0.000	0.000
2b	1.056	0.075	0.000	0.000	0.000
3a	−0.072	−0.098	−0.013	−0.029	0.003
3b	−0.022	0.020	−0.025	−0.004	0.000
3c	0.876	0.349	0.166	0.037	0.037
3d	−0.476	−0.072	−0.074	0.077	−0.010
4a	−0.090	0.089	−0.142	0.016	−0.079
4b	0.033	0.011	−0.106	0.023	0.042
5a	−0.961	−0.469	−0.072	−0.084	−0.016
5b	0.962	0.213	−0.037	0.070	0.047
6a	−0.839	0.121	−0.085	−0.141	−0.008
6b	0.273	0.363	−0.050	0.356	0.085
7a	0.995	0.308	0.010	0.027	0.020
7b	−0.792	−0.212	−0.059	−0.023	−0.011
10a	0.293	−0.121	−0.152	−0.058	−0.042
10b	−0.539	0.006	0.121	0.049	0.036
10c	0.265	−0.112	−0.204	−0.106	−0.100
10d	−0.355	0.003	0.153	0.080	0.077
11	0.140	−0.046	−0.123	−0.070	−0.072
12a	0.125	0.041	0.014	0.004	0.002
12b	−0.109	−0.036	−0.012	−0.003	−0.002
12c	0.028	0.008	0.002	0.000	0.001
12d	−0.023	−0.004	−0.001	0.000	0.000
13a	0.004	0.001	0.000	0.000	0.000
13b	−0.004	−0.001	0.000	0.000	0.000
14a	−0.540	−0.200	−0.070	−0.020	−0.012
14b	0.584	0.218	0.076	0.022	0.013
16	−0.056	−0.003	−0.008	0.000	−0.001
18a	−0.294	−0.124	−0.049	−0.014	−0.008
18b	0.277	0.114	0.044	0.012	0.006
18c	−0.466	−0.130	−0.035	−0.008	−0.003
18d	0.426	0.119	0.032	0.007	0.003
21a	0.288	0.100	0.036	0.010	0.006
21b	−0.288	−0.100	−0.036	−0.010	−0.006
22a	0.339	0.117	0.042	0.012	0.007
22b	−0.339	−0.117	−0.042	−0.012	−0.007

Table 37: Tabulated values of the systematic uncertainties of $\frac{d\sigma}{dt}(\gamma p \to \phi Y)$ for $90 < W < 100$ GeV, for systematic checks listed in Sec. 6 under the same indexes.

Systematic uncertainty of $\frac{d\sigma}{dt}(\gamma p \to \phi Y)$ (nb/GeV^2) $100 < W < 120$ GeV					
	t range (GeV^2)				
Check	1.2 - 1.8	1.8 - 2.7	2.7 - 3.6	3.6 - 4.8	4.8 - 6.5
1a	−0.713	−0.019	0.004	0.001	0.000
1b	0.272	−0.008	−0.001	0.000	0.000
2a	0.336	0.046	−0.002	0.000	0.000
2b	0.108	0.143	0.002	0.000	0.000
3a	−0.005	0.022	0.027	0.008	0.006
3b	0.005	−0.005	−0.014	−0.015	−0.002
3c	0.836	0.339	−0.038	0.024	0.022
3d	−0.127	−0.051	0.000	−0.034	0.022
4a	0.074	−0.052	−0.027	0.098	−0.033
4b	0.228	0.029	−0.019	0.059	0.054
5a	−0.810	−0.029	−0.045	0.049	0.032
5b	0.200	0.100	−0.012	0.086	0.019
7a	1.959	0.674	0.106	0.069	0.017
7b	−0.955	−0.225	−0.090	0.006	−0.010
6a	0.199	0.013	−0.145	−0.075	−0.084
6b	0.268	0.295	0.004	0.221	0.042
10a	0.430	−0.134	−0.188	−0.088	−0.030
10b	−0.724	0.019	0.135	0.067	0.024
10c	0.305	−0.115	−0.245	−0.160	−0.077
10d	−0.413	0.025	0.157	0.099	0.045
11	−0.944	0.019	0.051	−0.024	−0.038
12a	0.533	0.238	0.106	0.049	0.016
12b	−0.465	−0.207	−0.092	−0.042	−0.013
12c	−0.530	−0.256	−0.118	−0.054	−0.018
12d	0.703	0.333	0.149	0.070	0.023
13a	0.020	0.003	−0.001	0.000	0.000
13b	−0.020	−0.003	0.001	0.000	0.000
14a	−0.525	−0.203	−0.082	−0.036	−0.010
14b	0.570	0.221	0.088	0.039	0.011
16	−0.115	−0.005	−0.006	−0.005	0.000
18a	−0.349	−0.161	−0.076	−0.034	−0.009
18b	0.328	0.147	0.067	0.029	0.008
18c	−0.477	−0.145	−0.048	−0.016	−0.003
18d	0.440	0.134	0.044	0.015	0.003
21a	0.269	0.099	0.041	0.017	0.005
21b	−0.269	−0.099	−0.041	−0.017	−0.005
22a	0.317	0.117	0.048	0.020	0.006
22b	−0.317	−0.117	−0.048	−0.020	−0.006

Table 38: Tabulated values of the systematic uncertainties of $\frac{d\sigma}{dt}(\gamma p \to \phi Y)$ for $100 < W < 120$ GeV, for systematic checks listed in Sec. 6 under the same indexes.

t range (GeV^2)	$\langle t \rangle$ (GeV^2)	$\frac{d\sigma}{dt}(\gamma p \to J/\psi Y)$ (nb/GeV^2)	Stat. (nb/GeV^2)	Syst. (nb/GeV^2)	Total (nb/GeV^2)
1.20 - 1.50	1.34	13.48	2.77	$+3.16\ -2.83$	$+4.20\ -3.96$
1.50 - 2.00	1.73	9.49	1.75	$+0.91\ -1.13$	$+1.97\ -2.09$
2.00 - 2.50	2.23	6.25	1.53	$+1.34\ -0.94$	$+2.03\ -1.79$
2.50 - 3.25	2.84	3.65	0.87	$+0.36\ -0.71$	$+0.94\ -1.13$
3.25 - 4.50	3.81	2.04	0.56	$+0.34\ -0.59$	$+0.65\ -0.81$
4.50 - 6.50	5.39	1.21	0.44	$+0.24\ -0.37$	$+0.50\ -0.58$

Table 39: Tabulated values of $\frac{d\sigma}{dt}(\gamma p \to J/\psi Y)$ with statistical error (stat.), systematic uncertainty (syst.) and total error for the kinematic range $80 < W < 120$ GeV and $\frac{M_V^2}{-t} < 100$.

Systematic uncertainty of $\frac{d\sigma}{dt}(\gamma p \to J/\psi Y)$ (nb/GeV^2)						
	t range (GeV^2)					
Check	1.2 - 1.5	1.5 - 2.0	2.0 - 2.5	2.5 - 3.25	3.25 - 4.5	4.5 - 6.5
1a	0.116	0.032	0.026	0.015	0.007	0.004
1b	−0.068	−0.029	−0.007	−0.004	−0.002	−0.001
2a	−0.328	−0.250	−0.177	−0.119	−0.081	−0.032
2b	−1.534	−0.547	0.005	−0.053	−0.054	−0.018
3a	0.002	−0.541	0.063	0.015	0.010	0.006
3b	−0.129	0.153	−0.036	−0.036	−0.016	−0.003
3c	0.014	0.075	0.052	0.023	0.007	0.001
3d	−0.059	−0.082	−0.027	−0.024	−0.010	−0.005
4a	−1.402	0.319	−0.113	0.177	0.113	0.048
4b	−0.459	−0.096	−0.312	0.013	0.226	−0.022
5a	−0.318	0.296	0.122	0.094	0.043	0.024
5b	−0.165	−0.116	−0.082	−0.045	0.121	−0.013
6a	−0.962	−0.146	0.167	−0.045	−0.189	0.200
6b	0.181	−0.235	−0.767	−0.506	−0.508	−0.204
7a	−0.951	0.562	0.695	0.153	−0.070	−0.191
7b	2.825	−0.562	1.050	−0.404	0.000	−0.136
8a	−0.751	0.095	0.086	0.103	0.084	0.049
8b	0.937	−0.115	−0.122	−0.121	−0.090	−0.056
8c	−0.603	0.014	0.060	0.119	0.118	0.084
8d	0.688	−0.027	−0.094	−0.141	−0.131	−0.124
9	−0.133	0.126	0.010	−0.056	−0.090	−0.134
12a	0.505	0.356	0.258	0.140	0.080	0.049
12a	−0.431	−0.298	−0.217	−0.119	−0.067	−0.042
12c	−0.348	−0.186	−0.190	−0.080	−0.048	−0.034
12d	0.443	0.253	0.234	0.105	0.071	0.035
13a	−0.073	−0.021	0.007	0.011	−0.001	−0.003
13b	0.066	0.016	−0.009	−0.009	0.002	0.003
19a	−0.105	−0.074	−0.049	−0.028	−0.016	−0.009
19b	0.105	0.074	0.049	0.028	0.016	0.009
21a	0.229	0.161	0.106	0.062	0.035	0.021
21b	−0.229	−0.161	−0.106	−0.062	−0.035	−0.021
22a	0.270	0.190	0.125	0.073	0.041	0.024
22b	−0.270	−0.190	−0.125	−0.073	−0.041	−0.024

Table 40: Tabulated values of the systematic uncertainties of $\frac{d\sigma}{dt}(\gamma p \to J/\psi Y)$ for systematic checks listed in Sec. 6 under the same indexes.

$80 < W < 100$ GeV					
t range (GeV^2)	$\langle t \rangle$ (GeV^2)	$\frac{d\sigma}{dt}(\gamma p \to J/\psi Y)$ (nb/GeV^2)	Stat. (nb/GeV^2)	Syst. (nb/GeV^2)	Total (nb/GeV^2)
1.20 - 1.50	1.34	13.97	3.67	$+2.06\ -4.01$	$+4.21\ -5.44$
1.50 - 2.20	1.80	8.46	2.03	$+1.51\ -1.41$	$+2.53\ -2.47$
2.20 - 3.20	2.63	2.93	0.94	$+0.99\ -0.64$	$+1.37\ -1.14$
3.20 - 5.00	4.04	1.68	0.62	$+0.37\ -0.88$	$+0.72\ -1.07$
$100 < W < 120$ GeV					
t range (GeV^2)	$\langle t \rangle$ (GeV^2)	$\frac{d\sigma}{dt}(\gamma p \to J/\psi Y)$ (nb/GeV^2)	Stat. (nb/GeV^2)	Syst. (nb/GeV^2)	Total (nb/GeV^2)
1.20 - 1.50	1.35	14.31	3.75	$+3.85\ -1.38$	$+5.37\ -3.99$
1.50 - 2.20	1.83	8.05	1.88	$+1.42\ -1.12$	$+2.35\ -2.19$
2.20 - 3.20	2.64	5.66	1.33	$+1.26\ -0.60$	$+1.84\ -1.46$
3.20 - 5.00	3.93	2.16	0.67	$+0.32\ -0.49$	$+0.74\ -0.83$

Table 41: Tabulated values of $\frac{d\sigma}{dt}(\gamma p \to J/\psi Y)$ with statistical error (stat.), systematic uncertainty (syst.) and total error for the kinematic range $\frac{M_Y^2}{-t} < 100$ and two W bins $80 < W < 100$ GeV and $100 < W < 120$ GeV.

Systematic uncertainty of $\frac{d\sigma}{dt}(\gamma p \to J/\psi Y)$ (nb/GeV^2) $80 < W < 100$ GeV				
	t range (GeV^2)			
Check	1.2 - 1.5	1.5 - 2.2	2.2 - 3.2	3.2 - 5.0
1a	0.00	0.00	0.00	0.00
1b	−0.17	−0.04	−0.02	−0.01
2a	−0.60	−0.48	−0.17	−0.11
2b	−2.42	−0.92	−0.13	0.14
3a	0.08	−0.39	0.02	0.01
3b	−0.31	−0.11	−0.04	−0.02
3c	0.00	0.04	0.01	0.01
3d	−0.07	−0.08	−0.01	−0.01
4a	−2.58	0.05	−0.23	0.01
4b	−0.31	−0.25	−0.16	0.14
5a	−0.33	0.42	0.12	0.07
5b	−0.11	−0.08	−0.06	0.19
6a	−1.48	−0.43	−0.24	0.17
6b	−0.29	0.51	−0.41	−0.84
7a	−0.87	0.95	0.97	−0.32
7b	1.67	0.66	0.21	0.00
8a	−0.10	0.18	0.08	0.09
8b	0.07	−0.21	−0.10	−0.10
8c	−0.18	0.11	0.08	0.08
8d	0.16	−0.13	−0.10	−0.11
9	0.16	0.09	−0.03	−0.06
12a	0.36	0.24	0.08	0.05
12b	−0.28	−0.18	−0.06	−0.04
12c	0.31	0.22	0.07	0.05
12d	−0.19	−0.13	−0.04	−0.03
13a	−0.07	0.00	0.01	−0.03
13b	0.06	0.00	−0.01	0.02
20a	−1.30	−0.79	−0.27	−0.16
20b	1.30	0.79	0.27	0.16
21a	0.25	0.15	0.05	0.03
21b	−0.25	−0.15	−0.05	−0.03
22a	0.30	0.18	0.06	0.04
22b	−0.30	−0.18	−0.06	−0.04

Table 42: Tabulated values of the systematic uncertainties of $\frac{d\sigma}{dt}(\gamma p \to J/\psi Y)$ for $80 < W < 100$ GeV, for systematic checks listed in Sec. 6 under the same indexes.

Systematic uncertainty of $\frac{d\sigma}{dt}(\gamma p \to J/\psi Y)$ (nb/GeV^2) $100 < W < 120$ GeV				
	t range (GeV^2)			
Check	$1.2 - 1.5$	$1.5 - 2.2$	$2.2 - 3.2$	$3.2 - 5.0$
1a	0.21	0.04	0.03	0.01
1b	0.02	−0.01	0.01	0.00
2a	−0.13	−0.09	−0.07	−0.05
2b	0.18	0.24	−0.21	−0.11
3a	0.04	−0.40	0.08	0.02
3b	−0.16	0.29	−0.03	−0.01
3c	0.03	0.13	0.04	0.00
3d	−0.10	−0.08	−0.05	−0.01
4a	0.49	0.43	0.34	0.19
4b	−0.43	0.04	0.08	0.13
5a	0.16	0.13	0.08	0.03
5b	−0.16	−0.09	−0.06	−0.02
6a	0.67	0.79	−0.05	−0.27
6b	2.10	0.84	1.16	−0.31
7a	0.73	−0.16	−0.06	−0.04
7b	2.93	−0.90	−0.29	−0.03
8a	−0.55	0.04	0.15	0.10
8b	0.56	−0.05	−0.17	−0.10
8c	−0.55	−0.08	0.04	0.11
8d	0.53	0.02	−0.17	−0.17
9	−0.04	0.09	−0.03	−0.13
12a	0.76	0.43	0.30	0.11
12b	−0.66	−0.37	−0.26	−0.09
12c	−0.89	−0.50	−0.35	−0.12
12d	1.06	0.60	0.42	0.15
13a	−0.14	−0.05	−0.04	−0.01
13b	0.14	0.05	0.04	0.01
20a	−0.13	−0.07	−0.05	−0.02
20b	0.13	0.07	0.05	0.02
21a	0.26	0.15	0.10	0.04
21b	−0.26	−0.15	−0.10	−0.04
22a	0.30	0.17	0.12	0.05
22b	−0.30	−0.17	−0.12	−0.05

Table 43: Tabulated values of the systematic uncertainties of $\frac{d\sigma}{dt}(\gamma p \to J/\psi Y)$ for $100 < W < 120$ GeV, for systematic checks listed in Sec. 6 under the same indexes.

t range (GeV^2)	$\frac{d\sigma}{dt}(\phi)/\frac{d\sigma}{dt}(\rho)$	Stat.	Syst.	Total
1.20 - 1.55	0.127	0.008	+0.021 –0.018	+0.022 –0.020
1.55 - 1.90	0.157	0.009	+0.022 –0.017	+0.024 –0.019
1.90 - 2.30	0.175	0.013	+0.019 –0.020	+0.023 –0.023
2.30 - 2.70	0.172	0.015	+0.014 –0.014	+0.021 –0.021
2.70 - 3.20	0.189	0.022	+0.019 –0.036	+0.029 –0.042
3.20 - 3.80	0.193	0.030	+0.029 –0.038	+0.042 –0.049
3.80 - 4.80	0.228	0.039	+0.066 –0.053	+0.077 –0.066
4.80 - 6.50	0.228	0.052	+0.078 –0.070	+0.094 –0.087

Table 44: Tabulated values of the cross section ratio ϕ/ρ, with statistical error (stat.), systematic uncertainty (syst.) and total error for the kinematic range $80 < W < 120$ GeV and $\frac{M_V^2}{-t} < 100$.

t range (GeV^2)	$\frac{d\sigma}{dt}(\psi)/\frac{d\sigma}{dt}(\rho)$	Stat.	Syst.	Total
1.20 - 1.50	0.086	0.018	+0.021 –0.020	+0.028 –0.027
1.50 - 2.00	0.123	0.023	+0.014 –0.019	+0.027 –0.030
2.00 - 2.50	0.178	0.044	+0.038 –0.037	+0.058 –0.057
2.50 - 3.25	0.250	0.061	+0.023 –0.061	+0.065 –0.086
3.25 - 4.50	0.355	0.099	+0.070 –0.130	+0.121 –0.163
4.50 - 6.50	0.685	0.257	+0.226 –0.261	+0.342 –0.366

Table 45: Tabulated values of the cross section ratio ψ/ρ, with statistical error (stat.), systematic uncertainty (syst.) and total error for the kinematic range $80 < W < 120$ GeV and $\frac{M_V^2}{-t} < 100$.

References

[1] For a recent review see e.g. J.A. Crittenden, *Exclusive Production of Neutral Vector Mesons at the Electron-Proton Collider HERA,* Springer Tracts in Modern Physics, Volume 140 (Springer, Berlin Heidelberg, 1997).

[2] See H. Abramowicz and A. Caldwell, DESY 98–192 (1998), accepted by Rev. Mod. Phys., and references therein.

[3] L. Frankfurt and M. Strikman, Phys. Rev. Lett. 63 (1989) 1914.

[4] A.H. Mueller and W-K. Tang, Phys. Lett. B 284 (1992) 123.

[5] ZEUS Collaboration, J. Breitweg et al., Eur. Phys. J. C 14 (2000) 213.

[6] D.Yu. Ivanov, Phys. Lett. B 478 (2000) 101.

[7] J. Bartels et al., Phys. Lett. B 375 (1996) 301.

[8] G. Levman, ZEUS-Note 95-088.

[9] J.J. Sakurai, Ann. Phys. (NY) 11 (1960) 1.

[10] M. Gell-Mann and F. Zachariasen, Phys. Rev. 124 (1983) 953.

[11] T.H. Bauer et al., Rev. Mod. Phys. 50 (1978) 261.

[12] J.J. Sakurai and D. Schildknecht, Phys. Lett. B40 (1972), 121.

[13] T. Regge, Nuovo Cimento 14 (1959) 951.

[14] T. Regge, Nuovo Cimento 18 (1960) 947.

[15] P.D.B. Collins, "An introduction to Regge theory and high energy physics", Cambridge (Cambridge University Press) (1977).

[16] A. Donnachie, P.V. Landshoff, Nucl. Phys. B231 (1984) 189;
A. Donnachie, P.V. Landshoff, Phys. Lett. B191 (1987) 309;
A. Donnachie, P.V. Landshoff, Nucl. Phys. B303 (1988) 634;
A. Donnachie, P.V. Landshoff, Phys. Lett. B296 (1992) 227.

[17] I.Y. Pomeranchuk, Sov. Phys. JETP 7 499 (1985). Reactions of High Energy Particles", New Series, Vol. 12b, H. Schopper, Ed. 1987.

[18] K. Goulianos, "Diffractive Interactions of Hadron at High Energies." Phys. Rep. 101 (1983) 170.

[19] K. Schilling, G. Wolf, Nucl. Phys. B61 (1973) 381.

[20] L. Adamczyk, PhD thesis, Mining and Metallurgy U., Cracow, DESY-THESIS-1999-045 (1999).

[21] S.J. Brodsky et al., Phys. Rev. D50 (1994) 3134.

[22] M.G. Ryskin, Zeit. Phys. C57 (1993) 89;
M.G. Ryskin et al., Zeit. Phys. C76 (1997) 231.

[23] D.Yu. Ivanov, Phys. Rev. D 53 (1996) 3564.

[24] V.L. Chernyak and A.R. Zhitnitsky, Phys. Rep. 112 (1984) 173.

[25] I. Ginsburg and D. Yu. Ivanov, Phys. Rev. D54 (1996) 5523.

[26] H. Abramowicz, L. Frankfurt and M. Strikman, "Surveys in High Energy Physics" 11 (1999) 51.

[27] A. Kowal, ZEUS Note in preparation.

[28] G. Wolf, "HERA: physics, machine and experiments", Lectures given at *Inst. on Techniques and Concepts of High Energy Physics,* St. Croix, Virgin Islands, June 19-30, 1986, DESY 86-089 (1986).

[29] HERA, "A proposal for a large Electron-Proton Colliding Beam Facility at DESY", DESY HERA 81-10.

[30] The ZEUS Detector, Status Report 1993, DESY 1993.

[31] A. Andersen t al., Nucl. Instr. and Meth. A336 (1993) 23.

[32] M. Derrick et al., Nucl. Instrum. Methods A 309, 77 (1991); A. Bernstein et al., Nucl. Instrum. Methods A 336, 23 (1993).

[33] A. Andersen et al., Nucl. Instrum. Methods A 309, 101 (1991).

[34] N. Harnew et al., Nucl. Instr. and Meth. A 279 (1989) 290;
B. Foster et al., Nucl. Phys. B 32 (Proc. Suppl.) (1993) 181;
B. Foster et al., Nucl. Instr. and Meth. A338 (1994) 254.

[35] J. Andruszków et al., DESY 92-006 (1992).

[36] G.F. Hartner et al., ZEUS-Note 96-013.

[37] NOISE96S, ZEUS user library

[38] C. Youngman, "The ZEUS Data Acquisition System", DESY 92-150A; W.H. Smith et al., "The ZEUS Trigger System", ZEUS 89-084.

[39] TRAKCLU, ZEUS user library.

[40] M. Kasprzak, PhD thesis, Warsaw University, DESY F35D-96-16 (1996);
ZEUS note 95-069 (1995).

[41] B.R. Webber, Ann. Rev. Nucl. Part. Sci. 36 (1986) 253;
G. Marchesini et al., Comput. Phys. Comm. 67 (1992) 465.

[42] H.Abramowicz et all., Phys. Lett. B269 (1991) 465.

[43] R.L. Coll et al., Phys. Rev. Lett. 48 (1982) 1451.

[44] B. List, "Diffractive J/ψ production in electron-proton collisions at the Hera storage ring", Diploma Thesis (Tech. Univ. Berlin), 1993 (unpublished);
A. Mastroberardino, ZEUS Note 98-030;
A. Mastroberardino, ZEUS Note 98-057.

[45] Y. Akimov et al., Phys. Rev. D14 (1976) 3148.

[46] K. Goulianos, Phys. Rep. 101 (no. 3) (1983) 169.

[47] JETSET 6.3: T. Sjöstrand, Comput. Phys. Commun. 39 (1986) 347.

[48] B. Andersson et al., Phys. Rep. 97 (1983) 31.

[49] ZEUS Collaboration, J. Breitweg et al., Eur. Phys. J. C2 (1998) 247.

[50] R. Brun et al., "GEANT3", CERN DD/EE/11-1 (1989).

[51] MOZART, ZEUS internal package.

[52] Els de Wolf (editor) et al., "ZGANA, ZEUS trigger simulation library".

[53] D. Westphal, PhD Thesis, DESY Internal Report: F35D-93-04, April 1993

[54] ZEUS Luminosity Group, L. Adamczyk et al., ZEUS-Note 01-004.

[55] K. Piotrzkowski and L. Suszycki, BREMGE, *A Monte Carlo Generator of High Energy Electron-Proton and Electron-Nucleus Bremsstrahlung Event Generator,* Proc. of the Workshop, Physics at HERA, ed. W. Buchmüller and G. Ingelman, Hamburg (1991) 1463.

[56] Albrow et al., Nucl. Phys. B108 (1975) 1.

[57] UA8 Collaboration, A. Brandt et al., Nucle. Phys. B514 (1998) 3.

[58] P. Söding, Phys. Lett. 19 (1966) 702.

[59] M. Gluck, E. Reya and A. Vogt, Z. Phys. C67 (1995) 433.

[60] H. Plothow-Besch/CERN-ETT/TT, PDFLIB, User's Manual.

[61] H1 Collaboration, C. Adloff et al., DESY Report 00-070 (2000);
ZEUS Collaboration, J. Breitweg et al., DESY Report 00-084 (2000).

[62] ZEUS Collaboration, J. Breitweg et al., Eur. Phys. J. C 6 (1999) 603.

[63] ZEUS Collaboration, talk given at the XXXth International Conference oh High Energy Physics, Osaka, Japan, July 2000.

[64] J.R. Forshaw and M.G. Ryskin, Zeit. f. Phys. C 68 (1995) 137.

[65] J. Bartels et al., Phys. Lett. B 348 (1995) 589.

[66] J. Bjorken, Phys. Rev. D47 (1993) 101.

[67] D. Szuba, private communication.